



UNIVERSITÄT ROSTOCK

**From Clouds to Cores:
Advancing the Understanding of
Irradiated Giant Exoplanets**

Kumulative Dissertation
zur Erlangung des akademischen Grades
doctor rerum naturalium (Dr. rer. nat.)
der Mathematisch-Naturwissenschaftlichen Fakultät
der Universität Rostock

vorgelegt von
Anna Julia Poser,
geboren am 17. Februar 1992 in Hagen

Rostock, 2024

Datum der Einreichung: 12. Juni 2024
Datum der Disputation: 11. Oktober 2024

1. Gutachter und Betreuer: Prof. Dr. Ronald Redmer, Universität Rostock, Institut für Physik
2. Gutachterin: Prof. Dr. Ravit Helled, University of Zurich, Department of Astrophysics

Adresse: Universität Rostock
Institut für Physik
18059 Rostock

Für meine Familie.

It's been said that astronomy is a humbling, and I might add, a character-building experience. To my mind, there is perhaps no better demonstration of the folly of human conceits than this distant image of our tiny world. To me, it underscores our responsibility to deal more kindly and compassionately with one another and to preserve and cherish that pale blue dot, the only home we've ever known.

Carl Sagan (1934–1996)

Abstract

Past exoplanet space missions, such as the Kepler mission, primarily aimed at discovering new planets. In contrast, current and upcoming missions, such as the James Webb Space Telescope mission, are transforming the field by focusing on detailed atmospheric observations of the distant planets. These missions provide valuable data on the atmospheres, which deliver crucial constraints for atmospheric and interior models of planets.

This thesis examines the synergy between atmosphere, interior, and thermal evolution models that replicate observations to ultimately inform models of planetary formation and evolution.

The impact of the atmospheric thermal structure, particularly the pressure-temperature (P - T) conditions, on the composition and radius evolution of irradiated gas giant exoplanets is explored. Coupled atmosphere, interior, and thermal evolution models are employed to analyse how the effect of cloudy atmospheres impacts the inferred composition, specifically the heavy element content, and long-term radius evolution. The results highlight the importance of atmospheric processes that affect the deep atmosphere and thus the radiative-convective boundary.

Furthermore, the impact of the P - T conditions in the atmospheres of highly irradiated planets on transport properties, such as the electrical conductivity, is investigated. By applying an ionisation and transport model for the partially ionised plasma in the atmosphere, the efficiency of the Ohmic dissipation mechanism – proposed to inflate close-in gas giant planets – is reassessed. Magnetic induction processes for warm to ultra-hot giant planets are examined, revealing two regimes of processes that affect the efficiency of Ohmic heating in strongly irradiated gas planets.

This thesis advances the understanding of irradiated giant planets by shedding light on how their atmospheric conditions influence key bulk and atmospheric transport characteristics, directly linked to broader theories of planetary formation and evolution.

Kurzzusammenfassung

Vergangene Exoplanetenmissionen konzentrierten sich hauptsächlich auf die Entdeckung neuer Planeten. Im Gegensatz dazu fokussieren sich aktuelle und zukünftige Missionen wie die James Webb Space Telescope Mission auf präzise Atmosphärenbeobachtungen dieser weit entfernten Objekte. Diese Missionen liefern wertvolle Daten, die als Anhaltspunkte für Modelle der Atmosphären und inneren Struktur der Planeten dienen.

In dieser Arbeit wird die Synergie zwischen Atmosphären-, Struktur- und Evolutionsmodellen von bestrahlten Gasplaneten untersucht. Ziel dieser kombinierten Modelle ist es, Beobachtungen abzubilden und dadurch wertvolle Informationen über die Entstehung und Entwicklung von Planeten zu gewinnen.

Der Schwerpunkt liegt auf den Druck-Temperatur-Bedingungen (P - T) in den Atmosphären bestrahlter Gasplaneten. Durch die Verwendung kombinierter Atmosphären-, Struktur- und Evolutionsmodelle wird analysiert, wie sich die Auswirkungen von Wolken in der Atmosphäre auf die abgeleitete Zusammensetzung, insbesondere den Gehalt an schweren Elementen, und die thermische Evolution des Planeten auswirken. Ein spezifisches Atmosphärenmodell wird verwendet, um einen Effekt von Wolken in der Atmosphäre zu modellieren. Die Ergebnisse verdeutlichen die Bedeutung atmosphärischer Prozesse, die sich auf die tiefe Atmosphäre und damit auf die Grenze zum konvektiven Inneren auswirken.

Zusätzlich wird der Einfluss der P - T -Bedingungen auf die Transporteigenschaften, wie die elektrische Leitfähigkeit, untersucht. Ein Ionisierungs- und Transportmodell wird für das teilweise ionisierte Plasma in der Atmosphäre angewendet, um die Effizienz eines Mechanismus zur Aufblähung von Gasplaneten neu zu bewerten. Magnetische Induktionsprozesse für warme bis ultraheiße Gasplaneten werden untersucht, wobei zwei Regime identifiziert werden, die die Effizienz des Mechanismus bei stark bestrahlten Gasplaneten beeinflussen.

Diese Arbeit leistet einen Beitrag zum Verständnis von bestrahlten Gasplaneten, indem sie aufzeigt, wie die atmosphärischen Bedingungen den inneren Aufbau des Planeten und die Transporteigenschaften der Atmosphäre beeinflussen. Dies ist von Bedeutung für Theorien zur Entstehung und Evolution von Planeten.

Contents

1. Introduction	1
1.1. Interior Modelling of Giant Planets	4
1.1.1. Number and Availability of Observables	4
1.1.2. Warm Dense Matter: Equations of State	5
1.1.3. Atmospheric Thermal Structure	6
1.2. Exoplanetary Giant Planets Atmospheres	7
1.2.1. Thermal Structure by Observations	7
1.2.2. Thermal Structure by Theory	8
1.2.3. Cloudy Atmospheres	10
1.2.4. Ionised Atmospheres	12
1.3. Aim and Outline of this Thesis	12
2. Coupling Atmosphere, Interior, and Thermal Evolution Models	13
2.1. Interior and Thermal Evolution Modelling	13
2.1.1. Interior Structure	13
2.1.2. Radiative-Convective Boundary	15
2.1.3. Equations of State	16
2.1.4. Thermal Evolution	17
2.2. Atmospheric Modelling	18
2.2.1. Thermal Structures of Clear and Cloudy Atmospheres	19
2.2.2. Schematic of the Clear Thermal Structure	21
2.2.3. Calibration of the Free Parameters	23
2.2.4. Modifications of the Cloud Model	24
3. From Clouds to Cores: Results	25
3.1. Cloudy Atmospheres	25
3.1.1. On the Connections of Planetary Bulk and Atmospheric, and Stellar Abundances	25
3.1.2. Impact on the Derived Bulk Metallicity	28
3.1.3. Impact on the Thermal Long-Term Evolution	30
3.2. Ionised Atmospheres	33
3.2.1. On the Radius Anomaly of the Giant Planet Population	33
3.2.2. Ionisation and Transport	35
3.2.3. Magnetic Induction Processes	37
4. Summary and Perspectives	41
5. Publications	43
5.1. The Effect of Clouds as an Additional Opacity Source on the Inferred Metallicity of Giant Exoplanets	43

5.2. The effect of cloudy atmospheres on the thermal evolution of warm giant planets from an interior modelling perspective	62
5.3. Ionization and transport in partially ionized multicomponent plasmas: Application to atmospheres of hot Jupiters	79
5.4. Magnetic induction processes in hot Jupiters, application to KELT-9b	92
A. Appendix	107
A.1. Entropy of Hydrogen and Helium-EoS in the Temperature-Pressure Plane	107
A.2. Introduction to Mass Fractions, Solar Abundances, and Conversions	108
A.2.1. Mass Fractions, Number of Particles and Molecular Masses	108
A.2.2. Protosolar and Present-Day Photospheric Mass Fractions	109
A.2.3. From Metal Mass Fractions to Abundance Ratios	110
A.3. MOGROP	113
A.3.1. Programme Overview	113
A.3.2. Interior Phase Space and Evolution Curves	113
A.4. Interior Metallicity Relations	115
A.4.1. $M_{\text{core}}-T_{\text{int}}$ relation	115
A.4.2. $Z_{\text{P}}-T_{\text{int}}$ relation	115
A.4.3. Additional Calculations for WASP-39b	117
A.5. On Grey and Mean Opacities	119
A.5.1. Obtaining Planck and Rosseland Mean Opacities	119
A.5.2. Semi-grey Model Extension with Rosseland Mean Opacities	122
A.6. Condensate Clouds	126
A.6.1. Thermal Stability Curves	126
A.6.2. Selected Other Works on Cloud Opacities	129
A.6.3. Several Cloud Layers	129
A.7. Electromagnetic Processes in Atmospheres	130
A.8. Software	131
A.9. Fundamental Constants and Planetary Data	132
Bibliography	135
Curriculum Vitae	171

List of Abbreviations

AIMD	Ab Initio Molecular Dynamics
ARIEL	Atmospheric Remote-sensing Infrared Exoplanet Large-survey
BS10	Batygin and Stevenson (2010)
CD21	EoS by Chabrier and Debras (2021)
CoRoT	Convection, Rotation and Planetary Transits
DFT	Density Functional Theory
DOI	Digital Object Identifier
EoS	Equation of State
ESPRESSO	Echelle Spectrograph for Rocky Exoplanet- and Stable Spectroscopic Observations
GCM	General Circulation Model
HARPS	High Accuracy Radial Velocity Planet Searcher
HD	Henry Draper catalogue
HED	High Energy Density
JWST	James Webb Space Telescope
KELT	Kilodegree Extremely Little Telescope
MAL	Mass Action Law
MD	Molecular Dynamics
MOGROP	Modellierungsprogramm für große Planeten
NIRPS	Near Infra Red Planet Searcher
PLATO	Planetary Transits and Oscillations of stars
RCB	Radiative-Convective Boundary
RT	Radiative Transfer
RTE	Radiative Transfer Equation
SCvH95	EoS by Saumon, Chabrier, and van Horn (1995)
TESS	Transiting Exoplanet Survey Satellite
TOI	TESS Object of Interest
WASP	Wide Angle Search for Planets
WDM	Warm Dense Matter

1. Introduction

Past exoplanet missions like Kepler [1, 2] and CoRoT [3] focused primarily on the detection of planets. However, present and upcoming missions such as the JWST [4], PLATO [5, 6], and ARIEL [7, 8] missions¹ are revolutionising the field by shifting the focus to detailed atmospheric observations. The JWST mission, which started operating in July 2022, is filling the general public and the scientific community with enthusiasm and excitement. Its primary goal in exoplanetary science is to observe the atmospheres of distant planets in unprecedented detail. The first observations of the atmosphere of the gaseous exoplanet WASP-39b already yielded extraordinary results, providing insight into its formation history through the analysis of chemical fingerprints [9–14]. Recent JWST data have also helped to solve the mystery of WASP-107b, which had previously posed challenges to models of its interior and evolution due to its low density [15, 16]. The data suggest not only the existence of exotic silicate and sand clouds but also a depletion of methane in its atmosphere [17]. This depletion is likely caused by vertical mixing associated with high internal temperatures [18, 19], offering new constraints for coupled atmosphere and interior models, which ultimately helped solve the WASP-107b puzzle [20].

The synergy of atmosphere, interior, and thermal evolution models represents the cutting edge of planetary science. The coupled models, informed by observations of the atmospheres, drive the future of planetary modelling, offering deeper insights into the complex and fascinating processes of planetary formation and evolution.

Understanding a planet’s interior structure begins with its birth. Planets form around young stars in disks made mainly of gas and dust. The disk, which is a by-product of star formation, resembles the composition of the molecular cloud that the star has formed from. The initial primordial composition of the planet is determined by several aspects: the composition of the disk, the location of the planet within the disk [21–24], and the formation pathway. In addition, timescales are crucial: the heaviest planets, gaseous giant planets like Jupiter with 318 Earth masses (M_E)², are believed to form fast. They need to obtain their final composition before the gas vanishes in order to reach large masses, ranging from 100 to 1800 M_E [25–27]. Two formation pathways are commonly accepted for giant planets [28]: either they form through gas accretion onto a solid core of $\sim 10 M_E$ [29–31] where the core is the result of pebble or planetesimal accretion [32], or through gravitational disk instability where gas and dust collapse into clumps without first building up a core [33, 34]. The bulk and atmospheric composition of giant planets mirror the complex formation environment, their formation pathway, and their subsequent evolution [35]. Thus, their composition serves as an indirect window into these processes [36, 37], making giant planets essential objects in connecting the dots between planetary formation, evolution, and their current interior structure and composition [35]. Fig. 1.1 illustrates this connection. Furthermore, their large masses are key in shaping the final architecture of planetary systems through gravity [38, 39].

Historically, our understanding of the formation and evolution of giant planets has largely stemmed from observational data and interior structure models of the Solar System’s gas and ice giants – Jupiter, Saturn, Uranus, and Neptune [40, 41]. Understanding the outer planets has been a significant goal in the field of planetary science for decades [42]. Various spacecraft have visited the outer planets, providing vital data on rotational period, gravitational and magnetic fields, and atmospheric composition. Such data are central for characterising the

¹CoRoT (Convection, Rotation and Planetary Transits), JWST (James Webb Space Telescope), PLATO (Planetary Transits and Oscillations of stars), ARIEL (Atmospheric Remote-sensing Infrared Exoplanet Large-survey)

²Table A.5 displays planetary reference data, such as M_E , and fundamental constants.

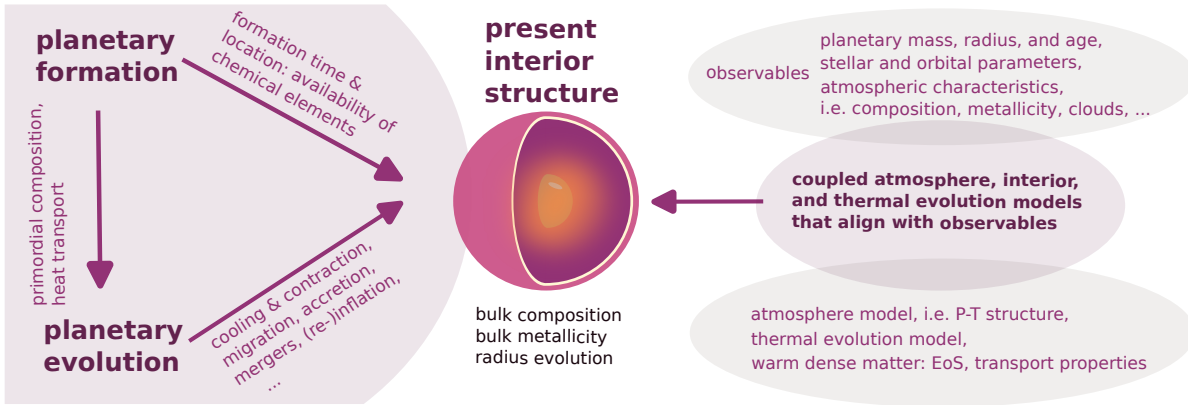


Figure 1.1.: Planetary formation, evolution, and the present interior structure are highly connected [35] (left side). The present interior structure serves as a window to past evolution and formation processes. Deriving the interior structure and composition with combined atmosphere, interior, and thermal evolution models is key for irradiated gas giants (right side). In particular, the atmosphere plays a crucial role for the energy transport.

interior composition and structure. Furthermore, progress in the warm dense matter field has significantly improved our understanding of how hydrogen, helium, and their mixtures, such as those with water or silicates, behave under extreme conditions of up to 10^4 K in temperature and 10^7 bar in pressure [43]. Comprehensive reviews of the giant planets of the Solar System have been updated, offering new insights into their complex interiors [25, 42, 44–49].

Since the mid-1990s, the discovery of planets outside our Solar System has profoundly both challenged and expanded our understanding and imagination of planetary formation and evolution. To date, 5632 exoplanets in 4188 planetary systems³ have been discovered and confirmed. The large number of exoplanets displays a diversity in orbital parameters and bulk compositions [51], underscoring the unique architecture of the Solar System. Beyond the familiar planetary classes of terrestrial and giant planets, represented by the inner and outer planets of our Solar System, planets that are intermediate in mass and size seem to be the most common, called mini-Neptunes and super-Earths [52]. The large number of discovered exoplanets facilitates demography studies, revealing, for instance, a gap in the size distribution of intermediate-sized planets, possibly due to photoevaporation [53, 54].

The detection of close-in planets, initiated with the Nobel Prize winning observation of the first exoplanet orbiting a Sun-like star [55, 56], highlights planetary migration as a fundamental process in the evolution of planetary systems, suggesting that these giant planets have formed ex situ and migrated to their current locations [57–60]. Recently, the close-in planet WASP-193b has been announced showing a remarkable, extremely low density of only 0.059 g/cm^3 , that is only 4.5% the density of Jupiter (and basically the density of cotton candy) [61]. Moreover, the unexpectedly large inflated radii of close-in planets, a phenomenon that is often referred to as the radius anomaly, suggest the presence and interplay of physical mechanisms that are not yet fully understood, as described in e.g. [62–65]. The deposition of stellar irradiation in the interior of planets, for example through Ohmic dissipation of induced currents, may play a major role in the inflation [66].

Up to now, Jupiter-like planets in small orbits, with a semi-major axis of less than $a < 0.1$ astronomical units (au) and typical orbital periods of just a few days, represent the most extensively studied group of exoplanets [67–69]. This increased focus is largely due to observational and publishing biases that favour detectable planets with pronounced characteristics. However, despite extensive research, these planets are actually quite rare within our Galaxy⁴. Studies

³<https://exoplanetarchive.ipac.caltech.edu/> [50], accessed on May 28, 2024

⁴An updated sample of papers on the occurrence rate of exoplanets can be found here: https://exoplanetarchive.ipac.caltech.edu/docs/occurrence_rate_papers.html, accessed on March 28, 2024

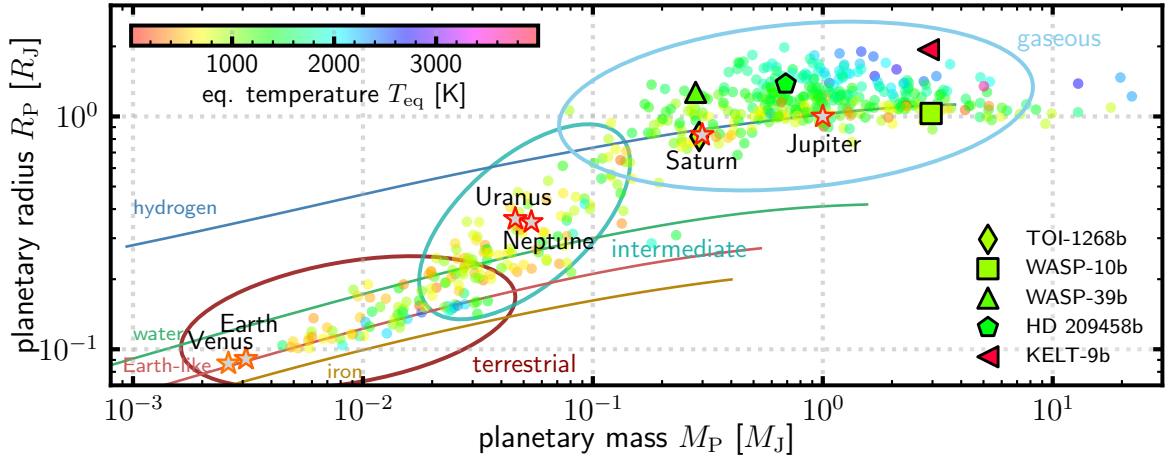


Figure 1.2.: Mass-radius diagram of exoplanets with relative mass and radius uncertainties smaller than 25% and 8%, respectively (from [PlanetS Catalog](#), accessed on April 15, 2024). Composition lines of pure iron, an Earth-like composition, water ice and cold hydrogen are shown as solid lines [75]. Planets whose composition is expected to be terrestrial, gaseous, or intermediate are indicated with ellipses. The Solar System planets are marked as stars. Individual gas planets modelled in this thesis are highlighted with symbols. Note, that the population shown does not mirror the observed or real distribution of exoplanets. Figure updated and modified from [35, 76, 77].

indicate that while 10% of all stars in our Galaxy have a giant planet at any orbital distance, only about 1 in 10 of these giant planet systems contains a giant planet within 0.1 au [68, 70–74].

The study of these highly irradiated close-in planets often starts with the detection of their transits, followed by Doppler spectroscopy, which together provide radius and mass estimates. The parameters are needed to characterise the bulk composition, making these planets particularly favourable for studying interior properties.

Exoplanets that have both mass and radius estimates are shown in Fig. 1.2, colour-coded with the equilibrium temperature (T_{eq}) which is a measure for the irradiation received by the parent star. A preliminary estimate of the composition of planets can be derived solely from the mass and radius, when compared with theoretically calculated mass-radius relations (solid lines). Based on their composition, the groups of terrestrial, gaseous, and intermediate planets are indicated by ellipses. The detected gaseous giant planets are highly irradiated, indicated by the high T_{eq} from 800 to 4000 K, compared to Jupiter (110 K) and Saturn (90 K). The strong irradiation makes the atmosphere play a key role in the characteristics of the planet.

Transiting irradiated giants are ideal for atmospheric follow-up studies through secondary eclipses and transmission spectroscopy. The latter technique makes use of the fact that during the planet’s transit some flux from the parent star passes through the thin outer atmosphere, imprinting small absorption features on the stellar spectrum across various wavelengths. These atmospheric observations yield fascinating data, including the presence of atmospheric clouds made of quartz and sand [17, 78], ionised species such as calcium [79], and extremely fast horizontal winds of about 40 km/s [80].

With ongoing and forthcoming space missions providing rich atmospheric data, integrating these observations with interior modelling is essential. The combination of atmosphere, interior, and thermal evolution models, which replicate observations, is critical. The thesis develops and applies the coupled approach of these models to two areas of exoplanetary science. First, the effect of cloudy atmospheres on the interior composition and radius evolution is explored. Second, the role of the atmospheric conditions on the Ohmic dissipation mechanism, which has been proposed to inflate gas giant planets, is investigated. The following serves as an introduction to the elements of this thesis.

1.1. Interior Modelling of Giant Planets

Interior models play an essential role in any assessment of the formation and evolution of planets, aiming to reveal the internal structure and the composition variation with depth [43]. These models enhance the understanding of planetary diversity, their formation conditions, shedding light on formation pathways, and the warm dense matter (WDM) inside.

Traditional interior modelling employs a set of structural equations to describe the distribution of mass, radius, pressure, density, and temperature within the planet’s interior. The same set of structural equations can be applied to brown dwarfs and stars, illustrating the fundamental similarities in the principles governing the internal structures [81–85]. The models rely on a priori assumptions, such as the number of layers based on the composition and heat transport mechanism, where the composition is described by physical equations of state (EoS). An alternative approach constructs interior models based on a mathematical representation of the density profile, called empirical structure models, without further assumptions on composition, providing another way to explore interiors [86–92]. The primary aim of interior modelling is to reproduce observed planetary properties, such as the radius of inflated close-in planets, using models with varying structures and compositions that align with the observables. A key output of these models is the bulk composition, particularly the mass of heavy elements (metals), which are all elements heavier than hydrogen (H) and helium (He).

Four main aspects determine the interior structure of giant planets [35]: (1) They cool and contract significantly over time because their H and He-dominated (H/He) envelopes are compressible. The evolution of their bulk composition is linked to the age of the planet as they emit their intrinsic heat. This intrinsic luminosity is parameterised by the intrinsic temperature T_{int} . Models of the interior structure are usually combined with models of gravitational contraction. Other critical aspects include (2) the number of observables (Sect. 1.1.1), (3) the EoS (Sect. 1.1.2), and (4) the atmospheric boundary conditions (Sect. 1.1.3). The latter is especially significant for irradiated atmospheres, where the thermal structure profoundly affects various aspects of the irradiated gas giants, which is a primary topic of this thesis.

The coupling of atmosphere, interior, and thermal evolution models is necessary to inform broader planetary formation and evolution models. In addition to models that are constructed to match observables, forward modelling aims at characterising objects using model grids based on chosen gravities or ages, providing observable properties like atmospheric spectra and luminosities, e.g. to inform observational campaigns. Examples are the ATMO2020 [93] and Sonora [94–96] grids.

1.1.1. Number and Availability of Observables

In general, the availability of observables, beyond the planetary mass, M_{P} , and radius, R_{P} , significantly improves the refinement of the model.

For the solar giant planets, a large number of observables are available through ground-based observations and spacecraft flybys, with Uranus and Neptune being less well known than Jupiter and Saturn. These data have substantially refined our models in terms of composition, distribution of elements, and heat transport mechanisms.

For example, Hubbard (1968) [97] argued that an adiabatic temperature gradient is implied by the observed net luminosity observations in the infrared [98], leading to a fully convective interior for Jupiter. This traditional, simplistic assumption of large-scale convection and thus homogeneous interiors is now questioned. Recent theoretical studies point to thermal boundary layers [99–101] or composition gradients leading to layered convection, e.g. double-diffusive convection [102, 103], potentially due to He rain-out [104–107]. Observational data, such as the oscillations in Saturn’s rings by the spacecraft Cassini, suggest a stable stratified layer extending to about 60% of its radius, arguing against traditional assumptions of convection stability [108, 109]. Additionally, Juno’s measurements of Jupiter’s gravitational moments

indicate a gradual core-envelope transition (also called a fuzzy or dilute core) instead of the traditional solid core [49, 110–113], and also a shallow wind depth that implies a stable stratified layer [114, 115]. Juno’s findings are reviewed in [113, 116, 117]. Further, a deep radiative zone has been identified [118], that is located between two convective layers, possibly due to a reduced H opacity [118–121]. Static and dynamic rotational states provide further constraints. Furthermore, Love numbers, indicating the deformation of Jupiter’s shape due to tidal forces, have been both measured and theoretically derived [122–124].

For extrasolar giant planets, essential observables include M_P , R_P , and age. Another quantity is the equilibrium luminosity $L_{\text{eq}} = 4\pi\sigma_B R_P^2 T_{\text{eq}}^4$, where σ_B is the Stefan-Boltzmann constant, representing the stellar energy absorbed and re-radiated by the planet. The characteristic temperature T_{eq} is calculated as

$$T_{\text{eq}} = (1 - A_B)^{1/4} \cdot f^{1/4} \cdot T_\star (R_\star/a)^{1/2}, \quad (1.1)$$

where T_\star and R_\star are the star’s effective temperature and radius, the Bond albedo A_B is a measure for the incident energy scattered [125], and the parameter f accounts for the heat distribution on the planet [126]. The classification of exoplanets often relates to the level of stellar irradiation and their radius or mass in comparison to the Solar System planets, such as warm Saturns, hot Neptunes, or ultra-hot Jupiters.

However, the observables for extrasolar giants are mainly related to atmospheric characteristics, for example, composition and abundances [79, 127–131] from which the magnetic field strength can be derived [132–134], clouds and hazes [135, 136], albedo [137, 138], wind speeds [80, 139], and atmospheric loss [140]. Sect. 1.2 addresses a few of the atmospheric properties. One proposed connection between the atmosphere and interior is the atmospheric metallicity Z_{atm} , which is derived from atmospheric abundances [69, 141]. The observables of clouds and atmospheric metallicity are key properties in this thesis, further detailed in Sect. 3.1.

1.1.2. Warm Dense Matter: Equations of State

Understanding the matter that makes up a planet is fundamental for modelling its interior structure and cooling behaviour. An early review by Stevenson (1982) [40] emphasised that planetary observations and high-pressure physics are pivotal in the development of planetary models.

A preliminary estimate of the composition of planets can be derived from their observed mass and radius; see Fig. 1.2. When these observables are compared with theoretically calculated mass-radius relations, it becomes evident that giant planets predominantly consist of H and He, along with a significant proportion of heavier elements [48]. Heavy elements, or metals, refer to all elements other than H and He. Metals are assumed to be planetary ices, such as water (H_2O), ammonia (NH_3) or methane (CH_4), and rocky material, dominated by iron (Fe), magnesium (Mg), silicon (Si), and oxygen (O), which form silicon dioxide (SiO_2), magnesium oxide (MgO) or much more complex molecules such as iron oxyhydroxides (FeOOH) under core conditions [142]. The term ice denotes compounds like H_2O , CH_4 , and NH_3 , which likely existed in solid form during the accretion phase [44] of the planet.

The equations of state (EoS) characterise the thermodynamic properties of matter within a planet. Often, various species are mixed via the linear mixing approximation [143–146], because the behaviours of real mixtures are poorly understood. The resulting EoS correlates pressure, temperature, and density along the radial structure of the planet. The conditions typically range from 10^2 K to 10^4 K in temperature and from 1 bar to 10^7 bar in pressure, falling within a regime known as WDM. This state is a transitional phase between solid and plasma, exhibiting properties of both and involving strongly coupled ions, degenerate electrons, and partial ionisation; see the reviews by [147–149]. High energy density (HED) experiments pass through this difficult region of phase space. An example is the laser-induced compression

of C–H mixtures which lead to the formation of nanodiamonds – under conditions that are proposed to occur in ice giants [150–154].

However, the capacity of laboratory experiments to cover the entire phase diagram is restricted, and theoretical calculations of the strongly interacting quantum systems of electrons and ions are used to complement the EoS data.

Theoretical calculations fall into two main categories. In the chemical picture, effective pair potentials, validated against experiments, describe particle interactions. By minimising the Helmholtz free energy, chemical equilibrium is obtained, giving access to indispensable variables such as the entropy S and adiabatic temperature gradient ∇_{ad} , while ensuring thermodynamic consistency. The physical picture uses quantum mechanics to treat electrons, known as *ab initio* molecular dynamics (AIMD). This method often combines density functional theory (DFT) for electronic structure [155, 156] with molecular dynamics (MD) for nuclei [157].

A specific challenge to be addressed is the change from molecular H_2 to atomic H^+ and the metallisation of He [158, 159]. The behaviour of mixtures is equally important, as demixing can occur in Saturn and Jupiter (H–He demixing) [107, 160–162] or in Neptune and Uranus (H_2O –H demixing) [163], contributing as a heat source and adding additional compositional layers. For Uranus and Neptune, ice-rock mixtures are probably important [164, 165]. Core erosion due to the solubility of H_2O , Fe, SiO_2 , and MgO in H is probable in the four giant planets [142, 166, 167]. Superionic phases of mixtures CH_4 – H_2O – NH_3 [168–172], or water [173, 174], influence the energy transport through additional layers. The related transport properties are increasingly important for understanding energy transport and the generation of magnetic fields [175–177].

Studying giant exoplanets offers a unique opportunity: They serve as natural laboratories, allowing us to understand matter under extreme conditions.

1.1.3. Atmospheric Thermal Structure

The atmosphere plays a critical role in the radiation transport, acting as a bottleneck for both the incoming irradiation and outgoing intrinsic radiation, thereby dictating the planet’s cooling process.

Gas planets are in an evolutionary phase where they transition from predominantly convective to more radiative to achieve equilibrium with their host star [178]. The atmospheres of highly irradiated gas planets are heated strongly by the absorption of the incident radiation, primarily in the upper layers. This results in a deep vertical isothermal radiative zone below the heated layer, before the contribution of intrinsic heat becomes significant [67, 178–183]. The final state will become isothermal. The formation of a radiative zone begins in the outer layers and progresses inward over time. The contraction and cooling of the planet from a high entropy state are facilitated by the expansion of this radiative zone due to high incident radiation [184]. Fig. 1.3 illustrates the thermal structure of the modestly irradiated solar Jupiter ($T_{\text{eq}} = 110$ K, $T_{\text{int}} = 100$ K) compared to the highly irradiated extrasolar Jupiter WASP-17b ($T_{\text{eq}} = 1700$ K, $T_{\text{int}} = 300$ K). For the latter, the isothermal region appears at $T_{\text{iso}} = 2100$ K whereas Jupiter does not show an isothermal region⁵. Following the deep isotherm of WASP-17b, the interior becomes adiabatic. The age of the planet is related to the loss of its intrinsic heat, which determines the isentrope. Close-in planets are expected to be tidally locked to their host stars [181, 185, 186], creating permanent day and nightsides with significant temperature differences [187], as illustrated in Fig. 1.3 for HD 209458b, driving atmospheric dynamics [188]. MgSiO_3 and Mg_2SiO_4 clouds may form [189], generally, the nightsides of close-in planets with $T_{\text{eq}} \leq 2100$ K are predicted to form silicate clouds [190]. Despite the temperature differences in the upper atmosphere, the overall planetary evolution is fundamentally governed by the global deep atmospheric temperature.

⁵A radiative isothermal zone is thought to build up for old, far-away planets as well (but much slower) when $T_{\text{int}} \ll T_{\text{eq}}$ and stellar absorption is dominant [179].

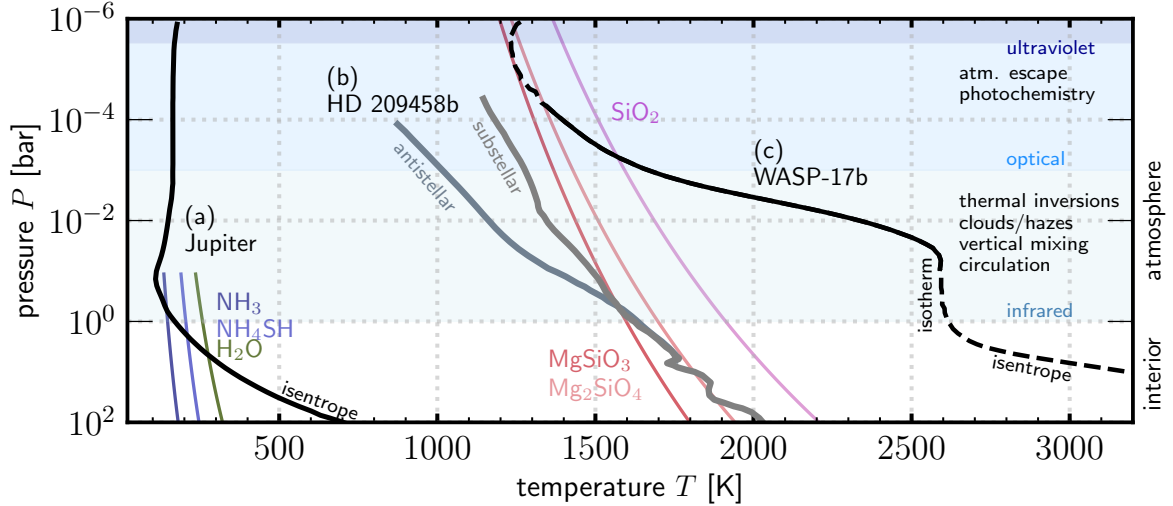


Figure 1.3.: Examples of P - T of gas giant planets (thick solid lines) are shown, amongst thermal stability curves of possible condensates (thin coloured lines). Clouds may occur above the point where the P - T profile crosses the condensation curves. The more irradiated and the older the planet is, the deeper the isotherm extends. Atmospheric processes are highlighted and the approximated wavelength-dependent atmospheric depth that can be probed is shown (background shades). From left to right: (a) Averaged P - T of Jupiter ($T_{\text{eq}} = 110$ K) [77]. (b) Results of 3D simulations of HD 209458b ($T_{\text{eq}} \approx 1500$ K), at the substellar and antistellar point [187, 189]. (c) The P - T that belongs to the best-fit model to the transmission spectrum of WASP-17b ($T_{\text{eq}} \approx 1700$ K) which shows a feature that resembles quartz (SiO_2) clouds [78], the solid part shows the probed P -range.

In summary, the atmosphere is an important outer boundary condition for interior and evolution modelling. This thesis accounts for the matching of the atmospheric with the interior structure. An atmospheric model, in detail the pressure-temperature (P - T) structure must account for both the irradiation of the parent star and the outward transport of intrinsic heat. The next Sect. 1.2 reviews the current state of theoretical and observational studies on the thermal structure of H/He-dominated atmospheres.

1.2. Exoplanetary Giant Planets Atmospheres

This section introduces the atmospheres of giant exoplanets, focusing on their thermal structure through observations and theory, Sect. 1.2.1 and Sect. 1.2.2. More in depth, cloudy and ionised atmospheres are highlighted in Sect. 1.2.3 and Sect. 1.2.4.

1.2.1. Thermal Structure by Observations

A direct assessment of the atmospheric P - T conditions of (giant exo-) planets is limited. Contrary, Earth's atmospheric conditions are directly assessed by utilising a wide array of techniques to explore not only the temperature structures, but also other parameters such as composition, humidity, and wind speeds in different temporal and spatial resolutions. In situ measurements and ground-, air- and space-based remote sensing techniques are applicable; an overview is given in [191]. In contrast, studying giant exo- and solar planets faces challenges due to vast distances and technological limits.

For the giant planets of the Solar System, both remote-sensing techniques (ground-, air-, and space-based telescopes) and spacecraft fly-bys are able to measure wind speeds, weather formations (and their evolution), and (vertical) composition by observing different wavelengths. From these observations, the temperature structure is indirectly derived [77, 192]. Notably,

Jupiter’s Juno mission aimed to map the atmospheric composition and temperature at all latitudes for pressures < 100 bar [193–195]. In situ measurements, such as those obtained by the Galileo entry probe diving into Jupiter’s atmosphere and the grand finale of the Cassini mission diving into Saturn’s atmosphere, provide further observables, including thermospheric temperatures and abundances, primarily from mass spectrometry [196, 197].

For exoplanets, in situ measurements are not feasible. Instead, remote-sensing techniques such as transit spectroscopy, high-resolution Doppler spectroscopy, or direct imaging spectroscopy provide atmospheric spectra [198, 199]. Secondary eclipse data also contribute by measuring the thermal emission from the planet, like those performed for HD 189733b [200, 201]. However, these are limited to narrow wavelength ranges and require further parameterisation to encompass the entire pressure spectrum [202]. Typically, observations probe the upper atmosphere at roughly 10^{-3} – 10 bar.

Theoretical models play a vital role in bridging the gap between observations and a comprehensive understanding of atmospheric phenomena. Through forward spectral modelling and retrieval techniques, theoretical models guide the design of observational studies and aid in the interpretation of spectral data [202]. This thesis places a particular emphasis on the theoretical models as they deliver the thermal structure over a wide pressure range, informed by observational data.

1.2.2. Thermal Structure by Theory

This section first outlines the factors and processes shaping the thermal profiles of irradiated giant planets. Second, it provides an overview of radiative transfer solutions, highlighting the deciding roles of opacity and optical depth. Fig. 1.3 shows the important processes at work in the atmosphere.

Factors Shaping the Thermal Structure. First, the atmospheric P – T profile is shaped by the absorption and re-emission of the stellar flux, the emission of the intrinsic flux from the interior, and the planet’s surface gravity – a planet with lower gravity emits from lower atmospheric pressures and the P – T profile shifts accordingly to lower pressures [203].

Second, the atmospheric composition plays an important role as it determines the scattering and absorption properties at the microphysics level. The atmospheres of gas giants are predominantly composed of H and He, called primary atmospheres. These atmospheres originate from the protoplanetary disk, rich in H, He, and heavier elements [204, 205], in contrast to secondary atmospheres formed by geochemical outgassing [206, 207]. Table 1 in Madhusudhan [198] provides an overview of the molecules and atoms identified in exo-atmospheres. Molecular and atomic abundances are often calculated from elemental abundances assuming chemical equilibrium.

Third, additional processes such as aerosol formation affect atmospheric composition and add opacity sources, influencing thermal structures through their heating or cooling effects [208, 209]. Clouds and hazes significantly impact temperature structures and are reflective, affecting the planetary albedo. These phenomena have been studied from both a theoretical [210–219] and an observational perspective [17, 135, 220–225]; see also Sect. 1.2.3.

Thermal inversions in the upper atmosphere, that is, increasing temperature with decreasing pressure, have been a subject of debate, for example, for HD 209458b [226–230]. The P – T can be inferred from secondary eclipse spectroscopy, probing the planet’s thermal emission in the infrared wavelength band [231]. Theoretically, optical or near-UV absorbers, such as titanium oxide (TiO) and vanadium oxide (VO), can cause these inversions [232, 233]. For ultra-hot Jupiters, inversions may be driven by absorbers such as Fe and Mg [234]. Until now, only some planets have shown evidence of inversions [235].

Non-equilibrium effects also play a critical role, altering thermal structures and chemical abundances due to factors like irradiation and atmospheric dynamics. In contrast to chemical equilibrium, where the molecular composition depends only on pressure, temperature, and

elemental composition, in the non-equilibrium state, it is controlled by the kinetics of individual reactions [236]. Photochemical processes such as photoionisation driven by the star's radiation may lead to atmospheric escape and significant changes in the composition of the upper atmosphere [237–240]. Photochemistry seems to alter the radiative transfer dramatically [236, 241–243]. Atmospheric dynamics, driven by stellar irradiation, further complicate the thermal profiles by influencing transport and mixing processes, for instance, also by increased heat transport through recombination from H to H₂ [244].

In conclusion, a comprehensive theoretical model of a planet's atmosphere – and consequently its thermal structure – must account for all these factors to accurately simulate radiative transfer (RT) processes.

Radiative Transfer. RT is a measure of how radiation changes as it moves through the layers of the atmosphere as photons encounter obstacles and interact. The radiative transfer equation (RTE) describes the change in a radiation beam as it travels some distance ℓ [245]. The changes are due to absorption, emission, and scattering processes, resulting in losses and additions to the beam [125, 245].

The description of radiation is intensity I , which is the energy of a number of identical photons in a beam of radiation [245]. Therefore, the intensity of radiation at location \mathbf{x} in direction $\hat{\mathbf{n}}$ at time t for a frequency ν is the energy flow per unit area dA , at time t , for frequency ν and solid angle subtended $d\Omega$ [$\text{J}/(\text{m}^2 \text{ s Hz sr})$], see Fig. 2.1 in [245]. The frequency ν is defined as c/λ , with c as the speed of light and λ as the wavelength.

The following equation is the formal radiative transfer equation:

$$\frac{dI(\mathbf{x}, \hat{\mathbf{n}}, \nu, t)}{d\ell} = \mathcal{E}(\mathbf{x}, \hat{\mathbf{n}}, \nu) - \kappa(\mathbf{x}, \nu)I(\mathbf{x}, \hat{\mathbf{n}}, \nu, t). \quad (1.2)$$

Intensity I along the distance ℓ changes due to two factors. First, matter causes extinction of radiation, adding a loss to the radiation beam: $-\kappa(\mathbf{x}, \nu)I(\mathbf{x}, \hat{\mathbf{n}}, \nu, t)$, where κ is the extinction coefficient. Second, matter emits radiation, and, specifically, the atmosphere emits its own thermal emission. The emission coefficient $\mathcal{E}(\mathbf{x}, \hat{\mathbf{n}}, \nu)$, also known as the source function, accounts for this. It is a complex quantity because scattering and thermal emission have to be taken into account.

The extinction coefficient is another word for opacity, referring to both absorption and scattering contributions. The atmosphere is made up of a large number of particles belonging to various species, each possessing unique absorption and scattering properties [125]. These properties are pressure-, temperature-, and wavelength-dependent:

$$\kappa = \kappa(P, T, \lambda). \quad (1.3)$$

Directly related to the concept of opacity is the optical depth. The optical depth τ (dimensionless) is a measure of how opaque the atmosphere is. Optically thin means $\tau \ll 1$ (a photon can travel a distance without being absorbed or scattered), while optically thick means $\tau > 1$. An expression of the optical depth [125] is directly correlated with the opacity κ ,

$$\tau = \int \kappa dm', \quad (1.4)$$

with m' as the atmospheric column mass. Another expression is $d\tau = -\kappa(\ell, \nu) d\ell$. Therefore, the opacity κ of an atmosphere determines the transparency (the optical depth) of the gas and therefore the radiation transport, see Eq. (1.2). Gas opacities, in contrast to cloud or haze opacities for example, are obtained from measurements or calculations, see for example [246]. In general, frequency-averaged opacities are useful in radiative transfer solutions. For example, the Planck mean opacity is valid in optically thin regions, whereas the Rosseland mean opacity is valid in optically thick regions [245, 247, 248]; see Sect. A.5 for more information.

Furthermore, the abundances of the molecules and atoms that are relevant at a given pressure

and temperature, as well as for a specific composition, must be determined. These are often acquired with thermodynamic equilibrium chemical abundance calculations, such as those presented in [249, 250].

Within the general framework of radiative transfer depicted above, one can solve the temperature structure for a gaseous atmosphere. Often assumptions concerning geometry, opacities, thermal and chemical equilibrium, and time-dependence (mainly neglected) are made.

(a) *Analytical 1D Models.* As pointed out by Fortney [251], a wide range of analytic solutions has been published in recent years, mainly focused on strongly irradiated planets, for example [180, 252–255]. In these models, the atmospheric temperature structure is a function of the characteristic temperatures describing energy fluxes, such as the effective temperature T_{eff} , the equilibrium temperature T_{eq} , and the intrinsic temperature T_{int} . They use wavelength-independent, grey opacities κ_{S} (in the visible wavelength range, shortwave), κ_{L} (in the infrared wavelength range, longwave), applying the dual-band approximation where the stellar irradiation and the planet’s thermal emission peak at different wavelength resulting in one incoming and one outgoing radiation stream. The models provide a relationship between pressure P , temperature T , and optical depth τ (P – T – τ). Compared to numerical atmosphere models, analytical models offer the advantage of computational efficiency. However, advanced models are frequently required to calibrate the free parameters of analytical models. The model of Guillot (2010) [180] (*Guillot10*) has been used in coupled atmosphere-interior models [256–258] and is preferred for retrieval models, as it captures the essential physics but is low parameterised [202]. The *Guillot10* model is used in this thesis; see Sect. 2.2.

(b) *Numerical 1D Models.* The main differences between analytical and numerical models are the opacity treatment and the inclusion of the computation of chemical abundances (mostly in chemical equilibrium). Examples for codes that are used for exoplanetary atmospheres are *McKay-Marley* code [259] (e.g. used in [260]), EXO-REM [261, 262], PETITCODE [263] and the codes from [264, 265]. The numerical models show differences in the treatment of aerosols such as clouds and hazes, scattering, opacities, and energy transport [266].

(c) *Numerical 3D Models.* 3D general circulation models (GCMs), which solve fluid motion equations and incorporate radiative and chemical schemes, were first applied to hot exoplanets in 2009 [267] and later advanced, e.g. [268]. Reviews can be found in [269, 270]. GCMs inform observations, as they include horizontal transport and circulation, e.g. [219, 271], and also yield deep atmospheric temperatures, as important for the coupling to 1D-interior and evolution models [272–274].

Further readings on (exo-)planetary atmospheres include general reviews [125, 245, 275], and specific discussions on theoretical and observational aspects of exoplanetary atmospheres [198, 199, 276–278].

1.2.3. Cloudy Atmospheres

Clouds are familiar features in our daily lives. H_2O clouds on Earth influence the global radiation budget and therefore the short- and long-term climate [279, 280]. However, clouds introduce significant uncertainty into climate models, due to their variable coverage, dynamics, changes in properties, and the interaction of evaporation, condensation, and phase changes, e.g. [281–283].

Aerosols – including clouds, dust, and haze – are prevalent in the atmospheres of Solar System planets, moons, and exoplanets; see for reviews [77, 284–286]. For example, on Mars, cirrus clouds have been investigated to contribute to a warming that may have led to liquid water for a short period of time [287], and the moons of the outer planets show hazes in their atmospheres, e.g. Pluto [288, 289], Triton [290] or Titan [291, 292]. The solar giants inhibit several layers of cloud and haze [77].

In Earth science, the terms clouds, dust, and haze refer to particle sizes, while in planetary sci-

ence, they indicate the origins of formation [293]. Following the definitions of Gao *et al.* [209], based on Hörst [294], dust refers to lifted solid particles, whereas haze refers to aerosols formed by photochemistry. Clouds form under thermochemical equilibrium via first-order phase transitions, when vapour pressure saturates due to vertical mixing in an atmospheric column, or via thermochemical reactions. The terms haze and cloud are often used interchangeably because they similarly affect the spectrum, despite differing in their formation processes. Fig. 1.3 shows the P - T structure of planets among the thermal stability curves of possible condensates. Refractory species like metal oxides, silicates, and sulphides can condense at high temperatures. To first order, the intersection of the P - T profile and the condensation curve hints at the condensable material and the lower cloud base pressure.

Observations. In exoplanetary atmospheres, clouds and hazes are common, with observational evidence often derived from spectral analysis via transmission spectroscopy, direct imaging, or phase curve measurements, e.g. [209, 295–297]. References for observational evidence of aerosols are listed in [209]. In addition to the review, newer observations indicating clouds or hazes have been conducted for the hot Jupiters WASP-17b [78], WASP-110b [298], and the warm Neptune WASP-107b [17].

In transmission spectroscopy, high-altitude scattering particles are needed to interpret spectral features, though their nature and origin are debated [299]. The effects of condensates on the transmission spectra are muting spectral features, showing a wavelength-dependent scattering, or causing a spectral slope over several-micron wavelength intervals [199, 300].

Observation-based cloud property derivation is complex due to uncertain microphysical processes and unknown properties of the condensing species. Microphysical processes include nucleation, bulk growth, evaporation, gravitational settling, element replenishment, or enrichment [215, 218]. However, optical and near-infrared transmission spectroscopy can examine cloud particle sizes, number density, and distribution, while mid-infrared vibrational modes determine their compositions. Interestingly, Kempton *et al.* [301] suggest that the ingress and egress spectra during a transit reveal the dominant aerosol formation mechanism, as haze is produced on the permanent dayside (proposed to be seen in the ingress spectrum, i.e. when the planet starts transiting its star), while clouds may form on the cooler nightside (to be seen in the egress spectrum, i.e. when the planet ends its transit). Moreover, haze properties have been inferred through laboratory experiments [302–308].

Theory. Theoretical modelling of aerosol properties and formation aims at helping to interpret observations. However, cloud formation is complex as the material properties of the condensing species need to be known, and several microphysical processes need to be understood. In addition, cloud inhomogeneities play a role for observations, due to dynamical processes such as atmospheric waves and cloud convection. There are two groups of models [309]: The first group are advanced models computing self-consistently the microphysics, e.g. DRIFT-PHOENIX [310], BT-SETTL [311–313], CARMA [314]. The second group encompasses parametric cloud models, e.g. the Ackerman and Marley [96, 315] or Tsuji [316] model. Reviews on aerosols in exoplanetary atmospheres, including observational and theoretical aspects, are given by [209, 285, 317], and theoretical cloud modelling is discussed in [213–215, 217, 218].

Effects of Clouds on P - T . Aerosols primarily alter atmospheric heat transport by warming the lower atmosphere through increased opacity and cooling the upper atmosphere by effectively radiating heat. Their large absorption cross sections enhance the warming effect. Also, they affect the planetary albedo through their high scattering efficiency, influencing the emissivity and leading to a change in the energy received by the planet [318–320]. Clouds significantly influence exoplanetary atmospheres by consuming elements and altering local chemistry, affecting atmospheric composition and adding opacity sources [208, 209]. For this thesis, an analytical formalism by Heng *et al.* [321] that accounts for the backwarming effect of clouds or hazes will be used to model the atmospheric P - T profile.

1.2.4. Ionised Atmospheres

In irradiated Jupiters, particularly ultra-hot Jupiters with equilibrium temperatures > 2000 K, extreme thermal conditions lead to significant atmospheric phenomena, including thermal dissociation and ionisation. For example, a theoretical study by Lothringer *et al.* [234] finds that thermal inversions lead to thermal dissociated species at 10 – 100 mbar. Ionised species have been detected in several ultra-hot Jupiters, e.g. Na I, Fe II, Ca II, Mg II [79, 140, 322, 323].

The ionisation degree α is necessary for understanding the potential formation of an ionosphere and magnetosphere [217, 324], and for evaluating the electrical conductivity. Helling *et al.* [324] find that the tidally locked HAT-P-7b has high levels of ionisation at the dayside, resulting in an ionosphere that extends deep into the atmosphere. In addition, discharge processes might occur on the nightside in the cloudy parts; see also [325–327]. They conclude that the whole atmosphere might couple to the magnetic field of the planet. The interaction of the ionised atmospheres with the internal magnetic field leads to various magneto-hydrodynamic processes (e.g. Ohmic dissipation [66], magnetic drag [328, 329]). In summary, in the irradiated atmospheres, thermal dissociation takes place, and interactions with the planetary magnetic field are expected.

1.3. Aim and Outline of this Thesis

The present thesis is concerned with advancing the understanding of irradiated giant planets. The focus lies on their atmospheric thermal structure (P – T) and its impact on the derived bulk composition, radius evolution, and possible (radius) inflation. Both the bulk metallicity and the radius evolution are connected from an interior modelling perspective, and both derived parameters are necessary to an understanding of planetary formation and evolution. The first part of this thesis incorporates the effect of clouds in coupled atmosphere, interior, and thermal evolution models. First, the effect of a cloud deck on the derived bulk metallicity of the planets WASP-39b and WASP-10b is explored. Further, the influence of a cloud deck on the thermal evolution of TOI-1268b and WASP-10b is analysed. The second part of this thesis investigates the impact of the P – T conditions on a mechanism that has been suggested to inflate irradiated giant planets. The mechanism, based on Ohmic dissipation of currents in the deep interior, relies on transport properties in the atmosphere, particularly the electrical conductivity.

MOGROP (MOdellierungsprogramm für GROße Planeten) models the interior structure and thermal evolution of gas and ice giant planets, developed by Dr. Nadine Nettelmann [330]. It has been widely used to study the interior structure and thermal evolution of Solar System giants [44, 99, 105, 331–341] and exoplanets [332, 333, 342, 343]. For the work at hand, MOGROP was adapted and extended: the atmosphere model by Heng *et al.* [321], which accounts for the effects of hazes and clouds in the P – T profile, was implemented. Additionally, the radiative-convective boundary calculation was improved, the cloud model was modified, and new EoS tables were implemented.

Chap. 1 introduces the population of irradiated giant planets, the interior modelling of gas planets and their atmospheric thermal structure, and exoplanetary clouds. Chap. 2 reviews MOGROP, including the interior and thermal evolution model in Sect. 2.1, and the atmospheric part extended in this thesis, detailed in Sect. 2.2. Chap. 3 introduces the thesis topics and their corresponding publications. The first topic (Sect. 3.1) is introduced with an overview on the connection of bulk and atmospheric metallicities, followed by results on the effect of clouds on the derived bulk metallicity in Sect. 3.1.2 and radius evolution in Sect. 3.1.3. The second topic, the radius anomaly of giant planets, (Sect. 3.2) is first introduced in Sect. 3.2.1, followed by the results in Sects. 3.2.2 and 3.2.3. Chap. 4 concludes with a summary of the thesis results. Chap. 5 includes the publications described in Chap. 3 and provides the contributions of the individual authors.

2. Coupling Atmosphere, Interior, and Thermal Evolution Models

In this chapter, the theoretical foundation for the forthcoming chapter is presented. Sect. 2.1 lays out the fundamentals of modelling the interior structure and thermal evolution of planets as implemented in MOGROP. Sect. 2.1.1 presents the equations for modelling the interior structure, the assumptions made on the energy transport, and the numerical solution. The coupling between the atmosphere and interior model is achieved by calculating the radiative-convective boundary (RCB) as shown in Sect. 2.1.2. The equations of state (EoS) are presented in Sect. 2.1.3. Sect. 2.1.4 sets the foundations of the contraction and thermal evolution modelling as implemented in MOGROP. The atmospheric models used in this thesis are presented in Sect. 2.2.

2.1. Interior and Thermal Evolution Modelling

2.1.1. Interior Structure

The ingredients that are needed to model the planet as implemented in MOGROP, are the basic structural equations, a description of the warm dense matter (WDM) inside the planet divided in layers, and assumptions on energy transport. These basics come together to create the interior model. Planetary structure models assume that giant planets are in hydrostatic equilibrium, exhibiting near-perfect spherical symmetry. Minor deviations caused by rapid rotation or tidal forces are sufficiently small, allowing their interiors to be effectively approximated by one-dimensional (radial) models based on mass conservation principles:

$$\frac{dm(r)}{dr} = 4\pi r^2 \varrho(r), \quad (2.1)$$

where each shell within a spherical, symmetric planet has a mass dm , a thickness dr , and a local density ϱ . The hydrostatic equilibrium equation reads

$$\frac{dP(r)}{dr} = -\frac{Gm(r)}{r^2} \varrho(r), \quad (2.2)$$

with P as pressure, and the gravitational constant G . The assumption is that the gravitational force is counteracted by pressure forces, maintaining the planet in a state of equilibrium for a prolonged duration. Furthermore, for close-in planets, it is generally assumed that most are tidally locked with their stars, resulting in synchronous rotation states.

The relation between pressure, temperature, and density is described by the EoS:

$$\varrho(r) = \varrho(P(r), T(r)), \quad (2.3)$$

where the density additionally depends on the composition of the matter inside the planet. This equation is a crucial component in the field of planetary science. Understanding $\varrho(P, T)$ requires understanding the distribution of the temperature profile $T(r)$. Generally, one would solve the thermodynamic equation

$$\frac{dT}{dr} = \frac{T}{P} \frac{dP}{dr} \nabla_T, \quad (2.4)$$

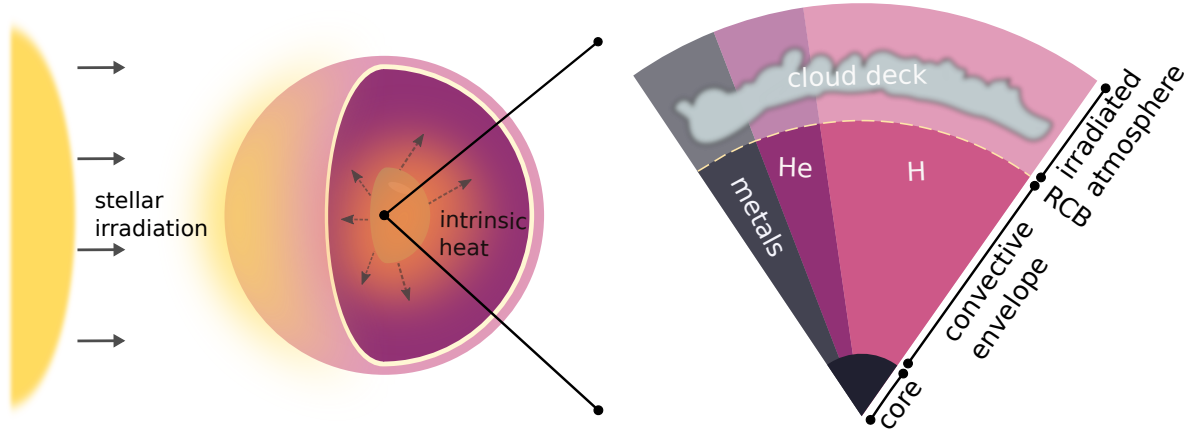


Figure 2.1.: Sketch of the coupled atmosphere and interior model as used in [Paper I](#), [Paper II](#), and [Paper III](#): A gaseous giant planet is irradiated by its host star. Modified from [Paper II](#).

where the temperature gradient ∇_T is defined as $\nabla_T := d \ln T / d \ln P$. Calculating the temperature distribution is a complex task that relies on the heat transfer mechanism occurring within the planet, such as radiation, conduction, and convection. Both the composition and the heat transport are assumptions that can vary with the additionally assumed number of layers within the model, i.e. a rocky isothermal core below a convective envelope consisting of a H_2O -rich H/He-mixture, and second convective envelope with a H_2O -poor H/He-mixture. The interiors of the giant planets are historically considered convective unstable – in other words, convection occurs and homogenises the interior [97, 344]. However, the real picture may be more complex, including inhomogeneous interiors (e.g. for Jupiter and Saturn [46, 338]) with compositional gradients, e.g. [105], or thermal boundary layers (e.g. for Uranus and Neptune [100, 101]), energy transport mechanisms such as layered convection (e.g. for Saturn [103]), or more exotic mechanisms such as fingering convection [102, 345]. For an overview on the theory of heat transport, see [346, 347] for stars, whose fundamentals are applicable to giant planets [348–350].

The mass dm in a single shell dr can change over time due to contraction, cooling, or mass transport. To provide a comprehensive picture, the structure equations mentioned above can be supplemented with equations that describe both the change of luminosity and composition, especially for non-adiabatic, i.e. not-fully adiabatic, interiors [25]. Examples of interior structure codes that incorporate such equations can be found in studies focusing on Uranus and Neptune [100, 101, 348] and giant planets [349].

In this thesis, a three-layer structure is assumed when performing interior calculations with MOGROP. The structure model consists of a radiative atmosphere, a convective envelope, and an isothermal core. A homogeneous planet without composition gradients is assumed. The atmosphere follows the P - T conditions accounting for both the star’s irradiation flux and the planet’s intrinsic heat flux, as described in more detail in Sect. 2.2. For the convective interior, the adiabatic gradient is $\nabla_{\text{ad}} = \left(\frac{\partial \ln T}{\partial \ln P} \right)_S$ and describes the change in temperature with pressure for a process occurring at constant entropy S , i.e. isentropic. The atmosphere and envelope are composed of a mixture of hydrogen, helium, and metals, while the core is made of rocks, as detailed in Sect. 2.1.3. Metals denote all elements heavier than hydrogen and helium. The proportions of the primary components are specified in terms of mass fractions within the planet; for example, for hydrogen, it is $X = \mu_X N_{\text{H}} / M_{\text{P}}$ where μ_X represents the molecular mass, N_{H} stands for the number of particles, and M_{P} denotes the mass of the planet. Furthermore, the helium mass fraction is defined as Y and the heavy element or metal mass fraction as Z . Taken together, $X + Y + Z = 1$. A detailed explanation of the terminology used can be found in Sect. A.2.

This model is well-suited for two reasons: First, for exoplanets, the key observables available are the planetary radius and mass, which the interior model adeptly matches. This is in contrast with the Solar System planets, where additional data such as net luminosity, magnetic, and gravity field measurements enable more elaborate models. Second, this thesis focuses on exploring the influence of the atmospheric thermal structure on the planet’s interior and its thermal evolution. This approach enables a focused study of core aspects, laying the groundwork for future, more detailed work.

Fig. 2.1 illustrates the interior model setup with its distinct layers and main constituents, illustrating the necessity to account for both the heat flux received from the host star and the planet’s intrinsic heat flux. Together, these factors significantly influence the thermal state of the planet, i.e. the P – T profile.

Within MOGROP, the planetary profile is calculated as follows: the temperature profile P – T is pre-computed, subsequently the density ρ is calculated. Eqs. (2.1–2.3) are then solved by numerical integration. Boundary conditions are required at $r = R_P$: $m(R_P) = M_P$ and $m(r = 0) = 0$ for $r(0) = 0$. Further, it is $P(r = R_P) = 10^{-6}$ GPa. Within the model setup of this thesis, first, the atmospheric P – T conditions are calculated, from which the radiative-convective boundary is determined, setting the starting point $(T_{\text{ad}}, P_{\text{ad}})$ for the P – T of the isentrope of the envelope.

To match the planetary radius R_P , given the planetary mass M_P , it is necessary to introduce an additional assumption about the presence of a heavy element core with mass M_{core} or to specify a certain metallicity Z_{env} for the envelope. In other words, the radius fixes the core mass M_{core} or, alternatively, Z_{env} . This property is used to derive the metallicity Z_P or the total mass of heavy elements M_Z of giant exoplanets [36, 44, 141, 342, 351, 352]. Mathematically, the bulk metallicity Z_P is

$$\begin{aligned} Z_P &= M_Z/M_P \\ &= (M_{Z,\text{atm}} + M_{Z,\text{env}} + M_{\text{core}})/M_P \\ &= Z_{\text{atm}} M_{\text{atm}}/M_P + Z_{\text{env}} M_{\text{env}}/M_P + M_{\text{core}}/M_P, \end{aligned} \quad (2.5)$$

with the total planetary mass $M_P = M_{\text{atm}} + M_{\text{env}} + M_{\text{core}}$. The bulk metallicity Z_P and the atmospheric metallicity Z_{atm} are important markers of planetary formation and evolution, see Sect. 3.1.1.

2.1.2. Radiative-Convective Boundary

The atmosphere connects to the convective envelope at the RCB. This boundary is defined by a specific pair of values $(T_{\text{ad}}, P_{\text{ad}})$ where the interior adiabat begins. The atmospheric model, particularly the P – T profile, determines this pair of values, making the atmospheric model a critical input and an important outer boundary condition for calculating the internal structure of irradiated giant planets. The shift from a radiative atmosphere to a convective interior is defined by comparing the adiabatic gradient with the local temperature gradient:

$$\nabla_{\text{local}} \geq \nabla_{\text{ad}}, \quad (2.6)$$

where $\nabla_{\text{ad}} = \left(\frac{\partial \ln T}{\partial \ln P}\right)_S$ is taken from the EoS tables for the precalculated atmospheric P – T profile. This method of transition was implemented to ensure a homogeneous description instead of setting a constant T_{ad} value for the isentrope to start. Fig. 2.2 illustrates the condition from Eq. (2.6) used to calculate the RCB for a given P – T profile. The upper panel shows the atmospheric P – T profiles for various T_{int} values up to the RCB which is indicated by dots, from which the interior isentrope follows. T_{int} is the parametrisation of the outgoing flux

of the planet. The lower panel shows the local and adiabatic gradient along the precalculated atmospheric P - T .

Compared to highly irradiated extrasolar giant planets, the giant planets in our Solar System experience much lower levels of irradiation. The isentrope starts at the surface of the planet which is defined at $P(R_P) = 1$ bar [40, 182, 342]. In contrast to the weak irradiation of the solar planets, radiative-convective equilibrium calculations of the atmospheres of their irradiated siblings predict a deep isothermal region, reaching up to several hundred bars, and thus shifting the RCB to larger pressures [67, 182, 183], which can be seen in the upper panel of Fig. 2.2. In addition, it has been found that high T_{eq} values deepen the RCB within the planet [179].

Further, the intrinsic outgoing flux of the planet, parametrised by T_{int} , significantly impacts the depth of the RCB, descending to higher pressures with decreased fluxes, largely determined by the entropy of the underlying adiabat [184, 353, 354]. The primary source of intrinsic flux originates from primordial heat and is closely linked to the planet's age as the planet cools. Consequently, it is essential to conduct thermal evolution calculations to accurately determine the inner boundary flux, see Sect. 2.1.4. However, often used in atmosphere models are values of $T_{\text{int}} \sim 100$ K, leading to large $P_{\text{ad}} \sim \text{kbar}$ and deep RCBs for irradiated planets, based on Jupiter's outgoing flux. Contrary, Thorngren *et al.* [354] show that for the radii of irradiated planets T_{int} values up to 700 K and therefore shallower RCBs are required. The coupled atmosphere, interior, and thermal evolution model in this thesis offers insight into how T_{int} and P_{ad} evolve over time [343].

2.1.3. Equations of State

Hydrogen and Helium. The phase diagrams of H and He are essential for understanding the composition of giant planets. For example, Jupiter and Saturn are composed of these elements by approximately 80–90% and 75–85% by mass [49], respectively. Their behaviour under high pressures remains not fully understood, despite being the lightest and most common abundant elements in the Universe. The EoS for astrophysical objects must span a wide range of temperatures T , densities ρ , and pressures P , typically ranging from low $T \approx 100$ K and $\rho < 0.1$ g/cm³, over the intermediate WDM regime to very high $T > 10^5$ K and $\rho > 10$ g/cm³. The last regime is already important for neutron stars and white dwarfs with up to 1000 g/cm³, and relativistic effects at $\sim 10^8$ K must be taken into account. In the WDM regime, the dissociation and metallisation transition occurs at $P \sim 100$ GPa and $T \sim 1000$ K. References to reviews on the behaviour of H and He under planetary conditions can be found in [43, 355]. In this thesis, the following two EoS for H and He are used:

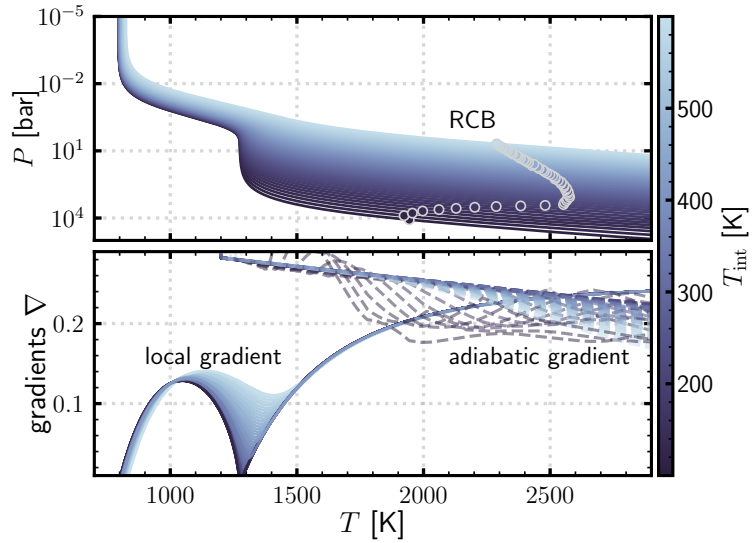


Figure 2.2.: Atmospheric P - T profiles for TOI-1268b ($T_{\text{eq}} = 915$ K) with the RCB marked as dots for various T_{int} values (upper panel). The lower panel shows the local (solid lines) and the adiabatic (dashed lines) gradient. The RCB is determined by the intersection of the local and adiabatic gradient.

- Saumon *et al.* (1995) [356] (SCvH95): SCvH95 is a successful empirical EoS, derived in the chemical picture. SCvH95 covers experimental data and simulations, but does not capture the behaviour when the interactions between particles become strong.
- Chabrier and Debras (2021) [357] (CD21): The EoS are based on the previous work by Chabrier *et al.* [358] (CMS19), but consider H/He interactions in the WDM regime, which are derived from ab initio simulations by Militzer and Hubbard [359], resulting in effective EoS for H/He. The previous CMS19-EoS combines several EoS: for low T - ρ , thus the mainly molecular/atomic regime, SCvH95 is used. For the intermediate T - ρ regime, where pressure dissociation and ionisation occurs, various ab initio data sets are used, without taking interactions in the mixture into account. In the fully ionised limit, thus high T - ρ , the analytical EoS of Chabrier and Potekhin [360] is used based on linear response theory to treat ion-electron interactions. The CD21-EoS effectively captures all current experimental results, i.e. the Hugoniot and isentropic shock experiments by Knudson and Desjarlais [361].

Fig. A.1 shows the EoS of CD21 and SCvH95 in the P - T - s space, where s is the specific entropy. The entropy is a crucial quantity, as the intrinsic heat flux is carried by convection, thus determining the thermal evolution of the giant planets. In Paper II, the thermal evolution using both EoS are compared, showing that the CD21-EoS leads to smaller planets, confirming Chabrier *et al.* [362]. Additional EoS are given in [337, 360, 363], among others. Other works have highlighted the importance of EoS for substellar objects, for example, for Jupiter [111, 331, 334, 364, 365], and brown dwarfs [337].

Heavy Elements. Two different EoS account for the metals in the envelope and in the core, i.e. ice (H_2O - CH_4 - NH_3 -mixture) in the envelope, and rock (SiO_2 - MgO - FeS - FeO -mixture) in the core. Both are analytical EoS (P - ρ) by Hubbard and Marley [366]. In Paper I, the four-times scaled SCvH95 He-EoS has been used to represent water.

Linear Mixing Approximation. Mixtures of different species are expected in the interior of planets. The linear mixing approximation, also called additive volume law, is applied. It allows combining the EoS of the single species by summing each pure specie weighted by their abundance, obtaining, for example, density or entropy [143–146]. The method is exact for ideal, non-interacting, and fully ionised mixtures, but not for interacting systems as important in the WDM regime. The EoS by CD21 takes the interactions into account.

2.1.4. Thermal Evolution

Closely connected to the current interior structure and intrinsic state of a giant planet is its thermal evolution [35]. Following their formation, giant planets undergo an evolutionary phase that leads to their current observed state. Starting from initially hot and bright objects that show an extended radius, their internal heat is gradually emitted. In this time, they cool due to the loss of internal heat, and their interiors undergo changes and contract [44, 367]. Thermal evolution modelling serves as a method to trace the history of each planet to its current condition [25]. The evolution of the radius over time shows the rate at which the energy is radiated away. Ideally, such models align the radius observed at the present age t_{age} of the planet: $R_{\text{P}}(t = t_{\text{age}}) = R_{\text{P,observed}}$.

For irradiated planets, their cooling process is significantly influenced by the radiative outer layer, which slows the cooling compared to non-irradiated planets, such as seen in HD 209458b [368]. Moreover, the presence and distribution of heavy metals within a planet also affect the rate of cooling [369, 370].

In addition to a planet’s intrinsic heat evolution, irradiation can drive atmospheric escape mechanisms like mass loss due to extreme ultraviolet radiation [237, 239, 240, 371–373]. Factors such as cometary bombardments and internal differentiation might also influence both

the atmosphere and the interior [192], although these aspects are beyond the scope of this thesis.

The method used to obtain the cooling curve $R_P(t)$ is valid when assuming an interior with homogeneous and adiabatic layers, i.e. the mean molecular weight per mass shell is conserved. A description of the method used in MOGROP can be found in [99, 330, 343]; for deviations to non-adiabatic models, see, for example, [25].

In order to obtain the cooling curve $R_P(t)$, the energy balance equation is needed, which reads

$$L_{\text{eff}}(t) - L_{\text{eq}}(t) = L_{\text{int}}(t) = \frac{dE_{\text{int}}(t)}{dt} = 4\pi R_P(t)^2 \sigma_B T_{\text{int}}(t)^4. \quad (2.7)$$

In Eq. (2.7), $L_{\text{eff}}(t) = 4\pi R_P(t)^2 \sigma_B T_{\text{eff}}(t)^4$, with σ_B as the Stefan-Boltzmann constant, is the net infrared luminosity the planet radiates into space, that includes both the energy loss from the interior and the transmitted sunlight. Electromagnetic radiation emitted by a body is known as heat radiation and is the only mechanism through which the planet can release heat into space, e.g. [277]. The Stefan-Boltzmann-law describes the total energy radiated per unit surface area of a blackbody across all wavelengths per unit time, L_{eff} , and sets the characteristic effective temperature T_{eff} . For irradiated atmospheres, it accounts for the intrinsic luminosity L_{int} and the transmitted luminosity L_{eq} .

The luminosity $L_{\text{eq}}(t) = 4\pi R_P(t)^2 \sigma_B T_{\text{eq}}^4$ is the stellar energy absorbed and re-radiated by the planet, with the characteristic temperature T_{eq} already defined in Eq. (1.1). T_{eq} is typically kept constant, but can vary due to migration or stellar evolution, $T_{\text{eq}} = T_{\text{eq}}(a, L_\star)$ [374, 375]. The evolving stellar irradiation was recently included in the code of Müller and Helled [376] for WASP-193b [61].

The intrinsic luminosity $L_{\text{int}}(t)$ is parameterised with the characteristic temperature T_{int} . Given T_{int} , the time interval dt is calculated that is needed to lose dE_{int} . This intrinsic heat loss can have several contributions [84]:

$$L_{\text{int}}(t) = L_{\text{sec}}(t) + L_{\text{radio}}(t) + L_{\text{extra}}(t). \quad (2.8)$$

The first contribution of Eq. (2.8) accounts for the heat loss of each envelope mass shell and of the core due to secular cooling which is given by

$$L_{\text{sec}}(t) = - \int_0^{M_P} dm T(m, t) \frac{ds(m, t)}{dt}, \quad (2.9)$$

where $s(m)$ is the specific entropy. A derivation of L_{sec} can be found in [330, 348]. The second term accounts for radiogenic heating of the core, which is of minor importance for H/He-dominated planets. However, for sub-Neptunes the contribution can be significant, enlarging the radius [377, 378].

The third summand L_{extra} summarises all extra energy sources, for example those from tidal heating [379, 380] or, in the case of Saturn or Jupiter, from the release of gravitational energy due to the separation of chemical components, e.g. [104, 339]. The inflation of hot Jupiters is often characterised by the extra energy necessary to explain their observed radii. The extra luminosity is parameterised in terms of L_{eq} [64, 65, 381], so that $L_{\text{extra}} = \varepsilon L_{\text{eq}}$, with ε as the heating efficiency after Thorngren and Fortney [64]. ε ranges up to 2.5% for irradiated Jupiters with $M_P > 0.5M_J$, depending on T_{eq} [64, 65].

2.2. Atmospheric Modelling

This section details the analytical atmospheric models used to simulate clear and cloudy thermal structures. The models of Guillot (2010) [180] (hereafter *Guillot10*), already implemented

in MOGROP, and Heng *et al.* (2012) [321] (hereafter *Heng12*) are presented. The *Heng12* model has been expanded and automated to improve computational efficiency.

Analytical models incorporate stellar and intrinsic radiation effects, crucial for determining deep atmospheric temperatures that determine the thermal evolution. They facilitate rapid computation for coupled atmospheric, interior, and evolution models, using a minimal set of parameters to capture the essential physics. In addition, the models are adaptable to planets with varying T_{eq} values. For this thesis, upper atmospheric conditions matter only for the thermal evolution of planets if they influence the deep temperature. The atmospheric mass is negligible and irrelevant for the derived bulk metallicity. For example, the atmospheric mass for WASP-10b is $< 1\% M_{\text{P}}$, for WASP-39b $< 2\% M_{\text{P}}$, whereas the radius of the atmosphere is up to $2\% R_{\text{P}}$ for WASP-10b and $50\% R_{\text{P}}$ for WASP-39b for high T_{int} values.

2.2.1. Thermal Structures of Clear and Cloudy Atmospheres

Guillot10 derive a P - T structure for the atmosphere of irradiated Jupiters, accounting for both the insolation by the star and the planet's intrinsic luminosity. Solving the moments of radiative transfer, the Eddington approximation as a closure relation is made. The two-stream (or dual-band) approximation applies, decoupling the radiation fields: Outgoing radiation is mostly emitted in the infrared, incoming radiation is mostly emitted in the visible part of the spectrum.¹ Scattering is neglected (mirroring a purely absorbing situation)², so that the semi-grey opacities in the long and shortwaves refer to absorption opacities. The model delivers the temperature structure in radiative equilibrium, i.e. each layer of the atmosphere emits the same amount of energy as it absorbs.

Heng12 generalises the *Guillot10* formalism to include additional effects on the P - T structure, such as scattering in the shortwave, collision-induced absorption, and clouds or hazes. Since the effects of clouds and hazes are similar, only the term clouds will be used hereafter. *Guillot10* is recovered, i.e. Eq. (49) in Guillot [180] in the case of no scattering and pure absorption. Additional longwave opacity sources are implemented as $\kappa_{\text{L}} = \kappa_{\text{L}}(m)$, in contrast to *Guillot10*, where κ_{L} is set to be constant.

The following description is based on the generalised *Heng12* formalism, specifically Sect. 3.3. of Heng *et al.* [321], and presents the P - T profiles, without providing a derivation. A typical P - T profile is illustrated in Sect. 2.2.2. This is followed by Sect. 2.2.3 on how the free parameters are calibrated.

The generalised temperature profile T - m , with m as the atmospheric column mass, reads:

$$\begin{aligned} \bar{T}^4 = & \frac{T_{\text{int}}^4}{4} \left(2 + 3 \int_0^m \kappa_{\text{L}} \, dm' \right) \\ & + \frac{T_{\text{eq}}^4}{2} \left[1 + \gamma E_2(\kappa_{\text{S}} m') + 3 \int_0^m \kappa_{\text{L}} E_3(\kappa_{\text{S}} m') \, dm' \right]. \end{aligned} \quad (2.10)$$

T_{int} and T_{eq} are the intrinsic and equilibrium temperatures, respectively, defined in Sect. 2.1.4. The grey opacities κ_{L} (longwave) and κ_{S} (shortwave) are crucial input parameters, where – in this generalised description – the longwave opacity can adopt an arbitrary functional form: $\kappa_{\text{L}} = \kappa_{\text{L}}(m)$. In contrast, the shortwave opacity is assumed to be constant. The ratio of the shortwave to the longwave opacity is $\gamma \equiv \kappa_{\text{S}}/\kappa_{\text{L}}$ and it is $\tau = \tau(m) \equiv \kappa_{\text{L}}(m) m$. The longwave optical depth is defined as $\tau_{\text{L}} = \int_0^m \kappa_{\text{L}}(m) \, dm'$. With the assumption that the gravity g [cm /s]

¹The decoupling of the radiation fields, after e.g. [382], is not always accurate for heavily irradiated planets. As the deep temperature rises, thermal emission shifts towards the visible. In some cases, such as when the parent star is an M-dwarf, the incoming and outgoing irradiation may not differ significantly due to low stellar effective temperatures [180].

²Scattering complicates radiative transfer solutions due to photons switching between rays, posing a long-standing issue [383]. Scattering processes, such as Rayleigh, Mie, and Thomson scattering, are crucial for determining the absorbed flux fraction and affect both thermal and visible radiation.

is constant over the thin atmosphere, it is $P = m g$, with m as the column mass per unit area of the atmosphere [g/cm^2] and P as the vertical pressure [bar], resulting from the hydrostatic equilibrium equation. The relation is used to convert m and P within the *Heng12* formalism.

After Abramowitz and Stegun [384], the exponential integrals are defined as

$$E_n(z) = \int_1^\infty t^{-n} \exp^{-zt} dt \text{ and } E_{n+1}(z) = \frac{1}{n} [\exp(-z) - z E_n].$$

Eq. (2.10) is equivalent to Eq. (31) in Heng *et al.* [321], using the Eddington coefficients $\mathcal{E}_1 = 1/3$ and $\mathcal{E}_2 = 1/2$, scattering factor $\xi = 1$ resembling no scattering, and $T_{\text{eq}} = T_{\text{irr}}/\sqrt{2}$.

(a) Clear atmosphere: case $\kappa_L(m) = \kappa_{L,0}$ (const.).

For a pressure and temperature independent opacity, it follows $\kappa_L(P) = \kappa_{L,0}$, Eq. (2.10) can be evaluated, so that $T(\tau)$ of the clear atmosphere results in

$$\begin{aligned} \bar{T}^4 = & \frac{3T_{\text{int}}^4}{4} \left(\frac{2}{3} + \tau \right) \\ & + \frac{3T_{\text{eq}}^4}{4} \left\{ \frac{2}{3} + \frac{2}{3\gamma} \left[1 + \left(\frac{\gamma\tau}{2} - 1 \right) \exp^{-\gamma\tau} \right] + \frac{2\gamma}{3} \left(1 - \frac{\tau^2}{2} \right) E_2(\gamma\tau) \right\}, \end{aligned} \quad (2.11)$$

where the longwave optical depth $\tau_L = \tau \equiv \tau_{L,0}$, and the ratio $\gamma = \kappa_S/\kappa_{L,0} \equiv \gamma_0$. The conversion from optical depth to pressure is $\tau = \kappa_{L,0}m = \kappa_{L,0}(P/g)$. Note that $\tau \sim \kappa_{L,0}P$. Eq. (2.11) equals Eq. (49) in Guillot [180].

(b) Cloudy/hazy atmosphere: case $\kappa_L(m) = \kappa_{L,0} + \kappa_c(m)$.

Accounting for the effect of a cloud/haze deck as an additional contribution to the total longwave opacity $\kappa_L(P)$ as

$$\kappa_L(P) = \kappa_{L,0} + \kappa_c(P). \quad (2.12)$$

The longwave optical depth $\tau_L(P)$ is

$$\tau_L(P) = \kappa_{L,0} \frac{P}{g} + \tau_c(P). \quad (2.13)$$

Heng12 parameterised a purely absorbing non-uniform cloud deck opacity:

$$\kappa_c(P) = \kappa_{c,0} \cdot \exp \left[-\Delta_c \left(1 - \frac{P}{P_c} \right)^2 \right]. \quad (2.14)$$

Here, P_c is the cloud deck location pressure [bar] and Δ_c is the dimensionless cloud deck thickness with smaller values describing a geometrically thicker cloud deck. $\kappa_{c,0}$ is the cloud deck opacity normalisation [cm^2/g]. The total cloud deck opacity κ_c takes on a Gaussian form. Fig. A.9 shows the cloud opacity as a function of pressure. Scattering is neglected. Note that longwave absorption and shortwave scattering by clouds have contrasting effects: enhanced longwave absorption cools the upper atmosphere while warming the lower. In contrast, shortwave scattering warms the upper atmosphere and cools the lower one. Among the solution presented here, *Heng12* provides a thermal structure with an uniform cloud/haze layer including longwave absorption *and* shortwave scattering, see Eq. (45) of [321]. In the presented case with a non-uniform absorption opacity due to clouds, no scattering is considered.

The corresponding cloud deck opacity reads

$$\begin{aligned} \tau_c(m) &= \int_0^m \kappa_c dm' \\ &= \frac{\kappa_{c,0}m_c}{2} \sqrt{\frac{\pi}{\Delta_c}} \left[\tilde{E} \left(\Delta_c^{1/2} \right) - \tilde{E} \left(\Delta_c^{1/2} \left(1 - \frac{m}{m_c} \right) \right) \right], \end{aligned} \quad (2.15)$$

with the error function $\tilde{E} \equiv \frac{2}{\pi} \int_0^x \exp(-y^2) dy$ defined by Arfken and Weber [385], and $m_c \equiv P_c/g$.

Inserting Eqs. (2.12–2.15) in Eq. (2.10), T - τ results in:

$$\begin{aligned} \bar{T}^4 = & \frac{3T_{\text{int}}^4}{4} \left(\frac{2}{3} + \tau_L \right) \\ & + \frac{3T_{\text{eq}}^4}{4} \left\{ \frac{2}{3} + \frac{2}{3\gamma_0} \left[1 + \exp(-\gamma\tau) \left(\frac{\gamma\tau}{2} - 1 \right) \right] \right. \\ & \left. + \frac{2\gamma}{3} E_2(\gamma\tau) \left[1 - \frac{\tau^2}{2} \left(\frac{\gamma}{\gamma_0} \right) \right] + 2\mathcal{J} \right\}. \end{aligned} \quad (2.16)$$

Eq. (2.16) equals Eq. (50) in Heng *et al.* [321], not including the effect of collision-induced absorption, as it would infer an additional parameter. The cloud integral \mathcal{J} needs to be evaluated numerically:

$$\begin{aligned} \mathcal{J} = & \int_1^\infty x^{-3} \mathcal{J}_0(m, x) dx \quad , \quad (2.17) \\ \text{with } \mathcal{J}_0 = & \frac{\kappa_{c,0} m_c}{2} \sqrt{\frac{\pi}{\Delta_c}} \cdot \exp \left(\frac{(\kappa_s m_c)^2}{4\Delta_c} x^2 - \kappa_s m_c x \right) \\ & \cdot \left[\tilde{E} \left(\Delta_c^{1/2} - \frac{\kappa_s m_c x}{2\Delta_c^{1/2}} \right) - \tilde{E} \left(\Delta_c^{1/2} \left(1 - \frac{m}{m_c} \right) - \frac{\kappa_s m_c x}{2\Delta_c^{1/2}} \right) \right]. \end{aligned}$$

The numeric implementation of the cloud integral \mathcal{J} , Eq. (2.17), and $T(P)$, Eq. (2.16), is given in [386].

In summary, the thermal structures can be solved for the clear P - T , Eq. (2.11), and cloudy P - T , Eq. (2.16), with the definitions shown in Table 2.1. The clear model parameters include T_{eq} , T_{int} , gravity g , and opacities $\kappa_{L,0}$ and κ_S . The cloudy model also requires P_c , Δ_c , and $\kappa_{c,0}$.

From a practical perspective, in the clear case, in a first step, τ is the coordinate resembling the vertical height coordinate of the atmosphere, and T via Eq. (2.11), giving T - τ . In a second step, P via $P = (\tau g)/\kappa_{L,0}$ is assigned. One could directly convert τ into the pressure coordinate P . However, this two-step approach has been used while investigating how to include non-constant opacities in the clear model, i.e. pressure and temperature dependent Rosseland-mean opacities $\kappa_R(P, T)$, see Sect. A.5.2. For the cloudy case, along the coordinates P or m the optical depths $\tau_L(P)$, $\tau(P)$, the cloud integral $\mathcal{J}(m)$, and $\gamma(P)$ are pre-calculated, and finally $T(\tau, \tau_L, \gamma, \mathcal{J})$ is obtained.

2.2.2. Schematic of the Clear Thermal Structure

To provide a first understanding of the different parts of the thermal structures, the P - T profiles, and their relation to planetary age and radius, the P - T profiles of a planet with a clear atmosphere, as result of Eq. (2.11), is presented. A similar explanation can be found in Marley and Robinson [277], see Figs. 1 and 2 therein.

Fig. 2.3 shows the several P - T profiles of the atmosphere and upper envelope of the warm Jupiter WASP-10b. The atmosphere profile is already coupled to the isentropes of the interior. Thermal evolution calculations have been performed to infer the age, linked to the radius R_P and the intrinsic temperature T_{int} . The opacities are set to $\kappa_{L,0} = 0.01 \text{ cm}^2/\text{g}$ and $\kappa_S = 0.00167 \text{ cm}^2/\text{g}$, with a resulting $\gamma = 0.167$, taken from Paper II.

The P - T profile is determined by T_{eq} , T_{int} , and the semi-grey opacities κ_L and κ_S . In Fig. 2.3, the influence of T_{int} is shown for $T_{\text{int}} = 200 - 1200 \text{ K}$, making up the various profiles that are colour-coded in blue shades. Each profile corresponds to a specific radius R_P and age of the planet. T_{eq} roughly determines the temperature range of the atmosphere, see also Fig. 1.3 for the thermal structure of planets with different T_{eq} . Note that T_{eq} is a function of

Generalised P-T	
T_{eq} [K]	equilibrium temperature
T_{int} [K]	intrinsic temperature
g [cm/s ²]	gravity of the planet
m [g/cm ²]	column mass per unit area
P [bar]	= m/g pressure
κ_{L} [cm ² /g]	total grey opacity in the longwave
τ	$\equiv \kappa_{\text{L}}m = \kappa_{\text{L}}(P/g)$ optical depth
τ_{L}	= $\int \kappa_{\text{L}} dm$
γ	= $\kappa_{\text{s}}/\kappa_{\text{L}}$
Clear P-T	
	($\kappa_{\text{L}} = \kappa_{\text{L},0}$, $\gamma = \gamma_0$, $\tau = \tau_{\text{L}}$)
$\kappa_{\text{L},0}$ [cm ² /g]	grey opacity in the longwave of the background gas
κ_{s} [cm ² /g]	grey opacity in the shortwave of the background gas
γ_0	= $\kappa_{\text{s}}/\kappa_{\text{L},0}$
Cloudy P-T	
	($\kappa_{\text{L}} = \kappa_{\text{L},0} + \kappa_{\text{c}}(m)$, $\tau_{\text{L}} = \tau_{\text{L},0} + \tau_{\text{c}}$)
P_{c}	cloud deck location
$\kappa_{\text{c},0}$	grey opacity in the longwave due to clouds
Δ_{c}	cloud deck thickness
m_{c}	= P_{c}/g

Table 2.1.: Overview of parameters in the *Heng12* formalism for calculating clear and cloudy P - T conditions. Input parameters printed in bold require calibration with advanced atmosphere models.

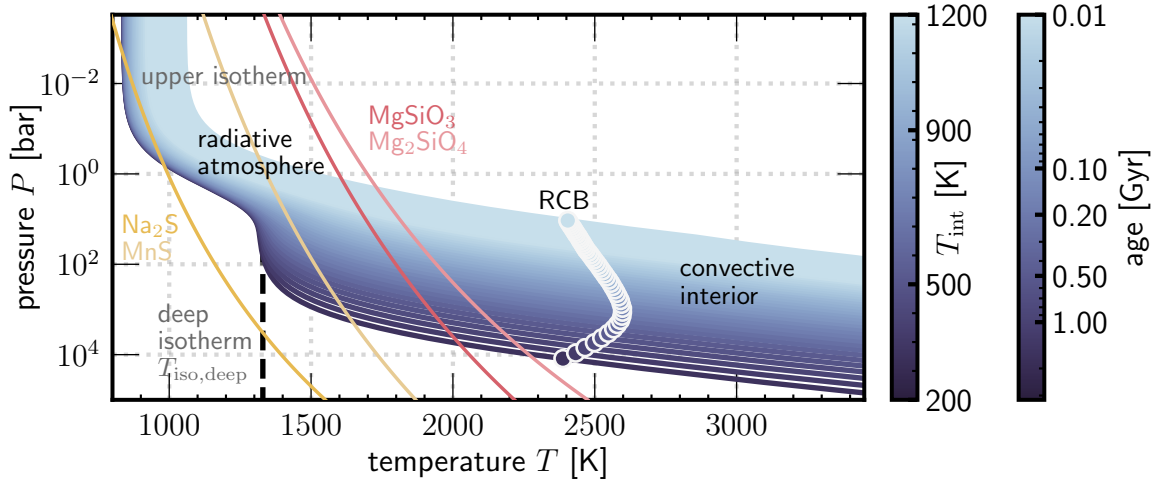


Figure 2.3.: Characteristic clear P - T profile with all for this thesis relevant parts of the atmosphere: The upper atmosphere, with the characteristic upper isotherm, the deep isotherm in the lower atmosphere with $T_{\text{iso,deep}}$, the coupling of the atmosphere and interior at the RCB and the ensuing isentrope of the interior. Shown are the isentropes for different intrinsic luminosities $T_{\text{int}} = 200 - 1200$ K (dark to light colours). The second colour scale shows the corresponding age evaluated from thermal evolution calculations (the age of WASP-10b is 0.19 – 0.35 Gyr). Coloured lines are condensation curves.

$T_{\text{eq}} = T_{\text{eq}}(a, L_{\star})$, see Sect. 2.1.4.

For the ratio of the opacities, $\gamma \leq 1$, no inversions occur. In Fig. A.5 the interplay of κ_{L} , κ_{S} , and γ (for $\gamma \leq 1$) is shown. Further parameter studies can be found in the original works of Guillot [180] and Heng *et al.* [321].

The profile shows the P - T conditions from the outer atmosphere to the upper interior ($P = 10^{-1} - 10^5$ bar, $T = 800 - 3500$ K). The atmosphere can broadly be divided into an *upper atmosphere*, and the *deep atmosphere*. The atmosphere connects to the interior at the RCB at the characteristic values P_{ad} , T_{ad} , and is followed by the isentrope of the interior for a given T_{int} , see Sect. 2.1.2. Generally, a hotter isentrope is related to a younger planet, and a cooler isentrope with an older planet as the planet emits the heat stored from its formation process over time.

The thermal atmospheric structure is characterised by an upper and deep isotherm with the characteristic values $T_{\text{iso,up}}$ and $T_{\text{iso,deep}}$. The lower isotherm is a result of the strong incident radiation ($T_{\text{eq}} \gg T_{\text{int}}$). This results in a deep vertical isothermal extended radiative zone, before the contribution of the intrinsic heat begins to play a substantial role [67, 178–183].

Contrary, the upper isotherm is a feature of the model assumptions. In comparison to numerical models, the semi-grey models overestimate the temperatures at low pressures and low optical depth. Parmentier and Guillot [255] derived a non-grey analytical model and compare both their non-grey analytical and the *Guillot10* grey analytical model to the results of a numerical model with full wavelength dependent opacities and angular dependence [387]. They find that non-grey effects significantly cool the upper atmosphere, with discrepancies to the grey model above 1 bar. Non-grey effects are due to opacities dominated by strong and narrow lines, or molecular bands, allowing the upper atmosphere to cool more efficiently [255]. The analytical solution is highly consistent with the line-by-line models in the deep atmosphere, confirming that the grey model is sufficient for models of global evolution calculations. However, the line blanketing effect, e.g. [388], may warm the lower atmosphere, inhibiting the cooling, if wide or molecular opacity bands are present [255]. The effect refers to absorption and re-emission at higher wavelength, i.e. into the infrared, acting like a blanket. In stellar physics, this is connected to the amount of metals in the star: The more metals, the stronger the effect.

2.2.3. Calibration of the Free Parameters

This thesis includes calibrating the free parameters of the atmosphere model that are listed in Table 2.1. For example, thermal evolution calculations determine the current T_{int} that matches the observed R_{P} . T_{eq} is calculable using R_{P} , A_{B} , a , T_{\star} , and R_{\star} , see Eq. (1.1). For the gravity g , the planetary mass M_{P} is required. Above all, it is essential to calibrate the opacities, which play a major role in radiative transfer and determining the thermal structure.

Clear Model. Crucial input parameters are the grey opacities $\kappa_{\text{L},0}$ and κ_{S} . In Paper I, previously published P - T structures, that result from numerical models with an advanced treatment of opacities, are compared to the P - T profiles presented in this work, aiming at matching the deep isotherms while adapting the γ -ratio, similar to the approach of Jin *et al.* [257]. Additionally, it is ensured that the thermal opacity $\kappa_{\text{L},0}$ closely resembles an averaged Rosseland-mean opacity across the entire atmosphere, as illustrated in Fig. 2 in Paper I and Fig. A.6. The Rosseland mean opacity is valid when the atmosphere is optical thick and photon transport is approximately diffusional, see Sect. A.5.1. In Paper II, a fit formula for $\gamma(T_{\text{eq}})$ is presented, employing the same method of matching grey profiles from this thesis to published thermal structures for multiple planets, as explained in Sect. 2.1.1 and Fig. 2 in Paper II.

Cloudy Model. For the cloudy model, among the γ -ratio, the specific parameters of the cloud opacity, Eq. (2.14), must be chosen. Equilibrium cloud formation starts when the vapour pressure of a condensable species reaches saturation through vertical mixing, e.g. [136]. Under equilibrium conditions, the location and composition of the cloud are roughly determined by where the condensation curve of the condensable species intersects the P - T profile. This equi-

librium cloud condensation scenario, initially developed for Jupiter by Lewis [389], is supported by evidence from comparisons of models and data of exoplanet and brown dwarf atmospheres. These curves are abundance dependent and independent of the planetary P - T profile, see Sect. A.6.1.

The free parameters are the cloud deck location P_c , the cloud deck thickness Δ_c , and opacity normalisation $\kappa_{c,0}$: The cloud deck location P_c is set by comparing the clear profile with condensation curves. For example, see Fig. 2.3, the intersection with sodium sulfide (Na_2S) would lead to two intersections at 0.003 bar and 0.9 bar, indicating the lower cloud base, e.g. [208]. In the expanded MOGROP code, the intersection is either calculated automatically between the pre-calculated clear atmospheric structure and the respective (pre-chosen) condensation curve, or P_c is fixed at a certain pressure. Thermal stability curves are presented in Sect. A.6.1 and Fig. A.8. The thickness of the cloud deck Δ_c as well as the opacity normalisation $\kappa_{c,0}$ are chosen in comparison with more advanced P - T solutions. In Paper I, literature values of the optical depth that include the simulation of clouds, such as those from [390, 391], are compared to the outcome of the analytical model, and $\kappa_{c,0}$ is adjusted accordingly, see Figs. 3 and 4 in Paper I. In Paper II, the cloud opacity values in the literature are used directly for $\kappa_{c,0}$, such as those of Dobbs-Dixon and Agol [392] and Lee *et al.* [393]. To cover a larger parameter space, ranges of $\kappa_{c,0} = 0.05 - 1.0 \text{ cm}^2/\text{g}$ and $\Delta_c = 10 - 100$ are used.

Despite challenges such as uncertainties in cloud opacity and height, and the lack of self-consistent coupling with the thermal structure, this analytical method is valid. It facilitates the study of effects on interior structure and thermal evolution, enabling the inclusion of more advanced models in the coupled atmosphere-interior and thermal evolution approach.

2.2.4. Modifications of the Cloud Model

Several Cloud Decks. The Solar System giant planets show several layers of different cloud species. For example, Jupiter inhibits clouds of NH_3 , NH_4SH , and H_2O at different pressure levels [77]. The possibility of the *Heng12* formalism to model several cloud layers by adding up each cloud layer's opacity has been explored, see Fig. A.9 in Sect. A.6.3. This approach introduces more free parameters for exoplanets without considering microphysics, hence it was not adopted in this thesis.

Cloud Gradients. In Paper I, the purely absorbing effect of clouds is modelled with the P - T expression by *Heng12*. However, one result of this paper shows that the P - T profile with clouds becomes physically unrealistic as the local temperature gradient exceeds the adiabatic gradient: $\nabla_{\text{local}} > \nabla_{\text{ad}}$, becoming super-adiabatic. In Paper II, a modification to the *Heng12* model is introduced, see also Sect. 3.1.3.

3. From Clouds to Cores: Results

This chapter discusses the results obtained with the coupled approach of atmosphere, interior, and thermal evolution models, applied to two research fields in exoplanetary science. First, the main quantity of interest is the derived bulk metallicity from coupled atmosphere, interior, and thermal evolution modelling. Sect. 3.1 presents the studies where a cloud layer was included in the atmosphere. The impact on the derived bulk metallicity, Paper I [394], and the impact on the radius evolution, Paper II [395], are analysed. Second, the radius anomaly of hot Jupiters seems to be connected with the stellar irradiation. One proposed mechanism is based on Ohmic dissipation, for which the atmospheric P - T conditions are important. The results in Paper III [396] and Paper IV [397] are presented in Sect. 3.2.

3.1. Cloudy Atmospheres

Modelling a planet’s interior structure and composition provides insights into its formation and evolution, particularly through parameters such as bulk composition and heavy element mass fraction Z_P . The connection between planetary bulk and atmospheric abundances, as well as planetary and stellar abundances, is presented in Sect. 3.1.1.

However, inferring the composition of planets from observables such as planetary mass, radius, and orbital distance along with stellar parameters is often challenging. Standard model assumptions may not yield an interior model that aligns with observations, e.g. the over-large radii of the inflated gas giant population or the excess luminosity of Saturn when applying a fully convective model [105, 203]. Formation models predict heavy element masses that do not align with the derived values, for example, the very dense gas planet HD 149026b [398–400]. Often, models fail to match all observables, suggesting missing physics in the underlying models.

The work in Sect. 3.1.2 models the interior of the inflated Saturn-mass planet WASP-39b, considering its atmospheric metallicity. It also estimates the bulk metallicity of the non-inflated Jupiter-mass planet WASP-10b. Sect. 3.1.3 examines the impact of clouds on the radius evolution and bulk metallicity of the non-inflated warm Saturn-mass TOI-1268b and WASP-10b. Both studies assume the effect of clouds as a non-standard model assumption.

3.1.1. On the Connections of Planetary Bulk and Atmospheric, and Stellar Abundances

In Paper I [394] and Paper II [395], the bulk metallicity of gas planets is derived with the coupled atmosphere, interior, and evolution models as described in the previous chapter. The bulk metallicity, which is the mass fraction of metals in the interior of the planet Z_P , is a key quantity for planetary formation and migration models, derived from the coupled models approach, compare Fig. 1.1. The atmospheric metallicity, which is the mass fraction of metals in the atmosphere of the planet Z_{atm} , is a closely related key quantity, derived from the atmospheric composition obtained from transmission spectra. This section serves as an introduction to the relation between planetary formation and the bulk and atmospheric metallicities of a gas planet. Fig. 3.1 illustrates the connection between planetary formation, evolution, and the planetary and stellar abundances.

Connecting the observed atmospheric properties with the past protoplanetary disk conditions is a main goal in planetary science to inform formation and evolution models. It involves deducing precise atmospheric abundances, as is now possible with missions such as JWST, and linking them to the bulk composition of the planet [401]. Especially the atmospheric

metal mass fraction of giant planets is thought to be an important indicator of formation paths [402, 403]: firstly, atmospheric metal enrichment complements the bulk material that initially formed within the protoplanetary disk from its building components, such as planetesimals, pebbles, and gases. The composition of these building components is shaped by the astrochemistry and processes that occur within the protoplanetary disk [21, 404]. The formation mechanism itself determines the relative importance of the components within the planet [405, 406]. In detail, the composition and amount of heavy elements accreted by the growing protoplanet will be influenced by its location in the disk, the time of formation in the disk, the conditions of the disk at that location and time, and its dynamical environment, i.e. if it appears near other planets [36]. Secondly, atmospheric abundances can inform evolution processes, such as migration. For example, high atmospheric abundances of sodium (Na) could be caused by the accretion of planetesimals rich in alkali metals at later time, or due to the accretion of metal-rich gas [407].

Connection between Bulk and Stellar Properties.

The relation between the properties of star and planets, specifically their metal mass fractions, Z_\star and Z_P , total planetary mass M_P , and heavy element mass M_Z has been extensively studied over the years [36, 141, 351, 408]. Using interior and evolution models, including the methods employed in this thesis, researchers have been able to infer the bulk composition of planets from observable parameters such as planetary mass, radius, and age. With an expanding sample of planets and evolving methods, this research continually advances.

In 2006, Guillot *et al.* [408] investigated a sample of nine transiting planets and in 2011, Miller and Fortney [351] looked at the growing sample of 14 planets. In 2016, Thorngren *et al.* [36] took 47 non-inflated planets and deduced the bulk metallicity.

The authors found a relation between the mass of heavy elements M_Z and the mass of the planet M_P , with $M_Z \propto \sqrt{M_P}$ (Fig. 7 in [36]). More, they found a downward trend for the relation of the metal mass fraction $Z_P - M_P$, and a pronounced downward trend for $(Z_P/Z_\star) - M_P$ (Figs. 10/11 in [36], Fig. 3 in [351], Fig. 16.2 in [409]). Planets with high metal abundance seem to occur less frequently around low-metallicity stars (Fig. 9 in [36]). The frequency of Jupiter-like planets appears to increase with the metallicity of their host stars [410]. Interestingly, Thorngren *et al.* [36] did *not* find a correlation of $M_Z - Z_\star$ or $M_P - Z_\star$, whereas the smaller sample size by Guillot *et al.* [408] suggested such a correlation.

In the core accretion model of giant planet formation, a solid core that has reached a critical mass M_{core} triggers runaway gas accretion, forming a massive envelope M_{env} [30, 33, 411], leading to the total planetary mass of $M_P = M_{\text{core}} + M_{\text{env}}$. Naively, core accretion produces giant planets with total metal masses M_Z of approximately $M_Z = M_{\text{core}} + Z_\star M_{\text{env}}$, implicitly assuming that the star and protoplanetary disk form from the same interstellar molecular cloud, and that the disk’s metallicity resembles that of the star. This would result in planets that are enriched in heavy elements compared to their host stars [36, 408]. In contrast, planets that are formed via gravitational instability are expected to mirror the composition of their

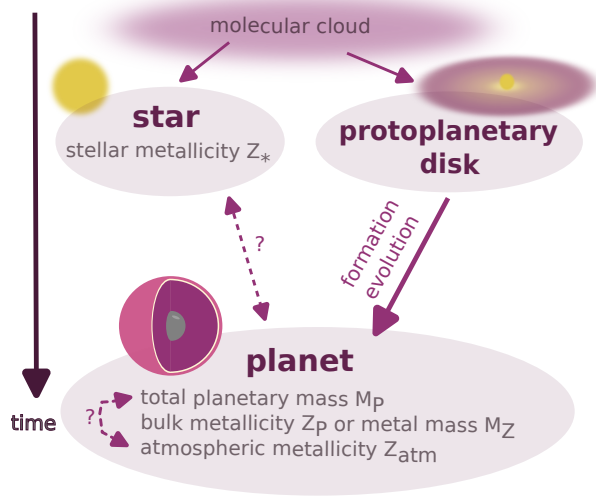


Figure 3.1.: Interior properties of giant planets are hints to past formation and evolution processes. Star and protoplanetary disk form from a molecular cloud, where the planet subsequently forms from the protoplanetary disk (solid arrows). Stellar and planetary bulk, as well as planetary bulk and atmospheric compositions are thought to be related (dashed arrows).

host star as they form without the need for a core.

Unfortunately, the picture is more complex and does not necessarily lead to a straightforward correlation between planetary metallicities and those of their host stars. First, the planets do not directly take on the composition of the star: the gas in the disk does not need to share the exact composition of the parent star due to condensation and movement of solids within the disk [404, 412], and late-stage accretion of additional planetesimal debris may occur, either adding to the core or envelope metal mass. More, all of the above studies found that several planets contain some hundreds M_E of heavy elements, called bulk heavy element enrichment. From an accretion perspective, this is an unsolved phenomenon, as the core mass is restricted to at most $M_{\text{core}} \approx 10\text{--}30M_E$ before runaway gas accretion starts [400, 413, 414], and planetesimal capture during runaway gas accretion results in only a few additional M_E of metals [415]. Bitsch *et al.* [414] show that through inward migration $M_Z \leq 100 M_E$ can be explained. Giant impacts, or planet merging, can enhance the metallicity as well, e.g. [416, 417].

Thus, both core accretion and gravitational disk instability probably produce giant planets with a range of metallicities [88, 418]. Atmospheric composition still may probe planet formation and evolution, distinguishing between both mechanisms.

Connection between Bulk and Atmospheric Metallicity. The atmospheric metal enrichment of giant planets is believed to be an important indicator of their formation paths [402, 403]. The deep interior’s composition is linked to the planet’s formation, whereas the outer envelope is also made up of materials that are accreted at later evolutionary stages [35]. By interpreting the transmission spectra of the atmospheres, the total atmospheric metallicity and abundance ratios such as the carbon-to-oxygen ratio (C/O), can be inferred from the strength of individual absorption features such as H_2O , e.g. [127, 129, 130, 223, 407, 419–421]. In Fig. 3.2, the observationally derived atmospheric metallicity of some planets over their planetary mass is shown. For the Solar System planets (dark blue dots), the metal enhancement decreases with increasing planet mass. This pattern is commonly believed to be the result of the relative importance of the accretion of solid planetesimals versus the accretion of the H/He-dominated gas in the core accretion formation mechanism. A similar pattern is expected for exoplanets; however, Fig. 3.2 shows a spread in observed metallicities, likely due to individual formation and migration scenarios. Welbanks *et al.* [407] find a downward trend when examining the atmospheric $[\text{H}_2\text{O}/\text{H}]$ from observations.

From an interior modelling perspective,

$$Z_{\text{atm}} \leq Z_{\text{env}} \quad (3.1)$$

should hold, as the atmosphere cannot be more metal-rich than the interior. The atmospheric metallicity Z_{atm} serves as an upper limit of the envelope metallicity Z_{env} . Instances where Z increases outward in the planet are short-lived, as they will be overcome by Rayleigh-Taylor instability or convection [141]. Observational astronomers often use a different nomenclature as interior modellers, and the conversion is not necessarily straightforward [427]; see Sect. A.2.3 for an overview. In addition, $Z_P \geq Z_{\text{env}}$ due to the possible presence of a core. Thus, atmospheric metallicity serves as an important constraint for interior models [35, 69, 141]. Using the relations above, Thorngren and Fortney [141] infer upper limits for atmospheric metallicities based on the derived bulk metallicities from coupled interior and evolution models, employing the aforementioned relations. This highlights the strong link between atmospheric observations and interior modelling.

However, linking the atmosphere to the bulk composition of a planet is complex. For a recent discussion, see [35, 405, 428] and references therein. Below are points on how atmospheric composition may or may not reflect bulk composition.

(1) The atmospheric composition of fully convective giant planets is expected to mirror the mixing ratios of heavy elements throughout their entire H/He envelope [36]. However, the

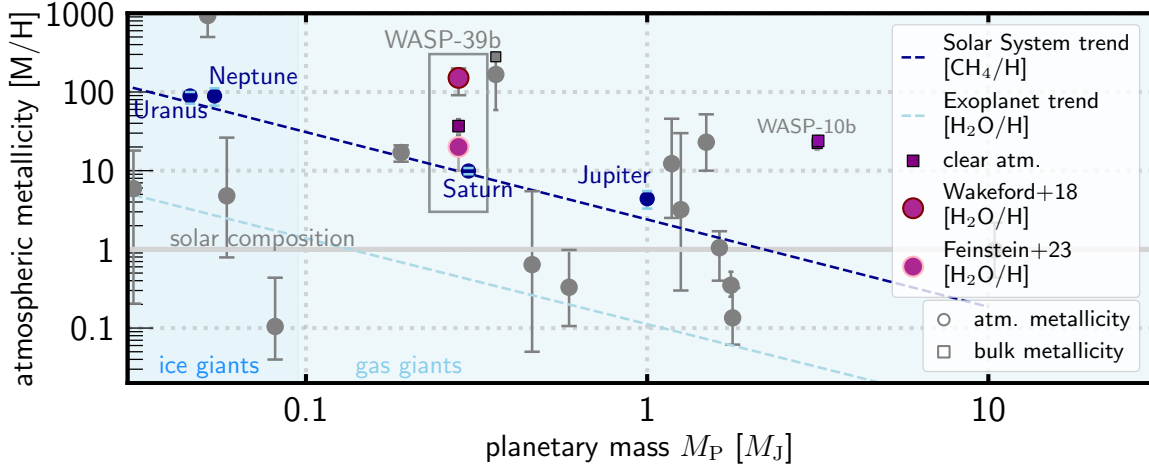


Figure 3.2.: The observationally derived atmospheric metallicity versus planetary mass for Solar System planets and selected exoplanets. The trends (dashed lines) are from Welbanks *et al.* [407], not all planets used for the exoplanet trend are shown. For the solar planets, CH_4 is used as indicator for the atmospheric metallicity, whereas H_2O serves as indicator for the exoplanets. A downward trend for the bulk metal mass fraction Z_P and M_P has been shown [36]. Data of exoplanets from private communication with H. Wakeford (April 2024), data of the Solar System planets from [422–425]. Adapted and modified from [407, 426].

mixing of metals throughout the envelope is unclear. A composition gradient could help prevent convection and thus prevent large-scale mixing [102, 350, 429], resulting from mixing of the solid core into the envelope (fuzzy core model) [49, 349, 430, 431], or from phase separations, the so-called rainouts [432]. For example, the reduction of neon (Ne) in Jupiter’s atmosphere [433] is thought to be connected to the H-He phase separation, as Ne was found to preferentially dissolve in the nonmetallic form of He rather than in the metallic form of H. (2) The composition also evolves due to evaporation that retains heavier elements (i.e. Jeans escape or Roche lobe overflow) [434] or by secular enrichment of infalling comets, e.g. [435]. (3) Due to inward migration after forming, the enrichment in metals can differ for individual elements, as shown in Hands and Helled [406], as planets accrete oxygen-poor material within the snowline, leading to an enrichment in alkali metals. Generally, inward migration can lead to an enhanced mass of heavy elements [400, 414]. (4) Giant impacts or planet merging can enhance the metallicity additionally, for example, as shown for Jupiter in Guillot [416].

(5) A recent study for Jupiter shows that the atmosphere may be disconnected from the interior due to a deep radiative zone between the outer envelope and the deep interior [121], suggesting that the atmospheric composition measured in exoplanets may also not accurately represent the bulk composition.

The connection between planetary bulk, atmospheric, and stellar metallicities provides a framework for understanding the various planetary formation and evolution pathways. The bulk metallicity Z_P as a result of coupled interior and evolution models is needed as input parameter. Model assumptions, such as the EoS of H/He, the assumed heat transport within the planet, the heavy element distribution, and the atmosphere model (investigated in this thesis), influence Z_P .

3.1.2. Impact on the Derived Bulk Metallicity

WASP-39b, a well-studied planet [9–12, 129, 243, 436–442], was first detected in transit by Faedi *et al.* [436] in 2011. Characterised as a highly inflated gas giant, it has a mass similar to Saturn ($0.28 M_J$), a large radius ($1.27 R_J$), and a low density of $0.14 \rho_J$. It orbits a quiet G-type

star, aged 9_{-4}^{+3} Gyr, making WASP-39b ideal for transmission spectroscopy due to its extended atmosphere. The atmosphere of WASP-39b has been observed by several groups using transmission spectroscopy in the infrared and optical wavelength bands [128, 438–440]. Atmospheric metallicity values varied widely, from 0.003 to $300\times$ solar metallicity, due to limited wavelength coverage, low signal-to-noise ratios, and differences in analysis [10]. In 2018, Wakeford *et al.* [129] added data from the near-infrared which allowed a detailed resolution of the water features. An atmospheric metallicity of $151_{-46}^{+48}\times$ solar ($100\text{--}200\times$ solar is $Z_{\text{obs,atm}} = 0.25 - 0.75$) was found to be the best fit for the transmission spectra. In a previous study, Thorngren and Fortney [141] estimated the bulk and atmospheric metallicity for 403 transiting planets using a Bayesian statistic approach. The bulk metallicity of WASP-39b ($Z_{\text{P,TF19}} = 0.22 \pm 0.03$), which is translated to an atmospheric metallicity of $45.5\times$ solar, did not match the observational data.

Motivated by the disagreement between observationally derived and model-predicted metallicities, the effect of clouds in the atmosphere on the model-derived metallicity was explored. The aim was to match the observed high atmospheric metallicity of WASP-39b by including the purely absorbing effect of a cloud/haze deck in the deep atmosphere, beyond the model approach by Thorngren and Fortney [141]. The coupled atmosphere-interior-evolution model, as presented in Chap. 2, was applied to both WASP-39b and WASP-10b. WASP-10b was chosen due to its larger mass ($2.96 M_{\text{J}}$), non-inflated nature ($1.03 R_{\text{J}}$, $T_{\text{eq}} = 950$ K), and age of 270 ± 80 Myr [443–445].

Approach. The approach is based on three steps: First, modelling the clear P – T structure (Figs. 1, 2 in Paper I) and the radius evolution (Figs. 5, 7 in Paper I). Second, comparing the clear atmospheric profile to condensation curves of possible cloud forming species in that temperature range and thus setting P_{c} , resulting in the cloudy P – T structures (Figs. 3, 4, 6 in Paper I). Third, the interplay of core mass M_{c} , Z_{env} , and Z_{atm} with and without cloudy P – T is explored (Figs. 8, 10 in Paper I).

Results. Different cloud scenarios were investigated, showing that cloud decks heat the lower atmosphere due to increased infrared opacity. This leads to a noticeable increase in the inferred presence of heavy elements. For WASP-10b, the core mass increased to 10%. For WASP-39b, the favoured cloud scenario with a cloud base at 30 bar yielded an envelope metallicity value ($Z_{\text{env,PNR19}} = 0.31$) still close to the lower limit of the observationally derived value. The results for WASP-39b are illustrated in Fig. 3.3. The metallicity value of Wakeford *et al.* [129] (upper purple dot) is in disagreement with the metallicity predicted by the model by Thorngren and Fortney [141] (grey square, TF19) and this paper (purple square), using a cloud-free atmosphere model. Including clouds in the model leads to larger metallicities (light- and dark-green squares). Furthermore, the additional heating required to explain the radius of the inflated WASP-39b was explored, finding $\varepsilon > 3\%$. Such elevated values could assist in align-

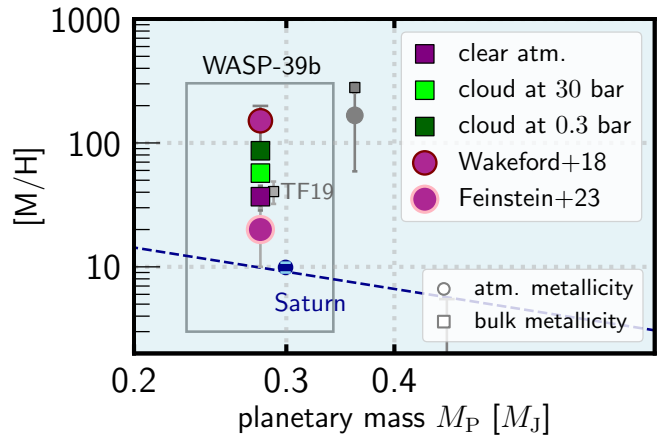


Figure 3.3.: Zoomed-in area of Fig. 3.2, with focus on the bulk (square) and atmospheric (circle) metallicity of WASP-39b. Displayed are the interior-model results from Paper I. The metallicity value from Wakeford *et al.* [129] was reached by including clouds in the atmosphere. However, the updated atmospheric metallicity value from Feinstein *et al.* [11] is in line with the clear atmosphere results.

Including clouds in the model leads to larger metallicities (light- and dark-green squares). Furthermore, the additional heating required to explain the radius of the inflated WASP-39b was explored, finding $\varepsilon > 3\%$. Such elevated values could assist in align-

ing the observationally derived metallicity with the metallicity inferred from interior models. More, clouds have an impact on both infrared *and* short-wavelength absorption and scattering. Therefore the ad-hoc *Heng12* model approach is compared with the self-consistent cloud models of Mollière *et al.* [446], pronouncing the complexity of cloud modelling (Fig. 11 in Paper I). In conclusion, this paper suggests that deep cloud decks below the pressure level of transmission spectra observations may influence the atmospheric P - T and thus the inferred metallicity.

Outlook. JWST will provide precise measurements across a broad wavelength range of transmission spectra, yielding new findings on composition and metallicity. WASP-39b has already led to numerous publications, e.g. [9–13, 243, 441], summarised in Seidel *et al.* [14]. Rustamkulov *et al.* [9] and Feinstein *et al.* [11] find a super-solar atmospheric metallicity that is roughly $[M/H]=10\times$ solar, reducing the earlier value by Wakeford *et al.* [129], as shown in Figs. 3.2 and 3.3 (light purple dot), delivering a metallicity that is explainable with the clear atmosphere model.

3.1.3. Impact on the Thermal Long-Term Evolution

In the first publication, the main focus was on the effect of a cloud deck on the derived metal content of the planet. It was intriguing to study how a cloud deck can influence the thermal evolution of a planet. Previous studies have focused on different types of planets and simulation methods. Kurosaki and Ikoma [447] show that condensation in heavily enriched atmospheres of ice giants accelerates the cooling as the planet emits more energy due to latent heat release. Vazan *et al.* [448] demonstrate a delayed cooling due to an atmosphere enriched in grains. Mordasini *et al.* [449] investigate the impact of grains on the mass-radius relations for a synthetic generated planet population. Linder *et al.* [450] find that including high-altitude clouds have only a limited influence on the evolution tracks of isolated and non-irradiated low-mass planets ($M_P < 0.6 M_J$). Burrows *et al.* [63] show that an enhanced atmospheric opacity leads to larger radii. The penetrating stellar irradiation flux, L_{eq} , is considered to be the main driver of the physics of the upper atmosphere, but the energy budget of a planet has several contributions: $L_{\text{eff}} = L_{\text{eq}} + L_{\text{int}}$, see Sect. 2.1.4 and Eq. (2.7). Fortney *et al.* [19] emphasise that not only the equilibrium flux, L_{eq} , but also the heat flux from the deep interior, L_{int} , shapes the atmosphere. The authors argue that the wide range of internal isentropes during the cooling of the planet, and the corresponding variation of surface gravity, can significantly impact the P - T profile.

In Paper II, the influence of a subsiding cloud deck, resulting from an evolving isentrope, on the thermal evolution of gas planets is explored. Two non-inflated planets, WASP-10b and TOI-1268b, are chosen to exclude any inflation mechanism. TOI-1268b is a warm Saturn-mass planet ($0.29 M_J$, $T_{\text{eq}} = 920$ K) with a density of $0.53 \rho_J$ orbiting a young star (110 – 1000 Myr) [451]. Their comparably low T_{eq} values raise the possibility of clouds.

The previous code underwent two key modifications: (1) the integration of the subsiding cloud deck and (2) the refinement of the cloud model, the latter being an improvement over the original model used in Paper I. Both modifications are presented below.

(1) *Subsiding Cloud Deck.* Unlike Paper I, where the cloud deck remained fixed at a specific pressure level P_c during the evolution, this study incorporates a *dynamic* cloud deck. Consequently, P_c subsides in response to the evolving cooler isentrope. The pressure level P_c is determined by calculating the intersection between the pre-calculated *clear* atmospheric profile and a condensation curve for each time step, corresponding to each T_{int} value. The possible condensate is chosen by comparing with other studies, such as Helling *et al.* [216], to reflect the most probable condensate in the deeper atmosphere. However, this approach is highly simplified, as multiple condensates may be present in an atmosphere, and the effects of interaction processes are not included.

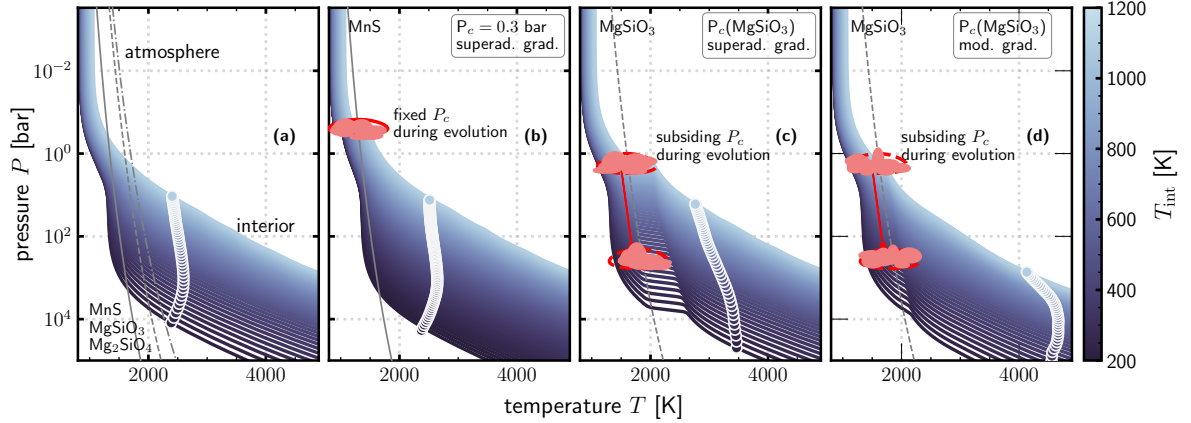


Figure 3.4.: Thermal atmospheric structure for WASP-10b under clear (a) and cloudy (b-d) conditions through the thermal evolution states of $T_{\text{int}} = 200 - 1200$ K. Condensation curves of condensable species are shown in grey lines. The clear model (a) serves as starting point for the cloud deck location P_c of the cloudy models. The other panels show the thermal structure with a fixed cloud deck location (b), and a dynamic cloud deck with subsiding P_c (c,d). Modified from Fig. 5 in [Paper II](#).

(2) *Refinement of the Cloud Model.* In [Paper I](#), the appearance of steep, super-adiabatic, temperature gradients is discussed when including clouds within the *Heng12* model. The temperature gradient can be sub-adiabatic, when latent heat takes over; see, for example, Kurosaki and Ikoma [447]. An adiabatic temperature gradient may occur if the opacity is high enough, as for ozone in the Earth’s atmosphere. If enough condensed matter exists, a super-adiabatic gradient is possible. This may be the case for CH_4 in Uranus and Neptune; see, for example, Guillot [452], Leconte *et al.* [453]. Without a concentration gradient, a super-adiabatic gradient does not occur. Within the *Heng12* model, for optically thin and high clouds this manner is reproduced, i.e. not showing a super-adiabatic gradient. For optically thicker and deeper clouds, the profile becomes super-adiabatic, which means that the temperatures below this layer are significantly higher than expected, see Sect. 4.1 in [Paper I](#).

Therefore, a condition for the local atmospheric gradient, ∇_{local} , is introduced, motivated by the work of Kurosaki and Ikoma [447]. ∇_{local} does not exceed the adiabatic gradient of the dry (clear) atmosphere:

$$\frac{d \ln T}{d \ln P} = \nabla_{\text{local}} \leq \nabla_{\text{ad,dry}}. \quad (3.2)$$

Fig. 4 in [Paper II](#) shows the local temperature gradients of the non-modified P - T profile (with super-adiabatic cloud gradient), and of the modified P - T profile (suppressing the super-adiabatic cloud gradient) as well as the resulting P - T profile. The temperature with the modification is cooler than with the super-adiabatic cloud gradient of the original *Heng12* model.

Fig. 3.4 shows examples of the atmospheric P - T profiles that include both modifications described above. Generally, the figure shows the P - T profiles at several ages for different atmospheric thermal conditions of WASP-10b. Fig. 3.4 (a) shows the clear atmosphere with the condensation curves of MnS, MgSiO₃ and Mg₂SiO₄. Fig. 3.4 (b) shows the resulting P - T conditions with a fixed cloud deck at $P_c = 0.3$ bar, set by the intersection with the condensation curve of MnS in the upper atmosphere. Fig. 3.4 (c) and (d) show the resulting profiles with a *subsiding* cloud deck location P_c , indicated by the arrow from high to low T_{int} values (light to dark tones), with the non-modified, i.e. super-adiabatic, cloud gradient and the modified cloud gradient, respectively. Notably, the RCB is changed by the modification of the cloud gradient (circles), which has effects on the thermal evolution of the planets.

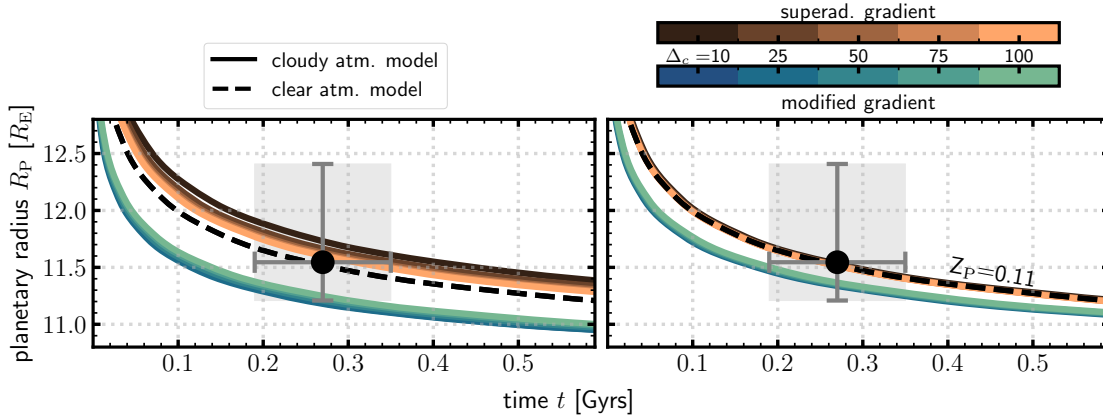


Figure 3.5.: Radius evolution curves for the non-inflated warm Jupiter WASP-10b ($T_{\text{eq}} = 950$ K) derived from coupled atmosphere, interior, and evolution models, comparing cloudy (solid) to a cloud-free (dashed) atmosphere. The left panel shows the results with the dynamic, i.e. subsiding cloud deck during evolution, whereas the right panel shows the cloud deck being fixed at $P_c = 0.3$ bar. The orange and blue colours indicate the non-modified, i.e. superad. gradient, and modified cloud model, that yields a slower versus a faster cooling, respectively. Modified from Fig. 9 in Paper II.

In addition to the modifications presented above, a fit formula for $\gamma(T_{\text{eq}})$ is presented, see Sect. 2.1.1 and Fig. 2 in Paper II. More, parameter studies of the cloud deck parameters were conducted, which required the development of a framework to streamline the process. The MOGROP version used required compilation for each parameter set, which was inefficient. To address this, CYTHON, a Python compiler for writing C extensions [454, 455], was employed along with the job manager SLURM [456].

Results. The thermal evolution of two irradiated gas planets is analysed employing the three-layer model presented in Sect. 2.1 - comprising an isothermal core, a convective envelope, and a radiative atmosphere. A purely absorbing cloud deck into the atmosphere was simulated, enhancing the warming in the deep atmosphere by adding an additional grey opacity in the long-wave. The cloud deck is located at the intersection with a condensation curve of a cloud-forming species, allowing to explore general trends in atmospheric temperature and the radius evolution with the ad-hoc cloud model. The key findings are summarised as follows.

1. *Radius Evolution:* Increased infrared opacity of cloud decks results in a warming effect on the lower atmosphere. This alteration can either slow down or speed up the cooling of the planet's thermal radius compared to a scenario without clouds. The exact effect depends on whether the cloud gradient is superadiabatic or not. The results with the varied atmospheric models that incorporate clouds demonstrate the substantial impact cloud decks can have on the thermal evolution of irradiated planets (Figs. 8 and 9 in Paper II). Fig. 3.5 shows an excerpt of the radius evolution of WASP-10b with the different atmosphere models.
2. *Radiative-Convective Boundary:* The location of the RCB in the P - T space is crucial for the outcome of the thermal evolution model, as it determines the isentrope (Fig. 10 in Paper II).
3. *Bulk Metallicity:* Atmospheric models including deep clouds can lead to a degeneracy in predicting the planets' bulk metallicity. For WASP-10b, findings indicate a metallicity range of $\approx Z_P^{+0.10}_{-0.06}$. For TOI-1268b, the range expands to $\approx Z_P^{+0.10}_{-0.05}$.

Furthermore, the radius evolution with both the H/He-EoS by SCvH95 and CD21 for the clear atmosphere is investigated, also varying the distribution of the metals (fully mixed planet versus

all metals in core), see Fig. 7 in [Paper II](#), showing a faster cooling for CD21 and fully mixed planets.

This study emphasises the need for models that integrate the interior, atmosphere, and thermal evolution of the planet, informed by atmospheric observations. Reducing uncertainties in the observed radius, mass of the planet, and stellar age, is crucial; see also Müller *et al.* [352], Müller and Helled [457].

To inform planetary formation models, interior models require atmospheric metallicity as an input parameter to create an accurate picture, as discussed in [Paper I](#). Missions such as the current JWST [4, 458], TESS [459] and future ARIEL [7, 8] missions are designed to address these requirements. Their goals include reducing observational uncertainties related to radius and stellar age and accurately determining the atmospheric metallicity of planets.

3.2. Ionised Atmospheres

In [Paper III](#) and [Paper IV](#), an ionisation and transport model for a multi-component plasma is developed and applied to the atmospheres of the hot Jupiter HD 209458b and ultra-hot Jupiter KELT-9b, respectively. The impact of the derived electrical conductivity profile on the Ohmic power is explored for both planets. [Paper IV](#) also presents a broader view of magnetic induction processes. Before presenting the publications, an introduction to the phenomenon of the radius anomaly in hot Jupiters is provided.

3.2.1. On the Radius Anomaly of the Giant Planet Population

One of the most intriguing characteristics of the observed giant planet population are the unexplained large radii of some of their members. The phenomenon, called the radius anomaly, is based on the difference between the observed and predicted radius: $\Delta R = R_{\text{observed}} - R_{\text{predicted}}$. The predicted radius is the result of coupled atmosphere, interior, and thermal evolution models.

HD 209458b was the first planet that was detected with the transit method and therefore a radius estimate, showing a radius of $1.4 R_J$ [460–462]. Subsequent coupled interior and evolution models indicated that a gas giant with the same characteristics as the planet – its mass, irradiation, and age – should have a smaller radius of $1.1 R_J$ [62, 184, 463]. Irradiation prevented the planet from cooling efficiently compared to non-irradiated planets, resulting in larger radii [63, 182]. However, it was shown that including the irradiation does not suffice to explain the inflated radius [62, 184]. Chabrier *et al.* [464] showed that an additional 1% of insolation energy could explain HD 209458b’s radius. HD 209458b became the first example of irradiated planets with larger-than-expected radii.

Since then, notable trends have emerged among the growing population of irradiated giant exoplanets: the radius inflation is strongly correlated with the incident stellar radiation but Weiss *et al.* [465] find no correlation with the semi-major axis of the planet. Gas giants with $T_{\text{eq}} < 1000$ K show no inflation [465–467]. For planets with $T_{\text{eq}} > 1200$ K there is a clear trend of $R_P \propto T_{\text{eq}}^{1/4}$ [351, 466, 468]. Additionally, planetary mass plays a major role in the extend of inflation, and planets $M_P < 1 M_J$ show the largest anomalous radii [64, 469]. The anomalous power, or the heating efficiency ε , which is needed to inflate the planet (see Sect. 2.1.4), has been found to be up to $\varepsilon \sim 3\%$ of the incident flux [64, 65, 67]. The ε - T_{eq} relation is described by a Gaussian function with a peak at $T_{\text{eq}} \approx 1860$ K ($\varepsilon_{\text{max}} \approx 2.50\%$) [65] or $T_{\text{eq}} \approx 1560$ K ($\varepsilon_{\text{max}} \approx 2.37\%$) [64]. For high $T_{\text{eq}} > 2000$ K, ε decreases.

As Nettelmann and Valencia [470] note, a central question in planetary science evolves around the mechanisms of heating¹ and/or cooling delay in these planets' interiors with several mechanisms proposed. They can be broadly divided into two groups: as planets start off as hot and extended objects after formation, certain mechanisms are consequently required to either (a) decelerate the cooling and contraction of the interior, thereby maintaining the inflated state, or (b) (re-) inflate the radius by introducing additional energy into the interior. For the latter, the depth of energy deposition plays an important role [381, 471]. Not all mechanisms are applicable to all planets, and several mechanisms be at work at the same time [65].

- (a) The first group of possible mechanisms includes an enhanced atmospheric opacity [63], or the existence of compositional gradients that lead to double-diffusive convection, reducing the heat transport [350, 472]. The latter has been proposed to influence solar Saturn and Jupiter [46, 102, 105, 106, 473].
- (b) The second group encompasses both tidal dissipation mechanisms, e.g. eccentricity tides due to the circularisation of the orbit [463, 474], or atmospheric thermal tides [475], and the deposition of the stellar irradiation in the interior. Based on hydrodynamical dissipation processes, heat is transported to the interior of the planet, e.g. by dissipation of atmospheric winds due to shear instabilities [184, 188], by vertical mixing [476–478], or via *Ohmic Dissipation*, which is the focus of this section. Komacek and Youdin [381] find that extra heat deposited in the convective layer suppresses cooling, whereas heat in the radiative layer does not until the heating rate is $\geq 10\%$ of the received stellar flux.
- (c) Another group of mechanisms is based on a variable amount of stellar radiation the planet receives during evolution, be it due to stellar evolution [374, 479, 480] or inward migration of the planet [375, 481].

Ohmic Dissipation. Batygin and Stevenson [66] proposed a magneto-hydrodynamic mechanism to inflate the gas giants. The mechanism involves alkali metals in the planet's atmosphere that partially thermally ionise because of the strong stellar irradiation, while embedded in a mostly neutral atmosphere. Strong zonal winds, driven by the stellar irradiation, move the ionised particles. Through interaction between the atmospheric flows and the planet's intrinsic magnetic field, interior currents are induced and travel into the planet's interior, dissipating ohmically and consequently depositing heat in the planetary interior. A sketch of the mechanism is shown in Fig. 3.6.

The depth and degree of Ohmic heating greatly depend on the at-

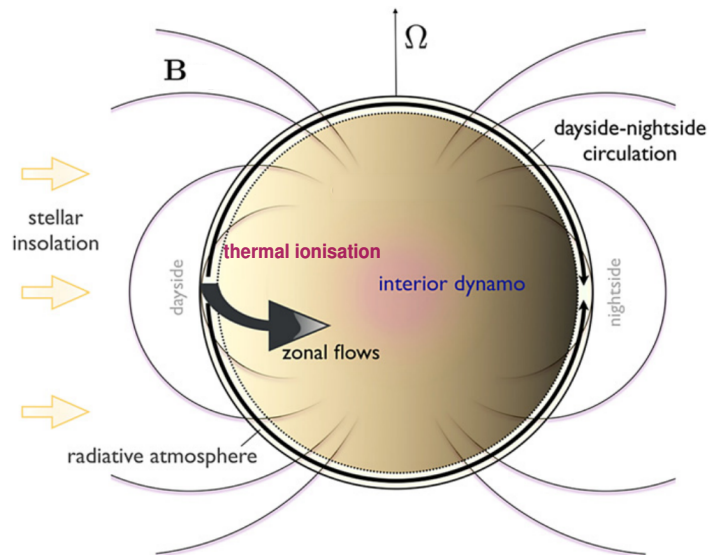


Figure 3.6.: Schematic of the interplay of the magnetic field \mathbf{B} from the deep interior, and the day- and night-side circulation due to the stellar irradiation. Modified from Fig. 1 in [482].

¹Here it is assumed that hot Jupiters are inflated due to processes that increase internal luminosity, and thus make the planet larger. High internal luminosities are connected with higher T_{int} values and a RCB at low pressures. It is known that high T_{eq} deepen the RCB within the planet, while high T_{int} values lower the RCB pressure, e.g. [179]. Sarkis *et al.* [65] demonstrate that these high internal temperatures, resulting in lower RCB pressures, are the dominant effect, with internal temperatures reaching up to 800 K.

ospheric parameters, such as heat redistribution and deposition, wind speeds and depth, the occurrence of magnetic drag [328, 483–485], and on the electrical conductivity of the plasma (focus in this work). Ohmic dissipation has been studied by several authors, e.g. [66, 328, 485–493]. It is one of the most favourable mechanisms to explain the radius anomaly, as its efficiency mirrors the statistically derived ε – T_{eq} distribution: Menou [494] shows that the strength of Ohmic dissipation first increases with increasing T_{eq} , and decreases after peaking at $T_{\text{eq}} \approx 1600$ K due to magnetic drag that breaks the winds, making Ohmic dissipation inefficient.

Assuming the planet has a large-scale dipolar magnetic field \mathbf{B} , the atmospheric zonal winds with velocity \mathbf{U} carry the free electrons across the field lines. An electric field \mathbf{E} is induced in response to the non-zero $\mathbf{U} \times \mathbf{B}$. The electric field will then drive current loops that could close in the atmosphere or in the interior, ohmically dissipating power (after [487]).

Electric currents \mathbf{j}_{ind} in the outer atmosphere are induced as described by Ohm’s law:

$$\mathbf{j}_{\text{ind}} = \sigma_e(\mathbf{U} \times \mathbf{B} + \mathbf{E}), \quad (3.3)$$

where \mathbf{U} is the wind field velocity of the neutral medium, \mathbf{B} the background magnetic field of the planet, \mathbf{E} the electric field, and σ_e the electrical conductivity.

The source of this mechanism is the irradiation that drives the winds carrying free electrons, leading to currents. The strength of the heating power \mathcal{P} , i.e. Ohmic power, due to the dissipation of \mathbf{j}_{ind} must be calculated in order to assess the strength of the mechanism. Generally, it is

$$d\mathcal{P}/dV = \mathbf{j}_{\text{ind}}^2/\sigma_e, \quad (3.4)$$

with dV as volume element.

3.2.2. Ionisation and Transport

Eq. (3.4) and Eq. (3.3) show that the electrical conductivity of the atmosphere is a crucial input parameter for the proposed mechanism of Ohmic dissipation. The transport property is determined by the composition and ionisation state of the partially ionised multi-component plasma that makes up the hot Jupiter atmosphere.

With the work presented in Paper III, ionisation and transport in partially ionised multi-component plasma is investigated. The aim is to calculate the electrical conductivity in a hot Jupiter atmosphere. Specifically, the developed ionisation and transport model is applied to the atmosphere of the inflated hot Jupiter HD 209458b in order to obtain the transport properties along the P – T structure. Consequently, the Ohmic power is estimated.

Ionisation and Transport Model. The first part of the paper presents the model to calculate the transport properties. The following summarises the calculation of transport properties. Initially, the plasma composition is derived by determining the partial number densities n_i of each species. Subsequently, the ionisation degree and the transport properties are computed.

1. The metals in the atmosphere of irradiated planets are partially or fully ionised due to thermal ionisation. Macroscopic electrical resistivity is produced by free electrons as they collide with ions, neutral particles, and other electrons. The relevant drivers for ionisation in the atmosphere are assumed to be H, He, the common metals calcium (Ca) and iron (Fe), and the alkali metals lithium (Li), sodium (Na), potassium (K), rubidium (Rb), and caesium (Cs), taking their abundances from Lodders [495] for $1\times$ solar abundance. The particle number densities (i.e. the plasma composition) follow from mass action laws (MALs) for the partially ionised plasma² making use of Saha-like equations for

²The mass action laws state that at equilibrium the ratio of the concentrations of products to reactants remains constant.

dissociation and ionisation reactions, assuming the plasma is in thermal and chemical equilibrium. The Saha equations relate the ionisation state of a gas to temperature and pressure. The number densities of each species n_i (molecules, atoms, and ions) for a given plasma temperature and mass density are numerically derived by solving the MALs and particle conservation equations.

2. For the calculation of transport properties, the ionisation degree of the plasma is required. Consequently, the ionisation degree α is calculated, defined as $\alpha = n_e/n_{\text{total}}$, where n_e is the free electron number density, and $n_{\text{total}} = n_{\text{atoms}} + 2n_{\text{H}_2} + n_e$ with $n_{\text{atoms}} = \sum_i n_{i,\text{atom}}$ is the number density of all atoms. The ionisation degree α increases with temperature and decreases with mass density.
3. The electronic transport properties, such as the electrical conductivity σ_e and total thermal conductivity λ are calculated following [496, 497]. The electrical conductivity is derived from electron-ion and electron-neutral transport cross sections, including corrections for electron-electron scattering effects [497].

The ionisation degree and electronic transport coefficients as functions of plasma temperature and density are analysed (Figs. 2, 3 in Paper III). The thermal conductivity and its specific contributions are also examined (Sect. 5 in Paper III).

Application to HD 209458b. The second part of the paper applies the ionisation and transport model to HD 209458b³, considering various thermal atmospheric structures, including those with and without thermal inversions and different deep isotherms (see Fig. 8 in Paper III). The ionisation degree, thermal conductivity, and, in particular, electrical conductivity were calculated along the P - T profiles (see Fig. 9 in Paper III). The aim was to compare these results to the electrical conductivity results of Batygin and Stevenson [66] (BS10, Fig. 2), using a P - T profile with an inversion at 30 mbar while also accounting for more recent thermal structures (see Fig. 8 in Paper III).

BS10 predict a deep minimum in the electrical conductivity, calculated with a simpler model, with σ_e decreasing by six orders of magnitude. In contrast, the current model shows a decrease of only two orders at the 30 mbar dip, see Fig. 10 in Paper III and Fig. 3.7. Changes in Ohmic heating compared to BS10 were estimated by rescaling their results using the updated conductivity profile. With the new conductivity two orders of magnitude lower in the induction layer, the electric currents and the Ohmic heating power are also reduced by two orders, as per Eq. (3.3). That would make the effect too small to explain the radius of the planet. However, the more recent thermal structures, with hotter deep isotherms and therefore reaching larger electrical conductivities, would provide sufficient power at the RCB to cause the planet's inflation.

Summary. A model for calculating the composition and transport properties, such as the electrical conductivity σ_e , of a multi-component plasma has been developed. Applying the model to the conditions in a hot Jupiter atmosphere shows that the results of σ_e differ in several magnitudes compared to simpler models of σ_e . This directly influences the estimates for the electric currents and the resulting Ohmic heating power. The study, Paper III, shows the importance of atmospheric P - T profiles for σ_e to estimate the strength of Ohmic heating. It also illustrates the connection between plasma, atmospheric, and planetary physics, highlighting the need for transport properties not only for the interior but also for the atmosphere.

³Planetary parameter of HD 209458b: $1.4 R_J$, $0.7 M_J$, 0.047 au , $0.35 \rho_J$, $T_{\text{eq}} = 1400 \text{ K}$, $2\text{--}6 \text{ Gyr}$ [128, 460]

3.2.3. Magnetic Induction Processes

Other electromagnetic effects in hot Jupiter atmospheres that are based on the coupling of the atmospheric winds and the planet’s deep-seated magnetic field also rely on an estimate of the electrical conductivity. For example, the ion-wind coupling produces a drag due to Lorentz forces (i.e. magnetic drag), potentially reducing the winds’ circulation efficiency and enhancing the temperature contrast between day and

nightside, e.g. [483, 494, 498]. Shallow atmospheric dynamos could be driven by horizontal variations due to the strong day and nightside temperature differences, possibly reducing the efficiency of Ohmic heating [499]. In addition to σ_e , the mechanisms of the induction process play a role, that is, linear or non-linear induction processes.

Paper IV presents a broad view on magnetic induction processes in irradiated Jupiters. The induction of atmospheric magnetic fields in irradiated Jupiters with $T_{\text{eq}} > 2000$ K (i.e. ultra-hot Jupiters) are discussed in comparison with hot Jupiters $T_{\text{eq}} \sim 1500$ K – exploring both linear and non-linear induction processes and the potential amplitudes of induced fields and electrical currents.

First, a general description of atmospheric magnetic field induction, internal dynamo processes, and the thermal ionisation of metals is given. Second, the theory is applied to the atmospheres of irradiated Jupiters. The magnetic Reynolds number is calculated for ≈ 350 irradiated Jupiters. As a case study, the ultra-hot Jupiter KELT-9b⁴ is analysed similar to HD 209458b in **Paper III**, estimating the Ohmic power.

Here, the results of the considerations on the induction processes and the implications for the Ohmic power and the analysis of the thermal ionisation are presented; see Sect. A.7 for more details.

Magnetic Induction Processes and Ohmic Dissipation. The theoretical analysis of induction processes in hot Jupiter atmospheres distinguishes between linear and non-linear regimes, quantified by the magnetic Reynolds number R_m . This number assesses the relative significance of induction versus diffusion in the magnetic field evolution:

$$R_m \approx \mu_0 \sigma_e U \min(d_\eta, d_U, d_B) \begin{cases} \leq 1, & \text{linear regime} \\ > 1, & \text{non-linear regime} \end{cases}, \quad (3.5)$$

where μ_0 is the vacuum permeability, U a typical flow velocity, and d the characteristic length scale for the electrical conductivity scale length, the flow, or the magnetic field (Eq. (4) in **Paper IV**).

In the linear regime, magnetic diffusion limits the growth of the induced field which remains weak compared to the background field. The Ohmic power, recall Eq. (3.4), is dependent

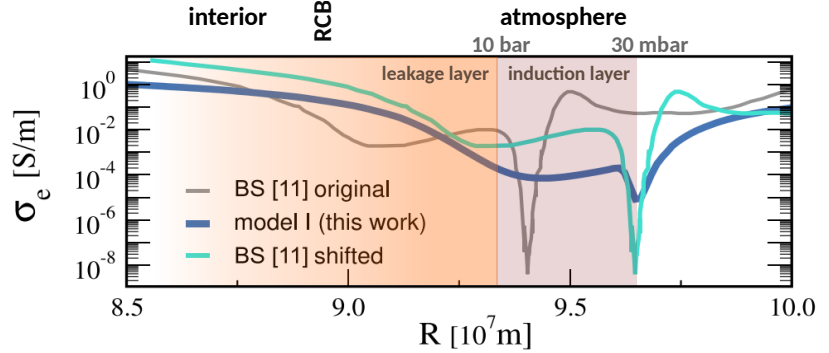


Figure 3.7.: Electrical conductivity σ_e along the radius axis of HD 209458b, compared to the results of BS10. The atmospheric thermal structure here shows an inversion at 30 mbar, compare Fig. 3.9, model I (dark blue). Modified from Fig. 10 in **Paper III**.

⁴planetary parameter of KELT-9b: $1.9 R_J$, $2.8 M_J$, 0.034 au, $0.5 \rho_J$, $300\text{--}600$ Myr [500], $T_{\text{eq}} \sim 4000$ K, $T_{\text{day}} = 4600$ K, $T_{\text{night}} = 3040$ K [501, 502]

on the induced current. Here, atmospheric currents are simply a function of wind speed, internal magnetic field strength, and σ_e . Therefore, the Ohmic power \mathcal{P} is scaling with σ_e , the wind speed U^2 , and the internal magnetic field strength B_{int}^2 : $\mathcal{P} \propto \sigma_e U^2 B_{\text{int}}^2$. This linear approximation has been used for HD 209458b in Paper III and often implicitly in other works, for example, in [66].

In the non-linear regime, the induced magnetic field B_Φ dominates the internal magnetic field, causing significant Lorentz forces. Magnetic field induction is rapid, halted only by non-linear effects like magnetic instabilities. The approximation of the induced current and the Ohmic power is complicated due to the non-linearity. The induced field is independent of σ_e . As a result, with higher σ_e , the Ohmic dissipation decreases: $\mathcal{P} \propto B_\Phi^2 / (\sigma_e d_U^2)$.

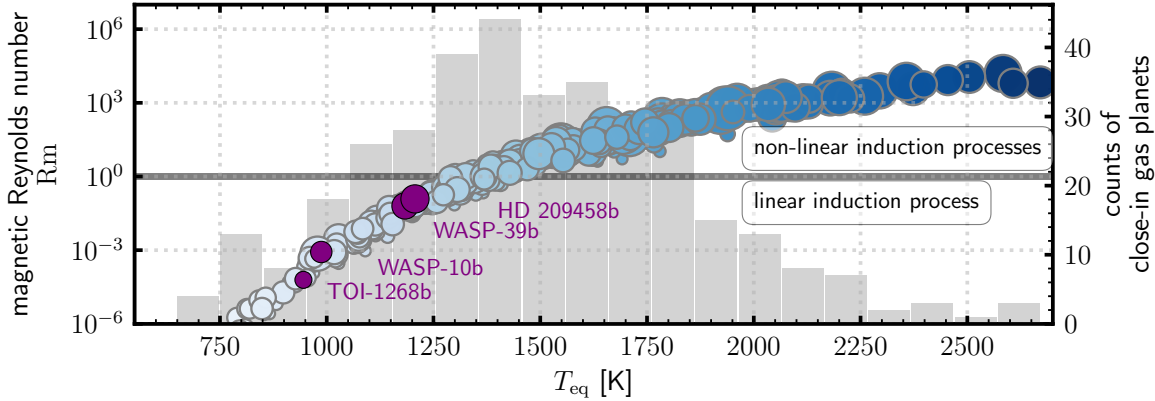


Figure 3.8.: Estimates of the magnetic Reynolds number R_m for ~ 350 irradiated gas planets with T_{eq} . The colours refer to T_{eq} . Highlighted with names are the individual planets from this thesis, not colour-coded with T_{eq} for visibility, point sizes scale with the planetary radius. R_m exceed unity at ≈ 1400 K, indicating the onset non-linear induction processes. KELT-9b is not shown due to its high $T_{\text{eq}} > 4000$ K. However, the input to R_m , σ_e , is calculated from a fixed density (10^{-4} kg/m³), even though the density dependence is weak (cmp. Fig. 2 in Paper IV). Modified from Fig. 3 in Paper IV.

Analysis of the Thermal Ionisation and $\sigma_e(T)$. Based on results obtained with the ionisation and transport model from Paper III, σ_e grows with temperature due to the increasing electron contributions of the alkali metals. Interestingly, $\sigma_e(T)$ shows steep slopes and flat plateaus, resulting from the species ionising step-wise at higher temperatures (see Fig. 2 in Paper IV). Potassium, the element with the lowest ionisation energy, is the main electron source at low temperatures, being highly ionised up to 2000 K, where it provides almost all of the free electrons. Sodium and calcium are starting to contribute at $T = 2300 - 3500$ K. σ_e reaches a plateau at ≈ 1 S/m until 3500 K where iron starts contributing. Hydrogen ionises above 5000 K. Due to their high ionisation energies and low mass fractions, lithium, rubidium, and caesium are negligible in this analysis. The temperature dependence of σ_e is most pronounced at low temperatures where potassium is partially ionised.

Furthermore, $R_m(T)$ is estimated based on the results of $\sigma_e(T)$. Interestingly, as seen in Fig. 2 in Paper IV, R_m exceeds unity at $T = 1300 - 1500$ K, indicating that planets hosting higher temperatures than that tend to host non-linear induction processes.

Estimation of $R_m(T_{\text{eq}})$. A planet-specific estimate of R_m is made, based on observable quantities (Eq. (30) in Paper IV), for ≈ 350 irradiated planets. The resulting $R_m(T_{\text{eq}})$ are shown in Fig. 3 in Paper IV and Fig. 3.8: R_m exceeds unity at $T_{\text{eq}} \approx 1400$ K, making non-linear processes probable for planets with higher T_{eq} values. At this temperatures, $T_{\text{eq}} \lesssim 1400$ K, the electrical conductivity arises from potassium's partial ionisation.

Application to HD 209458b and KELT-9b. The scheme above is applied to both planets in Sect. 3 in Paper IV, estimating the Reynolds number and therefore the induction process, and

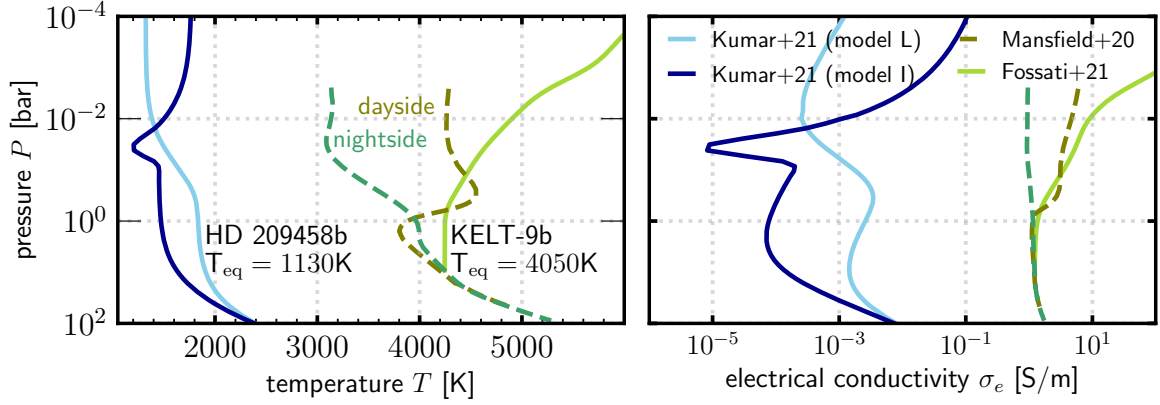


Figure 3.9.: Atmospheric temperature and electrical conductivity σ_e , obtained with the ionisation and transport model from Paper IV, along the planetary pressure coordinate. Modified from Figs. 4 and 5 in Paper III.

the desired Ohmic power. Table 1 in Paper IV provides the properties to derive the Reynolds number.

For HD 209458b ($T_{\text{eq}} \sim 1400$ K), $\sigma_e = 10^4 - 10^{-2}$ S/m, mainly due to the partial ionisation of potassium. Therefore, $\text{Rm} \leq 1$, and magnetic diffusion limits the growth of the induced field. The strength of the local currents is estimated to be 10^{-3} A/m². The Ohmic power is then $\mathcal{P} = 1.35 \times 10^{20}$ W⁵. A power of 4×10^{18} W would be required to explain the inflated radius. For KELT-9b ($T_{\text{eq}} \sim 4000$ K), σ_e is two to four orders of magnitude greater than for HD 209458b due to the higher temperatures, even on its nightside. Despite a significant temperature contrast of 1500 K between the day- and nightside, the variation in σ_e is minimal, as nearly all alkali metals are ionised, see Fig. 2 in Paper IV and Fig. 3.9. In addition to the high σ_e , higher wind speeds ($U_{\text{HD}} \sim 10^3$ m/s versus $U_{\text{KELT}} \sim 10^4$ m/s), lead to $\text{Rm} \sim 4 \times 10^4$, indicating time-variable induced fields and a non-linear induction process. The induced current strength is estimated to 0.1 A/m². The Ohmic power in the atmospheric layer of KELT-9b ranges from $\mathcal{P} = 10^{20} - 5 \times 10^{21}$ W, a small fraction of its total luminosity of $\sim 10^{24}$ W. This implies that other processes, such as tidal heating, are more crucial for maintaining its high luminosity.

Summary. Additional heating is required to explain the radii of the the inflated hot Jupiter population. The strength of the additional heating increases with T_{eq} , with a maximum at $T_{\text{eq}} = 1500$ K, followed by a decrease [64, 65]. Explanations of the decrease included Lorentz forces slowing winds at high T_{eq} [494]. The study, Paper IV, suggests that the higher conductivity in very hot planets ($T_{\text{eq}} \gtrsim 1400$ K) makes deep Ohmic heating ineffective due to non-linear induction processes.

⁵For a more in-depth estimation of the Ohmic power available in HD 209458b dependent on the assumed P - T profiles, see Paper III, Sect. VIc.

4. Summary and Perspectives

Summary. This thesis explores how atmospheric thermal structures (pressure-temperature, P - T) affect the bulk composition and radii of irradiated giant planets, including potential radius inflation. This is achieved by implementing an atmospheric model in a widely used interior code and performing coupled atmosphere, interior, and evolution calculations.

First, the impact of cloudy atmospheres on the inferred heavy element content and the thermal evolution of planetary radii is investigated [394, 395]. Using coupled atmosphere, interior, and evolution models, the planets WASP-39b, WASP-10b, and TOI-1268b were analysed to understand how cloudy atmospheres contribute to variations in characteristic interior parameters. The studies reveal that cloudy atmospheres introduce a degeneracy that complicates the interpretation of planetary interiors by examining the derived bulk metallicity and radius evolution. The findings highlight the importance of considering atmospheric processes that affect the lower atmosphere, such as the warming effect caused by clouds.

Second, ionised elements observed in the atmospheres of close-in planets support the idea that stellar irradiation leads to thermal ionisation. The interaction between planetary magnetic fields and atmospheric winds induces magneto-hydrodynamic effects, such as induced currents dissipating heat ohmically within the planetary interior, potentially inflating the radii. By developing and applying an ionisation and transport model for partially ionised multi-component plasma, the Ohmic dissipation mechanism for the planet HD 209458b was reassessed, revealing lower Ohmic power estimates than previous studies [396]. Further analysis suggests two regimes of magnetic induction in gas planets [397]: planets with $T_{\text{eq}} < 1400$ K exhibit linear induction processes due to a low electrical conductivity, while those with $T_{\text{eq}} > 1400$ K display non-linear processes, making deep Ohmic heating inefficient, such as for ultra-hot Jupiters as KELT-9b.

The results of this thesis underscore the importance of understanding the deep atmospheric P - T conditions for modelling the interior structure and evolution of irradiated giant planets. The thermal structure significantly contributes to the degeneracy of possible structure outcomes and influences the transport properties and magnetic induction processes.

Perspectives. Atmosphere and interior models face challenges with degeneracies in interior structure and composition. Reducing these uncertainties requires increasing the number of observables and improving the accuracy of fundamental parameters, such as the planetary radius.

Regarding the interior, measurements from transit light curves of the fluid Love number k_2 , a measure of tidal forces and therefore of the internal density distribution, have been achieved for two hot Jupiters [503, 504] and could be extended to more exoplanets [505–507]. These measurements can help decrease degeneracy in interior models [508–511]. Further, measurements of magnetic fields can inform interior, magneto-hydrodynamic, and plasma models [512, 513]. Magnetic fields could be assessed directly or indirectly [514] through observations such as the polarisation in the He 1083 nm absorption features [238, 515, 516] or indications of a magneto-tail [134].

Addressing theoretical uncertainties within coupled interior and evolution models is also vital [352]. Understanding the equations of state for warm dense matter is fundamental to resolving these uncertainties. This includes the solubility of matter in metallic hydrogen, e.g. [49, 104, 142, 167, 517], demixing, e.g. [153, 518–520], and material properties, i.e. thermodynamic and transport properties, to understand energy transport and the generation of planetary magnetic fields [175, 177, 521]. Focus must also be on equations of state and transport properties, like electrical conductivity, in irradiated atmospheres.

Regarding the atmosphere, space missions such as the current JWST [4], and the upcoming ARIEL [7, 8] and PLATO [5, 6] missions aim at characterising the atmospheres, measuring

albedos, day and nightside temperature contrasts, atmospheric abundances, and cloud properties.

Refining planetary models also depends on small error margins for input parameters like mass and radius, achieved through ground-based instruments like HARPS [522], NIRPS [523], and ESPRESSO [524]. The upcoming PLATO mission will provide precise stellar ages [5, 6]. In light of this work, adopting probabilistic inference methods like Markov chain Monte Carlo sampling to address observational uncertainties and infer the interior structure represents a next step, aligning with state-of-the-art techniques, e.g. [64, 106, 141, 457, 525–527].

Lastly, the detection towards both young (< 500 Myr) and small, low-mass planets is extremely promising to help to understand the formation and evolution of planets and planetary systems, e.g. [528, 529].

This thesis significantly contributes to the understanding of irradiated giant planets by shedding light on how their atmospheric conditions influence key bulk characteristics, which are directly linked to broader theories of planetary formation and evolution.

5. Publications

This chapter comprises four peer-reviewed publications [394–397]. The papers are available electronically on the journals' websites using the provided DOI information. The contributions of the individual authors are listed for each manuscript.

5.1. The Effect of Clouds as an Additional Opacity Source on the Inferred Metallicity of Giant Exoplanets

"Every new discovery is just a reminder... "We're all small and stupid."

Everything Everywhere All At Once (movie)

Atmosphere **2019**, 10(11), 664
DOI: [10.3390/atmos10110664](https://doi.org/10.3390/atmos10110664)

A. J. Poser

Preparation of the manuscript, code development, calculation of all coupled atmosphere, interior, and thermal evolution data, analysis and interpretation of the results

N. Nettelmann

Supervision of the project, preparation of the manuscript, interpretation of the results

R. Redmer

Supervision of the project, preparation of the manuscript, interpretation of the results



Article

The Effect of Clouds as an Additional Opacity Source on the Inferred Metallicity of Giant Exoplanets

Anna Julia Poser ^{1,*}, Nadine Nettelmann ² and Ronald Redmer ¹

¹ Institut für Physik, Universität Rostock, D-18051 Rostock, Germany; ronald.redmer@uni-rostock.de

² Institut für Planetenforschung, Deutsches Zentrum für Luft- und Raumfahrt (DLR) Berlin, D-12489 Berlin, Germany; nadine.nettelmann@dlr.de

* Correspondence: anna.poser@uni-rostock.de

Received: 16 October 2019; Accepted: 26 October 2019; Published: 30 October 2019



Abstract: Atmospheres regulate the planetary heat loss and therefore influence planetary thermal evolution. Uncertainty in a giant planet's thermal state contributes to the uncertainty in the inferred abundance of heavy elements it contains. Within an analytic atmosphere model, we here investigate the influence that different cloud opacities and cloud depths can have on the metallicity of irradiated extrasolar gas giants, which is inferred from interior models. In this work, the link between inferred metallicity and assumed cloud properties is the thermal profile of atmosphere and interior. Therefore, we perform coupled atmosphere, interior, and evolution calculations. The atmosphere model includes clouds in a much simplified manner; it includes long-wave absorption but neglects shortwave scattering. Within that model, we show that optically thick, high clouds have negligible influence, whereas deep-seated, optically very thick clouds can lead to warmer deep tropospheres and therefore higher bulk heavy element mass estimates. For the young hot Jupiter WASP-10b, we find a possible enhancement in inferred metallicity of up to 10% due to possible silicate clouds at ~ 0.3 bar. For WASP-39b, whose observationally derived metallicity is higher than predicted by cloudless models, we find an enhancement by at most 50%. However, further work on cloud properties and their self-consistent coupling to the atmospheric structure is needed in order to reduce uncertainties in the choice of model parameter values, in particular of cloud opacities.

Keywords: extrasolar planets: hot Jupiters; atmospheres; clouds; individuals: WASP-10b, WASP-39b

1. Introduction

Metallicity and core mass of giant planets contain information on protostellar disks and on the process of planet formation. Therefore, planetary metallicity, or bulk heavy element mass fraction Z_p , is an important parameter. Core accretion formation models that reproduce the metallicity of the solar system giant planets [1] predict a rapid decrease of Z_p with increasing planet mass M_p , still allowing for up to $14\times$ solar ($Z_p \sim 20\%$) for a Saturn-mass planet but for less than $3\times$ solar ($Z_p \sim 4.5\%$) for a $2 M_{\text{Jup}}$ planet.

Recently, Wakeford et al. (2018) [2] used transmission spectra to determine the metallicity in the atmosphere of the Saturn-mass planet WASP-39b. They retrieved a high value of $\sim 100\text{--}200\times$ solar. This is not only higher than the prediction from core accretion formation but also higher than the upper limit of $55\times$ solar for the atmospheric metallicity as inferred from structure models for this planet [3]. Moreover, for some massive giant planets such as the $3 M_{\text{Jup}}$ planet WASP-10b [4], structure models predict a significant heavy element enrichment of Z_p of 10% or more [5].

In this paper, we pursue the possibility of uncertainty in the planet's inferred bulk metallicity due to an additional opacity source of limited vertical extent. We call it a cloud layer; however, we do not model any physical aspect of real clouds except the potential additional longwave opacity. Because of their optical properties, clouds in the atmosphere are known to modify the observable transmission spectrum [6] and the temperature structure of the atmosphere itself [7]. Clouds also influence the atmospheric scale height, which provides a direct link to the mean molecular weight of the atmosphere [8]. Since the latter depends on atmospheric metallicity, its value can be inferred from the observed transmission spectrum in combination with radiative transfer calculations, which yield the scale heights of the observed portion of the atmosphere. In this work, we follow a different approach—inferring the atmospheric metallicity from planetary structure models that are primarily constrained by the observed mass, radius, and age of the star as explained below. In gaseous planets, the radiative atmosphere transitions smoothly into the adiabatic deep interior. The pressure—temperature (P – T) conditions at this transition influence the internal temperatures and the possible intrinsic heat loss [9]. Higher temperatures at a given pressure level in a fluid planet lead to lower densities and to expansion if not compensated for by an increase in heavy element abundance, an effect that is still relevant for the ice giants Uranus and Neptune [10]. Therefore, atmospheric temperature profile and our inference of a planet's metallicity are strongly coupled. We include a cloud layer into our coupled planetary atmosphere, interior, and evolution calculations by using the semi-analytic model of Heng et al. (2012) [11], which allows us to conveniently investigate the influence of assumed cloud opacity and assumed cloud pressure level on the atmospheric P – T profile. This model is applied to the two giant planets: WASP-10b and WASP-39b. Both planets may harbor clouds since their atmospheric P – T profiles intersect with a number of condensible species, as shown in Figure 1.

Candidates of cloud forming species for these planets are Na_2S , MnS , Cr , and silicates. This study is not the first one to investigate the influence of cloudy and cloud-free atmospheres on the evolution of gaseous planets. Clouds have been considered in models for planets with hydrogen-dominated atmosphere before. For instance, Linder et al. (2018) [12] studied the influence on the spectra and thermal evolution of weakly irradiated exoplanets while Kurosaki et al. (2017) [13] studied the influence of water clouds on the cooling of the ice giant Uranus. For strongly irradiated hot Jupiters, Barman et al. (2001) [14] find a large heating effect in the upper atmosphere from reflection of stellar incident flux and absorption of dust grains at infrared wavelengths in comparison to clear atmospheres, with consequences on the emergent spectra, while Baraffe et al. (2003) [15] find a minor influence of dust versus clear irradiated atmospheres for the luminosity evolution of hot Jupiters.

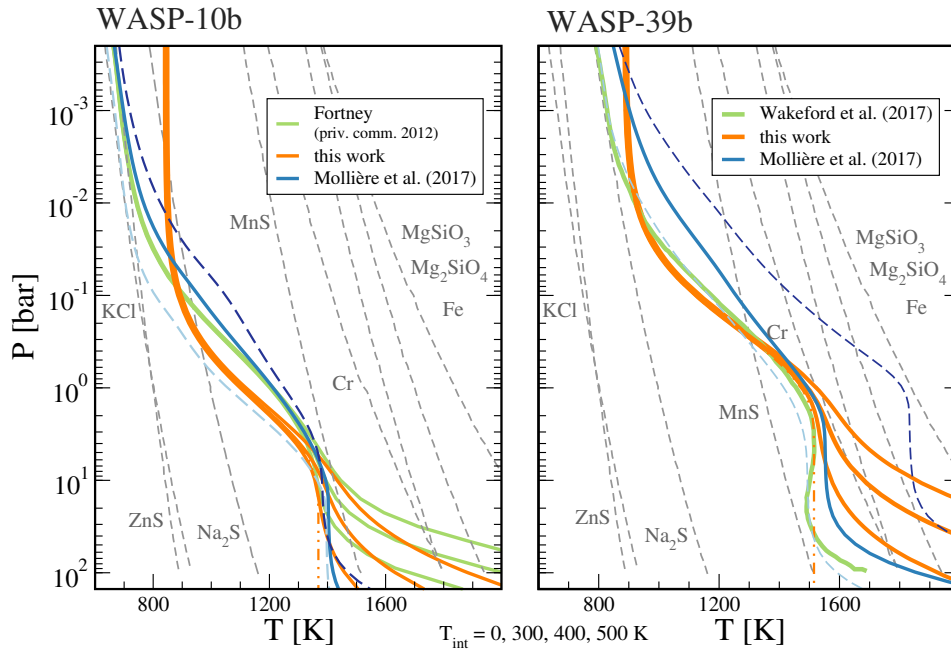


Figure 1. Condensation curves (grey dashed) of some species as labeled for solar-metallicity atmospheres (taken from Ref. [16]) and cloud-free P - T profiles (solid) for WASP-10b (left) and WASP-39b (right). Intersection points are possible cloud forming pressure levels. Orange P - T profiles are our fits to the profiles for WASP-10b from J. Fortney (pers. comm. 2012) as well as our fit to the global average profile of Wakeford et al. [2] for WASP-39b for different T_{int} values. Additionally, we show the obtained clear profiles by Mollière et al. [17] for their deduced atmospheric enrichment in $[\text{Fe}/\text{H}]$ (solid blue) and $10\times$ smaller vs. larger enrichment (dashed light blue vs. dashed dark blue).

In Section 2, we list the relevant observed system parameters and describe our modeling approach for the atmosphere with a cloud layer, the interior, and the thermal evolution. Results for WASP-10b are presented in Section 3 and for WASP-39b in Section 4. In particular, we take the Z_p value of Thorngren and Fortney (2019) [3] for WASP-39b as an input parameter for our models and see if the high predicted atmospheric metallicity of Wakeford et al. (2018) [2] can be reached just by including an additional opacity source which may mimic the effect of a cloud deck. We compare the obtained atmospheric models with self-consistent clear and cloudy models by Mollière et al. (2017) [17] in Section 5. A summary is given in Section 6.

2. Methods

2.1. Planet and Star Parameters

WASP-10b is a massive ($2.96 M_{\text{Jup}}$) and non-inflated ($T_{\text{eq}} = 950 \text{ K}$) hot Jupiter. Its young age of $270 \pm 80 \text{ Myr}$ [18–20] makes it an interesting object to study planet formation and evolution. While early radius estimates predicted a rather large radius of $\sim 1.27 R_{\text{Jup}}$ [19], subsequent careful analysis of the spots on the K5 dwarf host star suggested a 20% smaller planet radius of $1.02 R_{\text{Jup}}$ [4], which we use in this study.

WASP-39b is a Saturn-mass planet ($0.28 M_{\text{Jup}}$) with a large radius ($1.27 R_{\text{Jup}}$) and therefore low density $\rho = 0.141 \rho_{\text{Jup}}$ [21]. It is orbiting a late G-type star, which is smaller and, with an age of 9_{-4}^{+3} Gyr , possibly older than the Sun. The observational parameters used here for WASP-10b and WASP-39b are listed in Table 1.

Table 1. Stellar and planetary parameters.

	WASP-10b	WASP-39b ⁵
M_P	$2.96^{+0.22}_{-0.17} M_{\text{Jup}}$ ¹	$0.28 \pm 0.03 M_{\text{Jup}}$
R_P	$1.03^{+0.077}_{-0.03} R_{\text{Jup}}$ ⁴	$1.27 \pm 0.04 R_{\text{Jup}}$
a	$0.0369^{+0.0012}_{-0.0014} \text{AU}$ ¹	$0.0486 \pm 0.0005 \text{AU}$
e	0.013 ± 0.063 ³	0
$T_{\text{eq,A=0}}$	950^{+30}_{-26}K ⁴	$1116^{+33}_{-32} \text{K}$
P	3.09 d	4.05 d
M_*	$0.75 M_{\text{Sun}}$ ²	$0.93 \pm 0.03 M_{\text{Sun}}$
R_*	$0.67 R_{\text{Sun}}$ ⁴	$0.895 \pm 0.023 R_{\text{Sun}}$
T_*	$4675 \pm 100 \text{K}$ ¹	$5400 \pm 150 \text{K}$
age τ_*	$270 \pm 80 \text{Myr}$ ³	9^{+3}_{-4}Gyr

¹ Ref. [19], ² Ref. [18], ³ Ref. [20], ⁴ Ref. [4], ⁵ Ref. [21].

Since we are interested in the effect of clouds relative to cloudless atmospheres on the inferred planet metallicity, we compute here planet models for a variety of cloud parameters but do not account for the observational uncertainties in planet mass and radius. The only exception is thermal evolution calculations for WASP-39b, where we request its radius at present time to drop below the 1σ upper limit.

2.2. Interior

To estimate the present structure of the planets, we connect the atmosphere to the interior and perform thermal evolution calculations. For the interior, we assume a three-layer structure of rocky core, an adiabatic, convective envelope, and a radiative atmosphere. Atmosphere and envelope consist of a mixture of hydrogen, helium and metals. Respective equations of state (EOS) are combined via the linear mixing rule. By heavy elements or metals, we denote all elements or molecules heavier than helium. Z_{atm} and Z_{env} are the heavy element mass fractions in the atmosphere and envelope, respectively, which we assume to be equal, $Z_{\text{atm}} = Z_{\text{env}} = Z$. This is an assumption, not ruling out other relations between atmospheric and envelope abundances [17,22]. The planetary bulk heavy element mass fraction is $Z_P = Z_{\text{env}} M_{\text{env}} / M_P + M_{\text{core}} / M_P$, and M_{env} and M_{core} are the masses of envelope and core. For the solar reference metallicity we use $Z_{\odot} = 1.5\%$ [23]. For WASP-10b, we set $Z = Z_{\odot}$ and allow only the core mass to vary while, for WASP-39b, we allow also Z to vary. The helium to hydrogen mass fraction is set to the protosolar value of $Y = 0.27$, where $Y = M_{\text{He}} / (M_{\text{He}} + M_{\text{H}})$. For hydrogen and helium, we use the SCvH EOS [24]. Metals in the envelope are represented by that He-EOS scaled in density by a factor of four, or by the ice EOS presented in [25]. The rocky core obeys the pressure–density relation given in [25]. The density $\rho(P, T)$ is obtained from the linearly mixed EOS at the pressure P and temperate T by interpolation. We obtain the mixed EOS by adding heavy elements to the interior and the atmosphere via the linear mixing rule $\rho^{-1}(P, T) = \sum_i X_i / \rho_i(P, T)$, where X_i denotes the mass fraction of component i and $X_{\text{H}} := X$, $X_{\text{He}} := Y$, $X_Z := Z$ [26]. The density profile follows a pre-computed P – T profile along the adiabat of the envelope. Increasing the temperature at fixed pressure usually decreases the density. Lower densities in the mantle result in a larger core mass to conserve the given planet mass. This is why the P – T profile is so important. Otherwise, we rely on the usual structure equations for non-rotating, spherical giant planets as previously done in [26,27].

2.3. Atmosphere Model with Clouds

The atmosphere model yields the atmospheric P – T profile. We use the 1D, plane-parallel, analytical atmosphere model by Heng et al. (2012) [11] for hot Jupiters. It is based on the two-stream solution and dual band approximation, where the incoming and outgoing radiation fluxes are described by different frequency-averaged mean opacities. The incoming flux is represented by the short-wave opacity κ_S , equivalent to the opacity κ_{vis} for visual light used in [28], while the

outgoing flux is described by the long-wave opacity κ_L equivalent to κ_{th} in [28] for thermal radiation. Following Heng et al. [11], κ_S is constant with respect to temperature and pressure while κ_L may have a dependence on pressure. Indeed, gas opacities significantly depend on pressure because of pressure broadening or collision induced absorption. Cloud decks are included as an additional opacity source $\kappa_c(P)$ to the constant long-wave opacity $\kappa_{L,0}$ of the otherwise cloudless atmosphere,

$$\kappa_L(P) = \kappa_{L,0} + \kappa_c(P). \quad (1)$$

The analytic model atmosphere provides a relation between global mean temperature T and longwave optical depth $d\tau_L = \kappa_L dm$, where m is column mass from top to bottom, as well as the parameter $\tau = \kappa_L m$. We call the latter here optical depth although this holds only if $\kappa_L = \text{const.}$. The T - τ relation makes use of the Eddington coefficients $\mathcal{E}_1 = 1/3$ and $\mathcal{E}_2 = 1/2$ to close the set of equations for the moments of radiation transfer. It reads (cf. Equation (31) in [11])

$$T^4 = \frac{T_{\text{int}}^4}{4} \left(2 + 3 \int_0^m \kappa_L dm' \right) + \frac{T_{\text{eq}}^4}{2} \left[1 + \frac{\gamma}{\sqrt{\xi}} E_2 \left(\frac{\kappa_S m'}{\sqrt{\xi}} \right) + 3 \int_0^m \kappa_L E_3 \left(\frac{\kappa_S m'}{\sqrt{\xi}} \right) dm' \right], \quad (2)$$

with $E_j(x) = \int_1^\infty y^{-j} \exp(-xy) dy$ as the exponential integrals. Equation (2) depends on the cloud opacity through κ_L and the opacity ratio $\gamma = \kappa_S/\kappa_L$. Furthermore, the global mean temperature T depends on the intrinsic heat flux $F_{\text{int}} = \sigma_B T_{\text{int}}^4$, which is the outgoing flux from the planet at the bottom of the atmosphere, and on the zero-albedo irradiation flux $\sigma_B T_{\text{eq},0}^4 = \sigma_B T_\star^4 (R_\star/2a)^2$ where σ_B is the Stephan–Boltzmann constant. Thus, $(1-A)^{1/4} T_{\text{eq},0}$ is the globally averaged temperature a planet of albedo A would adopt if in radiation equilibrium with the incident flux. Since a scattering parameter $\xi < 1$ would be inconsistent with a non-uniform opacity, here $\kappa_L(P)$, we set $\xi = 1$ (no scattering) and take scattering into account only via the albedo in T_{eq} , which we set to $A_B = 0.3$ [29,30], while noting that other work suggests smaller values (e.g., [31]). More recently, the geometric albedo of several exoplanets has been derived from secondary eclipse data and found to be quite small, even less than 0.1 [32]. On the other hand, the Bond albedo value of Jupiter itself has recently been revised upward from its Voyager-data based value of 0.34 to the new Cassini-data based value of 0.5 [33]. To study the thermal evolution of irradiated giant planets as a function of uncertainty in albedo is left to future work. For a more consistent treatment of scattering in the presence of non-uniform absorption, see Ref. [34]. For the cloud-free ($\kappa_L = \kappa_{L,0}$) atmosphere without scattering ($\xi=1$), Equation (2) reduces to the global average temperature profile of Guillot (2010) [28]. The P - τ relation for constant gravity g and pressure-dependent longwave opacity reads

$$P = m \cdot g = (\tau/\kappa_L) g. \quad (3)$$

We use the cloud-free model to constrain the parameter γ . For WASP-10b, we fit to 1D, non-gray, atmospheric P - T profiles specifically calculated for this planet for different values of T_{int} [35] (see Figure 1). For WASP-39b, we fit κ_S and $\kappa_{L,0}$ to the global averaged P - T profile from Ref. [16] for a $1 \times$ solar composition metallicity. We find $\kappa_{L,0} = 0.0136 \text{ cm}^2/\text{g}$, $\kappa_S = 0.002 \text{ cm}^2/\text{g}$ ($\gamma = 0.147$) for WASP-10b and $\kappa_{L,0} = 0.006 \text{ cm}^2/\text{g}$, $\kappa_S = 0.00037 \text{ cm}^2/\text{g}$ ($\gamma = 0.062$) for WASP-39b. However, albeit using solar-composition models to fit our double-gray clear atmosphere, it is important to notice that an increase (or decrease) of atmospheric enrichment changes the position of the isotherm [36,37]. An increase in atmospheric metallicity leads to higher temperatures in the isothermal part of the atmosphere [38]. In the case of WASP-39b, where possibly the atmosphere is enriched by a factor of 100–200 \times solar value, the isotherm would be pushed to even hotter temperatures.

The results of these fits are shown in Figure 1. In Figure 2, we show the Rosseland mean opacities along the P - T profiles for the present planets using the fit formula of Valencia et al. [39] to the tabulated values of Freedman et al. [40]. We conclude that our obtained long-wave opacity values $\kappa_{L,0} \sim 0.01 \text{ cgs}$ are appropriate mean Rosseland mean opacities in the radiative atmospheres of both planets.

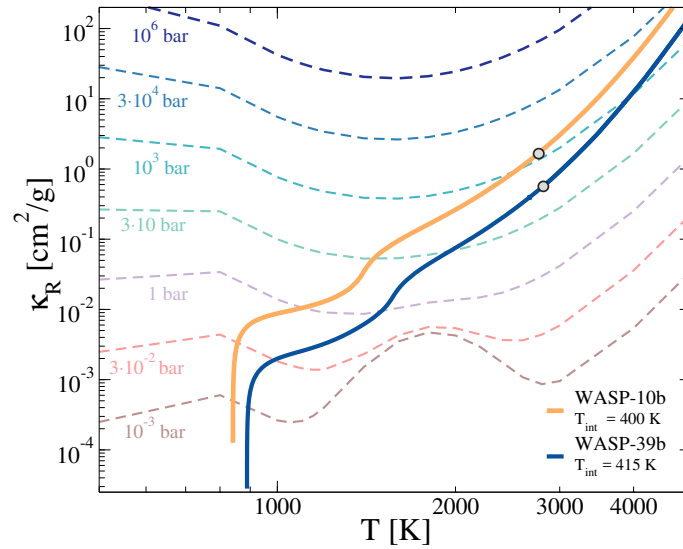


Figure 2. Fit of Valencia et al. [39] to the Rosseland mean opacities κ_R of Freedman et al. [40] along isobars (dashed) and κ_R along the present P - T profiles for WASP-10b (solid orange) and WASP-39b (solid blue). The transition from the atmosphere to the interior is marked by grey circles.

2.4. Cloud Model

The model of Heng et al. [11] for a purely absorbing cloud provides a simple toy model approach that reduces the complexity of the problem to few parameters while including the important greenhouse effect of clouds. The cloud opacity can be assumed to take the shape

$$\kappa_c(P) = \kappa_{c_0} \exp \left[-\Delta_c \left(1 - P/P_c \right)^2 \right] \quad . \quad (4)$$

The cloud opacity depends on the normalization factor κ_{c_0} , the location of the cloud deck P_c , and the cloud deck thickness parameter Δ_c , where small Δ_c values yield vertically extended cloud decks while large Δ_c values lead to thin cloud decks. By construction, the cloud opacity adopts a Gaussian shape. The cloud optical depth τ_c adds to the longwave optical depth τ_L . This is illustrated in Figures 3 and 4 for WASP-10b and WASP-39b, respectively, for cloud parameters considered in this work. The cloud normalization opacity κ_{c_0} was adjusted to reach optical depth values τ_L as in [7,41].

In this cloud model, cloud decks lead to warming of the atmosphere above the cloud, although high above the cloud deck the effect may reverse and lead to cooling (not shown in Figures 3 and 4). Nevertheless, the enhancement of opacity and optical depth in a limited region of the atmosphere leads to a strong heating of the deep atmosphere (left panel) and the typical isothermal region of temperature T_{iso} , which is most clearly seen for $T_{int} = 0$, is shifted toward higher T_{iso} values. For $T_{int} = 0$, the isothermal region extends all the way down to the center of the planet. Of interest to this study is the question of how much the warming effect of the clouds affects the deep interior of planets of finite intrinsic heat fluxes ($T_{int} > 0$), and how much this warming effect affects our inferred heavy element abundances.

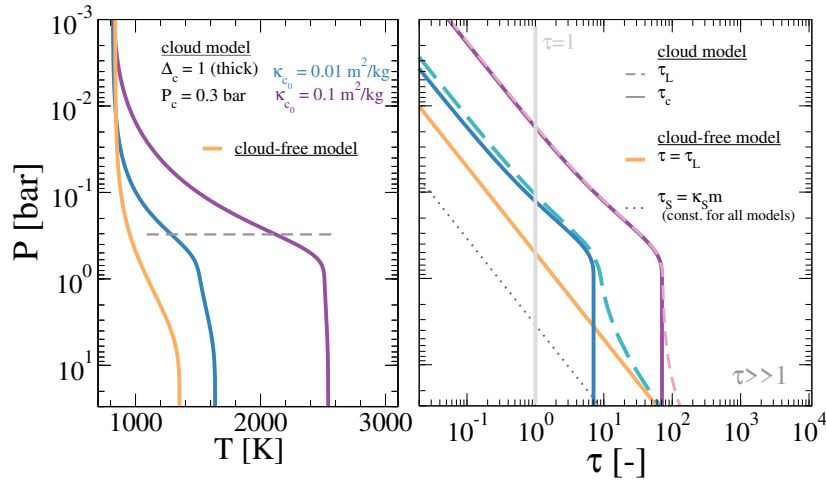


Figure 3. Influence of two cloud decks (optically thin, blue; optically thick, violet, cloud-free, orange) on the P - T relation of WASP-10b for $T_{\text{int}} = 0$ K (left) and P - τ -relation (right) for optical depth τ_L (dashed) and cloud optical depth τ_c (solid), which contributes to τ_L (cf. Equation (49) in [11]). The cloud decks are located at 0.3 bar and are of vertical extension $\Delta_c = 1$.

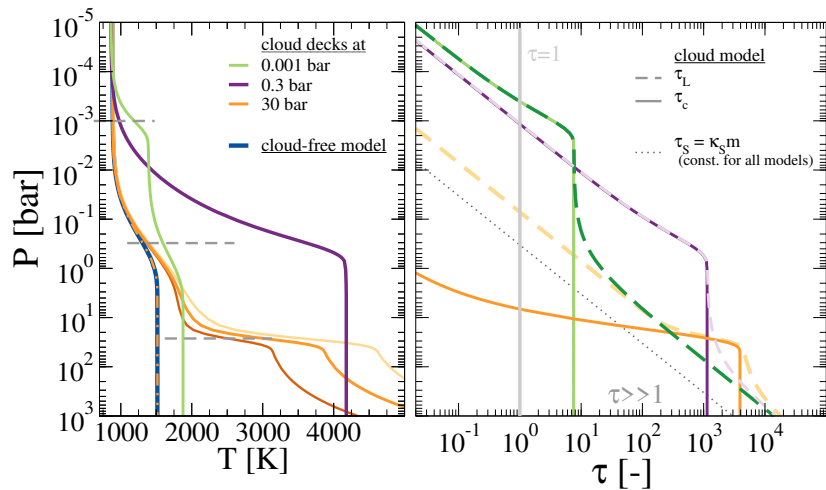


Figure 4. Similar to Figure 3 but for WASP-39b and three possible cloud locations at 0.001 (green), 0.3 (purple) and 30 bar (orange) as well as the cloud-free atmosphere (blue, only left panel). For the cloud deck at 30 bar, we show the resulting P - T profiles for $T_{\text{int}} = 300, 400, 500$ K (from darker to lighter orange) as well as the isotherm (dash-dotted, orange).

To address this question, we investigate six different possible cloud layers for WASP-10b and three for WASP-39b. They are selected based on the condensation curves of typical cloud species [16,42,43] shown in Figure 1. Possible cloud forming species and their approximate intersection pressures are listed in Table 2. We take those pressures as the cloud deck mean location P_c in Equation (4). We consider optically thick ($\kappa_{c0} \sim 10 \kappa_{L,0}$, $\tau_c > 1$, see Figures 3 and 4) and optically very thick ($\kappa_{c0} \sim 100 \kappa_{L,0}$, $\tau_c > 10$) cloud decks. However, for simplicity, we label them *optically thin* and *optically thick*, respectively. The vertical extension is set to $\Delta_c = 1$ where possible in order to allow for a non-zero (Δ_c sufficiently large) but not tremendously too strong (Δ_c sufficiently small) effect. In the real planet, several cloud decks may be present simultaneously and they may be patchy, while, in this model, only one permanent cloud deck is considered and assumed to be uniform.

Table 2. Cloud deck parameters considered in this work.

	Cloud Species	P_c [bar]	Δ_c [-]	κ_{c_0} [m ² /kg]
WASP-10b	KCl/ZnS	0.01	1	0.01
	KCl/ZnS	0.01	1	0.1
	Na ₂ S	0.3	1	0.01
	Na ₂ S	0.3	1	0.1
	MnS	10	10	0.01
	MnS	10	10	0.1
WASP-39b	Na ₂ S	0.001	1	0.2
	MnS	0.3	1	0.1
	MgSiO ₃ /Cr	30	10	0.01

2.5. Atmosphere-Interior Connection

The transition to the adiabatic interior is made where the local numeric temperature gradient $\nabla_{T,\text{local}}$ is larger than the adiabatic gradient ∇_{ad} taken from the EOS table. Further, we see a convective region forming in most cloudy models above the cloud deck. As the starting point for the adiabatic interior we take the lower intersection of $\nabla_{T,\text{local}}$ with ∇_{ad} . Generally, the boundary moves to lower pressures with increasing T_{int} and T_{eq} [9].

2.6. Planetary Evolution

To determine the present T_{int} value of a planet, we perform thermal evolution calculations. The planets are assumed to be of the same age as the parent star within an uncertainty of a few Myr. Further, we assume an orbital location constant in time. Of course, the planets once migrated to their present location, but this is thought to have happened on a comparably short timescale during the first 10 Myr [44]. Integrating the energy balance equation over time, we obtain the evolution of luminosity L and radius $R_P(t)$

$$L_{\text{eff}} - L_{\text{eq}} = L_{\text{int}} = L_{\text{sec}} + L_{\text{radio}} + L_{\text{extra}} \quad (5)$$

with $L_{\text{eq}} = 4\pi R_P^2 \sigma_B T_{\text{eq}}^4$ being the absorbed and re-emitted flux. The heat loss from the interior $L_{\text{int}} = 4\pi R_P^2 \sigma_B T_{\text{int}}^4$ contains three further components. $L_{\text{sec}} = -4\pi R_P^2 \int_0^M dm T(m) \frac{ds}{dt}$ accounts for cooling and contraction of the planet, L_{radio} stands for radiogenic heating, but is of minor importance for H/He-dominated gas giants, and $L_{\text{extra}} = \epsilon 4\pi R_P^2 \sigma_B T_{\text{eq}}^4$ denotes an extra energy that may be needed to inflate the planet. In Ref. [45], the statistically most likely values of ϵ as a function of irradiation flux are determined for a sample of planets that exclude planets with $M_P < 0.5 M_{\text{Jup}}$. Here, we need the extra heating term in order to reach the large age of the $0.28 M_{\text{Jup}}$ planet WASP-39b. Depending on the distribution of heavy elements in the envelope vs. core, we find $\epsilon = 2.75\text{--}4.00\%$ compared to the majority of hot Jupiters where $\epsilon = 1\text{--}3\%$ [45]. In Figure 5, we show the radius evolution of WASP-39b with and without extra heating. For the young WASP-10b, we do not need extra heating to explain its measured radius.

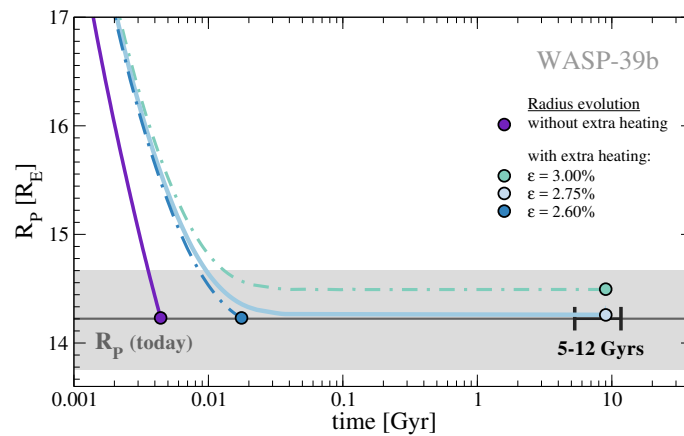


Figure 5. Radius evolution for WASP-39b with (bluish) and without (purple) extra heating. The planet stays hot and inflated for several Gyrs as the additional heating ϵ prevents further contraction.

3. Results for WASP-10b

In Figure 6, we show atmospheric P - T profiles for WASP-10b for finite T_{int} values for a cloud deck at 0.3 bar and two different cloud opacities $\kappa_c = 0.01$ and $0.1 \text{ m}^2/\text{kg}$.

As shown in Figure 3 for $T_{\text{int}} = 0 \text{ K}$, clouds can shift the temperature in the isothermal region significantly toward higher values. This is also the case for finite T_{int} values. Figure 6 also shows that clouds shift the onset of the adiabatic interior to deeper regions. Both effects become more pronounced with increasing cloud opacity. However, we find that the interior adiabat follows the adiabat of the cloud-free case of same T_{int} value.

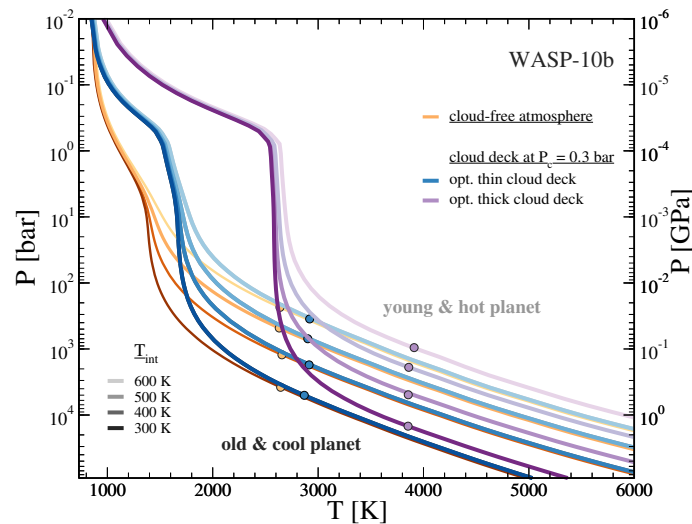


Figure 6. Atmospheric P - T profiles of WASP-10b for finite T_{int} values of 300, 400, 500, and 600 K (from bottom to top) and three cloud deck scenarios: optically thin at 0.3 bar (blue), optically thick at 0.3 bar (purple), and cloud-free (orange). Circles mark the transition between atmosphere and adiabatic interior.

The optically thin cloud (blue) in Figure 6 shifts T_{iso} by about 400 K from $\sim 1400 \text{ K}$ to $\sim 1800 \text{ K}$. Under these conditions, the initially assumed Na_2S molecules would no longer condense while silicate clouds (Mg_2SiO_3 and Mg_2SiO_4) might form in present WASP-10b. In this sense, we consider the optically thin cloud at 0.3 bar a more likely option for WASP-10b. On the other hand, the assumption of

the optically thick cloud at 0.3 bar (purple) clearly shifts T_{iso} far beyond any temperature regime where heavy elements might condense out. Similar reasoning applies to the four other cloud cases considered for WASP-10b. Our optically thick clouds cause too strong heating, evaporating any clouds, while in the atmosphere heated by the optically thin clouds condensable species could still condense out. This is the picture that emerges if using condensation curves for solar-metallicity atmospheres. Despite the apparent inconsistencies with the optically thick clouds, we keep them in the loop. This allows us to place an upper limit on the quantitative influence of assumed long-wave absorbers on the inferred metallicity.

We proceed with the case of the cloud at 0.3 bar and show the radius evolution in Figure 7.

Cooling times in agreement with the known age of the system can easily be obtained for all considered cloud models. Lower assumed T_{int} values for the present planet lead to longer cooling times. We find that optically thick clouds with their strong heating effect slow down the heat loss from the interior, leading to higher T_{int} values. They also slow down the contraction of the planet. To obtain a radius for the present planet in agreement with the known age and radius, the planet with optically very thick clouds must harbor a larger amount of heavy elements. That leads to the link between M_{core} in representation of planetary bulk heavy element mass Z_P and $T_{\text{int}}(t_0)$ shown in Figure 8. Thick lines in Figure 8 show the models matching R_P , M_P and the error range of the age of the system.

The higher is T_{iso} , rising with the optical thickness and P_c , the larger is the core mass. The more likely option of the optically thin cloud deck at 0.3 bar (solid dark blue) leads to a 10% higher core mass compared to the cloud-free model (orange). For optically thin clouds high in the atmosphere, the heating effect on the atmosphere is lower and the influence on inferred metallicity is negligible (the blue-dashed curve in Figure 8 coincides with the orange curve). For the optically thin clouds deep in the atmosphere the heating effect is strong and therefore we had to make the cloud more tenuous by increasing Δ_c instead. The maximum enhancement in inferred heavy element abundance is about 10% and well represented by the medium-height cloud at 0.3 bar. For optically thick clouds, which are not likely options, we obtain a maximum increase in inferred heavy element content of up to 100%.

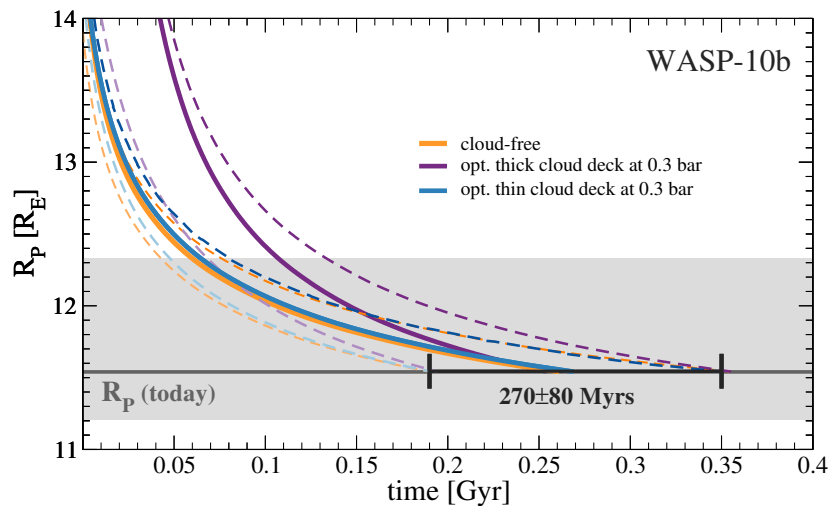


Figure 7. Radius evolution of WASP-10b for the cloud-free atmosphere (orange) as well as for optical thick (purple) and optical thin (blue) clouds decks at $P_c = 0.3$ bar. Solid lines yield a cooling time of 270 Myr while dashed lines within the 1σ uncertainty of the age, e.g., light dashed lines then describe models reaching the lower limit of the age constraint of 190 Myr.

Thorngren and Fortney (2019) find for WASP-10b $Z_P = 0.12 \pm 0.02$, using $M_P = 3.15 M_{\text{Jup}}$ and $R_P = 1.08 R_{\text{Jup}}$, in agreement with our results for the cloud-free model, where we obtain $Z_P = 0.13$ at $T_{\text{int}} = 400$ K.

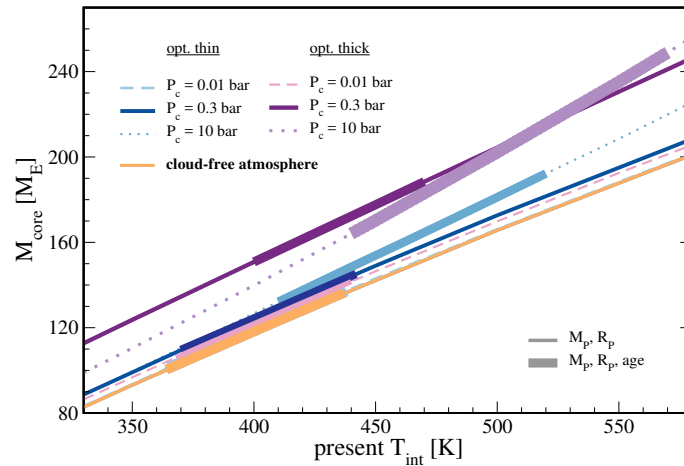


Figure 8. $M_{\text{core}}-T_{\text{int}}$ relation for WASP-10b assuming cloud-free atmosphere (orange) and six different cloud decks in the atmosphere. Thin lines indicate the results obtained by M_p, R_p , thick bars highlight the solutions that also satisfy the age constraint.

4. Results for WASP-39b

4.1. Cloud Height

In Figure 9, we show the atmospheric $P-T$ profiles for WASP-39b with and without cloud decks. We find that the high cloud deck at 0.001 bar would heat the upper atmosphere so much that only silicates could condense out at such low pressures.

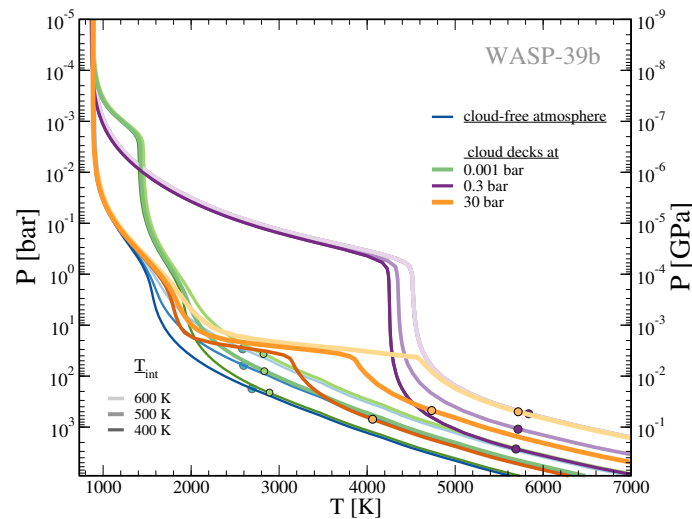


Figure 9. Atmospheric $P-T$ profiles of WASP-39b for finite T_{int} values of 400, 500, and 600 K for three decks located at 0.001 (green), 0.3 (purple), and 30 (orange) bar as well as the cloud-free atmosphere (blue). Circles mark the transition between atmosphere and adiabatic interior.

The analysis in Ref. [2] indicates the presence of clouds on only one side of the limb while a clear sky on the other. In their 3D global circulation models, a high-metallicity atmosphere was clearly required to explain the spectra while optically thick, uniform clouds would not much influence the fit. Thus, the observations do not well constrain the presence of clouds, in particular in the deep atmosphere below ~ 0.1 bar or deeper. We proceed with the cloud deck at 30 bar. According to Figures 1 and 9, this cloud deck could be a more likely solution for the 10–30 bar region while the heating of the

deeper troposphere for the deep-seated cloud at 30 bar is very strong. At 3000–4000 K, condensible species will not condense out. On the other hand, a uniform silicate cloud layer at 30 bar may impose a compositional gradient, which itself may inhibit convection unless the super-adiabaticity becomes sufficiently strong. As a result, the temperature gradient needed to transport the internal heat outward must be larger than in the adiabatic case without cloud. For the solar system giant planets, this effect may amount up to several 100 Kelvins [46]. Therefore, we consider the deep, optically thin cloud at 30 bar a possible option for WASP-39b. We caution that a number of further effects may lead to a more complex picture than drawn here. Condensation of heavier species decreases the mean molecular weight of the surrounding medium and condensates may decouple from the gas phase, affecting the density difference between vertically moving parcels and the background state and thus the possible stability. Moreover, since the Rosseland mean opacity depends on metallicity [40], redistribution of condensible species by condensation also influences the radiative gradient of the background state. Leconte et al. (2017) [46] also found that possible stability requires a sufficiently high mixing ratio of condensible species. Whether sufficient conditions for stability are satisfied in the atmospheres of the hot Jupiters remains to be investigated.

4.2. Metallicity

WASP-39b is an interesting planet because of its observationally determined atmospheric water abundance. Recently, Wakeford et al. (2018) completed the existing transmission spectrum data in the optical obtained with HST STIS [47] and VLT FORS2 [48] and in the infrared obtained with *Spitzer* IRAC [47] by adding spectral data in the near infrared using the HST WFC3 camera. The clearly detected water absorption features allowed them to retrieve the atmospheric metallicity, temperature, and cloudiness of the observationally accessible part of the atmosphere amongst other parameters. Combined likelihood analysis of their isothermal equilibrium model yielded a high-metallicity atmosphere of $\sim 151^{+48}_{-46}$ \times solar abundances, though their free-chemistry model yielded a lower metallicity of $\sim 117^{+14}_{-30}$ \times solar abundances.

The high metallicity of 100–200 \times solar corresponds to a heavy element mass fraction $Z_{\text{env}} \sim 0.25$ –0.75 (see Table 3). Cloud-free structure model of WASP-39b yield a maximum Z_p value of 0.25 [3], where $Z_p \geq Z_{\text{env}}$ due to the possible presence of a core.

First, we require our cloud-free models to have $Z_p = 0.22 \pm 0.03$ as found in Ref. [3] for cloud-free models. Because this planet seems to be inflated (see Section 2.6), we account for extra heating $\epsilon > 0$. For $Z_{\text{env}} = 0.05$, we find $\epsilon \approx 2.75\%$, whereas for $Z_{\text{env}} = 0.2$ we find $\epsilon \approx 3.90\%$. These ϵ values are then used also for the models with clouds. From our experience with the models for WASP-10b, where optically thin clouds have a minor effect on T_{int} , we also use the same range of T_{int} values as found for the cloud-free case, so that no additional evolution calculations are necessary. Figure 10 shows the results on Z_{env} and Z_p . Even for the extreme case of the optically thick cloud, high atmospheric metallicities of $Z_{\text{env}} \sim 0.5$ as observationally derived can barely be reached. Interestingly, however, for the optically thin deep cloud the enhancement in inferred metallicity amounts to about 50%, which allows us to obtain solutions just within the observational uncertainty of Wakeford et al. [2]. A summary of the metallicities for WASP-39b is given in Table 3.

With our favored cloud model for WASP-39b, the optically thin deep cloud, we obtain a maximum envelope metallicity of 0.3, which is 50% higher than our value in the cloud-free case. However, the maximum Z_{env} value still falls short of the observed value. Our results therefore confirm the conclusion of Thorngren and Fortney (2019) of additional sources of uncertainty relevant to WASP-39b. One source of uncertainty is the EOS. While the H/He-EOS was found to induce an uncertainty of a few percent only for massive hot Jupiters and brown dwarfs, wherein matter is largely degenerate [49], this effect might be stronger for warm, lower-mass planets where temperature effect on the P – ρ relation can be stronger. The composition of heavy elements matters as well. Icy cores typically have a 50% higher mass than rocky cores if otherwise the same modeling procedure is applied.

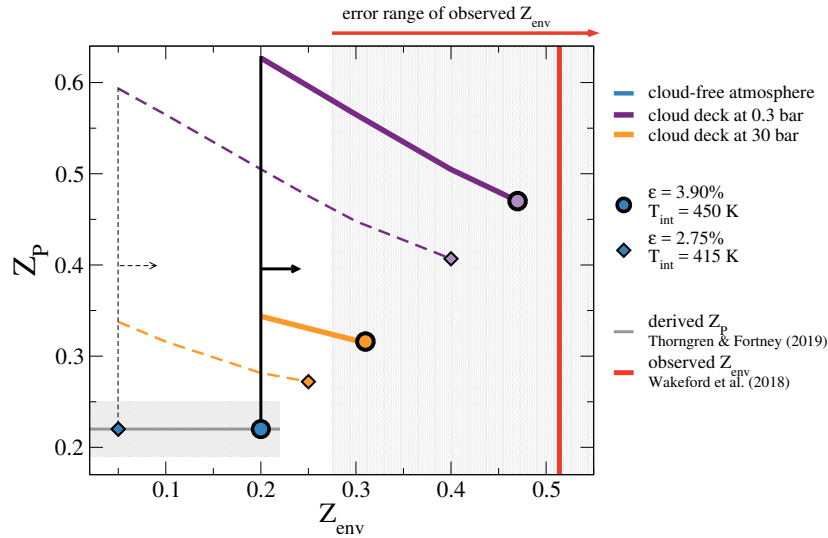


Figure 10. Range of envelope metallicity Z_{env} due to different atmosphere models without clouds (blue), with optically thick cloud deck at 0.3 bar (purple), and optically thin at 30 bar (favored case, orange). Circles/diamonds indicate the maximum Z_{env} value for a fully-mixed planet. The solid and dashed colored lines indicate models with different T_{int}/ϵ -values obtained for the cloud-free models. The arrows indicate the increase of Z_{env} when clouds are switched on.

Table 3. Constraints on atmospheric metallicity of WASP-39b.

WASP39-b		
Wakeford et al. (iso. eq.)	$[M/H]=151^{+48}_{-46} \times \text{solar}$	$Z_{\text{env}} = 0.514^{+0.25}_{-0.24}$
Wakeford et al. (free-chem.)	$[M/H]=117^{+14}_{-30} \times \text{solar}$	$Z_{\text{env}} = 0.45^{+0.09}_{-0.17}$
Thorngrén and Fortney	$Z:H_p = 40.51 \pm 8.3 \times \text{solar}$	$Z_p = 0.22 \pm 0.03 (=Z_{\text{env}}, \text{fully mixed})$
This work, cloud-free		$Z_{\text{env,max}} = 0.2$
This work, 0.3 bar cloud deck		$Z_{\text{env,max}} = 0.47$
This work, 30 bar cloud deck		$Z_{\text{env,max}} = 0.31$

Notes. For conversion of $[M/H]$ to Z , we use Equation (3) in [3] with water as heavy element. The ratio $Z:H_p$ is the atmosphere abundance for a fully mixed planet, as derived from interior models in [3], Equation (3).

Since WASP-39b is likely to be heavy element-rich, it could also be that the heavy elements are not homogeneously distributed but that their abundance increases with depth. Even slight compositional gradients can suppress convection and delay cooling. This may be the case in exoplanets [50] and in Saturn itself [51].

5. Comparison to Self-Consistent Cloud Models

Clouds will not only be important at infrared wavelengths, but they can also contribute to absorption and scattering of irradiation at short wavelengths. This is neglected in the cloud model we use. Out of the codes capable of calculating the structure of self-luminous and/or irradiated planets (e.g., [52–54]), we here compare the ad-hoc approach of Heng et al. (2012) [11] to the self-consistent atmosphere models with clouds of Mollière et al. (2017) [17], who used the *petitCODE* [37]. Within this code, models with clouds and different metallicities have been calculated specifically for WASP-10b and WASP-39b. That code calculates radiative-convective equilibrium atmospheric structures and spectra of extrasolar planets self-consistently, assuming chemical equilibrium. The radiative transfer model implements absorption, emission and scattering. It implements the Ackerman and Marley (2001) [55] cloud model for clouds composed of MgAl_2O_4 , Mg_2SiO_4 , Fe, KCl and Na_2S . Particle opacities are calculated using Mie theory (assumption of spherical, homogeneous grains) or the distribution of

hollow spheres (approximating irregularly shaped dust aggregates). For both planets, WASP-10b and WASP-39b, we plot the clear and cloudy solutions of Mollière et al. (2017) in comparison to our clear and cloudy atmosphere models for $T_{\text{int}} = 400$ K in Figure 11. Mollière et al. (2017) used cloud models which differ in the assumptions of the grain shape, the standard settling parameter f_{sed} from the Ackerman and Marley model, the maximum cloud mass fraction, the width of the cloud particle size distribution as well the inclusion of iron clouds (see Table 2 in [17]). The different model assumptions result in different atmospheric structures. For temperate giant planets, such as WASP-10b and WASP-39b, they investigated cold cloud models as well, where only Na_2S and KCl are considered as possible cloud species (Figure 11, red) as for this temperature regime higher temperature condensates may not mix up from their deep cloud deck locations.

For both planets, the cloudy atmospheric structures from Mollière et al. (2017) lead to both cooler and hotter isotherms. Their favored *cold* cloud models, only using Na_2S and KCl as cloud species, lead to cooler isotherm for all different cloudy model parameters compared to the clear atmosphere in orange. In contrast, in this work, the fit parameter of the double-gray atmosphere and the added cloud opacity lead to a warmer atmosphere beneath the cloud deck for all of our assumed cloud decks in the atmosphere. For WASP-10b, there is only one model (dashed light blue) that yields a hotter isotherm, whereas for WASP-39b there are three cloudy models that yield a hotter isotherm compared to the cloud-free case. This comparison suggest that our favored 0.3 bar cloud model for WASP-10b may be supported by the *hot* cloud model of Mollière et al. (2017), down to significant depths of ~ 1 kbar, while for WASP-39b our favored 30 bar cloud model is supported to ~ 100 bar and thus may overestimate the here obtained influence on the Z_{env} of WASP-39b.

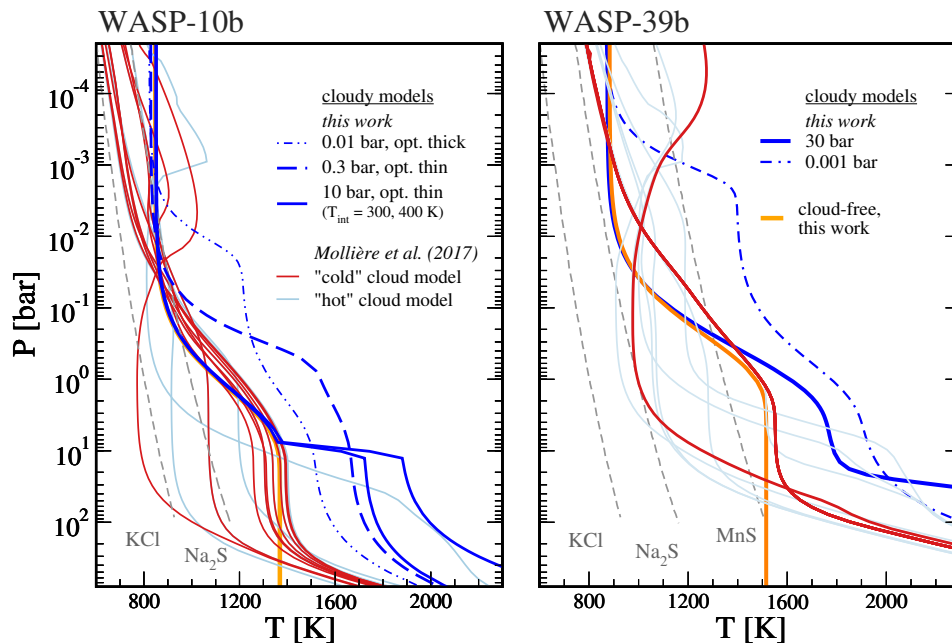


Figure 11. Atmospheric temperature structures for WASP-10b (left) and WASP-39b (right). Our result for the clear atmosphere is shown in orange for $T_{\text{int}} = 0$ K as well some of our cloudy solutions in dark blue. The bunch of profiles in red (*cold models*) and light blue (*hot models*) are from Mollière et al. (2017) for different cloud model parameter, see text. The condensation curves assume solar elemental abundance.

6. Conclusions

We performed coupled atmosphere, interior, and evolution calculations for the two giant planets WASP-10b and WASP-39b and investigated the effect of additional absorbers, which we call cloud

decks, of the inferred metallicity. We assumed cloud optical thicknesses of $\tau_c \approx 1\text{--}10$ (named optically thin) and $\tau_c \approx 1\text{--}100$ (named optically thick), as well as different cloud heights in the atmosphere corresponding to certain condensible species. The clouds decks are purely absorbing and based on the model of Heng et al. (2012) [11]. Our major findings are as follows:

- (I) Through their additional infrared opacity, these cloud decks tend to warm the atmosphere beneath. This leads to a more or less pronounced enhancement in inferred heavy element abundance.
- (II) For the optically thicker cloud decks, the heating is too strong so that condensible species would no longer condense out. This puts an upper limit on the enhancement in metallicity of 100% on both planets.
- (III) For optically thin clouds, the heating of the atmosphere can be sufficiently small so that condensible species can condense out. In this case, we find an increase of the core mass of up to 10% for WASP-10b.
- (IV) For WASP-39b we find a maximum atmospheric metallicity of $Z_{\text{env}} = 0.31$ if we assume a deep cloud at 30 bars in the troposphere that in addition would lead to inhibited convection. Even in this favored case, the possible envelope metallicity is still near the lower limit of the observationally inferred value. Further effects that lead to a heating of the planet are clearly required. Since the heating efficiency is empirically not yet constrained, as it is for hot Jupiters [45], $\epsilon > 3\%$ is not excluded for such planets. Such high values would help to bring the observationally inferred Z in agreement with interior-model inferred Z .

Due to the complexity of modeling clouds in a realistic manner, we applied a simple cloud model that is a crude representation of real cloud decks. The predictive power of that model stands and falls with the assumed cloud opacity, cloud height, and cloud thickness, which are poorly known parameters. Another important point is how to couple this cloud model to the atmospheric structure self-consistently. Nevertheless, this work suggests that deep cloud decks below the pressure level accessible to transmission spectra observations may influence the temperature structure in the atmosphere and the inferred metallicity to some extent. A more sophisticated approach is desired.

Author Contributions: A.J.P. developed large parts of the computer code used to perform the model computations, obtained the results presented here, and prepared the figures. A.J.P. and N.N. wrote the paper, and R.R. approved it. N.N. and R.R. designed the project. All authors discussed and contributed to the methodology.

Funding: A.J.P. and R.R. thank the DFG for support within the SPP 1992.

Acknowledgments: We thank the referees for helping to improve this manuscript. We thank R. Neuhäuser and G. Maciejewski for discussions on the observational parameters of WASP-10b. N.N. thanks the Swiss PlanetS Program for hospitality in March 2018. We thank P. Mollière for providing us with data from petitCODE for the atmospheres of WASP-10b and WASP-39b, and thank J. Fortney and L. Scheibe for discussions.

Conflicts of Interest: The authors declare no conflict of interest.

References

1. Venturini, J.; Alibert, Y.; Benz, W. Planet formation with envelope enrichment: New insights on planetary diversity. *A&A* **2016**, *596*, A90.
2. Wakeford, H.R.; Sing, D.K.; Deming, D.; Lewis, N.K.; Goyal, J.; Wilson, T.J.; Barstow, J.; Kataria, T.; Drummond, B.; Evans, T.M.; et al. The complete transmission spectrum of WASP-39b with a precise water constraint. *Astron. J.* **2018**, *155*, 29. [[CrossRef](#)]
3. Thorngren, D.; Fortney, J.J. Connecting giant planet atmosphere and interior modeling: constraints on atmospheric metal enrichment. *Astrophys. J. Lett.* **2019**, *874*, 6. [[CrossRef](#)]
4. Maciejewski, G.; Raetz, S.; Nettelmann, N.; Seeliger, M.; Adam, C.; Nowak, G.; Neuhäuser, R. Analysis of new high-precision transit light curves of WASP-10 b: starspot occultations, small planetary radius, and high metallicity. *A&A* **2011**, *535*, A7.
5. Thorngren, D.P.; Fortney, J.J.; Murray-Clay, R.A.; Lopez, E.D. The mass-metallicity relation for giant planets. *Astrophys. J.* **2016**, *831*, 64. [[CrossRef](#)]

6. Morley, C.V.; Fortney, J.J.; Kempton, E.M.-R.; Marley, M.S.; Vissler, C.; Zahnle, K. Quantitatively assessing the role of clouds in the transmission spectrum of GJ 1214b. *Astrophys. J.* **2013**, *775*, 33. [[CrossRef](#)]
7. Lines, S.; Mayne, N.J.; Boutle, I.A.; Manners, J.; Lee, G.K.H.; Helling, C.; Drummond, B.; Amundsen, D.S.; Goyal, J.; Acreman, D.M.; et al. Simulating the cloudy atmospheres of HD 209458 b and HD 189733 b with the 3D Met Office Unified Model. *A&A* **2018**, *615*, A97.
8. Miller-Ricci, E.; Seager, S.; Sasselov, D. The Atmospheric Signatures of Super-Earths: How to Distinguish Between Hydrogen-Rich and Hydrogen-Poor Atmospheres. *Astrophys. J.* **2009**, *690*, 1056. [[CrossRef](#)]
9. Thorngren, D.P.; Gao, P.; Fortney, J.J. The intrinsic temperature and radiative-convective boundary depth in the atmospheres of hot Jupiters. *Astrophys. J. Lett.* **2019**, *884*, L6. [[CrossRef](#)]
10. Podolak, M.; Helled, R.; Schubert, G. Effect of non-adiabatic thermal profiles on the inferred composition of Uranus and Neptune. *Mon. Not. R. Astron. Soc.* **2019**, *487*, 2653–2664. [[CrossRef](#)]
11. Heng, K.; Hayek, W.; Pont, F.; Sing, D.K. On the effects of clouds and hazes in the atmospheres of hot Jupiters: Semi-analytical temperature-pressure profiles. *Mon. Not. R. Astron. Soc.* **2012**, *420*, 20–36. [[CrossRef](#)]
12. Linder, E.F.; Mordasini, C.; Mollière, P.; Marleau, G.D.; Malik, M.; Quanz, S.P.; Meyer, M.R. Evolutionary models of cold and low-mass planets: Cooling curves, magnitudes, and detectability. *A&A* **2019**, *623*, A85.
13. Kurosaki, K.; Ikoma, M. Acceleration of Cooling of Ice Giants by Condensation in Early Atmospheres. *Astron. J.* **2017**, *153*, 260. [[CrossRef](#)]
14. Barman, T.S.; Hauschildt, P.H.; Allard, F. Irradiated Planets. *Astrophys. J.* **2001**, *556*, 885–895. [[CrossRef](#)]
15. Baraffe, I.; Chabrier, G.; Barman, T.S.; Allard, F.; Hauschildt, P.H. Evolutionary models for cool brown dwarfs and extrasolar giant planets. The case of HD 209458. *A&A* **2003**, *402*, 701–712.
16. Kataria, T.; Sing, D.K.; Lewis, N.K.; Visscher, C.; Showman, A.P.; Fortney, J.J.; Marley, M.S. The atmospheric circulation of a nine-hot-Jupiter sample: Probing circulation and chemistry over a wide phase space. *Astrophys. J.* **2016**, *821*, 9. [[CrossRef](#)]
17. Mollière, P.; van Boekel, R.; Bouwman, J.; Henning, T.; Lagage, P.O.; Min, M. Observing transiting planets with JWST. Prime targets and their synthetic spectral observations. *A&A* **2017**, *600*, A10.
18. Johnson, J.A.; Winn, J.N.; Cabrera, N.E.; Carter, J.A. A smaller radius for the transiting exoplanet WASP-10b. *Astrophys. J. Lett.* **2009**, *692*, L100–L104. [[CrossRef](#)]
19. Christian, D.J.; Gibson, N.P.; Simpson, E.K.; Street, R.A.; Skillen, I.; Pollacco, D.; Collier Cameron, A.; Joshi, Y.C.; Keenan, F.P.; Stempels, H.C.; et al. WASP-10b: A 3MJ, gas-giant planet transiting a late-type K star. *Mon. Not. R. Astron. Soc.* **2009**, *392*, 1585. [[CrossRef](#)]
20. Maciejewski, G.; Dimitrov, D.; Neuhäuser, R.; Tetzlaff, N.; Niedzielski, A.; St. Raetz; Chen, W.P.; Walter, F.; Marka, C.; Baar, S.; et al. Transit timing variation and activity in the WASP-10 planetary system. *Mon. Not. R. Astron. Soc.* **2010**, *411*, 1204–1212. [[CrossRef](#)]
21. Faedi, F.; Barros, S.C.C.; Anderson, D.R.; Brown, D.J.A.; Collier Cameron, A.; Pollacco, D.; Boisse, I.; Hébrard, G.; Lendl, M.; Lister, T.A.; et al. WASP-39b: A highly inflated Saturn-mass planet orbiting a late G-type star. *A&A* **2011**, *531*, A40.
22. Mordasini, C.; van Boekel, R.; Mollière, P.; Henning, T.; Benneke, B. The imprint of exoplanet formation history on observable present-day spectra of hot Jupiters. *Astrophys. J.* **2016**, *832*, 41. [[CrossRef](#)]
23. Lodders, K. Solar system abundances and condensation temperatures of the elements. *Astrophys. J.* **2003**, *591*, 1220. [[CrossRef](#)]
24. Saumon, D.; Chabrier, G. An equation of state for low-mass stars and giant planets. *Astrophys. J. Suppl.* **1995**, *99*, 713–741. [[CrossRef](#)]
25. Hubbard, W.B.; Marley, M.S. Optimized Jupiter, Saturn, and Uranus interior models. *Icarus* **1989**, *78*, 102. [[CrossRef](#)]
26. Nettelmann, N.; Fortney, J.J.; Kramm, U.; Redmer, R. Thermal evolution and structure models of the transiting super-Earth GJ 1214b. *Astrophys. J.* **2011**, *733*, 2. [[CrossRef](#)]
27. Fortney, J.J.; Nettelmann, N. The interior structure, composition, and evolution of giant planets. *Space Sci. Rev.* **2010**, *152*, 423–447. [[CrossRef](#)]
28. Guillot, T. On the radiative equilibrium of irradiated planetary atmospheres. *A&A* **2010**, *520*, A27.
29. Marley, M.S.; Gelino, C.; Stephens, D.; Lunine, J.I.; Freedman, R. Reflected spectra and albedos of extrasolar giant planets. I. Clear and cloudy atmospheres. *Astrophys. J.* **1999**, *513*, 879–893. [[CrossRef](#)]
30. Gelino, G.; Marley, M.; Stephens, D.; Lunine, J.; Freedman, R. Model Bond Albedos of Extrasolar Giant Planets. *Phys. Chem. Earth* **1999**, *24*, 573–578. [[CrossRef](#)]

31. Sudarsky, D.; Burrows, A.; Pinto, P. Albedo and reflection spectra of extrasolar giant planets. *Am. Astron. Soc.* **2000**, *538*, 885–903. [[CrossRef](#)]
32. Madhusudhan, N.; Knutson, H.; Fortney, J.J.; Barman, T. Exoplanetary atmospheres. In *Protostars and Planets VI*; University of Arizona Press: Tucson, AZ, USA, 2014.
33. Li, L.; Jiang, X.; West, R.A.; Gierasch, P.J.; Perez-Hoyos, S.; Sanchez-Lavega, A.; Fletcher, L.N.; Fortney, J.J.; Knowles, B.; Porco, C.C.; et al. Less absorbed solar energy and more internal heat for Jupiter. *Nat. Commun.* **2018**, *9*, 3709. [[CrossRef](#)] [[PubMed](#)]
34. Heng, K.; Mendonça, J.M.; Lee, J.M. Analytical models of exoplanetary atmospheres. II. Radiative transfer via the two-stream approximation. *Astrophys. J. Suppl.* **2014**, *215*, 4. [[CrossRef](#)]
35. Fortney, J.J.; Marley, M.S.; Barnes, J.W. Planetary radii across five orders of magnitude in mass and stellar insolation: Application to transits. *Astrophys. J.* **2007**, *659*, 1661–1672. [[CrossRef](#)]
36. Fortney, J.J.; Saumon, D.; Marley, M.; Lodders, K.; Freedman, R. Atmosphere, Interior, and Evolution of the Metal-rich Transiting Planet HD 149036b. *Astrophys. J.* **2006**, *642*, 495. [[CrossRef](#)]
37. Mollière, P.; Van Boekel, R.; Dullemond, C.; Henning, T.; Mordasini, C. Model atmospheres of irradiated exoplanets: The influence of stellar parameters, metallicity, and the C/O ratio. *Astrophys. J.* **2015**, *813*, 47. [[CrossRef](#)]
38. Wakeford, H.R.; Visscher, C.; Lewis, N.K.; Kataria, T.; Marley, M.S.; Fortney, J.J.; Mandell, A.M. High-temperature condensate clouds in super-hot Jupiter atmospheres. *Mon. Not. R. Astron. Soc.* **2017**, *464*, 4247. [[CrossRef](#)]
39. Valencia, D.; Guillot, T.; Parmentier, V.; Freedman, R.S. Bulk composition of GJ 1214b and other sub-neptune exoplanets. *Astrophys. J.* **2013**, *775*, 10. [[CrossRef](#)]
40. Freedman, R.; Marley, M.; Lodders, K. Line and mean opacities for ultracool dwarfs and extrasolar planets. *Astrophys. J. Suppl.* **2008**, *174*, 504–513. [[CrossRef](#)]
41. Marley, M.S. The Role of Condensates in L- and T-dwarf Atmospheres. In *From Giant Planets to Cool Stars*; ASP Conference Series; ASP: San Francisco, CA, USA, 2000.
42. Lodders, K.; Fegley, B. Chemistry of low mass substellar objects. In *Astrophysics Update 2*; Springer: Heidelberg, Germany, 2006.
43. Morley, C.V.; Fortney, J.J.; Marley, M.S.; Zahnle, K.; Line, M.; Kempton, E.; Lewis, N.; Cahoy, K. Thermal emission and reflected light spectra of super earths with flat transmission spectra. *Astrophys. J.* **2015**, *815*, 110. [[CrossRef](#)]
44. Alexander, R.; Armitage, P. Giant planet migration, disk evolution, and the origin of transitional disks. *Astrophys. J.* **2009**, *704*, 989. [[CrossRef](#)]
45. Thorngren, D.P.; Fortney, J.J. Bayesian Analysis of Hot-Jupiter Radius Anomalies: Evidence for Ohmic Dissipation? *Astron. J.* **2018**, *155*, 214. [[CrossRef](#)]
46. Leconte, J.; Selsis, F.; Hersant, F.; Guillot, T. Condensation-inhibited convection in hydrogen-rich atmospheres. *A&A* **2017**, *598*, A98.
47. Sing, D.K.; Fortney, J.J.; Nikolov, N.; Wakeford, H.R.; Kataria, T.; Evans, T.M.; Aigrain, S.; Ballester, G.E.; Burrows, A.S.; Deming, D.; et al. A continuum from clear to cloudy hot-Jupiter exoplanets without primordial water depletion. *Nature* **2016**, *529*, 59–62. [[CrossRef](#)] [[PubMed](#)]
48. Nikolov, N.; Sing, D.K.; Gibson, N.P.; Fortney, J.J.; Evans, T.M.; Barstow, J.K.; Kataria, T.; Wilson, P.A. VLT FORS2 comparative transmission spectroscopy: Detection of Na in the atmosphere of WASP-39b from the ground. *Astrophys. J.* **2016**, *832*, 191. [[CrossRef](#)]
49. Becker, A.; Lorenzen, W.; Fortney, J.J.; Nettelmann, N.; Redmer, R.; Schöttler, M. Ab initio equation of state for hydrogen (H-REOS.3) and helium (He-REOS.3) and their implications for the interior of brown dwarfs. *Astrophys. J. Suppl.* **2014**, *215*, A21. [[CrossRef](#)]
50. Chabrier, G.; Baraffe, I. Heat transport in giant (exo)planets: A new perspective. *Astrophys. J. Lett.* **2007**, *661*, L81–L84. [[CrossRef](#)]
51. Leconte, J.; Chabrier, G. Layered convection as the origin of Saturn’s luminosity anomaly. *Nat. Geosci.* **2013**, *6*, 347–350. [[CrossRef](#)]
52. Malik, M.; Kitzmann, D.; Mendonça, J.; Grimm, S.; Marleau, G.D.; Linder, E.; Tsai, S.M.; Heng, K. Self-luminous and Irradiated Exoplanetary Atmospheres Explored with HELIOS. *Astron. J.* **2019**, *157*, 170. [[CrossRef](#)]

Atmosphere **2019**, *10*, 664

18 of 18

53. Allard, F.; Hauschildt, P.; Alexander, D.; Tamanai, A.; Schweitzer, A. The Limiting Effects of Dust in Brown Dwarf Model Atmospheres. *Astrophys. J.* **2001**, *556*, 357. [[CrossRef](#)]
54. Hauschildt, P.; Baron, E. Numerical Solution of the Expanding Stellar Atmosphere Problem. *J. Comput. Appl. Math.* **1999**, *109*, 41. [[CrossRef](#)]
55. Ackerman, A.; Marley, M. Precipitating condensation clouds in substellar atmospheres. *Astrophys. J.* **2001**, *556*, 872. [[CrossRef](#)]



© 2019 by the authors. Licensee MDPI, Basel, Switzerland. This article is an open access article distributed under the terms and conditions of the Creative Commons Attribution (CC BY) license (<http://creativecommons.org/licenses/by/4.0/>).

5.2. The effect of cloudy atmospheres on the thermal evolution of warm giant planets from an interior modelling perspective

All our science, measured against reality, is primitive and childlike - and yet it is the most precious thing we have.

Albert Einstein (1879-1955)

Monthly Notices of the Royal Astronomical Society (2024) **529**, 2242-2257

DOI: [10.1093/mnras/stae645](https://doi.org/10.1093/mnras/stae645)

A. J. Poser

Preparation of the manuscript, initial project idea, code development, calculation of all coupled atmosphere, interior, and thermal evolution data, analysis and interpretation of results

R. Redmer

Supervision of the project, preparation of the manuscript



The effect of cloudy atmospheres on the thermal evolution of warm giant planets from an interior modelling perspective

A. J. Poser^{*} and R. Redmer

Institute of Physics, University of Rostock, D-18059 Rostock, Germany

Accepted 2024 February 28. Received 2024 February 21; in original form 2023 September 18

ABSTRACT

We are interested in the influence of cloudy atmospheres on the thermal radius evolution of warm exoplanets from an interior modelling perspective. By applying a physically motivated but simple parametrized cloud model, we obtain the atmospheric P – T structure that is connected to the adiabatic interior at the self-consistently calculated radiative–convective boundary. We investigate the impact of cloud gradients, with the possibility of inhibiting superadiabatic clouds. Furthermore, we explore the impact on the radius evolution for a cloud base fixed at a certain pressure versus a subsiding cloud base during the planets’ thermal evolution. We find that deep clouds clearly alter the evolution tracks of warm giants, leading to either slower/faster cooling than in the cloudless case (depending on the cloud model used). When comparing the fixed versus dynamic cloud base during evolution, we see an enhanced behaviour resulting in a faster or slower cooling in the case of the dynamic cloud base. We show that atmospheric models including deep clouds can lead to degeneracy in predicting the bulk metallicity of planets, Z_P . For WASP-10b, we find a possible span of $\approx Z_{P-0.06}^{+0.10}$. For TOI-1268b, it is $\approx Z_{P-0.05}^{+0.10}$. Further work on cloud properties during the long-term evolution of gas giants is needed to better estimate the influence on the radius evolution.

Key words: planets and satellites: atmospheres – planets and satellites: gaseous planets – planets and satellites: individual: (WASP-10b, TOI-1268b) – planets and satellites: interiors.

1 INTRODUCTION

Giant planets are essential for understanding how planets form and evolve because they hide important information within their interiors (e.g. Turrini et al. 2018; Helled et al. 2021). In particular, both the mass of the heavy elements and their distribution within the planet are of interest, as the bulk and atmospheric composition of the planets are related to their formation and evolutionary history. For example, the heavy element content of the planet may be correlated with the star’s metallicity, both forming from the same protostellar cloud (e.g. Guillot et al. 2006; Thorngren et al. 2016).

Characterization of the interior is initially based on observational parameters of the planet, such as planetary mass, radius, and stellar age, as a proxy for the age of the planetary system and the planet itself. The ensuing description of the current (today’s) bulk structure then relies on purely numerical models and delivers, among other things, the desired heavy-element content. Making use of the full set of observational parameters, one has to couple atmosphere, interior, and thermal evolution models (e.g. Fortney, Marley & Barnes 2007; Baraffe, Chabrier & Barman 2008; Poser, Nettelmann & Redmer 2019; Müller & Helled 2023a, b).

In this context, the atmosphere of the planet plays a unique role. It is critical for the planet’s radiative budget, in particular for irradiated planets, as it serves as a bottleneck for both the incoming stellar irradiation and the emitted intrinsic flux. As a result, it has a direct

impact on the planet’s cooling behaviour because the intrinsic heat from the inside is radiated away through the atmosphere over time.

Over the past years, several atmosphere models have been developed that account for stellar irradiation and intrinsic heat flux, including atmospheric characteristics such as grains, hazes, and clouds (e.g. Guillot 2010; Heng et al. 2012; Mollière et al. 2015; Baudino et al. 2017; Malik et al. 2019).

Few earlier works have investigated the impact of the atmospheric conditions including grains and clouds on the planets’ long-term thermal evolution: For example, Kurosaki & Ikoma (2017) show that condensation in heavily enriched atmospheres of ice giants accelerates the cooling as the planet emits more energy due to latent heat release. In contrast, Vazan et al. (2013) show a delayed cooling due to an atmosphere enriched in grains for giant planets.

For isolated, non-irradiated low-mass planets ($M_P < 0.6 M_J$), Linder et al. (2019) find that including clouds or using different atmospheric codes have only a limited influence on the evolution tracks.

In many atmospheric models, the stellar irradiation flux is considered to be the main driver of the physics of the upper atmosphere. Fortney et al. (2020) emphasize that not only the equilibrium temperature (T_{eq}) as a measure for the stellar irradiation characterizes the atmosphere of giant planets but also the heat flux from the deep interior (characterized by the intrinsic temperature T_{int}), stressing that the appearance of clouds might as well depend on the atmospheric pressure–temperature conditions (P – T) in the deep atmosphere.

^{*}E-mail: anna.poser@uni-rostock.de

In coupled atmosphere-interior models with convective interiors, the atmosphere connects to the inner envelope at the radiative–convective boundary (RCB; e.g. Poser et al. 2019; Thorngren & Fortney 2019; Thorngren, Gao & Fortney 2019). During the planets’ long-term evolution, the RCB moves towards higher pressures for progressing time-steps as the planet cools down. To the best of our knowledge, the effect of deep-seated cloud decks on the RCB and on the long-term thermal evolution of warm irradiated planets has not been studied so far. Knowing the impact on the evolution curves may help characterize giant planets with regard to their heavy element mass and distribution.

Therefore, we aim at estimating the influence of atmospheric P – T conditions with and without clouds on the long-term evolution of irradiated giant planets. In detail, we vary the atmospheric model while performing thermal evolution calculations for two young warm giant planets, TOI-1268b and WASP-10b. We concentrate our study on warm Jovian planets as they do not show an inflated radius. Inflated gas giants with $T_{\text{eq}} > 1000$ K need an additional amount of extra energy that would induce another model uncertainty (Thorngren & Fortney 2018; Sarkis et al. 2021). Also, it is more probable that clouds occur at lower T_{eq} (e.g. Fortney et al. 2020).

In this paper, we look at the difference of cloud-free and cloudy P – T structures, exploring how a possibly variable cloud deck location affects the evolution. Our idea is that during evolution, the deep parts of the atmosphere cross the condensation curves of possible cloud condensation curves at different pressure levels, resulting in changing (evolving) cloud deck bases. For our purpose, we apply the approach of Poser et al. (2019), adapting and extending the cloud model by Heng et al. (2012). In that approach, the semigrey atmosphere model is employed for coupled interior and thermal evolution calculations. It allows us to approximate the complex radiative transfer and microphysics of cloudy atmospheres in a much simplified manner suitable for this study. A cloud deck is added as an additional absorber in the longwave ignoring shortwave scattering. To understand the general impact of cloud decks in the interior modelling procedure, we also investigate the influence on the T_{int} – Z_{env} phase space.

The paper is structured as follows. Section 2 outlines our modelling approach to study the thermal evolution of gaseous planets, focusing in Sections 2.1 and 2.3 on the description of the atmospheric model. Section 2.2 briefly describes the interior and thermal evolution model, while Section 2.4 summarizes the modelling procedure. The planets under study, TOI-1268b and WASP-10b, are introduced in Section 3.1. Presenting the results, we first show the impact on the *static* T_{int} – Z_{env} phase spaces for both planets in Section 3.2, comparing both cases with and without clouds. *Static* means, our approach matches the planetary mass and radius, without performing additional evolution calculations matching the planets’ age. In Section 3.3, we show the radius evolution curves for a clear atmosphere. In Section 3.4, we present the main results quantifying how the radius evolution changes for different cloudy models. A discussion of the results follows in Section 4.

2 MODEL

Fig. 1 shows a sketch of the combined atmosphere and interior model setup applied. The planet is made up of up to three layers: a radiative atmosphere, an adiabatic envelope, and an isothermal solid core, following our previous approach in Poser et al. (2019). We continue by presenting the atmosphere model accounting for a cloud deck in Section 2.1, followed by a short description of the interior and thermal evolution model in Sections 2.2 and 2.3. We outline our

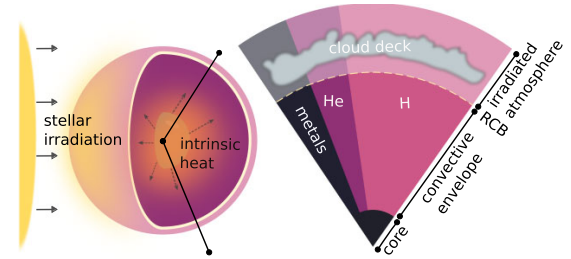


Figure 1. The model setup in this work: A Jovian planet is irradiated by its star. The atmosphere acts as a bottleneck for the incoming irradiation flux and the outgoing intrinsic heat flux, indicated by arrows. The interior consists of a radiative atmosphere, an outer convective envelope, and an isothermal core. The main constituents are hydrogen and helium, replenished by metals. We consider clouds in the atmosphere and combine atmosphere, interior, and thermal evolution models to obtain the radius evolution of the planet. The atmosphere model is used as an outer boundary condition for the interior model, connecting both models at the RCB.

modelling process in Section 2.4, which sets the foundation for the results presented in Section 3.

2.1 Atmosphere

To account for radiative transfer in the atmosphere, we make use of (semi-)analytical 1D, plane-parallel atmosphere models. The clear, cloud-free model goes back to the work of Guillot (2010). It depends on the equilibrium temperature T_{eq} , the intrinsic temperature T_{int} , and a semigrey description of opacities in the short- and longwave wavelength range: κ_S , κ_L . The cloudy atmosphere model is based on the work of Heng et al. (2012) extending the work of Guillot (2010) to include the effect of a cloud deck. Here, clouds are added as additional absorbers in the longwave (Section 2.1.2). These models have been employed in prior studies for coupled atmosphere-interior calculations. (e.g. Jin et al. 2014; Poser et al. 2019; Kumar et al. 2021; Dietrich et al. 2022; MacKenzie et al. 2023).

2.1.1 The parameter γ of the basic grey atmosphere model

Both clear and cloudy atmosphere models account for radiative transfer via semigrey opacities κ_L , κ_S . The parameter $\gamma = \kappa_S/\kappa_L$ is an essential input to the models, determining the amount of absorption of the incoming flux. To determine the ratio γ , and consequently to use it for the atmosphere model of our planets, our objective is to find a correlation between γ and the equilibrium temperature T_{eq} of irradiated gas planets.

We fitted the $T(P)$ relation by Guillot (2010) for clear atmospheres to published P – T profiles of warm to ultrahot Jupiters with different equilibrium temperatures by matching the deep isothermal regions manually. The deep isothermal region is characterized by the temperature T_{iso} . Note, that varying κ_L for constant γ does not affect the location of the deep isothermal region as the optical depth τ is proportional to $\propto \kappa_L P$ (assuming constant gravity in the thin atmosphere). But with larger κ_L , the isotherm expands to lower pressures, resulting in a vertical shift of the isotherm.

We find the following fit for $\gamma(T_{\text{eq}})$ for $T_{\text{eq}} = (500\text{--}4000)\text{K}$:

$$\gamma(T_{\text{eq}}) = 6.24 - 4.78 \log(T_{\text{eq}}) + 0.92 (\log(T_{\text{eq}}))^2, \quad (1)$$

which is shown in Fig. 2 in black solid. We estimate a deviation in γ of $\approx \pm 0.1$, based on different possible P – T -profiles resulting

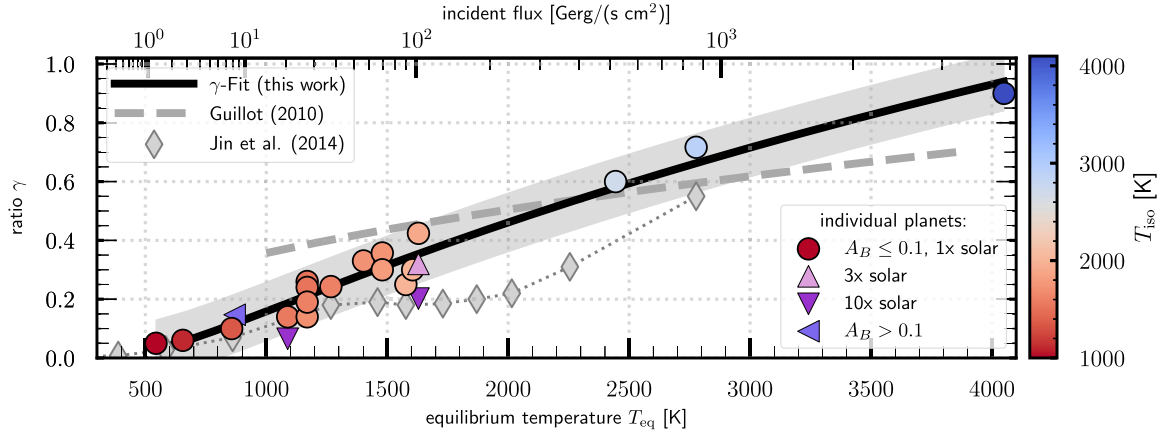
2244 *A. J. Poser and R. Redmer*

Figure 2. The parameter $\gamma = \frac{\kappa_S}{\kappa_L}$ is an essential input parameter for semi-analytical atmosphere models. We derive a γ - T_{eq} relation useful for a fast calculation of the temperature–pressure conditions. The resulting fit is shown in black. For comparison, we show the relation by Guillot (2010) in grey dashed and the results from Jin et al. (2014) in grey diamonds. T_{iso} is the temperature of the deep isotherm of the atmospheric P - T profile which may extend to several hundred bars. We match the isotherm obtained with the analytical, clear Guillot (2010) model to the isotherm of previously published atmosphere models, which are based on a more complex solution of radiative transfer and treatment of opacities. Generally, with higher metallicities, the γ value shifts to smaller values as the deep isotherm becomes hotter.

in different isothermal regions. For example, for HD 189733b with $T_{\text{eq}} = 1170$ K, we fit to four different published profiles and get $\gamma = 0.14$ – 0.19 . In Table A1, we present the observational data and publications of the planets used for the fits. The equilibrium temperature of each planet is either given in publications or we calculate $T_{\text{eq}} = (1 - A)^{1/4} \cdot T_{\text{eq},0}$ with $T_{\text{eq},0}$ as the given zero-albedo equilibrium temperature, and given or estimated albedo $A \approx [0-0.1]$, or via the definition of the irradiation temperature: The equilibrium temperature is defined as $T_{\text{eq}} = ((1 - A) \cdot f)^{1/4} \cdot T_{\text{irr}}$, where the irradiation temperature is $T_{\text{irr}} = T_* \cdot (R_*/a)^{1/2}$. Here, we set $f = 1/4$ as the heat redistribution factor. Other parameters are albedo A , T_* and R_* , are the stellar effective temperature and stellar radius, respectively, and a is the spatial separation between star and planet. Additionally, we plot planets with higher metallicity or higher albedo in Fig. 2, see Table A2.

Our resulting fit formula differs from the proposed γ -relation by Guillot (2010), and from the results by Jin et al. (2014). Guillot (2010) set $\kappa_L = 10^{-2} \text{ cm}^2 \text{ g}^{-1}$ and $\kappa_S = 6 \times 10^{-3} \sqrt{(T_{\text{irr}}/2000 \text{ K})} \text{ cm}^2 \text{ g}^{-1}$, specifically adapting these values for HD 209458b.

We expect the fit, equation (1), to be a useful tool when using the Guillot (2010) or Heng et al. (2012) models.

2.1.2 Cloud parameter for the semi-analytical Heng model

Heng et al. (2012) use a parametrized depiction of a purely absorbing cloud deck where the long-wave opacity κ_L is modified by an additional cloud deck opacity κ_c . A cloud deck can be added through an additional contribution to the longwave opacity κ_L :

$$\kappa_L(P) = \kappa_{L,0}(P) + \kappa_c(P). \quad (2)$$

For the cloud-free Guillot model, it is $\kappa_L = \kappa_{L,0}$. For both planets, we use $\kappa_{L,0} = 10^{-2} \text{ cm}^2 \text{ g}^{-1}$ which we found to be an appropriate mean Rosseland mean opacity in Poser et al. (2019). The advantage of the Heng model lies in its simplicity of formulation and the reduced number of free parameters. It only allows for the case of a purely absorbing cloud deck without scattering, so that the resulting cloud

decks have a warming effect (for $\gamma < 1$) – which serves as an upper limit of the influence on the radius evolution.

The cloud opacity takes on a Gaussian form, describing a non-uniform cloud deck:

$$\kappa_c(P) = \kappa_{c,0} \cdot \exp \left[-\Delta_c \left(1 - \frac{P}{P_c} \right)^2 \right]. \quad (3)$$

The cloud deck thickness Δ_c , the cloud deck position P_c , and the cloud opacity normalization $\kappa_{c,0}$ account now for an additional opacity in the longwave. A thinner cloud deck corresponds to a larger value of Δ_c .

Please note that equation (3) can easily be extended to several cloud decks (by adding up each deck’s κ_c), as one expects several cloud decks to be present in an atmosphere, e.g. in Jupiter, Uranus, and Neptune (e.g. West 2017; Bjoraker et al. 2018; Bhattacharya et al. 2023; Wong et al. 2023). However, we decided to use only one cloud deck to minimize the amount of free parameters.

In the following paragraphs, we describe how we choose the free parameter of equation (3).

Cloud deck location P_c

For the purpose of this work, we implicitly assume that clouds are formed by equilibrium processes and that we can comment on potential cloud layers by comparing the clear P - T profiles to condensation curves of possible cloud-forming species (e.g. Mbarek & Kempton 2016; Ohno & Okuzumi 2018). In this work, the intersection between the clear atmospheric profile and the respective condensation curve (e.g. MgSiO_3) yields the cloud deck pressure P_c . However, the cloud formation process is much more complex and dynamic, as assumed in this work, see Helling (2019, 2021) for reviews. For our work, we need to deduce cloud parameters from studies that include advanced condensation chemistry. Helling et al. (2021) compare cloud properties for hot to ultrahot gas giants. For the coolest planet in their sample, WASP-43b with $T_{\text{eq}} = 1400$ K, they find metal oxides (e.g. SiO , MgO), high-temperature condensates (e.g. iron Fe) and silicates (e.g. enstatite MgSiO_3 and forsterite Mg_2SiO_4) to be possible condensates, looking at gas pressures $P < 10^2$ bar. However, input to their models are 3D P - T structures obtained by

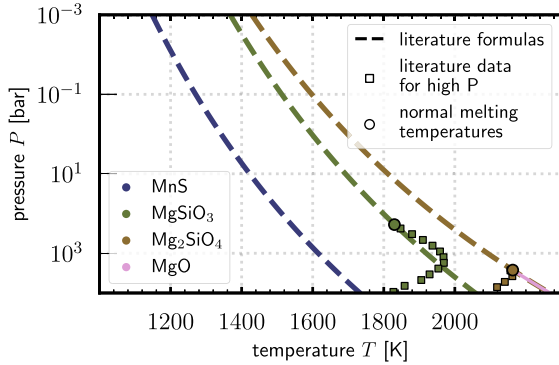


Figure 3. Fits to condensation curves of manganese sulfide (MnS), enstatite (MgSiO_3), and forsterite (Mg_2SiO_4) as used in this work based on previously published formulas of Visscher et al. (2006) and Visscher et al. (2010) (dashed) for solar metallicity $[\text{M}/\text{H}] = 0$. Additionally, we show the values from Visscher et al. (2010) at high pressures (squares) for Mg_2SiO_4 and MgSiO_3 as well as their melting temperatures (circles). Their condensation temperatures are depressed for high pressures which is not captured by the fits (dashed).

global circulation models (GCMs) with a specific (and constant) T_{int} value. Our work assumes a deep isotherm extending to a few kbar for low T_{int} values for evolved planets which may change pressure range considered for condensation to occur. For our calculations here, we continue by using the condensation curves of MgSiO_3 for WASP-10b and TOI-1268b, when we calculate the intersection *dynamically*, see Section 2.3.

Here, we aim at modelling the effect of a (one) possible cloud deck in the deep atmosphere within the coupled thermal evolution calculations. The cloud deck location is the intersection of the pre-calculated clear P - T profile with a condensation curve. We use the previously published P - T relations for condensation curves by Visscher, Lodders & Fegley (2006, 2010) that are also dependent on the metallicity $[\text{M}/\text{H}]$. We show their models for $[\text{M}/\text{H}] = 0$ ($1 \times$ solar metallicity) in dashed in Fig. 3. Furthermore, for Mg_2SiO_4 and MgSiO_3 , we plot the normal melting temperatures (circled) and the condensation curves for higher pressures (squared) as published by Visscher et al. (2010). Both Mg_2SiO_4 and MgSiO_3 are reduced at higher pressures because SiO gets replaced by SiH_4 (Visscher et al. 2010). This behaviour is not included in our fit. Furthermore, MgO condenses at $P > 10^{3.5}$ bar (Visscher et al. 2010) which in turn is represented by our fit for Mg_2SiO_4 for $P > 10^{3.5}$ bar. In support of this, Helling et al. (2021) study cloud properties for a range of gas giants, e.g. suggesting that metal oxides (SiO, MgO) become more common than silicates (Mg_2SiO_4 , MgSiO_3) at higher pressures.

Cloud deck opacity and thickness

To account for the remaining parameters, the cloud deck opacity $\kappa_{c,0}$ and the cloud deck thickness Δ_c , we compare our model with the P - T structure solutions with clouds from Linder et al. (2019), in particular the ones simulated with PETITCODE (Mollière et al. 2015; Baudino et al. 2017; Mollière et al. 2017), and with the cloud opacities of Helling & Casewell (2014), Lee et al. (2017), and Dobbs-Dixon & Agol (2013).

In this study, we use $\kappa_{c,0} = 0.05$ – $1.0 \text{ cm}^2 \text{ g}^{-1}$ and a cloud deck thickness of $\Delta_c = [10, 25, 50, 75, 100]$ which we base on the comparison with the results in the papers mentioned above. Following equation (2), the opacity at cloud level is characterized by

Clouds and the radius evolution of giant planets 2245

a Rosseland mean opacity. Please note that – depending on the cloud location – a Planck mean opacity might be a better approximation, as the Rosseland mean opacity is better suited for regions, as it is the deep atmosphere because it weighs more for wavelengths that contribute a low opacity (Freedman et al. 2014; MacKenzie et al. 2023).

Atmospheric pressure–temperature gradients

Kurosaki & Ikoma (2017) study the effect of low-temperature condensation clouds on the radius evolution using the pseudo-moist adiabatic temperature gradient for the troposphere. Motivated by our previous study and Kurosaki & Ikoma (2017), we introduce a modification of the local atmospheric gradient, so that it does not exceed the adiabatic gradient of the dry (clear) atmosphere:

$$\nabla_{\text{local}} \leq \nabla_{\text{ad,dry}}. \quad (4)$$

Fig. 4 (left) depicts the implications for the P - T profile. Fig. 4 (right) shows both the superadiabatic/non-modified (dashed) and the modified gradient (solid) over the same pressure range. Here, for two T_{int} values, we show the clear profile (dotted) and two cloudy profiles with superadiabatic (dashed) and the modified gradient (solid).

First, the warming effect of the cloud deck with the modified gradient is reduced compared to the unmodified gradient. Furthermore, the P - T profiles with the modified gradient result in a cooler adiabat than for the clear case (for a constant T_{int} of the atmosphere model), and the upper atmosphere is not influenced. This is opposite to Kurosaki & Ikoma (2017), where the inclusion of condensation shifts the P - T profile to lower temperatures for evolving times/cooling of the planet.

Further, Kurosaki & Ikoma (2017) connect the atmosphere to the interior at a fixed pressure P_{ad} where the (convective) interior starts. In this work, the RCB is calculated by equation (5), comparing adiabatic and local gradients of the P - T profile of the atmosphere. This yields an individual pair of $(T_{\text{ad}}, P_{\text{ad}})$ for different P - T conditions. In Fig. 4, we plot the RCB as circles. The different P - T profiles lead to different $(T_{\text{ad}}, P_{\text{ad}})$ values for the RCB.

Despite the differences, we continue with our modification of the atmospheric model description as we expect the reradiated energy (due to latent heat release) does *not* directly influence the adiabat of the interior but the overall (enhanced) emission is then mirrored by the colder adiabat for a given T_{int} value.

2.2 Interior and thermal evolution model

The interior model is composed of three discrete layers (atmosphere, envelope, and core), see Fig. 1. While the atmosphere and the envelope differ in the assumed energy transport, the mass fractions of hydrogen X , helium Y , and metals Z are the same in atmosphere and envelope ($X + Y + Z = 1$). The helium/hydrogen mass fraction abundance for all models is $Y := M_{\text{H}}/(M_{\text{H}} + M_{\text{He}}) = 0.27$ (Bahcall, Pinsonneault & Wasserburg 1995).

The transition from the radiative atmosphere to the convective interior is determined by the adiabatic and local numeric temperature gradients:

$$\nabla_{\text{local}} \geq \nabla_{\text{ad}}, \quad (5)$$

where $\nabla_{\text{ad}} = \left(\frac{\partial \ln T}{\partial \ln P} \right)_s$ is taken from the EoS tables. The RCB is then defined by $(T_{\text{ad}}, P_{\text{ad}})$ characterizing the entropy s of the interior adiabat. To account for the thermal evolution of the planet, we assume:

$$L_{\text{eff}} - L_{\text{eq}} = L_{\text{int}} = L_{\text{secular}} + L_{\text{radio}}. \quad (6)$$

The luminosity L_{eff} describes the effective luminosity reradiated over the entire surface of the planet. $L_{\text{eq}} = 4\pi R_p^2 \sigma_B T_{\text{eq}}^4$ is the

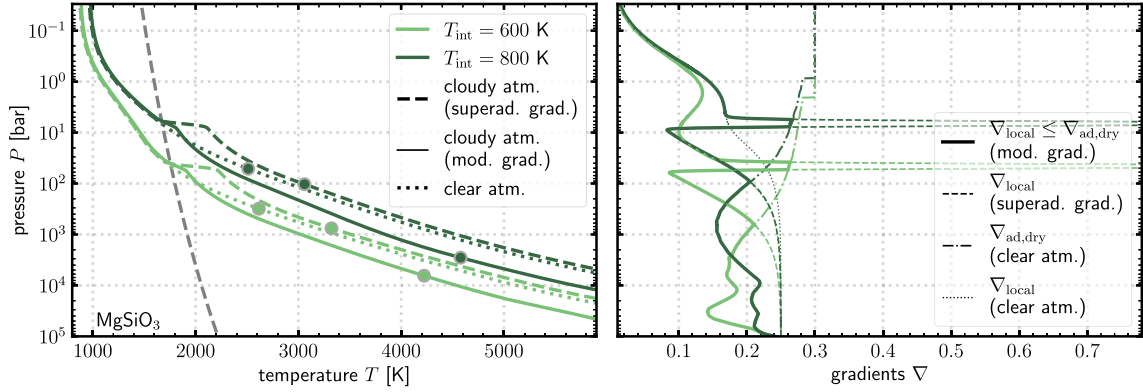
2246 *A. J. Poser and R. Redmer*

Figure 4. Left: Pressure–temperature profiles of the atmosphere for two intrinsic temperatures $T_{\text{int}} = 600, 800$ K (colour-coded) for a warm Jupiter. The clear P – T profile is shown (dotted), as well as the cloudy atmosphere profile Heng et al. (2012) (dashed), and the cloudy P – T profile with modified *adiabatic* gradient (solid). Transitions to the interior are marked by a dot. The cloud base P_c is chosen by the intersection with the condensation curve of MgSiO_3 . Right: The local gradient of the cloudy atmosphere (dashed), the adiabatic gradient of the clear atmosphere (dashed dotted), and the modified gradient of the cloudy atmosphere (solid) are shown.

absorbed and re-emitted stellar flux. The interior heat loss has different contributions:

$$L_{\text{secular}} = - \int_0^{M_p} dm T(m, t) \frac{ds(m, t)}{dt} \quad (7)$$

accounts for cooling and contraction of the planet, and the radiogenic heating is denoted as L_{radio} . For further information on the evolution and interior calculations, see Poser et al. (2019).

Several other works have shown that the thermal evolution of a planet is influenced by the choice of the equation of state (EoS) for hydrogen, helium, and metals (e.g. Vazan et al. 2013; Miguel, Guillot & Fayon 2016). We compare the influence of hydrogen and helium EoS by Chabrier & Debras (2021) (CD21) and Saumon, Chabrier & van Horn (1995) (SCvH95) on the clear radius evolution and the static T_{int} – Z_{env} phase space in Section 3.2. For the cloudy radius evolution, we use the newer H/He – EoS by CD21 (Section 3.4). Note that the SCvH95 – EoS is based on a chemical model, while that of CD21 includes ab initio data in particular for the warm dense matter region. The metals of the envelope (Z_{env}) are represented as ice, while the core is made of rocks (both EoS from Hubbard & Marley (1989)).

Other model assumptions that may influence the heat transport and consequently the thermal evolution of the planet are the possibility of thermal boundary layers (e.g. Nettelmann et al. 2016; Scheibe, Nettelmann & Redmer 2019; Bailey & Stevenson 2021; Scheibe, Nettelmann & Redmer 2021), inefficient convection due to compositional gradients causing double-diffusive or layered convection (e.g. Stevenson 1985; Leconte & Chabrier 2012, 2013), or non-adiabatic interiors (Debras & Chabrier 2019; Debras, Chabrier & Stevenson 2021).

2.3 Variable cloud deck location during the long-term evolution

In this work, we want to investigate the effect of the cloud deck location during the planets’ thermal evolution with two approaches. The first uses a *fixed* cloud deck location for all P – T profiles for the various T_{int} values during the evolution of the planet. The second, which we denote further as *dynamic* or *subsiding* P_c , uses the intersection between the pre-calculated clear profile (for each T_{int} value) and the respective condensation curve. With that approach,

the effect of cloud decks deep in the atmosphere at several hundred bar can be modelled at low T_{int} values (as for an old or already cooled down planet).

We show the effects of both approaches on the P – T profiles in Fig. 5, using WASP-10b as an example. Starting on the left, Fig. 5(a) shows clear, non-cloudy, P – T profiles for $T_{\text{int}} = 300$ – 1000 K. They intersect the condensation curves of MnS , MgSiO_3 , and Mg_2SiO_4 at high pressures ($P > 1$ bar). Then, we show the P – T profiles obtained with a fixed cloud deck pressure $P_c = 0.3$ bar in subfigure (b). The very right subfigures (c) and (d) show the results obtained with the *dynamic* approach where P_c is subsiding with the evolving age of the planet. With that, we mimic an atmosphere variable in time – not only in T_{int} , but also in the total cloud opacity $\kappa_c(P, P_c)$, see equation (3).

Specifically, for WASP-10b and TOI-1268b, we take the intersections with MgSiO_3 when we calculate the intersection *dynamically*. Else, for the *fixed* case, where the cloud base pressure P_c is constant throughout the thermal evolution, we choose $P_c = 1, 10$ bar for TOI-1268b and $P_c = 0.3$ bar for WASP-10b.

2.4 Overview of the model procedure

In this section, we give an overview of our method. The key components are as follows:

(i) *Interior structure.* We construct the planetary profile along the mass coordinate m – mass m , radius r , temperature T , pressure P , density ρ , and entropy s – from $m = 0$ to $m = M_p$. This model matches the given (observationally derived) planetary mass M_p and radius R_p . Assuming a bulk composition of hydrogen, helium, and metals with a fixed H/He ratio and a specified metal mass fraction for the atmosphere Z_{atm} and envelope Z_{env} , our model iteratively determines the core mass M_{core} to obtain M_p :

$$M_p = M_{\text{atm}} + M_{\text{env}} + M_{\text{core}}, \quad (8)$$

where M_{atm} and M_{env} are the total mass of the atmosphere and envelope of the three-layer model.

Static T_{int} – Z_{env} phase space. The intrinsic temperature T_{int} of the planet is a crucial input, dictating the internal heat. A higher T_{int}

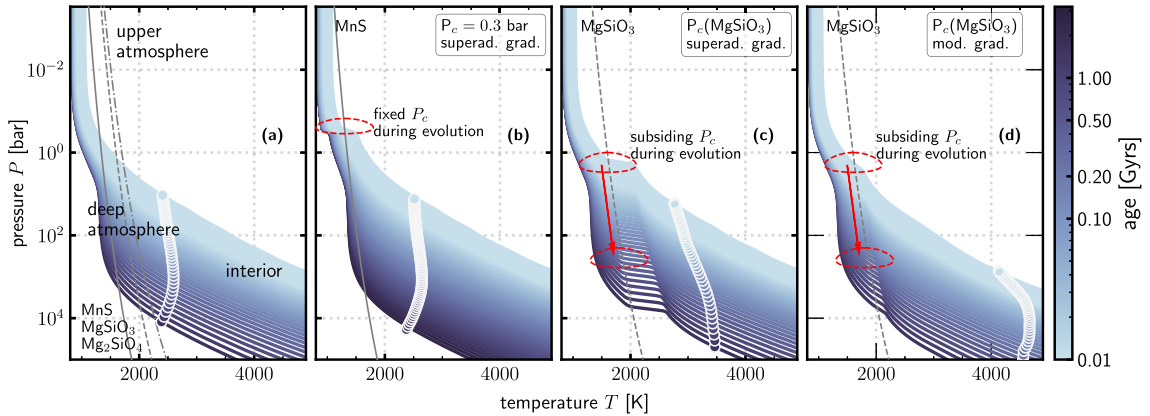


Figure 5. Pressure–temperature profiles of the atmosphere for WASP-10b under clear (a) and cloudy (b–d) conditions for $T_{\text{int}} = 200\text{--}1100$ K. The condensation curves ($M/H = 0$) of different cloud-forming species (grey) cross the entire atmosphere during the T_{int} evolution. The RCB (dot) connects the atmosphere to the interior. The clear P – T atmosphere model (a) serves as a starting point for the cloud deck location of the cloudy atmosphere models. The three right subfigures show the resulting P – T conditions during evolution with a fixed cloud deck location ($P_c = 0.3$ bar) (b), and a *dynamic* cloud deck with subsiding P_c (c, d). Parameters are $\kappa_{c,0} = 0.1 \text{ cm}^2 \text{ g}^{-1}$, $\Delta_c = 75$. The profiles are coloured based on the age of the planet, determined through thermal evolution calculations. The corresponding radius evolution curves are shown in the second row of Fig. 9.

results in a lower envelope density and thus variations in $M_{Z, \text{env}}$ for a given Z_{env} , affecting the core mass M_{core} to align with the given planetary mass. For $Z_{\text{env}} = Z_{\text{atm}}$, it is for the total planetary metallicity Z_P with the total mass of the metals M_Z :

$$Z_P = M_Z/M_P = Z_{\text{env}} (M_{\text{atm}} + M_{\text{env}})/M_P + M_{\text{core}}/M_P \quad (9)$$

The $T_{\text{int}}\text{--}Z_{\text{env}}\text{--}Z_P$ phase space is explored in Section 3.2 to understand the relationship between these parameters. Higher T_{int} values typically lead to higher values of Z_P due to an increasing core mass, as depicted in Fig. 6. Here, the x -axis label, *present intrinsic temperature* T_{int} , is intended to illustrate that the models displayed are possible solutions that yield the observed M_P and R_P (but not necessarily the age constraint). In order to make Fig. 6, we calculate for $Z_{\text{env}} = 0\text{--}0.52$ (in intervals of 0.01) for $T_{\text{int}} = 0\text{--}1000$ K (in intervals 10 or 50 K) single interior structure models. That makes for each bulge $\approx 1000\text{--}5000$ models. We do not employ any Bayesian or Markov chain Monte Carlo (MCMC) methods in our algorithm, as it has not been specifically designed to accommodate such techniques at this time. We refer to this as *static*, indicating that the phase space illustrates the influence of the model assumptions and does not consider the thermal evolution of the planet but instead represents the parameter space.

(ii) *Radius evolution.* By considering the age of the planetary system, we set tighter constraints on the metal content of the planet. First, for a fixed set of M_P , M_{core} , Z_{env} , we calculate interior models for $\approx 60\text{--}80$ T_{int} values in the range of 100–1000 K. Here, the free parameter is the radius of the planet R_P : the higher T_{int} , the larger R_P . Applying equation (7) allows us to calculate the evolution of the radius of the planet, $R_P(t)$. The results are shown in Sections 3.3 and 3.4.

3 RESULTS

We introduce the planets for this study in Section 3.1. We then continue to present the results for the static $T_{\text{int}}\text{--}Z_{\text{env}}$ phase space in Section 3.2. From a modelling perspective, the $T_{\text{int}}\text{--}Z_{\text{env}}$ phase space contains information on the metal content of the planet. We present the impact of the observational uncertainties in mass and

radius on the $T_{\text{int}}\text{--}Z_{\text{env}}$ phase space, the impact of the H/He-EoS (SCvH95 versus CD21), and finally, the impact when including the cloud models. While our main focus lies in understanding the impact of clouds on the radius evolution, the radius evolution with a clear atmosphere (no clouds) serves as anchor point for the comparison. Subsequently, in Section 3.3, we present the clear radius evolution for both planets. The key results, the effects of various cloud models on the radius evolution, are presented in Section 3.4.

3.1 Choice of planets

We consider two planets similar in their young age and equilibrium temperature, but with different densities and masses. The first one, TOI-1268b (Dong et al. 2022; Šubjak et al. 2022), has a similar mass as the hot Saturn WASP-39b, but a higher density of $\rho = 0.53 \rho_{\text{Jup}}$ due to its smaller radius compared to WASP-39b’s density of $\rho = 0.14 \rho_{\text{Jup}}$ (Faedi et al. 2011). With an age of 110–1000 Myr, it falls within a group of young (< 1 Gyr) gas giants with measured masses and radii, making the planet a candidate for testing evolution and formation theories. TOI-1268b resides at the inflation threshold (Sarkis et al. 2021) and is probably not inflated. The second planet, WASP-10b, is characterized by an age of 190–350 Myr (Christian et al. 2009; Johnson et al. 2009; Maciejewski et al. 2011a), a mass of $2.96 M_{\text{Jup}}$, and a planetary radius of $1.02 R_{\text{Jup}}$ (Maciejewski et al. 2011b). We extend our studies of WASP-10b in Poser et al. (2019) to this paper. The observational parameters used in this work are listed in Table 1.

We have chosen the planets for different reasons: First, they reside at the inflation limit. This allows us to reduce a possible additional uncertainty due to the amount of extra energy needed to explain the inflated radius (Thorngren & Fortney 2018; Sarkis et al. 2021). Second, it is more probable that clouds occur at lower T_{eq} (e.g. Fortney et al. 2020). However, the planets differ in mass and overall density, comparing possible arising uncertainties for both a warm Saturn (TOI-1268b) and a warm Jupiter (WASP-10b). Furthermore, the investigation of explicit young planets contributes to understanding formation and (early) evolution processes.

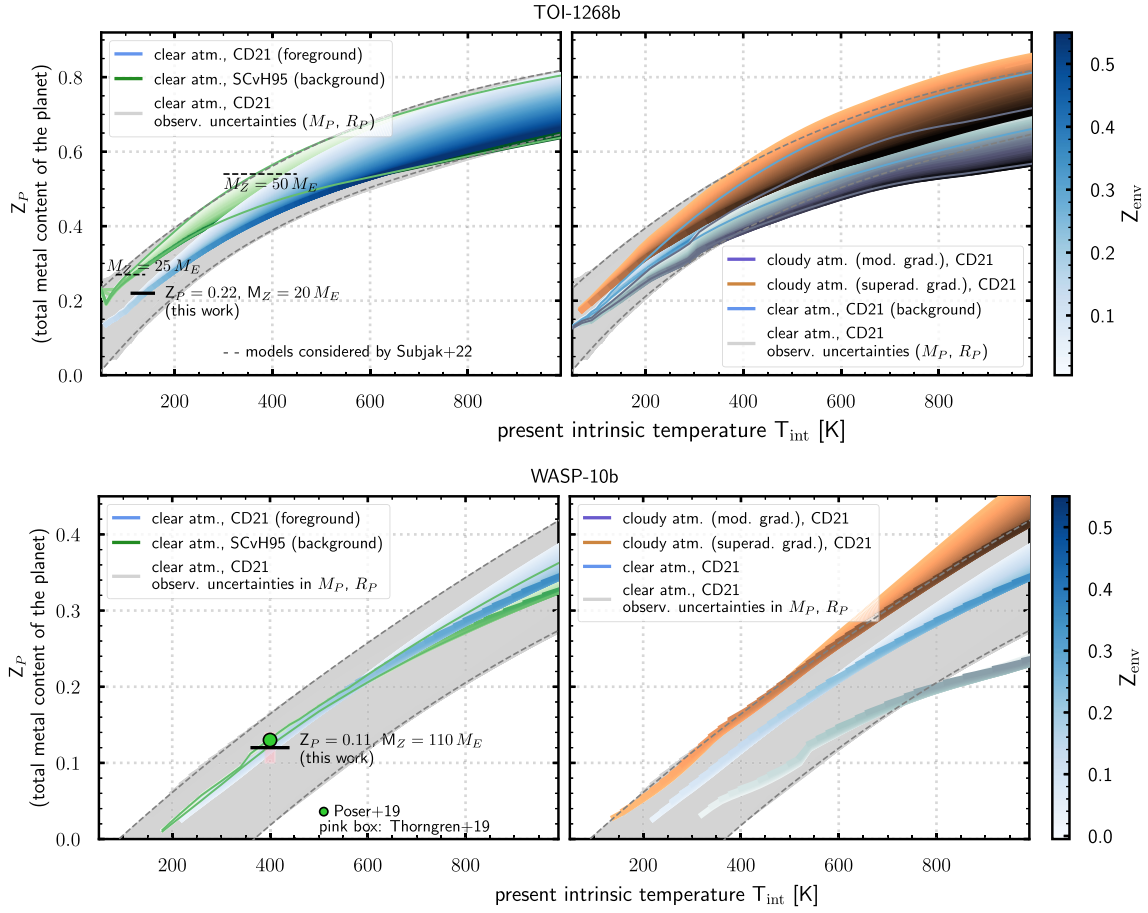
2248 *A. J. Poser and R. Redmer*

Figure 6. Phase space ($T_{\text{int}}-Z_P-Z_{\text{env}}$) of our interior model setup for TOI-1268b and WASP-10b, highlighting the influence of uncertainties in mass and radius, EoS and atmosphere model. The higher the present T_{int} , the more metals can (theoretically) be included in the envelope (with higher Z_{env} values possible), and subsequently a higher Z_P may arise. The same degree of colour shade is used in the upper and lower panels (lighter shade: lower Z_{env} , darker shade: higher Z_{env}). The vertical black lines show Z_P values obtained by other works: for TOI-1268b, the black dashed line indicates the Z_P values considered by Šubjak et al. (2022), whereas the solid lines indicate the derived Z_P value from this work. The contour lines of models in the background are shown for visualization. Additionally, the grey area, contoured by grey dashed lines, indicates the resulting model space when taking the observational uncertainties in M_P and R_P into account (shown for CD21 EoS and a clear atmosphere model).

3.2 Static $T_{\text{int}}-Z_{\text{env}}$ phase spaces

3.2.1 General description of the $T_{\text{int}}-Z_{\text{env}}$ phase space and approach

We here show the static $T_{\text{int}}-Z_{\text{env}}$ phase space, spanning the ($T_{\text{int}}-Z_P-Z_{\text{env}}$)-plane. We want to see how the space changes when applying different model atmospheres, comparing to the reference clear atmosphere case. We compare the effects to the observational uncertainties and the impact of different H/He-EoS.

The first step towards the static interior modelling is to find the γ value of a clear atmosphere using the fit-formula, see equation (1). We find $\gamma = 0.152$ for TOI-1268b ($T_{\text{eq}}(T_*, R_*, a) = 913$ K) and $\gamma = 0.167$ for WASP-10b ($T_{\text{eq}}(T_*, R_*, a) = 960$ K). Interestingly, we find that in the case of WASP-10b, our parameter choice results in the same $P-T$ structure as in Poser et al. (2019), fitted to a known $P-T$ structure. We conclude that the fit formula gives a good first-order estimate of the $P-T$ structure for irradiated planets with an

unknown $P-T$ structure. Continuing our previous work on WASP-10b and WASP-39b, we set $\kappa_{L,0} = 0.01 \text{ cm}^2 \text{ g}^{-1}$ (equivalent to κ_L for the clear model).

In the second step, we model the $T_{\text{int}}-Z_{\text{env}}$ phase space: The combination of a given planetary mass and radius leads to an inferred heavy element mass Z_P . Without the age constraint of the system, the parameter space of possible solutions can be large, as shown in Fig. 6. The parameter space is a function of the atmosphere and interior model setup, and input parameter, e.g. the EoS and distribution of the heavy elements (fully mixed planet versus all metals in the core). A possible constraint for the envelope metallicity Z_{env} can be given by the derived atmospheric metallicity (e.g. Wakeford et al. 2017; Poser et al. 2019; Müller & Helled 2023a).

In Fig. 6, we show the relation of the total heavy element content Z_P , the metal distribution (displayed as Z_{env}), and the internal heat flux, represented by the intrinsic temperature T_{int} for TOI-1268b (upper row) and WASP-10b (lower row). For both planets, the influence of different H/He EoS and the influence of observational

Table 1. Stellar and planetary parameters.

	TOI-1268b ¹	WASP-10b
Planetary parameter		
$M_p [M_{\text{Jup}}]$	0.29 ± 0.04	$2.96^{+0.222}_{-0.17}$
$R_p [R_{\text{Jup}}]$	0.82 ± 0.06	$1.03^{+0.0775}_{-0.03}$
$T_{\text{eq,A}=0} [\text{K}]$	919	950^{+30}_{-26}
$\rho [\rho_{\text{Jup}}]$	0.53	1.43
Orbital parameter		
e	$0.09^{+0.04}_{-0.03}$	0.013 ± 0.063^4
$a [\text{AU}]$	0.072 ± 0.01	$0.0369^{+0.0012}_{-0.0014}$
$P [\text{d}]$	8.15	3.09
Stellar parameter		
$M_* [M_{\odot}]$	0.96 ± 0.04	0.75^3
$R_* [R_{\odot}]$	0.92 ± 0.06	0.67^5
$T_* [\text{K}]$	5300 ± 100	4675 ± 100^2
age $\tau_* [\text{Myr}]$	110-1000	270 ± 80^4

References. ¹Subjak et al. (2022), ²Christian et al. (2009), ³Johnson et al. (2009), ⁴Maciejewski et al. (2011a), ⁵Maciejewski et al. (2011b).

uncertainty are shown in the first column, the possible degeneracy due to the chosen atmospheric model is shown in the second column.

In general, with hotter interiors (higher T_{int}), the more heavy elements can be included in the planet. The uppermost line of each bulge in each subfigure highlights the case in which all metals are in the core ($Z_{\text{env}} = 0$). For a fully mixed planet ($M_{\text{core}} = 0$), the maximum Z_{env} is then the lower limit of the $T_{\text{int}}-Z_{\text{env}}$ phase space bulge: For a given T_{int} , the total metal content of the planet is higher if all metals reside in the core than in the envelope (due to different EoS for the metals in the core and envelope).

The matching T_{int} value for the observed mass, radius, and age has to be determined with calculations of the thermal evolution, see Section 3.3.

3.2.2 Impact of the observational uncertainties in planetary mass and radius

The left subfigures show the $T_{\text{int}}-Z_{\text{env}}$ phase space with a clear, non-cloudy atmospheric model. The blue-shaded bulge in the foreground shows the $T_{\text{int}}-Z_{\text{env}}$ phase space with the CD21 EoS for H/He. The uni-colour grey area depicts the uncertainty in observational mass and radius, displayed for the model setup using the CD21 EoS for H/He. It is the combination of M_p and R_p resulting in the largest and smallest density within the observational uncertainty (e.g. for the most dense combination of WASP-10b: $M_p = 3.18 M_{\text{Jup}}$, $R_p = 1.00 R_{\text{Jup}}$). The most probable value for Z_p lies then in between the grey dashed boundaries. A statistical analysis is left for future work. We point out that Müller, Ben-Yami & Helled (2020) investigated the influence of observational uncertainties on the modelling process.

Generally, the $T_{\text{int}}-Z_{\text{env}}$ phase space for WASP-10b is narrower than the one for TOI-1268b due to the different bulk densities. For TOI-1268b, it is possible to include up to $Z_p = 0.8$ for high intrinsic temperatures ($T_{\text{int}} = 1000 \text{ K}$). For the same intrinsic temperature, WASP-10b may include only up to $Z_p = 0.4$.

3.2.3 Impact of the H/He EoS

The green bulges in the background show the results using SCvH95 EoS – instead of the newer CD21 – for H/He. For TOI-1268b, for a

given $T_{\text{int}} < 600 \text{ K}$, we can include more metals in the planets using SCvH95 EoS instead of CD21 EoS. The newer CD21 EoS leads to denser planets than SCvH95, so that we need a smaller core mass to match M_p , leading to a smaller Z_p . For $T_{\text{int}} > 600 \text{ K}$, using CD21 leads to slightly higher metallicities than using SCvH95. For WASP-10b, we see a similar behaviour with a turning point at $T_{\text{int}} \approx 550 \text{ K}$. For $T_{\text{int}} < 550 \text{ K}$, the difference between CD21 and SCvH95 is not as large as for TOI-1268b and increases for higher T_{int} .

A comparison between SCvH95, CD21, and the EoS published by Chabrier, Mazevet & Soubiran (2019) (CMS19) for H/He has been investigated for the evolution tracks of brown dwarfs by Chabrier et al. (2023). As they point out, the new CD21 EoS leads to cooler isentropes in the convective interiors than SCvH95 and CMS19. We can see this behaviour as well when we can include more metals (for $T_{\text{int}} < 600 \text{ K}$), see also Section 3.3 for a comparison in the radius evolution.

3.2.4 Impact of the atmosphere model including clouds

The right subfigures show the $T_{\text{int}}-Z_{\text{env}}$ phase space using cloudy atmosphere models instead of a clear model. For both planets, we depict the model space for two different sets of cloud models. For TOI-1268b, we use $\kappa_{\text{c},0} = 0.1 \text{ cm}^2 \text{ g}^{-1}$ and $\Delta_c = 10$, and as cloud base P_c the intersection with the condensation curve of MgSiO_3 which may differ for each T_{int} value. For WASP-10b, we use $\kappa_{\text{c},0} = 0.2 \text{ cm}^2 \text{ g}^{-1}$ and $\Delta_c = 10$, and the same $P_c(\text{MgSiO}_3)$. In both subfigures, the orange model space uses the non-modified (superadiabatic) cloud gradient, while the grey-lilac model space employs the modified gradient for the ($P-T$) profile of the atmosphere.

Including a purely absorbing cloud layer in the atmosphere alters the phase space. Inserting the cloud deck with superadiabatic cloud gradient allows for a higher metal content (higher Z_p) in the envelope compared to the clear case (as shown in Poser et al. (2019)). We can see that as the orange bulge shifts to higher metallicities. This is because the change of the atmosphere model with the non-modified gradient shifts the interior model towards higher entropies which leads to a higher Z_p . The case of the cloud deck with modified gradient (grey-lilac model space), conversely, restricts the amount of metals within the planet's interior as the atmosphere model leads to lower entropies compared to the clear atmosphere model.

This behaviour is mainly determined by the RCB. The location of the RCB plays an important role for the $T_{\text{int}}-Z_{\text{env}}$ phase space, see also Thorngren et al. (2019). In our model, it is self-consistently determined by the adiabatic and local gradients in the atmosphere. Compared to the clear model, the cloudy atmosphere model with the modified gradient shifts the RCB to lower pressures and temperatures. As a result, the entropy is shifted to lower values, leading to a colder interior.

For TOI-1268b, the impact of the two cloud models chosen here, is of about 10 percent in Z_p . For example, for $T_{\text{int}} = 200 \text{ K}$, we obtain a span of the total heavy element content of $Z_p = 0.25-0.35$ between both cloud models.

For the higher density WASP-10b, the narrower form of the clear atmosphere $T_{\text{int}}-Z_{\text{env}}$ phase space is mirrored for the cloudy atmosphere. Compared to TOI-1268b, the differences of the cloudy atmosphere spaces to the clear case are larger due to a larger grey cloud opacity and lie in the range of the observational uncertainties.

One can see a bend of the cloudy atmosphere model with modified gradient (grey-lila bulge) at $T_{\text{int}} \approx 500 \text{ K}$. This may be due to the calculation of the RCB and the ensuing adiabat. When calculating the RCB, the atmospheric local gradient is compared with the adiabatic

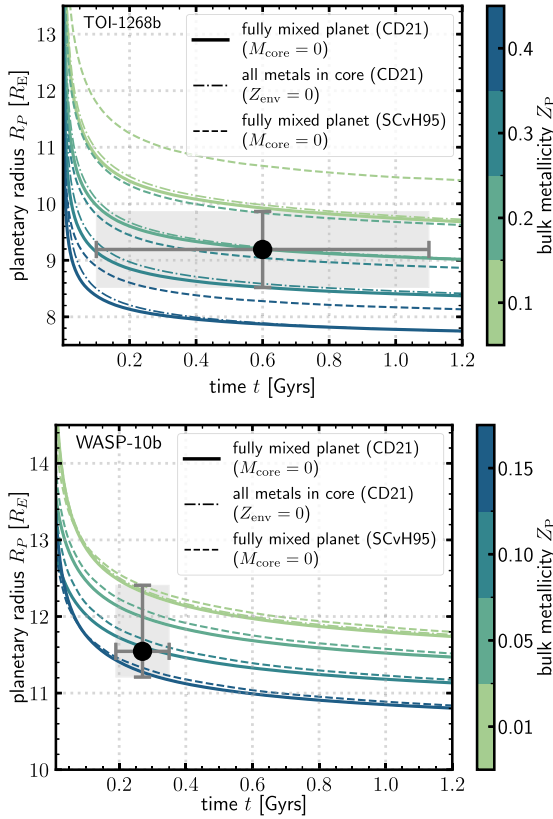
2250 *A. J. Poser and R. Redmer*

Figure 7. Radius evolution curves for TOI-1268b and WASP-10b with a clear atmosphere. The grey box represents the uncertainty in measured radius and age. For TOI-1268b, we compare the H/He EoS of CD21 (solid) and SCvH95 (dashed) on the radius evolution. Additionally, evolution curves for different total Z_p in the planet (different colours) are shown, as well as the influence of the metal distribution inside the planet: The planet cools faster for a fully mixed (solid) versus all metals in the core (dash-dotted). For WASP-10b, the difference between a fully mixed planet versus all metals in the core is smaller than for TOI-1268b. Here, a slight difference is noticeable only for $Z_p = 0.01$.

gradient which we get from the EoS tables. As soon as the local gradient becomes larger than the adiabatic, we set the RCB, see equation (5) and Fig. 4. For smaller T_{int} values, we see that the intersection shifts to higher temperatures, so that we have a bend in the RCB in the P - T space, similar to that seen in Fig. 5(d) where the RCB (white circled dots) is in the range of 4000–5000 K.

3.3 Clear radius evolution

In Fig. 7, we plot several possible evolution curves for TOI-1268b and WASP-10b. For both planets, we show the influence of the H/He EoS, and in the case of TOI-1268b, we additionally show the effect of the metal distribution.

For TOI-1268b, the difference in H/He EoS of CD21 (solid) and SCvH95 (dashed) is up to $1 R_E$. It mirrors the results from the static $T_{\text{int}}-Z_{\text{env}}$ phase space, where a difference between the EoS is apparent. The larger Z_p , the smaller the difference between both EoS, as the amount of H/He decreases. Müller et al. (2020) showed the same systematic for the use of CMS19 and SCvH95 EoS.

To derive the metallicity of the planets, Šubjak et al. (2022) compares its planetary mass and radius with the isochrones calculated from the evolution curves of Fortney et al. (2007), finding a total heavy element mass of $M_Z = 50 M_E$ to be a good fit. We modelled the thermal evolution within our model setup and found, in contrast to Šubjak et al. (2022), a heavy element content of about $\approx 15 - 25 M_E$ ($Z_p \approx 0.1 - 0.3$) that matches the observed mass, radius, and age, see Fig. 7 for TOI-1268b. The best match is for $Z_p = 0.22$ ($M_Z = 20 M_E$). This would correspond to the present intrinsic temperatures ≈ 160 K. The heavy element content would be similar to the expected amount of heavy elements in the cold Solar System analogue Saturn (e.g. Helled 2019). We assume the difference of our findings and those of Šubjak et al. (2022) primarily stems from the H/He EoS by Fortney et al. (2007) (SCvH95).

In contrast to TOI-1268b, for the heavier WASP-10b, the difference between both EoS for the radius evolution is more subtle and the derived metal content would not change much. For WASP-10b, we find a heavy element content of $M_Z \approx 0-130 M_E$ ($Z_p \approx 0-0.15$) which is consistent with the findings of others, for example Thorngren & Fortney (2019). Looking at the static $T_{\text{int}}-Z_{\text{env}}$ phase space for WASP-10b, the green point in Fig. 6 shows the interior model used in Poser et al. (2019) whereas the underlying pink box shows the probable $T_{\text{int}}-Z_{\text{env}}$ phase space suggested by Thorngren & Fortney (2019). They used a Bayesian model to infer the metallicity of the planets, placing an upper limit on the atmospheric metallicity.

3.4 Cloudy radius evolution

Now we present our main results in Figs 8 and 9. Both figures display radius evolution curves for TOI-1268b and WASP-10b, respectively. Here, we investigate the impact of different atmospheric pressure-temperature conditions, including clouds as an additional opacity source, on the long-term radius evolution. We perform a parameter study for both planets, varying the main parameter of our atmosphere model in each panel.

As visual anchor points, we plot the observational uncertainty in planetary radius and stellar age (grey area in the background). We calculate the evolution curves of the clear and various cloudy radius evolution curves for a fixed Z_p (TOI-1268b: $Z_p = 0.27$ (with $Z_{\text{env}} = 0.015$, $M_{\text{core}} = 24 M_E$), WASP-10b: $Z_p = 0.11$ (with $Z_{\text{env}} = 0.015$, $M_{\text{core}} = 100 M_E$) to compare within a set of models. Here, $Z_{\text{env}} = 0.015$ is the protosolar value (Lodders 2003) which we define as $1 \times$ solar metallicity or $[M/H] = 0$. As we have seen before in Section 3.3 and Fig. 8, the thermal evolution is heavily dependent on the bulk metallicity of the planet Z_p . Additionally, we show reference models with a clear, non-cloudy atmosphere for different Z_p (thin black dashed lines). As we are interested in the influence of the different parameters of the atmosphere model on the radius evolution, we vary the grey cloud opacity normalization $\kappa_{c,0}$ in each row of the matrix, and within each panel we vary the cloud deck thickness $\Delta_c = 10-100$ where a small number describes a (geometrically) thicker cloud deck. Furthermore, for each set of $(\kappa_{c,0}/\Delta_c)$ we vary the gradient, see Section 2.1. The atmospheric profiles from the Heng model may result in a superadiabatic P - T gradient in the atmosphere (orange tones) whereas we modify the P - T profile so that we inhibit the superadiabaticity (blue tones). We are particularly interested in two different options for the long-term evolution of the atmospheric model. The first column shows the results for a *dynamic* cloud deck position (subsiding P_c) during evolution, which changes the location in the atmosphere of the added longwave opacity, see Section 2.3.

Clouds and the radius evolution of giant planets 2251

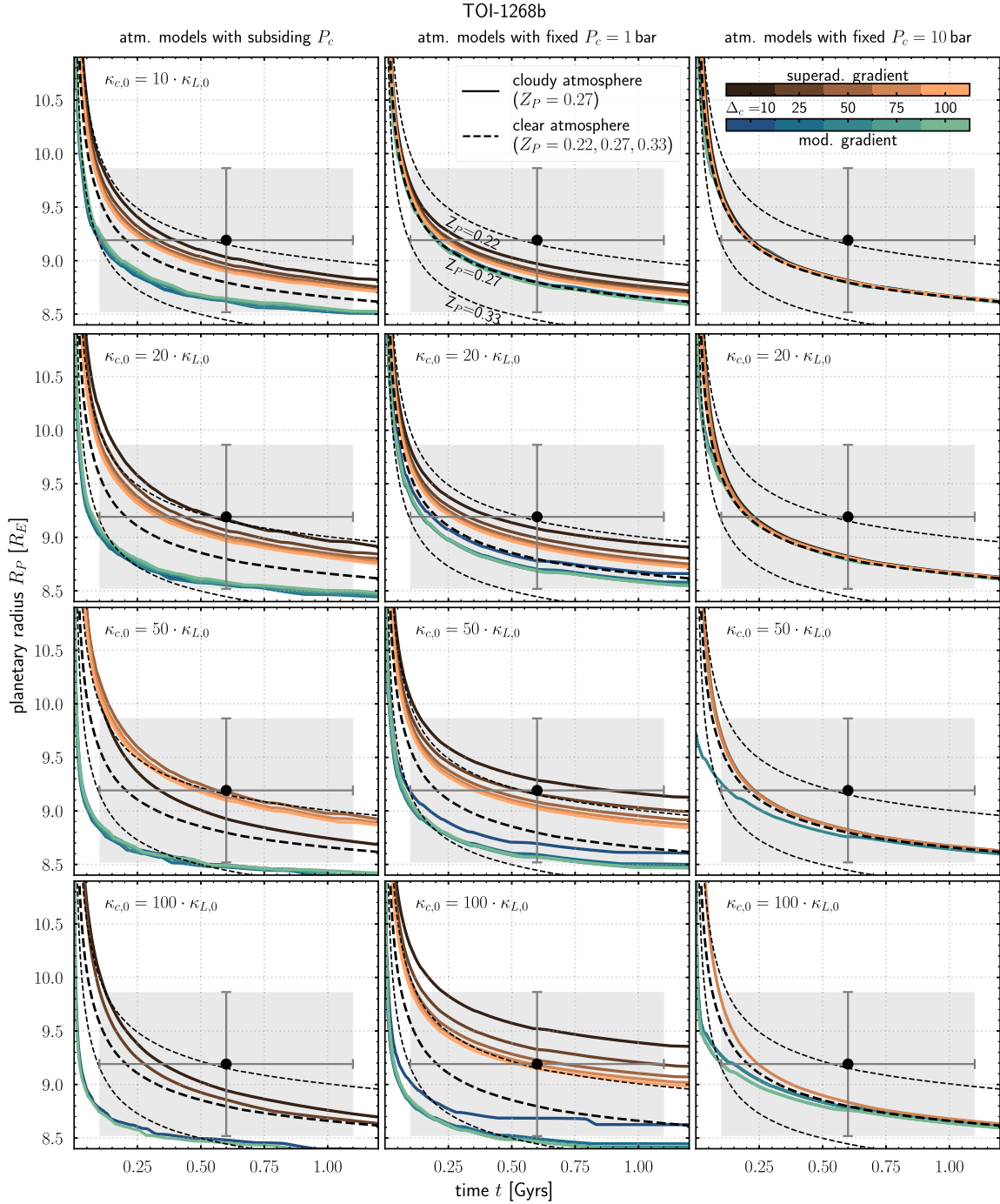


Figure 8. Radius evolution curves for TOI-1268b with subsiding P_c (left column) using MgSiO_3 as possible condensate in the deeper atmosphere and fixed $P_c = 1, 10$ bar (middle and right column). The evolution model with subsiding P_c has a greater impact on the radius evolution than models with a fixed cloud deck. The grey box in each panel represents the uncertainty in measured radius and age. Each panel compares the radius evolution without clouds (dashed curves) and with clouds (solid coloured) for a set of $\kappa_{c,0}$ and Δ_c . The cloudy models are calculated for $Z_P = 0.27$, the corresponding clear model is shown in thick dashed black. Each panel shows the results of the modified gradient (blue tones) and the superadiabatic gradient (orange tones). Additionally, we show in thin dashed black the results with a clear atmosphere for $Z_P = 0.22, 0.33$.

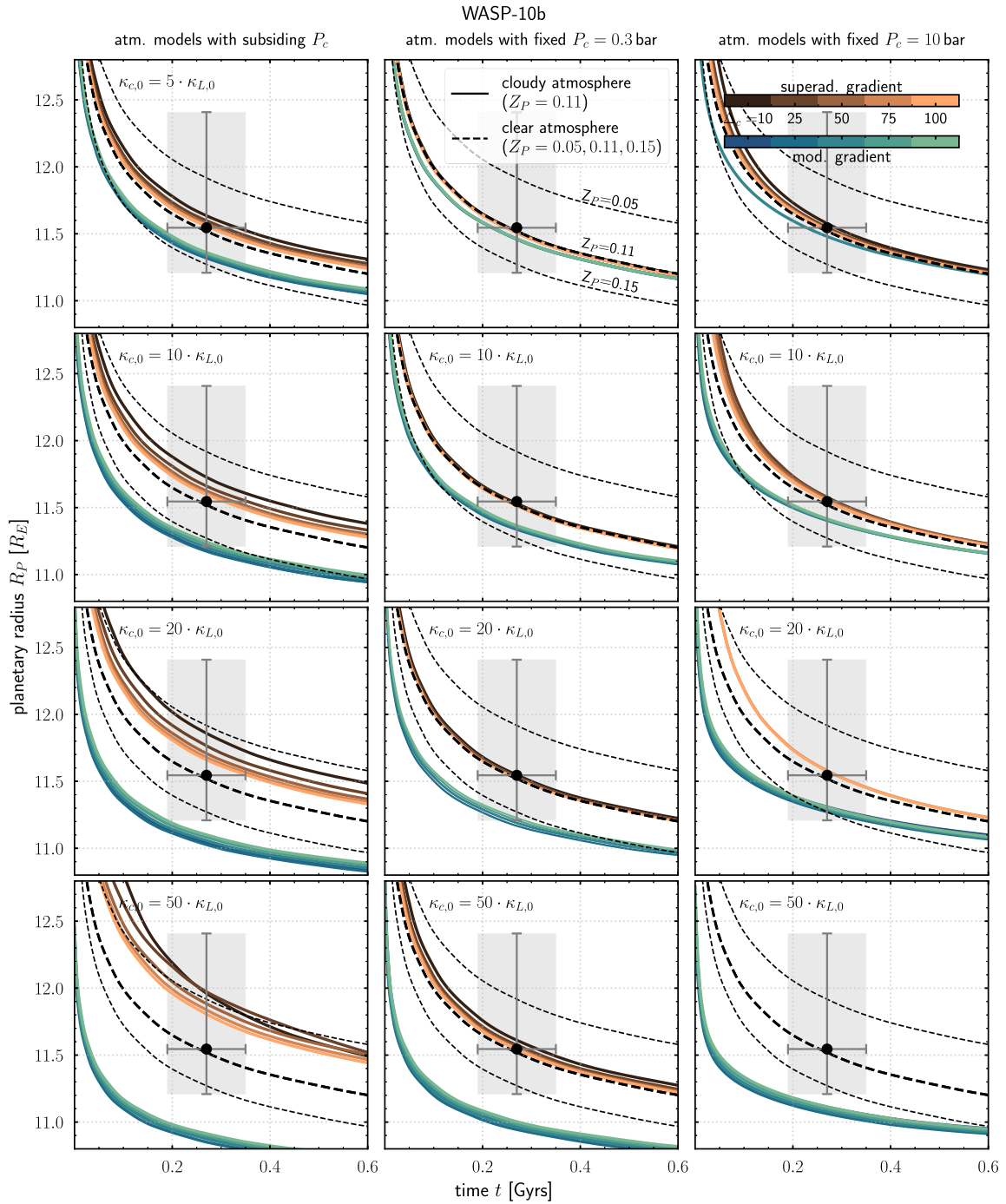
2252 *A. J. Poser and R. Redmer*

Figure 9. Same as Fig. 8, but for WASP-10b. The first column shows the results that include the dynamic model to calculate P_c using MgSiO_3 as the possible condensate, while the second uses the fixed location at $P_c = 0.3$ bar. The cloudy evolution curves have been calculated for $Z_P = 0.11$, the corresponding clear model is shown in thick dashed black. Additionally, we show in thin dashed black the results with a clear atmosphere for $Z_P = 0.05, 0.15$. Each panel shows the results of the modified gradient (blue tones) and the superadiabatic gradient (orange tones). The atmospheric profiles of Fig. 5 are input for the evolution curves of the second row. In cases where the evolution curves for the complete set of parameters are not shown, for example, $\kappa_{c,0} = 50 \cdot \kappa_{L,0}$ at $P_c = 10$ bar, it indicates that we did not obtain a numerical result.

The second and third columns show the results for the evolution curves for a fixed cloud base pressure P_c .

We detected the following trends for WASP-10b and TOI-1268b:

(i) There is a clear influence of the different cloud gradients on the planets thermal evolution. The cloudy atmospheres with the modified and the superadiabatic cloud gradient separate into two bundles of evolution curves for all parameter sets. The atmosphere models with the superadiabatic gradient (orange) slow down the cooling, keeping the planet hotter than in the clear case. Contrary, the curves with the modified non-superadiabatic gradient (blue) accelerate the cooling. Especially for very early time-scales, the cloud decks enhance the cooling and fuel the rapid contraction of the planet. For example, for TOI-1286b (Fig. 8), this is apparent for $t < 0.25$ Gyr. In further evolution, this rapid cooling stops and the planet shrinks more slowly ($t > 0.25$ Gyr). The findings of rapid cooling are consistent with the previous work of Kurosaki & Ikoma (2017) for Uranus. However, our results are based on a colder adiabat for a given T_{int} due to our modification of the cloud model and may not directly represent atmospheric physics as in Kurosaki & Ikoma (2017).

(ii) Variation in the thickness of the cloud deck thickness Δ_c has different effects: In the case of the non-modified, superadiabatic cloud gradient (orange), we see that the smaller Δ_c is, the larger is the effect of keeping the planet hot, as the greenhouse effect comes more into play (smaller Δ_c equals a larger cloud deck thickness). The behaviour is systematic. In the case of the modified gradient (blue), for the modified, non-superadiabatic evolution curves and the subsiding P_c , the (geometrical) thickness has a minor influence.

(iii) With larger cloud opacity normalization $\kappa_{c,0}$, the effects of the above points are even more pronounced. For models with superadiabatic cloud gradient, the heat is trapped more efficiently, and the cooling slows down more enhanced. In addition, the influence of the thickness of the cloud deck on the evolution of the radius increases as the set of respective evolution curves spreads more. For the modified cloud gradient, the larger $\kappa_{c,0}$, the more pronounced is the cooling of the very young planet, and the difference from the clear case becomes larger. For WASP-10b (Fig. 9), the effect of the cloud deck thickness behaves systematically for both gradients, leading to a light spread of evolution curves for the modified cloud gradient and a larger spread for the superadiabatic gradient compared to the clear case. For TOI-1268b (Fig. 8), the effect of an enhanced systematic influence of the cloud deck thickness with larger cloud opacity is given for the superadiabatic gradient, but not for all parameter combinations of the models with the modified gradients.

(iv) Lastly, we want to focus on the effects of a variable cloud deck location versus a fixed cloud deck location during the long-term evolution, see Section 2.3. For TOI-1268b, the first column takes into account the variability of the cloud deck location. The second and third columns keep the cloud deck fixed at $P_c = 10$ bar and $P_c = 10$ bar, respectively. The fixed cloud deck at $P_c = 10$ bar has a minor influence compared to the other two columns and the clear case. Only for $t < 0.25$ Gyr is the effect of faster cooling apparent for models with a modified cloud gradient. Interestingly, the influence of the variable cloud deck location compared to the fixed cloud deck at $P_c = 1$ bar depends on the cloud deck opacity. For $\kappa_{c,0} = (10, 20) \kappa_{L,0}$, the effect of the variable cloud deck is greater. The effect reverses for $\kappa_{c,0} = (50, 100) \kappa_{L,0}$, where the effect is larger for the fixed cloud deck location. For WASP-10b, the effect of a variable cloud deck location compared to a fixed cloud deck location is greater for all $\kappa_{c,0}$.

Our aim is to investigate the effects and impact of atmosphere models with and without clouds on the long-term evolution, which

is ultimately important to take into account to determine the planets' bulk metallicity. Therefore, we estimate the effect on Z_p as follows:

We find for TOI-1268b a total heavy element mass of approximately $10-18 M_E < M_Z < 27-35 M_E$ with a clear atmosphere using CD21 ($Z_p \approx 0.1-0.3$ with CD21, $Z_p \approx 0.2-0.38$ with SCvH95) within the observational error bars. We find that including a cloudy atmosphere model for a specific Z_p can result in similar clear evolution curves for $\approx Z_p \pm 0.05$ when taking into account a variable cloud deck position during the planet's long-term evolution. For the fixed cloud deck position at $P_c = 1$ bar and high $\kappa_{c,0} = (50, 100) \kappa_{L,0}$ we find that the curves equal $\approx Z_p^{+0.10}_{-0.05}$.

For WASP-10b, we find a total heavy element mass of approximately $M_Z < 140 - 160 M_E$ with a clear atmosphere using CD21 ($Z_p \approx 0-0.15$ with CD21, $Z_p \approx 0.01-0.17$ with SCvH95). We find that including a cloudy atmosphere model for a specific Z_p can result in similar clear evolution curves for $\approx Z_p^{+0.06}_{-0.03}$ (for smaller $\kappa_{c,0} = (5, 10) \kappa_{L,0}$) when taking into account a variable cloud deck position during the planet's long-term evolution. For the variable cloud deck position and high $\kappa_{c,0} = (20, 50) \kappa_{L,0}$ we find that the curves equal $\approx Z_p^{+0.10}_{-0.06}$.

We argue that the atmosphere model is therefore a source of degeneracy while determining the planets' metallicity and suggest taking into account the atmospheric $P-T$ structure during the planet's evolution. This is especially important when the observational uncertainties become smaller with upcoming missions.

Note that we have not applied a statistical approach. We computed the thermal evolution of individual models (≈ 200), adjusting the parameter space of the atmosphere model rather than accounting for observational uncertainties such as the mass of the planet. Regarding the interplay between observational and theoretical uncertainties, Müller et al. (2020) discovered that theoretical uncertainties can be comparable to or even exceed observed uncertainties. However, we have not specifically explored this dynamic within our set of planets in this particular study.

4 DISCUSSION

Matching the observed radius, mass, and age of the planet with numerical models naturally leads to a number of degeneracies of the resulting interior structure. In this work, we show the impact of H/He EoS, the distribution of metals, and the uncertainty of the observable parameters (planetary mass and radius) on the $T_{\text{int}}-Z_{\text{env}}$ phase space of the two warm giant planets. We highlight the additional uncertainty that comes into play with a cloudy atmosphere model which we focus on in this paper. Second, by comparing the radius evolution curves using different atmospheric models, we confirm the results of previous publications that atmospheric conditions have an impact on the planets' thermal evolution (e.g. Vazan et al. 2013; Kurosaki & Ikoma 2017). We refine this result by inserting cloud decks into the atmosphere, looking at the effects of the $P-T$ structure on the planet's evolution. We want to point out and discuss the obtained results in the following paragraphs.

First, there are several caveats regarding the atmosphere model used in our study: The real atmosphere is much more diverse than represented by our 1D averaged atmospheric model. Pressure and temperature vary in 3D and in time. Most of the hot Jupiters are tidally locked, with the effect of day/night side temperature gradients with a varied heat distribution depending on T_{eq} . Furthermore, an enhanced atmospheric metallicity pushes the $P-T$ profile to higher temperatures (e.g. Fortney et al. 2006; Drummond et al. 2018), which may underestimate the cloud base. Observational measurements, such as phase curve observations and transmission spectra, can only

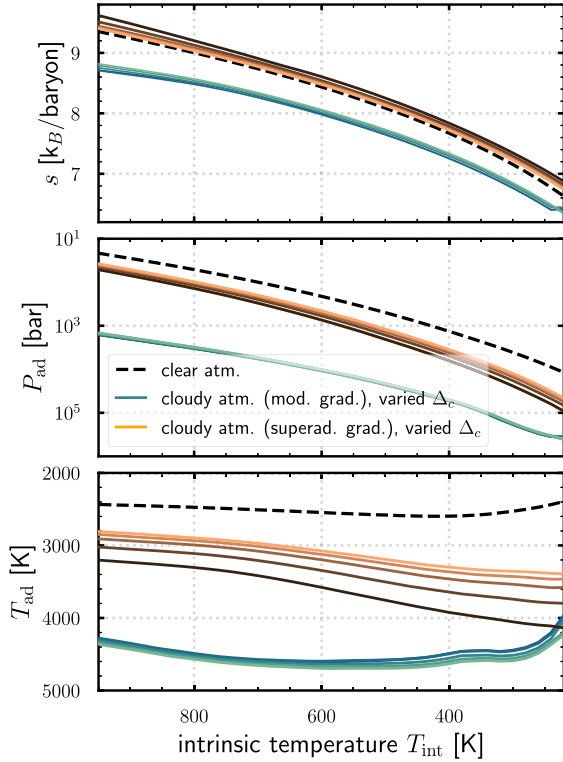
2254 *A. J. Poser and R. Redmer*

Figure 10. Exemplary, we plot values of the adiabatic temperature T_{ad} , pressure P_{ad} as the RCB values (lower panels) and resulting entropy s (upper panel) for the evolution of T_{int} during the thermal evolution of WASP-10b for different model atmospheres. The parameters of the atmosphere models correspond to $\kappa_{c,0} = 10 \kappa_{L,0}$ and subsiding P_c (MgSiO_3), see Fig. 9. The dashed line indicates the reference clear atmospheric case. We calculate the RCB by comparing the local and adiabatic gradients, see equation (3).

give estimates of the physical conditions, e.g. resulting in broad assumptions on temperature and pressure. The occurrence of clouds may depend on stellar irradiation: By analysing the spectra of a sample of irradiated planets, Estrela, Swain & Roudier (2022) find a group of atmospheres with a trend from cloudy/hazy to clear, in the range of $T_{\text{eq}} = 500\text{--}1500$ K. We infer that both planets of this study with $T_{\text{eq}} \approx 900$ K could possibly accommodate clouds. We note that clouds may additionally not occur as one permanent cloud deck, but patchy. Furthermore, within the atmosphere model used, we consider the effect of clouds as purely absorbing without scattering effect. Adding an extra cloud opacity in the longwave then leads to a warming Greenhouse effect, which places an upper limit on our considerations. In addition, we do not consider the possible interaction of cloud decks. We note that there must be enough material to condense out in the deep atmosphere regions to build up a cloud deck, and that rainout may play a role (e.g. Mbarek & Kempton 2016).

Second, an important aspect of our coupled atmosphere-interior-evolution model is the connection to the deep interior at the RCB. The location of the RCB determines the interior adiabat and hence influences the planets’ thermal evolution. At the RCB, temperature fluctuations may not be as strong as in the upper atmosphere,

influencing the P – T profile in a minor way. On the other hand, the chosen atmosphere model does greatly impact the RCB and hence the cooling behaviour. In Fig. 10, we show the development of the entropy of the interior and the corresponding T_{ad} , P_{ad} during the planet’s evolution, plotted over the intrinsic temperature. For this example, we use the results of Fig. 9 (model parameter: $\kappa_{c,0} = 10 \kappa_{L,0}$ and subsiding P_c (MgSiO_3)). The reference case with the clear atmosphere is shown in black dashed. In line with the results of the radius evolution, the faster cooling of the atmospheric models with the modified gradient (blue curves) is due to the lower entropy of the adiabat. On the contrary, the slower cooling is due to a higher entropy. The adiabatic pressure P_{ad} is higher than in the clear case for a specific T_{int} value. The adiabatic temperature T_{ad} is ≈ 1000 K higher for the atmospheric model with the modified gradient. In Figs 5(a), (c), and (d), the position of the RCB is shown as a circle. The wobble in T_{ad} for $T_{\text{int}} < 500$ K stems from the calculation of the RCB where we compare the gradients, equation (5), using the adiabatic gradient from the EoS tables. We want to point out that, regardless of the physical phenomena, the RCB is impacting the thermal long-term evolution of the planet.

Third, looking at the impact of observational uncertainties versus the uncertainty given due to the atmosphere model with and without clouds, we note that the results due to different atmospheric models for nearly all parameters lie in the uncertainty range of radius and age. Better constraints on planetary radius, mass, and stellar age are needed to characterize the planets and to narrow down the parameter space, such as aimed at by space missions, e.g. *PLATO* (Rauer et al. (2014)).

In general, the findings of this study confirm that the atmosphere plays a crucial role for the radius evolution of a planet. Further, time-variable cloud decks may have a significant impact on the contraction of the planet, adding substantially to the model degeneracy when coupling atmosphere-interior-thermal evolution models for warm giant planets. We suggest taking into account the time variability of the deep atmosphere during the long-term evolution of gas giants.

5 SUMMARY AND CONCLUSIONS

In this paper, we explore the impact of cloud decks on the $T_{\text{int}}\text{--}Z_{\text{env}}$ phase space and radius evolution for two young warm gas giants, WASP-10b and TOI-1268b. The main focus of this paper was to extend the previous work on the effect of clouds on the thermal evolution of irradiated gas planets. We focus on cloud decks in the deep atmosphere. Ultimately, this may help to constrain the metal content of the planet.

This work is based on the previous work by Poser et al. (2019). We used a conventional three-layer model consisting of a core, an adiabatic envelope, and a radiative atmosphere to model the thermal evolution of the planets. For the pressure and temperature of the atmosphere, we used a semi-analytical model with grey opacities. To account for cloud decks in the atmosphere, we added a purely absorbing cloud deck resulting in a warming effect for the deep atmosphere. The cloud deck is described as an additional grey opacity, added to the long-wave opacity. We assume the cloud deck to be formed where there is an intersection with a condensation curve of a cloud forming species. Within this model, it is possible to investigate general trends in the atmospheric temperature structure for the (thermal) radius evolution. To illustrate the impact of cloud decks, we compare several atmospheric model setups during the planets’ thermal evolution. We summarize our main findings as follows:

(i) The additional infrared opacity due to clouds warms the atmosphere beneath. The warming has an impact on the thermal radius evolution of the planet. We found that it can lead to a slower or faster cooling compared to the clear, non-cloudy case. The specific outcome (slower or faster cooling) hinges on the choice of cloud gradient, whether superadiabatic or not, see Figs 8 and 9.

(ii) When comparing the effect of a fixed cloud base level versus a dynamic cloud base level during the planets' thermal evolution, there is a slight dependence on the cloud opacity for TOI-1268b: For smaller cloud opacities ($\kappa_{c,0} < 20 \kappa_{L,0}$), we see an enhanced behaviour that results in a faster/slower cooling behaviour (depending on the cloud gradient used) for the dynamic cloud base level. For WASP-10b, the dynamic cloud base shows a stronger effect than the fixed cloud deck case for all cloud opacities.

(iii) We demonstrate that atmospheric models including deep clouds can lead to a degeneracy in predicting the planets' bulk metallicity. For the Jupiter-mass WASP-10b, we find a possible span of $\approx Z_P^{+0.10}_{-0.06}$. For the Saturn-mass TOI-1268b, this range extends to $\approx Z_P^{+0.10}_{-0.05}$.

Additionally, we find that the choice of the EoS (CD21 versus SCvH95) plays a more significant role in affecting the less dense warm Saturn TOI-1268b compared to the denser warm Jupiter WASP-10b. When comparing the impact of the atmosphere model on the radius evolution of both planets, we find that quantifying the results with respect to the planets' density is not feasible. However, it is likely that such quantification could be achieved with a larger sample size, which we did not undertake. Our findings are based on a non-statistical approach, calculating individual models, solely varying the parameter of the atmosphere model. The results can be seen as a first step towards a more sophisticated modelling approach, including the observational uncertainties.

However, this study is important in the context of modelling the interior properties of giant planets. It highlights the importance of coupled interior, atmosphere, and thermal evolution models and underlines the role of atmospheric chemistry and cosmochemistry.

Overall, we stress the importance of reducing not only the observational uncertainties in planetary radius and mass but also the uncertainty in stellar age as a proxy for the planets' age, supporting the work of, e.g. Müller et al. (2020) and Müller & Helled (2023b). Additionally, to further inform planetary formation models, interior models require the planets' atmospheric metallicity as input parameter to point a proper picture. Missions such as *JWST*, *TESS*, and the upcoming ESA *ARIEL* mission will address these points, aiming at reducing observational error bars for radius and stellar age as well as providing values of the planets' atmospheric metallicity.

ACKNOWLEDGEMENTS

We thank N. Nettelmann for valuable input to the manuscript, and for data included in the $\gamma(T_{\text{eq}})$ -fit. We thank L. Scheibe, M. Schörner, C. Kellermann, and S. Schumacher for helpful discussions. This work is supported by the DFG project SPP-1992 'Exploring the Diversity of Extrasolar Planets'. We thank the anonymous referee for helpful feedback that greatly improved the manuscript.

DATA AVAILABILITY

The data that support the findings of this study are available from the corresponding author upon reasonable request.

REFERENCES

- Bahcall J. N., Pinsonneault M. H., Wasserburg G. J., 1995, *Rev. Mod. Phys.*, 67, 781
- Bailey E., Stevenson D. J., 2021, *Planet. Sci. J.*, 2, 64
- Baraffe I., Chabrier G., Barman T., 2008, *A&A*, 482, 315
- Baudino J.-L., Mollière P., Venot O., Tremblin P., Bézard B., Lagage P.-O., 2017, *ApJ*, 850, 150
- Bhattacharya A. et al., 2023, *ApJ*, 952, L27
- Bjoraker G. L., Wong M. H., De Pater I., Hewagama T., Ádámkóvics M., Orton G. S., 2018, *AJ*, 156, 101
- Chabrier G., Debras F., 2021, *ApJ*, 917, 4
- Chabrier G., Mazevet S., Soubiran F., 2019, *ApJ*, 872, 51
- Chabrier G., Baraffe I., Phillips M., Debras F., 2023, *A&A*, 671, A119
- Christian D. J. et al., 2009, *MNRAS*, 392, 1585
- Debras F., Chabrier G., 2019, *ApJ*, 872, 100
- Debras F., Chabrier G., Stevenson D. J., 2021, *ApJ*, 913, L21
- Dietrich W., Kumar S., Poser A. J., French M., Nettelmann N., Redmer R., Wicht J., 2022, *MNRAS*, 517, 3113
- Dobbs-Dixon I., Agol E., 2013, *MNRAS*, 435, 3159
- Dong J. et al., 2022, *ApJ*, 926, L7
- Drummond B., Mayne N. J., Baraffe I., Tremblin P., Manners J., Amundsen D. S., Goyal J., Acreman D., 2018, *A&A*, 612, A105
- Estrela R., Swain M. R., Roudier G. M., 2022, *ApJ*, 941, L5
- Faedi F. et al., 2011, *A&A*, 531, A40
- Fortney J. J., Marley M. S., Lodders K., Saumon D., Freedman R., 2005, *ApJ*, 627, L69
- Fortney J. J., Saumon D., Marley M. S., Lodders K., Freedman R. S., 2006, *ApJ*, 642, 495
- Fortney J. J., Marley M. S., Barnes J. W., 2007, *ApJ*, 659, 1661
- Fortney J. J., Shabram M., Showman A. P., Lian Y., Freedman R. S., Marley M. S., Lewis N. K., 2010, *ApJ*, 709, 1396
- Fortney J. J., Visscher C., Marley M. S., Hood C. E., Line M. R., Thorngren D. P., Freedman R. S., Lupu R., 2020, *AJ*, 160, 288
- Fossati L. et al., 2020, *A&A*, 643, A131
- Freedman R. S., Lustig-Yaeger J., Fortney J. J., Lupu R. E., Marley M. S., Lodders K., 2014, *ApJS*, 214, 25
- Guillot T., 2010, *A&A*, 520, A27
- Guillot T., Santos N. C., Pont F., Iro N., Melo C., Ribas I., 2006, *A&A*, 453, L21
- Helled R., 2019, Oxford Research Encyclopedias: Planetary Science. Oxford Univ. Press, Oxford
- Helled R. et al., 2022, *Exp. Astron.*, 53, 323
- Helling C., 2019, *Annu. Rev. Earth Planet. Sci.*, 47, 583
- Helling C., 2021, in Madhusudhan N., ed., Clouds in Exoplanetary Atmospheres, ExoFrontiers: Big Questions in Exoplanetary Science. IOP Publishing, Bristol, UK, p. 20
- Helling C., Casewell S., 2014, *A&AR*, 22, 80
- Helling C. et al., 2021, *A&A*, 649, A44
- Heng K., Hayek W., Pont F., Sing D., 2012, *MNRAS*, 420, 20
- Hubbard W. B., Marley M. S., 1989, *Icarus*, 78, 102
- Lin S., Mordasini C., Parmentier V., Van Boekel R., Henning T., Ji J., 2014, *ApJ*, 795, 65
- Johnson J. A., Winn J. N., Cabrera N. E., Carter J. A., 2009, *ApJ*, 692, L100
- Kramm U., Nettelmann N., Fortney J. J., Neuhäuser R., Redmer R., 2012, *A&A*, 538, A146
- Kreidberg L. et al., 2018, *AJ*, 156, 17
- Kumar S., Poser A. J., Schöttler M., Kleinschmidt U., Dietrich W., Wicht J., French M., Redmer R., 2021, *Phys. Rev. E*, 103, 063203
- Kurosaki K., Ikoma M., 2017, *AJ*, 153, 260
- Leconte J., Chabrier G., 2012, *A&A*, 540, A20
- Leconte J., Chabrier G., 2013, *Nat. Geosci.*, 6, 347
- Lee G. K., Wood K., Dobbs-Dixon I., Rice A., Helling C., 2017, *A&A*, 601, A22
- Linder E. F., Mordasini C., Mollière P., Marleau G. D., Malik M., Quanz S. P., Meyer M. R., 2019, *A&A*, 623, A85
- Lodders K., 2003, *ApJ*, 591, 1220

2256 *A. J. Poser and R. Redmer*

- MacKenzie J., Grenfell J. L., Baumeister P., Tosi N., Cabrera J., Rauer H., 2023, *A&A*, 671, A65
- Maciejewski G. et al., 2011a, *MNRAS*, 411, 1204
- Maciejewski G., Raetz S., Nettelmann N., Seeliger M., Adam C., Nowak G., Neuhäuser R., 2011b, *A&A*, 535, A7
- Madhusudhan N., Seager S., 2009, *ApJ*, 707, 24
- Malik M., Kitzmann D., Mendonça J. M., Grimm S. L., Marleau G.-D., Linder E. F., Tsai S.-M., Heng K., 2019, *AJ*, 157, 170
- Mansfield M. et al., 2020, *ApJ*, 888, L15
- Mbarek R., Kempton E. M.-R., 2016, *ApJ*, 827, 121
- Miguel Y., Guillot T., Fayon L., 2016, *A&A*, 596, A114
- Miller-Ricci E., Fortney J. J., 2010, *ApJ*, 716, L74
- Mollière P., Van Boekel R., Dullemond C., Henning T., Mordasini C., 2015, *ApJ*, 813, 47
- Mollière P., Van Boekel R., Bouwman J., Henning T., Lagage P. O., Min M., 2017, *A&A*, 600, A10
- Morley C. V., Knutson H., Line M., Fortney J. J., Thorngren D., Marley M. S., Teal D., Lupu R., 2017, *AJ*, 153, 86
- Müller S., Helled R., 2023a, *Front. Astron. Sp. Sci.*, 10, 123
- Müller S., Helled R., 2023b, *A&A*, 669, A24
- Müller S., Ben-Yami M., Helled R., 2020, *ApJ*, 903, 147
- Nettelmann N., Wang K., Fortney J. J., Hamel S., Yellamilli S., Bethkenhagen M., Redmer R., 2016, *Icarus*, 275, 107
- Ohno K., Okuzumi S., 2018, *ApJ*, 859, 34
- Poser A. J., Nettelmann N., Redmer R., 2019, *Atmosphere*, 10, 664
- Rauer H. et al., 2014, *Exp. Astron.*, 38, 249
- Sarkis P., Mordasini C., Henning T., Marleau G. D., Mollière P., 2021, *A&A*, 645, A79
- Saumon D., Chabrier G., van Horn H. M., 1995, *ApJS*, 99, 713
- Scheibe L., Nettelmann N., Redmer R., 2019, *A&A*, 632, A70
- Scheibe L., Nettelmann N., Redmer R., 2021, *A&A*, 650, A200
- Stevenson D. J., 1985, *Icarus*, 62, 4
- Šubjak J. et al., 2022, *A&A*, 662, A107
- Thorngren D. P., Fortney J. J., 2018, *AJ*, 155, 214
- Thorngren D. P., Fortney J. J., 2019, *ApJ*, 874, L31
- Thorngren D. P., Fortney J. J., Murray-Clay R. A., Lopez E. D., 2016, *ApJ*, 831, 64
- Thorngren D., Gao P., Fortney J. J., 2019, *ApJ*, 884, L6
- Turrini D. et al., 2018, *Exp. Astron.*, 46, 45
- Vazan A., Kovetz A., Podolak M., Helled R., 2013, *MNRAS*, 434, 3283
- Visscher C., Lodders K., Fegley B., Jr, 2006, *ApJ*, 648, 1181
- Visscher C., Lodders K., Fegley B., Jr, 2010, *ApJ*, 716, 1060
- Wakeford H. R. et al., 2017, *AJ*, 155, 29
- West R. A., 2017, in Deeg H. J., Belmonte J. A., eds, *Handbook of Exoplanets, Temperature, Clouds, and Aerosols in Giant and Icy Planets*. Springer, Cham, New York, p. 265
- Wong M. H., Bjaraker G. L., Goullaud C., Stephens A. W., Luszcz-Cook S. H., Atreya S. K., de Pater I., Brown S. T., 2023, *Remote Sens.*, 15, 702

APPENDIX: PLANETARY DATA USED FOR THE γ -FIT FORMULA

Table A1. Planetary parameter used for the γ -fit shown in Fig. 2. Note that κ_L here refers to the notation of the clear atmosphere model by Guillot (2010). It corresponds to $\kappa_{L,0}$ in the notation used by Heng et al. (2012).

Planet	Gravity [cm s ⁻²]	T_{eq} [K]	A_B	[M/H]	T_{iso} [K]	γ	κ_L [m ² kg ⁻¹]	κ_S [m ² kg ⁻¹]	
GJ1214b	880.0	544.0	0.1	1	1000.0	0.050	1.0e-03	5.00e-05	Miller-Ricci & Fortney (2010)
GJ436b	1270.0	655.0	0.1	1	1100.0	0.060	1.0e-03	6.00e-05	Morley et al. (2017)
generic	2570.0	857.0	0.1	1	1350.0	0.100	1.0e-03	1.00e-04	Fortney et al. (2007)
WASP-39b	430.4	1088.4	0.1	1	1546.0	0.154	5.0e-04	7.70e-05	Wakeford et al. (2017)
HD189733b	2120.0	1169.0	0.1	1	1700.0	0.140	1.0e-03	1.40e-04	Madhusudhan & Seager (2009)
HD189733b	2120.0	1169.0	0.1	1	1500.0	0.260	1.0e-03	2.60e-04	Fortney et al. (2010)
HD189733b	2120.0	1169.0	0.1	1	1520.0	0.240	1.0e-03	2.40e-04	Fortney et al. (2010)
HD189733b	2120.0	1169.0	0.1	1	1600.0	0.190	1.0e-03	1.90e-04	Heng et al. (2012)
fid. planet	1500.0	1267.0	0.0	1	1602.0	0.243	7.0e-04	1.70e-04	Jin et al. (2014)
HD209645b	965.0	1402.0	0.1	1	1720.0	0.330	1.0e-03	3.30e-04	Fortney et al. (2005)
HD209458b	924.7	1479.5	0.0	1	1732.0	0.357	7.0e-04	2.50e-04	Fortney et al. (2005)
HD209458b	924.7	1479.5	0.0	1	1796.0	0.300	2.0e-04	6.00e-05	Fortney et al. (2005)
fid. planet	1500.0	1577.0	0.0	1	1995.0	0.250	6.0e-04	1.50e-04	Jin et al. (2014)
HAT-P-13b	1286.0	1605.0	0.1	1	2000.0	0.300	1.0e-03	3.00e-04	Kramm et al. (2012)
HD149026b	1697.7	1629.0	0.1	1	1900.0	0.424	1.0e-03	4.24e-04	Fortney et al. (2006)
WASP-103b	1574.0	2444.0	0.1	1	2700.0	0.600	1.0e-03	6.00e-04	Kreidberg et al. (2018)
fid. planet	1500.0	2777.0	0.0	1	2905.0	0.717	6.0e-03	4.30e-03	Jin et al. (2014)
KELT-9b	1902.5	4050.0	0.0	1	4100.0	0.900	1.0e-03	9.00e-04	Fossati et al. (2020); Mansfield et al. (2020)

Clouds and the radius evolution of giant planets 2257

Table A2. Planets *not used* for the γ -fit, but displayed in Fig. 2. Here, the metallicities are larger than 1x solar abundance, or it is $A_B > 0.1$. Note that κ_L here refers to the notation of the clear atmosphere model by Guillot (2010). It corresponds to $\kappa_{L,0}$ in the notation used by Heng et al. (2012).

Planet	Gravity [cm s^{-2}]	T_{eq} [K]	A_B	[M/H]	T_{iso} [K]	γ	κ_L [$\text{m}^2 \text{kg}^{-1}$]	κ_S [$\text{m}^2 \text{kg}^{-1}$]	
WASP-10b	6915.9	869.0	0.3	1	1360.0	0.147	1.4e-03	2.00e-04	Fortney et al. (2007)
WASP-39b	430.4	1088.4	0.1	10	1835.0	0.065	1.3e-03	8.27e-05	Mollière et al. (2015)
HD149026b	1697.7	1629.0	0.1	3	2000.0	0.320	1.0e-03	3.20e-04	Fortney et al. (2006)
HD149026b	1697.7	1629.0	0.1	10	2200.0	0.202	1.0e-03	2.02e-04	Fortney et al. (2006)

This paper has been typeset from a \LaTeX file prepared by the author.

5.3. Ionization and transport in partially ionized multicomponent plasmas: Application to atmospheres of hot Jupiters

The universe is so much bigger than you realize.

Everything Everywhere All At Once (movie)

Physical Review E **103**, 063203 (2021).
DOI: [10.1103/PhysRevE.103.063203](https://doi.org/10.1103/PhysRevE.103.063203)

S. Kumar

Preparation of the manuscript, further development of the code for the transport properties, analysis and interpretation of the results

A. J. Poser

Preparation of the manuscript, calculation of the atmospheric thermal profiles of HD 209458b, and of the coupled atmospheric, interior, and thermal evolution data, analysis and interpretation of the results

M. Schöttler

Development of the initial code for the transport properties

U. Kleinschmidt

Application and first benchmarking of the initial code for the transport properties

W. Dietrich

Preparation of the manuscript, analysis of the planetary magnetic field and induction process, interpretation of the results

J. Wicht

Supervision of the project, analysis of the planetary magnetic field and induction process, preparation of the manuscript

M. French

Supervision of the project, preparation of the manuscript

R. Redmer

Supervision of the project, preparation of the manuscript

Ionization and transport in partially ionized multicomponent plasmas: Application to atmospheres of hot Jupiters

Sandeep Kumar ^{1,*}, Anna Julia Poser ¹, Manuel Schöttler,¹ Uwe Kleinschmidt ¹, Wieland Dietrich ²,
Johannes Wicht,² Martin French ¹ and Ronald Redmer ¹

¹*Institut für Physik, Universität Rostock, 18051 Rostock, Germany*

²*Max-Planck-Institut für Sonnensystemforschung, 37077 Göttingen, Germany*



(Received 16 February 2021; accepted 17 May 2021; published 4 June 2021)

We study ionization and transport processes in partially ionized multicomponent plasmas. The plasma composition is calculated via a system of coupled mass-action laws. The electronic transport properties are determined by the electron-ion and electron-neutral transport cross sections. The influence of electron-electron scattering is considered via a correction factor to the electron-ion contribution. Based on these data, the electrical and thermal conductivities as well as the Lorenz number are calculated. For the thermal conductivity, we consider also the contributions of the translational motion of neutral particles and of the dissociation, ionization, and recombination reactions. We apply our approach to a partially ionized plasma composed of hydrogen, helium, and a small fraction of metals (Li, Na, Ca, Fe, K, Rb, and Cs) as typical for atmospheres of hot Jupiters. We present results for the plasma composition and the transport properties as a function of density and temperature and then along typical P - T profiles for the outer part of the hot Jupiter HD 209458b. The electrical conductivity profile allows revising the Ohmic heating power related to the fierce winds in the planet's atmosphere. We show that the higher temperatures suggested by recent interior models could boost the conductivity and thus the Ohmic heating power to values large enough to explain the observed inflation of HD 209458b.

DOI: [10.1103/PhysRevE.103.063203](https://doi.org/10.1103/PhysRevE.103.063203)

I. INTRODUCTION

Partially ionized multicomponent plasmas are composed of molecules, atoms, and ions of various species as well as of free electrons. The plasma parameters of density and temperature determine their ionization degree and thus also their equation of state and transport properties such as electrical and thermal conductivity [1–8]. Profound knowledge of the thermophysical properties of such plasmas is important for applications in astrophysics, atmospheric science, and plasma technology. For instance, Earth's ionosphere [9,10] and the atmospheres of hot Jupiters [11,12] can be treated as low-density partially ionized multicomponent plasmas. Another example is the formation of stars out of initially cold and dilute clouds which consist mostly of molecular hydrogen, helium, and a small fraction of heavier elements and collapse due to gravitational instability [13,14]. The evolution to a protostar, which is much hotter and denser, runs through the plasma regime, where dissociation and ionization processes determine the heating and contraction dynamics essentially. The quenching gas in high-power circuit breakers [15] or arc plasmas [16] are examples of important technical applications of multicomponent partially ionized plasmas (PIPs).

The transport properties of partially ionized plasmas are determined by the ionization degree and the charge state distribution of its constituents. This defines the number of free electrons and the strength of the collisional interactions between the plasma species and determines their mobility. At

low temperatures, the ionization degree is very low and the transport properties are dominated by neutral particles (atoms and molecules), while charged particles become more and more important with increasing temperature due to thermal ionization. Such thermal ionization conditions are typical for the outer atmospheres of planets in close proximity to their star, like hot Jupiters and hot mini-Neptunes [17]. The electrical conductivity, in particular due to the ionization of alkali metals, can rise to values where magnetic effects become important for the evolution and dynamics of the planetary interior.

Hot Jupiters orbit their parent stars in close proximity and are locked in synchronous rotation, which means that they always face the same side to the star. Several physical mechanisms are discussed to explain why the radii of hot Jupiters are significantly larger than expected [12,18,19]. One possibility is Ohmic dissipation that directly scales with the electrical conductivity.

The differential stellar irradiation drives fierce winds in the outer atmosphere that tend to equilibrate the difference in dayside and nightside temperatures. Interaction of the winds with a planetary magnetic field induces electric currents that can flow deeper into the planet. When efficient enough, the related Ohmic heating transports a sufficient fraction of the stellar irradiation received by the planet to deeper interiors where it could explain the inflation.

Accurate data on the composition and the transport coefficients along realistic pressure-temperature (P - T) profiles of hot Jupiters are also critical input in corresponding magnetohydrodynamics simulations [20]. Using the corresponding plasma composition, i.e., the molar fractions of the various

*sandeep.kumar@uni-rostock.de

species, and the absorption coefficient of the plasma, the opacity of the planet's atmosphere can be calculated, which in turn determines the P - T profile [21].

In this paper we calculate the ionization degree, the electrical and thermal conductivity, and the Lorenz number for a PIP as a function of temperature and mass density. Mass-action laws (MALs) are used to calculate the composition of the PIP [22–26]. We assume that the plasma is in thermal and chemical equilibrium so that Saha-like equations for each dissociation and ionization reaction can be derived, from which the partial densities of all species are calculated, i.e., the plasma composition. Furthermore, the electron-ion and electron-neutral transport cross sections have to be determined [27]. The effect of electron-electron scattering is considered by introducing a correction factor to the electron-ion contribution according to the Spitzer theory [28]. Note that the influence of the electron-electron interaction on the transport coefficients is currently of interest also for dense nonideal plasmas [29,30]. The contributions of the translational motion of neutrals and of the heat of dissociation, ionization, and recombination reactions to the thermal conductivity of PIP were also studied. For a benchmark we have compared the thermal conductivity of hydrogen plasma obtained from our model to the experimental arc-discharge results of Behringer and van Cung [31]. In the next step we study the general trends of the ionization degree and of the transport coefficients with respect to the plasma density and temperature. Finally, we calculate the ionization degree as well as the electrical and the thermal conductivity along typical P - T profiles through the atmosphere of the inflated hot Jupiter HD 209458b. These results are then used to assess the Ohmic heating in the planet's atmosphere and to infer whether this effect is efficient enough to explain the inflation. Batygin and Stevenson [11] (BS) have used simplified expressions for the calculation of the plasma composition (ionization scaled with the density scale height) and the electrical conductivity (weakly ionized gas) and concluded that Ohmic heating is indeed sufficient to explain the inflation of this hot Jupiter. We use our refined conductivity values to calculate updated estimates for the Ohmic heating in HD 209458b.

Our paper is organized as follows. In Sec. II we outline the theoretical basics for the calculation of the equation of state and the composition of the PIP. Section III provides the basic formulas used for the calculation of the electronic transport coefficients in the PIP. In Sec. IV we report the results for the ionization degree and the electronic transport coefficients in dependence on the plasma temperature and mass density. Section V gives details of the calculation of the translational motion of neutral particles and of the contribution of the heat of dissociation, ionization, and recombination reactions to the thermal conductivity. In Sec. VI, results for the ionization degree and the transport coefficients along typical P - T profiles through the atmosphere of the hot Jupiter HD 209458b are presented. A summary and conclusions are given in Sec. VII.

II. EQUATION OF STATE AND COMPOSITION

We consider an ideal-gaslike model for the partially ionized plasma and calculate its chemical composition using a canonical partition function $Z(\{N_i\}, V, T)$, which depends on

TABLE I. Abundances of constituents considered in this work, with the molar and mass fractions according to Refs. [32,33].

Element	Molar fraction (%)	Mass fraction (%)
H	92.23	74.84
He	7.76	25.02
Li	1.75×10^{-7}	9.82×10^{-7}
Na	1.79×10^{-4}	3.3×10^{-3}
K	1.18×10^{-5}	3.74×10^{-4}
Ca	1.88×10^{-4}	6.1×10^{-3}
Fe	2.7×10^{-3}	0.119
Rb	2.21×10^{-8}	1.52×10^{-6}
Cs	1.16×10^{-9}	1.23×10^{-7}

the number of particles N_i of species i as well as on the volume V and temperature T of the plasma. We assume the constituent elements H, He, Li, K, Na, Rb, Ca, Fe, and Cs to be the relevant drivers of ionization in hot Jupiter atmospheric plasmas. The abundances of these constituents are given in Table I, which is adopted from Refs. [32,33].

In a mixture of c noninteracting chemical species, the partition function $Z(\{N_i\}, V, T)$ can be written as a product

$$Z(\{N_i\}, V, T) = \prod_{i=1}^c z_i(N_i, V, T), \quad (1)$$

with

$$z_i(N_i, V, T) = z_i^{\text{trans}}(N_i, V, T) [z_i^{\text{int}}(T)]^{N_i}, \quad (2)$$

where $z_i^{\text{trans}}(N_i, V, T)$ is the translational partition function of species i and $z_i^{\text{int}}(T)$ is its one-particle internal partition function (IPF). The translational partition function is given by

$$z_i^{\text{trans}}(N_i, V, T) = \frac{V^{N_i}}{N_i! \lambda_{th,i}^{3N_i}}, \quad (3)$$

in which $\lambda_{th,i} = h/\sqrt{2\pi m_i k_B T}$ is the thermal wavelength with the Planck constant h , the mass m_i of species i , and the Boltzmann constant k_B . The internal partition function modes are considered to be independent of each other, which gives the formula [34]

$$z_i^{\text{int}} = z_i^{\text{nuc}} z_i^{\text{el}} z_i^{\text{vib}} z_i^{\text{rot}}, \quad (4)$$

where z_i^{nuc} , z_i^{el} , z_i^{vib} , and z_i^{rot} are the nuclear, electronic, vibrational, and rotational partition functions of the species i , respectively.

The nuclear IPF is considered as

$$z_i^{\text{nuc}} = 2I_i^{\text{ns}} + 1, \quad (5)$$

which depends on the spin quantum number I_i^{ns} of the nucleus. The electronic partition function is approximated as follows:

$$z_i^{\text{el}} = (2J + 1) \exp(-E_i^0/k_B T). \quad (6)$$

Here E_i^0 is the energy and J the electronic angular momentum quantum number of the atom, ion, or molecule in the ground state. We do not consider excited states in this study because their population is small for the plasma parameters considered here so that their effect on ionization and transport is negligible. Note that each excited state introduces a new species for

which all related atomic, ionic, or molecular parameters need to be known for the calculation of the plasma composition and the transport cross sections which would unnecessarily complicate the PIP model as long as their effect is small. For the calculation of the vibrational and rotational partition functions of the H_2 molecule we use the high-temperature approximation

$$z_{H_2}^{\text{vib}} = \frac{1}{1 - \exp(-\theta_v/T)}, \quad (7)$$

$$z_{H_2}^{\text{rot}} = \frac{T}{2\theta_r}, \quad (8)$$

where $\theta_v = h\nu/k_B$ and $\theta_r = h^2/8\pi^2Ik_B$ are the vibrational and rotational temperatures, respectively. The latter depends on the moment of inertia $I = \mu_{HH}r^2$ of the H_2 molecule; $\mu_{HH} = m_H/2$ is its reduced mass and r its bond length.

The plasma considered here is in thermal and chemical equilibrium, so the particle densities follow from MALs as follows [26]:

$$\prod_i n_i^{v_{i,a}} = \prod_i \frac{(z_i^{\text{int}})^{v_{i,a}}}{(\lambda_{i,h,i}^3)^{v_{i,a}}} \equiv K_a(T). \quad (9)$$

In this expression, $n_i = N_i/V$ are number densities of species i , $K_a(T)$ is the reaction constant, and $v_{i,a}$ are the stoichiometric coefficients of the reaction a . The $v_{i,a}$ for the reaction products and reactants are chosen to be positive or negative, respectively. The MALs and particle conservation equations of the PIP are solved numerically to calculate the number density of each species for a given temperature and mass density. We allow the constituents to be doubly ionized at maximum. This sets a maximum temperature of about 30 000 K for our applications, which corresponds to about 10% of the lowest third ionization energy (30.651 eV for Fe [35]) of all constituents considered. The MALs for dissociation and ionization read

$$\frac{n_H^2}{n_{H_2}} = K_H, \quad (10)$$

$$\frac{n_{\text{ion},i}^+ n_e}{n_{\text{atom},i}} = K_{\text{ion},i}^+, \quad (11)$$

$$\frac{n_{\text{ion},i}^{2+} n_e}{n_{\text{ion},i}^+} = K_{\text{ion},i}^{2+}, \quad (12)$$

in which n_{ion}^+ and n_{ion}^{2+} denote the number densities of a singly or doubly charged ion, respectively. The charge neutrality condition in the PIP leads to the equation

$$n_e = \sum_i n_{\text{ion},i}^+ + \sum_i 2n_{\text{ion},i}^{2+}, \quad (13)$$

where n_e represents the free electron number density in the PIP. Mass conservation in the plasma provides the relation

$$\rho = \sum_{i=1}^c m_i n_i, \quad (14)$$

where ρ is mass density of the plasma. The relative abundance χ_r of each constituent with respect to the H abundance is set as follows:

$$\chi_{r,i} = \frac{n_{\text{atom},i} + n_{\text{ion},i}^+ + n_{\text{ion},i}^{2+}}{2n_{H_2} + n_H + n_{H^+}}. \quad (15)$$

Most of the parameters such as ground-state energies E_i^0 , ionization energies, total angular momentum quantum numbers J , and atomic weights m_i of the species are taken from the NIST database [35]. The nuclear partition function and ground-state energy of the H_2 molecule are taken as $z_{H_2}^{\text{nuc}} = 4$ and $E_i^0 = -31.738$ eV [26], respectively. The ground-state energy of the H_2 molecule already includes the vibrational ground-state energy. Therefore, the vibrational partition function (7) includes only excited states. We have taken $\theta_v = 6321.3$ K and $\theta_r = 88.16$ K for the vibrational and rotational temperatures of the H_2 molecule [36], respectively. The number densities n_i of each species (molecules, atoms, and ions) for a given plasma temperature and mass density are calculated by solving the coupled equations (10)–(15) using the Newton-Raphson method. The resulting ionization degree α of the plasma is defined as

$$\alpha = \frac{n_e}{n_{\text{total}}}, \quad (16)$$

with $n_{\text{total}} = n_{\text{atoms}} + 2n_{H_2} + n_e$ and the density of all atoms $n_{\text{atoms}} = \sum_i n_{i,\text{atom}}$.

The numerical calculations were benchmarked against the analytical solution of Eqs. (17)–(19) for a pure hydrogen plasma composed of H_2 , H, H^+ , and electrons:

$$\frac{m_{H_2}}{K_{H_2}} n_H^2 + m_H n_H + m_{H^+} \sqrt{n_H K_H^+} - \rho = 0. \quad (17)$$

In the analytical model, the density of H atoms n_H is obtained from the solution of Eq. (17). Furthermore, using n_H , we can calculate n_{H_2} and n_{H^+} via the following equations:

$$n_{H_2} = \frac{n_H^2}{K_H}, \quad (18)$$

$$n_{H^+} = \sqrt{n_H K_H^+}. \quad (19)$$

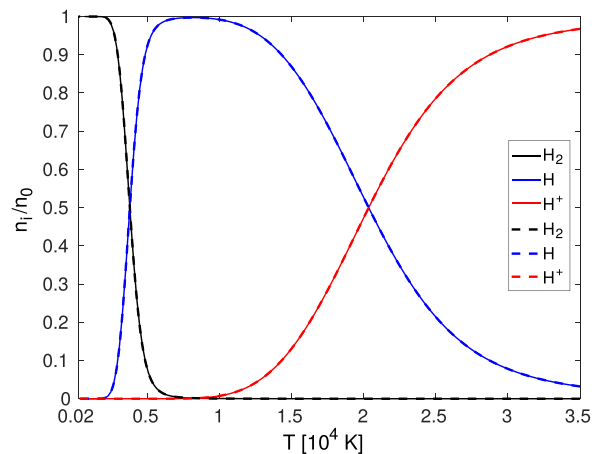


FIG. 1. Composition of hydrogen plasma as a function of temperature for a mass density of $\rho = 10^{-5}$ g/cm³. Solid lines show analytical results via Eqs. (17)–(19) and dashed lines numerical results. The normalization $n_0 = n_{H_2} + n_H + n_{H^+}$ refers here to the total number density of hydrogenic species in the plasma.

For benchmarking, the mass density ρ of the plasma is kept constant at 10^{-5} g/cm³ and the composition is calculated as a function of the temperature (see Fig. 1). The analytical and numerical results are virtually identical. At low temperatures, hydrogen is a molecular gas; the molecules dissociate into atoms with increasing temperature. At even higher temperature, the ionization processes lead to a hydrogen plasma. For further validation, we compare our results for the ionization degree with those of Schlages *et al.* [37] and find good agreement.

III. ELECTRONIC TRANSPORT COEFFICIENTS

The electronic contribution to the electrical conductivity σ_e , the thermal conductivity λ_e , and the Lorenz number L are defined as [27,38]

$$\sigma_e = e^2 K_0, \quad (20)$$

$$\lambda_e = \frac{1}{T} \left(K_2 - \frac{K_1^2}{K_0} \right), \quad (21)$$

$$L = \left(\frac{e}{k_B} \right)^2 \frac{\lambda_e}{\sigma_e T}, \quad (22)$$

where e is the elementary charge and K_n are Onsager coefficients ($n = 0, 1, 2$) that are composed of individual specific Onsager coefficients $K_{n,es}$ via

$$K_n^{-1} = \sum_s K_{n,es}^{-1}. \quad (23)$$

The expressions for $K_{n,eN}$ and $K_{n,eI}$ are taken from French and Redmer [27] and describe the contribution of electron scattering from neutral (index N) and ionic (index I) species, respectively. We have considered electron-neutral scattering only for H, H₂, and He atoms or molecules because of the very small overall abundance of the heavier elements. The analytical expression of the specific Onsager coefficients for electron-neutral scattering for Eq. (23) is

$$K_{n,eN} = \frac{2^{11/2} \pi^{1/2} (n+3)! \epsilon_0^2 (k_B T)^{n+3/2} n_e}{3 Z_N^2 e^4 m_e^{1/2} n_N \ln A_N(x_N)}. \quad (24)$$

The specific Onsager coefficients for electron-ion scattering for Eq. (23) read

$$K_{n,eI} = \frac{2^{11/2} \pi^{1/2} (n+3)! \epsilon_0^2 (k_B T)^{n+3/2} n_e}{3 Z_I^2 e^4 m_e^{1/2} n_I \ln \Lambda(B_n)}. \quad (25)$$

The logarithmic functions $\ln A_N(x_N)$ and $\ln \Lambda(B_n)$ are defined in Ref. [27]. Electron-electron scattering is accounted for by correction factors according to Spitzer and Härm [28] in the Onsager coefficients for electron-ion scattering $K_{n,eI}$. The respective formula and parameters are taken from French and Redmer [27]. The effect of electron-electron scattering on the electrical and thermal conductivity of dense plasmas in the warm dense matter regime has been studied by Reinholz *et al.* [29] using the linear response theory and by Dejarlais *et al.* [30] using the Kohn-Sham density functional theory. The expressions for the Onsager coefficients including

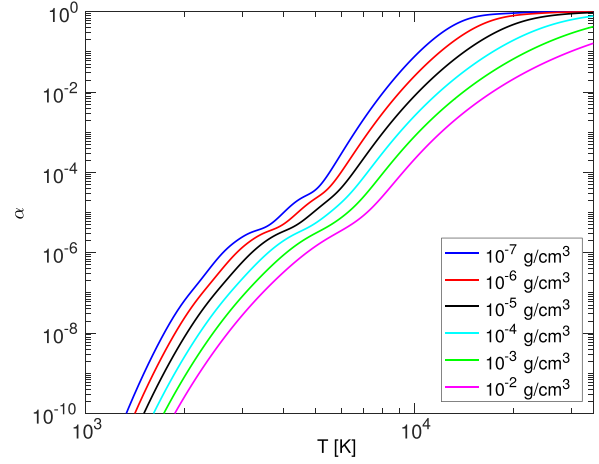


FIG. 2. Ionization degree of the PIP as a function of temperature for different mass densities.

electron-electron scattering are

$$K_{0,el+ee} = \frac{f_e}{f_I} K_{0,eI}, \quad (26)$$

$$K_{1,el+ee} = \frac{a_e f_e}{a_I f_I} K_{1,eI} + \frac{5}{2} k_B T \left(\frac{f_e}{f_I} - \frac{a_e f_e}{a_I f_I} \right) K_{0,eI}, \quad (27)$$

$$K_{2,el+ee} = \frac{L_e f_e}{L_I f_I} \left(K_{2,eI} - \frac{K_{1,eI}^2}{K_{0,eI}} \right) + \frac{K_{1,el+ee}^2}{K_{0,el+ee}}, \quad (28)$$

where the factors f_I , f_e , a_I , a_e , L_I , and L_e are defined in Ref. [27].

IV. RESULTS FOR ELECTRONIC TRANSPORT IN PIP

The plasma composition, i.e., the partial number densities n_i of each species obtained from solving the coupled equations (10)–(15), is a necessary input for the calculation of the electronic transport coefficients. Therefore, we first show the behavior of the ionization degree as a function of the temperature at different mass densities in Fig. 2. The ionization degree α is increasing with the temperature due to thermal ionization of the constituents and decreasing with the mass density of the plasma.

The variation of σ_e and λ_e with the temperature at different mass densities is displayed in Figs. 3 and 4, respectively. The curves for σ_e and λ_e show a systematic increase with temperature, caused by thermal ionization of the constituents in the order of their ionization energies, which leads to an enhancement of the free electron density in the PIP. On the other hand, σ_e and λ_e are decreasing with mass density due to more frequent scattering processes with neutral species. At high temperatures (above 20 000 K), σ_e and λ_e are increasing with mass density, oppositely to their low-temperature characteristics. This reversal is emerging because the ionization degree is still increasing with temperature for the higher densities but it is already saturated for the lower densities. The quantities

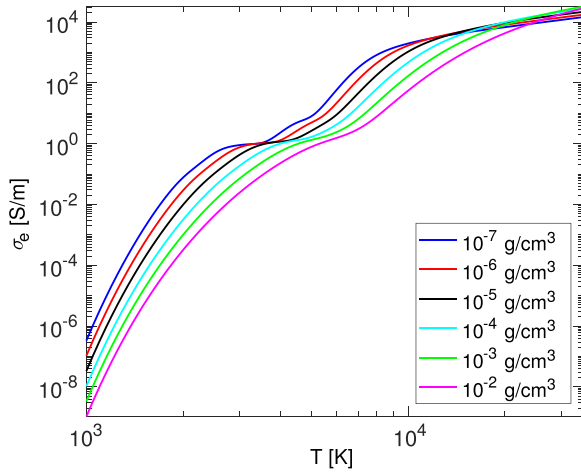


FIG. 3. Electrical conductivity of the PIP as a function of temperature for different mass densities.

α , σ_e , and λ_e show plateaulike structures. When the plateau is reached, all metals (see Table I) are ionized but H and He require still higher temperatures to contribute to the ionization degree significantly and thus to the electrical and thermal conductivities, which lead to the increase after the plateau. The Lorenz number shown in Fig. 5 first increases with the temperature and, after passing through a maximum, decreases for still higher temperatures. This behavior is shifted systematically towards higher temperatures with increasing density. The high- and low-temperature limiting values of L are determined by the known Spitzer limit in the fully ionized plasma and electron-neutral cross sections in the weakly ionized gas, respectively. The occurrence of the pronounced maximum in L is caused by different energetic weightings of the cross sections in the specific Onsager coefficients [see Eqs. (24) and (25)]. It should be noted that the correction due to electron-

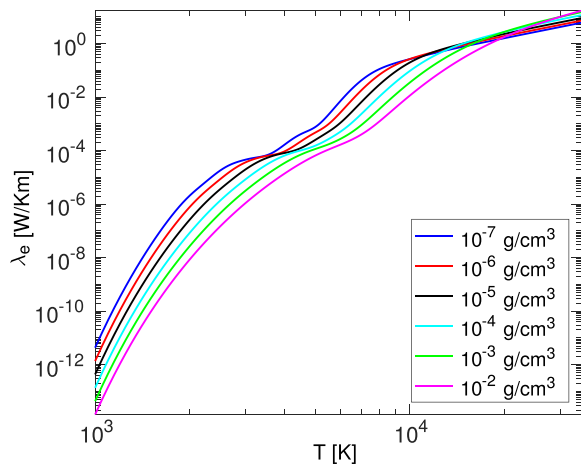


FIG. 4. Thermal conductivity of the PIP as a function of temperature for different mass densities.

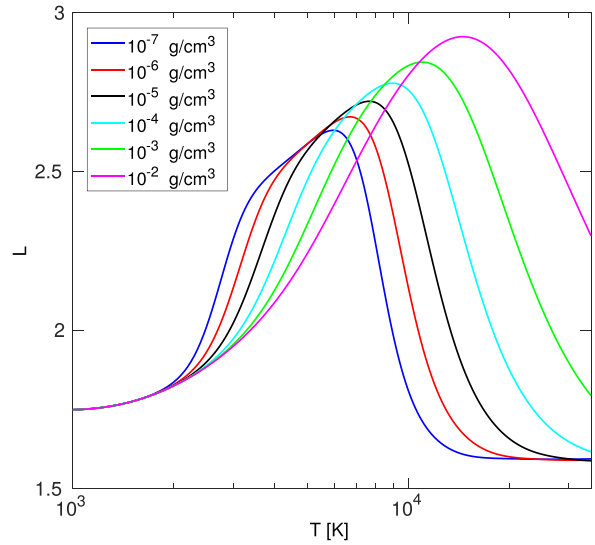


FIG. 5. Lorenz number of the PIP as a function of temperature for different mass densities.

electron scattering is only important when the majority of constituent elements are at least singly ionized.

V. THERMAL CONDUCTIVITY FROM NEUTRALS AND CHEMICAL REACTIONS

At low temperatures, the ionization degree is small and therefore the neutral particles contribute significantly to the heat transport. In addition to their translational contribution λ_{tr} , the occurrence of dissociation and ionization reactions also enhances the thermal conductivity in the corresponding temperature region, described by a term λ_r . These contributions have to be added to the electronic heat conductivity λ_e so that the total thermal conductivity λ of the PIP is given by

$$\lambda = \lambda_e + \lambda_{tr} + \lambda_r. \quad (29)$$

We have neglected the translational contribution of ions to the thermal conductivity because it is very small in comparison to that of the electrons λ_e [39,40]. For the neutrals, we have adopted the Chapman-Enskog model for the calculation of the translational heat transport. The first-order expression for λ_{tr} for a single-component gas is given by [41]

$$\lambda_i^{tr} = \frac{25}{32} \left(\frac{k_B T \pi}{m_i} \right)^{1/2} \frac{C_{v,i}}{\Omega_{ii}^{(2,2)}(T)}, \quad (30)$$

where $\Omega_{ii}^{(2,2)}(T)$ is a collision integral and $C_{v,i} = 3k_B/2$ is the heat capacity for atoms of species i at constant volume. The collision integral depends upon the energy-dependent transport cross section. We have simplified the collisional integral by assuming the atoms or molecules to be rigid spheres of diameter d_{ii} so that $\Omega_{ii}^{(2,2)}(T)$ becomes temperature independent and is reduced to πd_{ii}^2 . The simplified formula of λ_i^{tr} is then

given by

$$\lambda_i^{tr} = \frac{25}{32} \left(\frac{k_B T \pi}{m_i} \right)^{1/2} \frac{C_{v,i}}{\pi d_{ii}^2}. \quad (31)$$

The vibrational heat capacity C_{v,H_2}^{vib} of hydrogen molecules is calculated using the harmonic approximation [34]

$$C_{v,H_2}^{vib} = k_B \left(\frac{\theta_v}{T} \right)^2 \frac{\exp(\frac{\theta_v}{T})}{[\exp(\frac{\theta_v}{T}) - 1]^2}. \quad (32)$$

The rotational heat capacity C_{v,H_2}^{rot} of hydrogen molecules is calculated by considering $T \gg \theta_r$ so that

$$C_{v,H_2}^{rot} = k_B. \quad (33)$$

For a multicomponent plasma as considered here, we use a generalized formula for the calculation of the translational thermal conductivity of mixtures, which reads [42–44]

$$\lambda_{tr} = \sum_i \frac{x_i \lambda_i^{tr}}{1 + \sum_{j \neq i} \frac{x_j}{x_i} \phi_{ij}}. \quad (34)$$

Here x_i is the molar fraction of species i and $\phi_{ij} = (2\mu_{ij}/m_i)^2$ depends on the reduced mass μ_{ij} and mass of species i .

In the calculation of λ_r we assume that the chemical reactions occur in different temperature regions, so their contributions are additive, according to an expression given by Butler and Brokaw [45,46],

$$\lambda_r = \sum_a \frac{(\Delta H_a)^2}{RT^2} \frac{1}{A_a}, \quad (35)$$

with

$$A_a = \sum_{k=1}^{\beta-1} \sum_{l=k+1}^{\beta} \left(\frac{RT}{PD_{kl}} \right) x_k x_l \left[\left(\frac{v_{k,a}}{x_k} \right) - \left(\frac{v_{l,a}}{x_l} \right) \right]^2, \quad (36)$$

where ΔH_a is the heat of the reaction a , β is the number of species involved in the reaction, k represents the k th species, R is the universal gas constant, $P = \sum_i n_i k_B T$ is the ideal pressure, and D_{kl} is the binary diffusion coefficient between components k and l . The heat of the reaction ΔH_a is calculated from the reaction constant by van't Hoff's equation [47,48]

$$\frac{\Delta H_a}{RT^2} = \frac{d \ln K_a}{dT}. \quad (37)$$

We use the following expression for the neutral-neutral and neutral-ion binary diffusion coefficients [49]:

$$PD_{kl} = \frac{3}{16} \frac{\sqrt{2\pi k_B^3 T^3 / \mu_{kl}}}{\pi d_{kl}^2}. \quad (38)$$

For the electron-neutral and electron-ion diffusion coefficients, we have used the Darken relation and the adiabatic approximation [50], which leads to

$$D_{ke} = x_k D_e + x_e D_k \approx x_k D_e. \quad (39)$$

This expression depends only on the self-diffusion coefficient D_e of the electrons that can be related to their electrical conductivity using the Nernst-Einstein relation

$$PD_{ke} = \frac{x_k}{x_e} \left(\frac{k_B T}{e} \right)^2 \sigma_e. \quad (40)$$

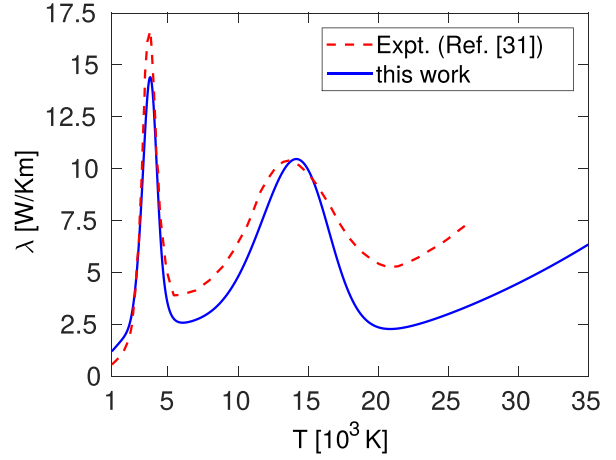


FIG. 6. Thermal conductivity of partially ionized hydrogen plasma as a function of temperature at a constant pressure of 1 bar. We compare our results with the arc-discharge experiment of Behringer and van Cung [31], which was evaluated using the local thermodynamic equilibrium assumption.

We consider the λ_{tr} and λ_r contributions to the thermal conductivity only for species and reactions containing the elements H and He. The hard-sphere diameters of H_2 , H, and He are taken from Table II in Ref. [51], specifically of H- H_2 collision data at 3500 K. We have parametrized the effective H- H^+ interaction diameter in our model by matching the height of the second peak in the thermal conductivity profile with that from hydrogen arc-discharge experiments at $P = 1$ bar [31]; the comparison is shown in Fig. 6. The He- He^+ and $He^+ - He^{2+}$ interaction diameters have been calculated from Eq. (38) by using the diffusion coefficient value of Devoto and Li at 24 000 K [52]. All hard-sphere diameter values used for the calculation of the thermal conductivity are compiled in Table II.

The variation of λ , λ_r , λ_{tr} , and λ_e with the temperature is displayed in Fig. 7, again for a constant density of 10^{-5} g/cm³. The λ_{tr} contribution fully determines the total thermal conductivity at the lowest temperatures considered here. Note that the electronic contribution can be neglected there because the ionization degree is virtually zero (see Fig. 1). The first peak in λ at about 4000 K emerges due to the dissociation reaction heat conductivity of H_2 molecules in the PIP. This

TABLE II. Square of the hard-sphere diameters d_{ij} for the interactions between the various species as used in the calculation of the thermal conductivity.

Collision	d_{ij}^2 (\AA^2)
$H_2 - H_2$	2.634
$H - H_2$	2.634
$H - H$	2.634
$H - H^+$	11.00
$He - He$	2.634
$He - He^+$	13.978
$He^+ - He^{2+}$	13.978

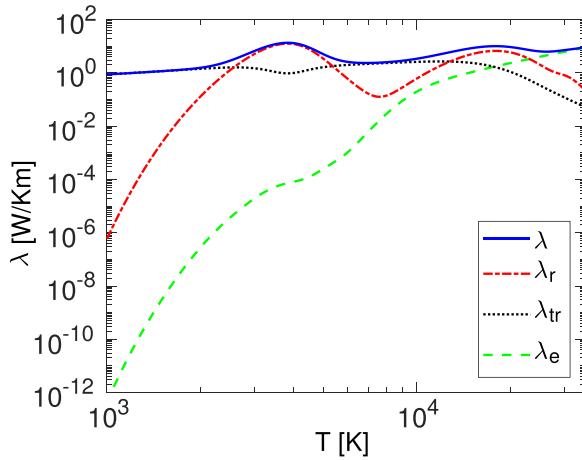


FIG. 7. Total thermal conductivity λ according to Eq. (29) as a function of temperature at 10^{-5} g/cm³. The contributions of the translational motion of neutrals λ_r and of the heat of chemical reactions λ_r and the electronic contribution are shown separately.

contribution becomes smaller at higher temperatures because most of the H₂ molecules are dissociated into H atoms. As temperature increases further, the H atoms are ionized, which leads to a second peak in the thermal conductivity at about 20 000 K due to the corresponding ionization reaction heat. A shoulder in λ_r emerges at about 30 000 K due to the ionization of He. The free electron density n_e is systematically increasing with temperature so that λ_e dominates the thermal conductivity λ in the high-temperature limit above 25 000 K and both λ_{tr} and λ_r can be neglected there.

VI. APPLICATION TO THE ATMOSPHERE OF THE HOT JUPITER HD 209458b

HD 209458b was the first exoplanet observed transiting its host star [53]. With an orbital period of 3.5 days, a semimajor axis of only 0.047 AU, a radius of $1.36R_J$, and a mass of $0.69M_J$, HD 209458b is clearly an inflated hot Jupiter [54]. Here R_J and M_J denote Jupiter's radius and mass, respectively.

In this section we apply the methods discussed above to HD 209458b and discuss how the updated electrical conductivity would affect Ohmic heating. The electrical currents responsible for the Ohmic heating could penetrate down to a pressure level of few kbar according to BS. We therefore focus the application of our PIP model on this pressure range and start by discussing the corresponding P - T profile.

A. The P - T profile of the atmosphere

We calculate the composition and the transport coefficients of the planetary PIP for the four planetary models shown in Fig. 8. The atmospheric models are obtained by fitting semianalytical one-dimensional parametrizations to pressure-temperature profiles suggested in the literature, following the approach by Poser *et al.* [55]. The parametrization guarantees a consistent description and allows us to extend all models to

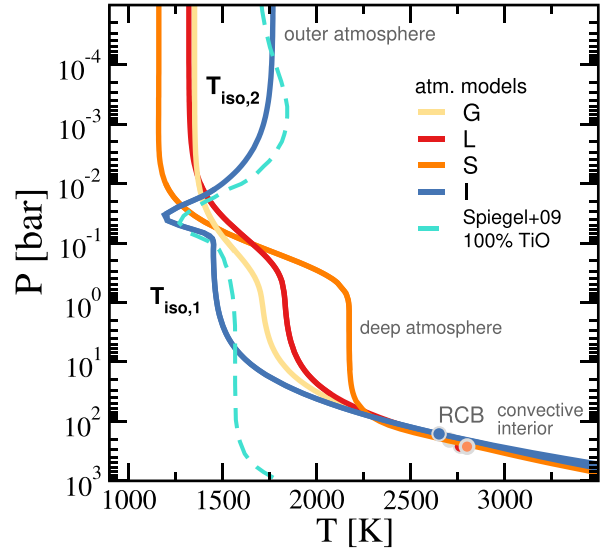


FIG. 8. Pressure-temperature profiles of the atmosphere of HD 209458b. Shown are the four atmospheric models used in this work, three without an inversion, namely, G (yellow), L (red), and S (orange), and one with an inversion in the temperature, I (blue), located at about 0.03 bar. Further features of the models are displayed: the location of the radiative-convective boundary, the onset of the convective interior, and the characteristic temperatures $T_{iso,1}$ and $T_{iso,2}$.

the same pressure range and to connect them to an adiabatic interior.

Model G is based on the globally averaged theoretical P - T curve by Guillot [56], while model L replicates the most recent result by Line *et al.* [57], which is based on high-resolution spectroscopy data of the Hubble Space Telescope and data from the Spitzer Space Telescope for the planet's dayside. Both profiles turn out to be very similar. Profiles S and I follow suggestions by Spiegel *et al.* [58]. While profile S has a particularly high temperature between 0.3 and 100 bar, model I, based on the variant with a solar abundance of TiO by Spiegel *et al.* [58], shows a temperature inversion at pressures smaller than 30 mbar. The reason is that the highly abundant TiO serves as an additional absorber in the upper atmosphere and leads to the rise in temperature.

Our parametrization of model I is broadly similar to the original profile of Spiegel *et al.* [58] but assumes a shallower transition to the convective interior and thus predicts higher temperatures for pressures beyond 10 bar. In addition, our temperatures are up to 100 K lower than the original in the isothermal region between 1 and 10 mbar. Between 10^{-2} and 10^{-3} bar, the original shows a local maximum that is not present in our model. The temperatures in profile I are therefore up to 200 K colder than in the original paper.

We connect our atmosphere profiles to an adiabatic interior model at the pressure level where the atmospheric temperature gradient matches with the adiabatic gradient. The respective transition points are marked with circles in Fig. 8. The interior model is derived from the usual structure equations for nonrotating spherical gas planets (see, e.g., [59]). Like BS, we use a solar helium mass fraction of $Y = 0.24$, assume no planetary

SANDEEP KUMAR *et al.*PHYSICAL REVIEW E **103**, 063203 (2021)

core, and set the heavy-element mass fraction of both the atmosphere and the interior to the solar reference metallicity of $Z_{\odot} = 0.015$ [33]. For H and He we use the equation of state (EOS) of Saumon *et al.* [60]. Heavy elements are represented by the ice EOS of Hubbard and Marley [61]. The upper boundary of our interior model is set to $P_{\text{out}}(R_P) = 10^{-2}$ bar. The heat flux from below is determined by the interior model (no core). The observed radius inflation is then obtained by adding extra energy during the thermal evolution [55,62].

Batygin and Stevenson also used variants of the original model I by Spiegel *et al.* [58] for their Ohmic dissipation study. Like us, they assumed a transition to an adiabatic interior model in a comparable pressure range. Their exact profiles have not been published but are likely similar to our model I.

Beyond the radiative-convective boundary (RCB), the atmosphere models span a large temperature range of up to 750 K around 1 bar. This may partly be owed to the large local variation in brightness temperature with a dayside-to-nightside difference of about 500 K [63] but mostly reflects the different model assumptions and a lack of observational constraints [64]. Note, however, that the most recent observation-based model by Line *et al.* [57] could not confirm the inversion discussed by Spiegel *et al.* [58] and covers an intermediate-temperature range.

All of our atmosphere models have two nearly isothermal regions. The deeper region, labeled $T_{\text{iso},1}$ in Fig. 8, is a typical feature in strongly irradiated planets [12,65]. The shallower isothermal region $T_{\text{iso},2}$ from the 10 mbar level to the outer boundary of our models is typical for analytical, semigray atmosphere models (see, e.g., [66]). For profiles G, L, and S, both regions are connected by a pronounced temperature drop of several hundred degrees Kelvin. In the inversion profile, the temperature first drops but then increases towards the outer boundary.

B. Transport properties of the atmosphere

We have calculated the ionization degree α , the electrical conductivity σ_e , and the thermal conductivity λ along our four P - T models for HD 209458b (see Fig. 9). The ionization degree [Fig. 9(b)] and the electrical conductivity [Fig. 9(d)] are closely related and follow a very similar behavior (see Sec. IV). The thermal conductivity profile [Fig. 9(c)] also shows a similar form but with much smaller variations.

In the two isothermal regions of each profile, the decreasing density causes α and σ_e to increase outward. However, the drastic changes of temperature in the intermediate regions influence α and σ_e in more characteristic ways. This is especially the case in the inversion region in profile I (blue), where we find pronounced minima of α and σ_e near 30 mbar (see Fig. 9).

Due to the large differences between the models, the ionization degree and electrical conductivity differ by up to three orders of magnitude for the same pressure. The drop in electrical conductivity between the two isothermal regions varies from one order of magnitude in model G to more than three orders of magnitude in model S. The increase from the inner isothermal region to the RCB varies from a bit more than two orders of magnitude in model S to four orders of magnitude in

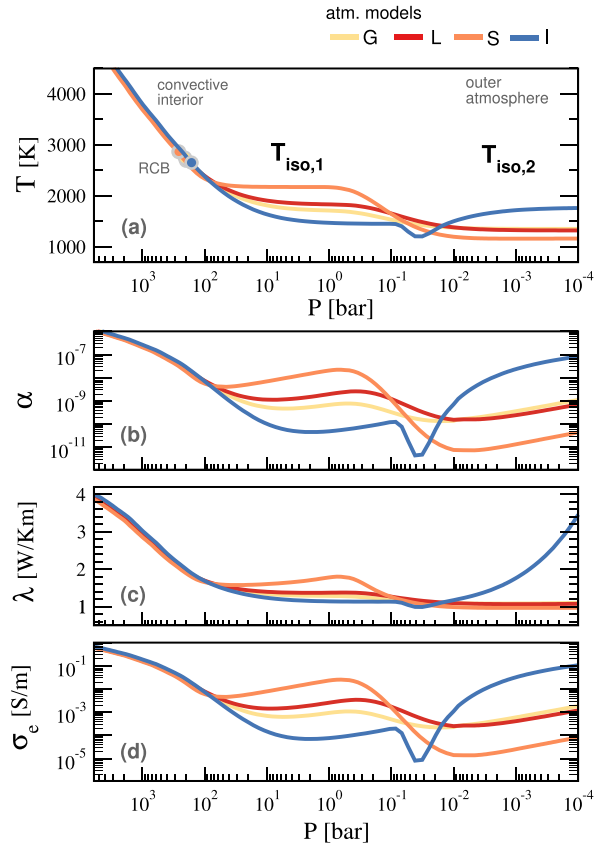


FIG. 9. Temperature T , ionization degree α , thermal conductivity λ , and electrical conductivity σ_e for different planetary interior models along the pressure axis of HD 209458b, specifically, for the four atmospheric models used in this work: G (yellow), L (red), S (orange), and one with an inversion, I (blue). Circles in the temperature profile represent the location of the radiative-convective boundary.

model I. In contrast, the variation of the thermal conductivity between the models is much smaller. The reason is that thermal conductivity is determined mostly by collisions between neutral particles in the relevant temperature range and is thus not susceptible to the strongly changing ionization degree.

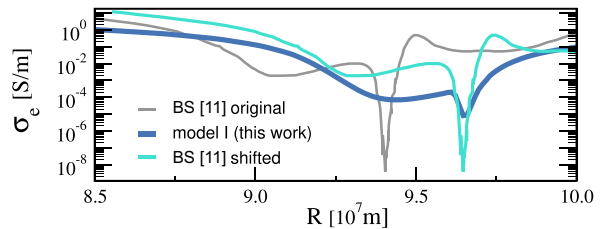


FIG. 10. Electrical conductivity σ_e for model I along the radius axis of HD 209458b, compared to the results of Batygin and Stevenson [11]. We show their original data (gray) as well as a shifted version (cyan) to ease the comparison (see the text).

Figure 10 compares the electrical conductivity for model I with the results taken from Fig. 2 in [11]. The associated pressure profile $P(r)$ is obtained by solving the equation of hydrostatic equilibrium. Each of the curves has a pronounced minimum in the electrical conductivity. Note that these minima are located at different radii in Fig. 10, which is likely caused by a different planetary radius assumed by BS that unfortunately was not stated in their paper. For better comparison, we also show a shifted Batygin-Stevenson profile in Fig. 10 that aligns both minima.

The electrical conductivity minimum predicted by BS is extraordinarily deep, with σ_e dropping by six orders of magnitude. In contrast, the temperature dependence of our model (see Fig. 3) yields a conductivity drop by only two orders of magnitude at the 300 K temperature dip of our model I.

In the inner isothermal region, the electrical conductivity is two orders of magnitude lower than suggested by BS. Unfortunately, we do not know the exact atmosphere model used by BS but, as discussed above, it seems conceivable that the temperatures in this region are about 100 K lower than assumed by BS for their Fig. 2. According to Fig. 3, however, this would only explain a conductivity difference by about a factor 5. At very low pressures and also toward the RCB, the electrical conductivities become more similar, likely because our model assumes higher temperatures. At the RCB, our electrical conductivity is about one order of magnitude lower than suggested by BS.

C. Ohmic dissipation

The electric currents \vec{j}_e in the outer atmosphere are induced by the interaction of the fierce atmospheric winds with the planetary magnetic field according to Ohm's law

$$\vec{j}_e = \sigma_e(\vec{U} \times \vec{B}_0 - \vec{\nabla}\Phi), \quad (41)$$

where \vec{U} is the wind velocity, \vec{B}_0 the internally produced background field, and Φ the electric potential. Note that we use a fluid approach where the velocity describes the motion of the neutral medium (neutrals, ions, and electrons). Furthermore, we use a linear approximation, assuming that the magnetic field locally produced by the currents is smaller than the background field [67,68]. Using the fact that the currents are divergence-free, i.e., $\vec{\nabla} \cdot \vec{j}_e = 0$, allows calculating the missing electric potential (BS). The global heating power from Ohmic dissipation is then simply given by the following volume integral:

$$\dot{Q} = \int \frac{j_e^2}{\sigma_e} dV. \quad (42)$$

Being driven by the differential irradiation, the depth of the winds is limited [69]. Batygin and Stevenson assume that they penetrate down to the 10 bar level. Because the minimum in the electrical conductivity around 30 mbar provides a boundary for the electric currents, only the layer from 10 bar up to this minimum has to be considered for inducing the currents that could potentially penetrate deeper into the planet. We refer to this region as the induction layer. While the electric currents in the induction layer already provide very powerful heating, the deeper penetrating currents are more relevant for explaining the inflation. We refer to the deeper layer where

these currents remain significant as the leakage layer, which may extend from 10 bar to a few kbar (BS).

With no appreciable flows being present between 10 bar and the RCB, the respective currents in the leakage layer obey the simpler relation

$$\vec{j}_e = -\sigma_e \vec{\nabla}\Phi. \quad (43)$$

The electric potential differences $\vec{\nabla}\Phi$ are determined by the action in the induction layer and the electrical conductivity distribution. Batygin and Stevenson therefore call the leakage layer the inert layer. The electrical conductivity profile controls how deep the currents produced in the induction layer flow into the leakage layer.

We can now roughly quantify the changes in Ohmic heating compared to those of BS by simply rescaling their results with our electrical conductivity profiles. Batygin and Stevenson assumed a simple flow structure with typical velocities of $U = 1$ km/s and a background field strength of $B_0 = 10$ G. Because our electrical conductivity is about two orders of magnitude lower in the induction layer, the induced electric currents are two orders of magnitude weaker, according to Eq. (41). Consequently, the Ohmic heating power (42) is also two orders of magnitude lower.

In the leakage layer, the currents encounter a conductivity that is more similar to the one assumed by BS. Assuming that the conductivity is one order of magnitude lower (see Fig. 10), the deeper Ohmic heating is about 10^{-3} times smaller than in the work of BS. Explaining the inflation of HD 209458b requires a power of about 4×10^{18} W to be deposited at or below the RCB [19]. While the models considered by BS deposit up to 10^{20} W in the convective interior, the lower electrical conductivity of model I would render Ohmic heating too inefficient.

However, as shown above, the Ohmic heating processes depend strongly on the conductivity and thus on the atmosphere model. Because of the higher temperatures, the electrical conductivity in the induction layers of the most-up-to-date model L is comparable to that assumed by BS; consequently, the induced currents also have a similar magnitude. If assuming once more a ten times lower conductivity in the leakage layer, the leakage layer heating will be ten times stronger than in the work of BS, which is more than enough to explain the inflation. For model S, the heating will be even stronger because of the particularly high temperatures in the induction region.

Because the electrical currents depend linearly on the wind velocity U and the background field strength B_0 , the heating power (42) scales quadratically with both of these quantities. Updating the value of $U = 1$ km/s assumed by BS with a newer estimate of $U = 2$ km/s [70] thus increases Ohmic heating by a factor of 4. On the contrary, an indirect reassessment of the magnetic field strength of HD 209458b suggests that it may as well be on the order of 1 G [71] rather than the 10 G assumed by BS. This would reduce the Ohmic heating power by a factor of 100 and may once more render the process too inefficient to explain the inflation.

All the estimates discussed above represent a linear approximation, assuming that the magnetic field produced by the locally induced currents is smaller than the background field in Eq. (41) [67,68,72]. The ratio of the locally induced

field to the background field is roughly given by the magnetic Reynolds number

$$\text{Rm} = Ud\sigma_e\mu_0, \quad (44)$$

where μ_0 is the magnetic permeability of vacuum and d the electrical conductivity scale height

$$d = \frac{\sigma_e}{|\partial\sigma_e/\partial r|}. \quad (45)$$

The linear approximation therefore breaks down when Rm exceeds one. When assuming $U = 1$ km/s and the value $d = 3 \times 10^2$ km as suggested by Fig. 10, this happens where the electrical conductivity is larger than $\sigma_e = 10^{-2}$ S/m in the induction region. Model S, where $T_{\text{iso},1} = 2200$ K, is the only model for which the linear approximation is certainly questionable.

Observations suggest that dayside and nightside temperatures of HD 209458b differ by roughly 500 K [63]. The fact that this difference is smaller than expected is, like the pronounced hot-spot shift [63], likely the result of heat distribution by the fierce winds in the upper atmosphere. The temperature dependence proposed here predicts that the electrical conductivity in the nightside induction region is about 10^3 times lower than on the dayside. We thus expect that dayside heating would dominate.

VII. CONCLUSION

We have presented a model for calculating the chemical composition and electrical and thermal conductivity of low-density multicomponent plasmas suitable for applications in atmospheres of hot Jupiters. This model is based on mass-action laws and cross sections for all binary particle interactions and generalizes an earlier model for the thermoelectric properties of one-component plasmas [25] to multicomponent plasmas. We have shown that the results for the ionization degree and in particular for the electrical conductivity can differ by several orders of magnitude from simpler models applied to hot Jupiter [11,73] or hot Neptune atmospheres [17].

Note that the plasma becomes nonideal with increasing depth (i.e., density), so interaction contributions have to be treated when evaluating MALs for deeper atmosphere regions. Furthermore, simple expressions for the cross sections as used here no longer apply and the different scattering processes have to be treated on the T matrix level by calculating the corresponding scattering phase shifts (see, e.g., [5,23–25,74]). It would also be interesting to study the influence of the magnetic field of the planet on the transport properties, in particular for the hot and dilute outer atmosphere (ionosphere). This is a subject left for future work.

The plasma is strongly coupled and degenerate in the deep interior of the planet, so first-principles approaches have to be applied in order to calculate the corresponding equation

of state data, the ionization degree, and the transport properties. For instance, extensive molecular-dynamics simulations have been performed for the ions in dense H-He plasmas in combination with electronic structure calculations using density functional theory (density functional theory–based molecular-dynamics method). The corresponding results provide a reliable database to determine interior profiles for density, temperature, and pressure [75] and to simulate the dynamo process based on further material properties such as electrical and thermal conductivities [76,77] for Jupiter [78] and Jupiter-like planets. The deep interior, however, is not important for the study of Ohmic dissipation in the outer atmosphere, so the current results persist.

We have therefore used our results to predict the thermal and electrical conductivities for four different models proposed for the atmosphere of the hot Jupiter HD 209458b. The estimates suggest that the electrical conductivity is between one and two orders of magnitude lower than assumed by BS [11] in their study of Ohmic heating. While BS concluded that this additional heat source could explain the observed inflation of HD 209458b, our updated conductivities reduce the effect by up to three orders of magnitude and would make Ohmic heating too inefficient.

However, newer internal models [57] suggest significantly higher temperatures in the planet’s atmosphere than assumed for these estimates. The resulting higher electrical conductivity would guarantee more than enough Ohmic heat to explain the inflation, even for our lower electrical conductivity values. The large uncertainties in the atmospheric temperature, but also in the planet’s magnetic field strength [71], yet prevent us from giving reliable estimates of Ohmic heating in the atmosphere of HD 209458b.

Our estimates for the electric currents and thus for the Ohmic heating power largely follow simple scaling arguments based on previous attempts [11,72]. It would be interesting to run refined numerical models that solve for electrical currents using the updated conductivities proposed here. Because of the significant radial and dayside-to-nightside variation in temperature, the electrical conductivity will also have a three-dimensional field structure, making three-dimensional simulations essential. Repeating the simplified calculations by BS would be a first step. However, full magnetohydrodynamic simulations are required should the locally induced magnetic fields and associated Lorentz forces prove important.

ACKNOWLEDGMENTS

We thank Jan Maik Wissing for providing altitude data of the thermosphere and Nadine Nettelmann, Ludwig Scheibe, Martin Preising, and Clemens Kellermann for helpful discussions. This work was supported by the Deutsche Forschungsgemeinschaft within the Priority Program SPP 1992 “The Diversity of Exoplanets” and the Research Unit FOR 2440 “Matter under Planetary Interior Conditions.”

[1] W. Ebeling, V. E. Fortov, Y. L. Klimontovich, N. P. Kovalenko, W. D. Kraeft, Y. P. Krasny, D. Kremp, P. P. Kulik, V. A. Riaby,

G. Röpke, E. K. Rozanov, and M. Schlanges, *Transport Properties of Dense Plasmas* (Akademie-Verlag, Berlin, 1983).

- [2] K. Günther and R. Radtke, *Electric Properties of Weakly Non-ideal Plasmas* (Akademie-Verlag, Berlin, 1984).
- [3] W.-D. Kraeft, D. Kremp, W. Ebeling, and G. Röpke, *Quantum Statistics of Charged Particle Systems* (Akademie-Verlag, Berlin, 1986).
- [4] V. Fortov and I. Iakubov, *Physics of Nonideal Plasma* (Hemisphere, New York, 1990).
- [5] R. Redmer, *Phys. Rep.* **282**, 35 (1997).
- [6] A. Likalter, *Phys. Scr.* **55**, 114 (1997).
- [7] A. A. Ovechkin, P. A. Loboda, and A. L. Falkov, *High Energy Density Phys.* **20**, 38 (2016).
- [8] M. R. Zaghoul, *Plasma Phys. Rep.* **46**, 574 (2020).
- [9] M.-B. Kallenrode, *Space Physics* (Springer, Berlin, 2001).
- [10] J. M. Wissing and M.-B. Kallenrode, *J. Geophys. Res.* **114**, A06104 (2009).
- [11] K. Batygin and D. J. Stevenson, *Astrophys. J. Lett.* **714**, L238 (2010).
- [12] T. D. Komacek and A. N. Youdin, *Astrophys. J.* **844**, 94 (2017).
- [13] N. Yoshida, K. Omukai, and L. Hernquist, *Science* **321**, 669 (2008).
- [14] S.-I. Inutsuka, *Prog. Theor. Exp. Phys.* **2012**, 01A307 (2012).
- [15] C. M. Franck and M. Seeger, *Contrib. Plasma Phys.* **46**, 787 (2006).
- [16] X. Guo, X. Li, A. B. Murphy, and H. Zhao, *J. Phys. D* **50**, 345203 (2017).
- [17] B. Pu and D. Valencia, *Astrophys. J.* **846**, 47 (2017).
- [18] P. Sarkis, C. Mordasini, T. Henning, G. Marleau, and P. Molliere, *Astron. Astrophys.* **645**, A79 (2021).
- [19] A. Burrows, I. Hubeny, J. Budaj, and W. B. Hubbard, *Astrophys. J.* **661**, 502 (2007).
- [20] T. Rogers and A. Showman, *Astrophys. J. Lett.* **782**, L4 (2014).
- [21] R. S. Freedman, M. S. Marley, and K. Lodders, *Astrophys. J. Suppl. Ser.* **174**, 504 (2008).
- [22] R. Redmer, T. Rother, K. Schmidt, W. D. Kraeft, and G. Röpke, *Contrib. Plasma Phys.* **28**, 41 (1988).
- [23] R. Redmer, *Phys. Rev. E* **59**, 1073 (1999).
- [24] S. Kuhlbrodt and R. Redmer, *Phys. Rev. E* **62**, 7191 (2000).
- [25] S. Kuhlbrodt, B. Holst, and R. Redmer, *Contrib. Plasma Phys.* **45**, 73 (2005).
- [26] M. Schöttler, R. Redmer, and M. French, *Contrib. Plasma Phys.* **53**, 336 (2013).
- [27] M. French and R. Redmer, *Phys. Plasmas* **24**, 092306 (2017).
- [28] L. Spitzer and R. Härm, *Phys. Rev.* **89**, 977 (1953).
- [29] H. Reinholz, G. Röpke, S. Rosmej, and R. Redmer, *Phys. Rev. E* **91**, 043105 (2015).
- [30] M. P. Desjarlais, C. R. Scullard, L. X. Benedict, H. D. Whitley, and R. Redmer, *Phys. Rev. E* **95**, 033203 (2017).
- [31] K. Behringer and N. van Cung, *Appl. Phys.* **22**, 373 (1980).
- [32] K. Lodders, in *Lecture Notes of the Kodai School on Synthesis of Elements in Stars held at Kodaikanal Observatory, India, 2008*, edited by A. Goswami and B. E. Reddy (Springer, Heidelberg, 2010), pp. 379–417.
- [33] K. Lodders, *Astrophys. J.* **591**, 1220 (2003).
- [34] R. Pathria and P. D. Beale, in *Statistical Mechanics*, 3rd ed., edited by R. Pathria and P. D. Beale (Academic, Boston, 2011), pp. 141–178.
- [35] A. Kramida, Y. Ralchenko, J. Reader, and NIST ASD Team, NIST Atomic Spectra Database, version 5.7.1, available at <https://physics.nist.gov/asd>, National Institute of Standards and Technology, Gaithersburg, 2019.
- [36] F. Bošnjaković and K. F. Knoche, *Technische Thermodynamik: Teil I* (Steinkopff, Heidelberg, 1998).
- [37] M. Schlanges, M. Bonitz, and A. Tschtschjan, *Contrib. Plasma Phys.* **35**, 109 (1995).
- [38] Y. T. Lee and R. M. More, *Phys. Fluids* **27**, 1273 (1984).
- [39] V. Imshennik, *Sov. Astron.* **5**, 495 (1962).
- [40] H. Reinholz, R. Redmer, and D. Tamme, *Contrib. Plasma Phys.* **29**, 395 (1989).
- [41] G. C. Maitland, M. Rigby, E. B. Smith, and W. A. Wakeham, *Intermolecular Forces: Their Origin and Determination*, International Series of Monographs on Chemistry Vol. 3 (Clarendon, Oxford, 1981).
- [42] E. Mason and S. Saxena, *Phys. Fluids* **1**, 361 (1958).
- [43] R. S. Brokaw, *J. Chem. Phys.* **29**, 391 (1958).
- [44] M. P. Saksena and S. C. Saxena, *Appl. Sci. Res.* **17**, 326 (1967).
- [45] R. S. Brokaw, *J. Chem. Phys.* **32**, 1005 (1960).
- [46] J. N. Butler and R. S. Brokaw, *J. Chem. Phys.* **26**, 1636 (1957).
- [47] H. Hanley, R. McCarty, and H. Intemann, *J. Res. Natl. Bur. Stand.* **74A**, 331 (1970).
- [48] G. M. Kremer, *An Introduction to the Boltzmann Equation and Transport Processes in Gases* (Springer Science+Business Media, New York, 2010).
- [49] J. O. Hirschfelder, C. F. Curtiss, R. B. Bird, and M. G. Mayer, *Molecular Theory of Gases and Liquids* (Wiley, New York, 1964), Vol. 165.
- [50] J. P. Hansen and I. R. McDonald, *Theory of Simple Liquids* (Elsevier, Amsterdam, 1990).
- [51] J. Vanderslice, S. Weissman, E. Mason, and R. Fallon, *Phys. Fluids* **5**, 155 (1962).
- [52] R. Devoto and C. Li, *J. Plasma Phys.* **2**, 17 (1968).
- [53] D. Charbonneau, T. M. Brown, D. W. Latham, and M. Mayor, *Astrophys. J.* **529**, L45 (2000).
- [54] D. K. Sing, J. J. Fortney, N. Nikolov, H. R. Wakeford, T. Kataria, T. M. Evans, S. Aigrain, G. E. Ballester, A. S. Burrows, D. Deming, J. M. Désert, N. P. Gibson, G. W. Henry, C. M. Huitson, H. A. Knutson, A. L. D. Etangs, F. Pont, A. P. Showman, A. Vidal-Madjar, M. H. Williamson *et al.*, *Nature (London)* **529**, 59 (2016).
- [55] A. J. Poser, N. Nettelmann, and R. Redmer, *Atmosphere* **10**, 664 (2019).
- [56] T. Guillot, *Astron. Astrophys.* **520**, A27 (2010).
- [57] M. R. Line, K. B. Stevenson, J. Bean, J.-M. Desert, J. J. Fortney, L. Kreidberg, N. Madhusudhan, A. P. Showman, and H. Diamond-Lowe, *Astrophys. J.* **152**, 203 (2016).
- [58] D. S. Spiegel, K. Silverio, and A. Burrows, *Astrophys. J.* **699**, 1487 (2009).
- [59] N. Nettelmann, J. J. Fortney, U. Kramm, and R. Redmer, *Astrophys. J.* **733**, 2 (2011).
- [60] D. Saumon, G. Chabrier, and H. M. van Horn, *Astrophys. J. Suppl. Ser.* **99**, 713 (1995).
- [61] W. B. Hubbard and M. S. Marley, *Icarus* **78**, 102 (1989).
- [62] D. P. Thorngren and J. J. Fortney, *Astrophys. J.* **155**, 214 (2018).
- [63] R. T. Zellem, N. K. Lewis, H. A. Knutson, C. A. Griffith, A. P. Showman, J. J. Fortney, N. B. Cowan, E. Agol, A. Burrows, D. Charbonneau, D. Deming, G. Laughlin, and J. Langton, *Astrophys. J.* **790**, 53 (2014).
- [64] B. Drummond, E. Hébrard, N. J. Mayne, O. Venot, R. J. Ridgway, Q. Changeat, S.-M. Tsai, J. Manners, P. Tremblin, N. L. Abraham, D. Sing, and K. Kohary, *Astron. Astrophys.* **636**, A68 (2020).

SANDEEP KUMAR *et al.*PHYSICAL REVIEW E **103**, 063203 (2021)

- [65] J. J. Fortney, K. Lodders, M. S. Marley, and R. S. Freedman, *Astrophys. J.* **678**, 1419 (2008).
- [66] V. Parmentier and T. Guillot, *Astron. Astrophys.* **562**, A133 (2014).
- [67] J. Liu, P. M. Goldreich, and D. J. Stevenson, *Icarus* **196**, 653 (2008).
- [68] J. Wicht, T. Gastine, and L. D. V. Duarte, *J. Geophys. Res.—Planets* **124**, 837 (2019).
- [69] R. Perna, K. Heng, and F. Pont, *Astrophys. J.* **751**, 59 (2012).
- [70] I. A. G. Snellen, R. J. de Kok, E. J. W. de Mooij, and S. Albrecht, *Nature (London)* **465**, 1049 (2010).
- [71] K. G. Kislyakova, M. Holmström, H. Lammer, P. Odert, and M. L. Khodachenko, *Science* **346**, 981 (2014).
- [72] J. Wicht, T. Gastine, L. D. V. Duarte, and W. Dietrich, *Astron. Astrophys.* **629**, A125 (2019).
- [73] X. Huang and A. Cumming, *Astrophys. J.* **757**, 47 (2012).
- [74] J. R. Adams, H. Reinholz, and R. Redmer, *Phys. Rev. E* **81**, 036409 (2010).
- [75] N. Nettelmann, B. Holst, A. Kietzmann, M. French, R. Redmer, and D. Blaschke, *Astrophys. J.* **683**, 1217 (2008).
- [76] M. French, A. Becker, W. Lorenzen, N. Nettelmann, M. Bethkenhagen, J. Wicht, and R. Redmer, *Astrophys. J. Suppl. Ser.* **202**, 5 (2012).
- [77] A. Becker, M. Bethkenhagen, C. Kellermann, J. Wicht, and R. Redmer, *Astron. J.* **156**, 149 (2018).
- [78] T. Gastine, J. Wicht, L. D. V. Duarte, M. Heimpel, and A. Becker, *Geophys. Res. Lett.* **41**, 5410 (2014).

5.4. Magnetic induction processes in hot Jupiters, application to KELT-9b

"Because you look around and every street, every boulevard, is its own special art form and when you think that in the cold, violent, meaningless universe that Paris exists, these lights, I mean come on, there's nothing happening on Jupiter or Neptune, but from way out in space you can see these lights, the cafés, people drinking and singing."

Midnight in Paris (movie)

Monthly Notices of the Royal Astronomical Society **517**, 3113-3125 (2022).

DOI: [10.1093/mnras/stac2849](https://doi.org/10.1093/mnras/stac2849)

W. Dietrich

Preparation of the manuscript, calculations of the magnetic Reynolds number, analysis of the magnetic induction processes, analysis and interpretation of the results

S. Kumar

Preparation of the manuscript, calculation of the transport properties for HD 209458b and KELT-9b, analysis and interpretation of the results

A. J. Poser

Preparation of the manuscript, calculation of the atmospheric and interior profiles for HD 209458b and KELT-9b, analysis and interpretation of the results

M. French

Preparation of the manuscript, interpretation of the results

N. Nettelmann

Preparation of the manuscript, interpretation of the results

R. Redmer

Supervision of the project, preparation of the manuscript

J. Wicht

Supervision of the project, preparation of the manuscript, analysis of the magnetic induction processes



Magnetic induction processes in hot Jupiters, application to KELT-9b

Wieland Dietrich¹,^{1*} Sandeep Kumar,^{2,3} Anna Julia Poser,⁴ Martin French,⁴ Nadine Nettelmann,⁵ Ronald Redmer⁴ and Johannes Wicht¹

¹Max Planck Institute for Solar System Research, D-37077 Goettingen, Germany

²Center for Advanced Systems Understanding (CASUS), D-02826 Görlitz, Germany

³Helmholtz-Zentrum Dresden-Rossendorf (HZDR), D-01328 Dresden, Germany

⁴Institut für Physik, Universität Rostock, D-18051 Rostock, Germany

⁵Institut für Planetenforschung, Deutsches Zentrum für Luft- und Raumfahrt, D-12489 Berlin, Germany

Accepted 2022 September 29. Received 2022 September 28; in original form 2022 August 11

ABSTRACT

The small semimajor axes of hot Jupiters lead to high atmospheric temperatures of up to several thousand Kelvin. Under these conditions, thermally ionized metals provide a rich source of charged particles and thus build up a sizeable electrical conductivity. Subsequent electromagnetic effects, such as the induction of electric currents, Ohmic heating, magnetic drag, or the weakening of zonal winds have thus far been considered mainly in the framework of a linear, steady-state model of induction. For hot Jupiters with an equilibrium temperature $T_{\text{eq}} > 1500$ K, the induction of atmospheric magnetic fields is a runaway process that can only be stopped by non-linear feedback. For example, the back-reaction of the magnetic field on to the flow via the Lorentz force or the occurrence of magnetic instabilities. Moreover, we discuss the possibility of self-excited atmospheric dynamos. Our results suggest that the induced atmospheric magnetic fields and electric currents become independent of the electrical conductivity and the internal field, but instead are limited by the planetary rotation rate and wind speed. As an explicit example, we characterize the induction process for the hottest exoplanet, KELT-9b, by calculating the electrical conductivity along atmospheric P – T profiles for the dayside and nightside. Despite the temperature varying between 3000 and 4500 K, the resulting electrical conductivity attains an elevated value of roughly 1 S m^{-1} throughout the atmosphere. The induced magnetic fields are predominately horizontal and might reach up to a saturation field strength of 400 mT, exceeding the internal field by two orders of magnitude.

Key words: magnetic fields – plasmas – planets and satellites: atmospheres – planets and satellites: gaseous planets.

1 INTRODUCTION

Hot Jupiters (HJs) orbit their parent stars in very close proximity and are locked in synchronous rotation, which means that they always face the same side to the star (Guillot et al. 1996; Showman, Lewis & Fortney 2015). The elevated electrical conductivity caused by thermal ionization of metals and the fierce irradiation-driven winds induce strong electric currents. If these currents flow deeper into the atmosphere, the related Ohmic heating could explain the planetary radius inflation (Batygin & Stevenson 2010; Kumar et al. 2021). Some authors also suggest that Lorentz forces might become strong enough to alter the atmospheric circulation and, thus, the brightness distribution (Perna, Menou & Rauscher 2010; Rogers & Showman 2014). Even a self-excited atmospheric dynamo that operates independently of the deep-seated, convective dynamo seems possible. Rogers & McElwaine (2017) suggest that such dynamo action is promoted by the strong horizontal variation of the electrical conductivity caused by the large difference between dayside and nightside temperatures.

The interpretation of the observational data for HJs relies heavily on a reliable estimate of the electrical conductivity and the mechanisms of the induction process (Batygin & Stevenson 2010; Rogers & McElwaine 2017). So far, only a linear approximation of the induced electrical currents has been applied. However, this might be only justified in HJs with equilibrium temperatures in the 1000–1500 K range, such as HD 209458b (Kumar et al. 2021).

For hotter HJs, such as the group of ultrahot Jupiters (UHJs, $T_{\text{eq}} > 2200$ K; Parmentier et al. 2018), the electrical conductivity, σ_e , might reach much higher values because the temperatures are sufficient to ionize more abundant metals, such as sodium, calcium, or even iron. We therefore calculate the ionization degree and electrical conductivity to characterize the induction process in a prominent UHJ, KELT-9b, the hottest planet detected so far. It orbits its host star, a main-sequence A0-type star, in only 1.48 d while receiving strong stellar irradiation (Gaudi et al. 2017). It has a radius of $\approx 1.9R_J$ and an age of 300–600 Myr (Gaudi et al. 2017). It has been suggested that dayside and nightside temperatures are as high as 4600 and 3040 K, respectively (Mansfield et al. 2020; Wong et al. 2020). Another recent study reports dayside temperature of up to 8500 K in the low pressure range of the atmosphere (Fossati et al. 2020, 2021). Such high temperatures lead to significant ionization and dissociation of atmospheric constituents (Hoeijmakers et al. 2019), which is

* E-mail: dietrichw@mps.mpg.de

© The Author(s) 2022.

Published by Oxford University Press on behalf of Royal Astronomical Society. This is an Open Access article distributed under the terms of the Creative Commons Attribution License (<http://creativecommons.org/licenses/by/4.0/>), which permits unrestricted reuse, distribution, and reproduction in any medium, provided the original work is properly cited.

3114 *W. Dietrich et al.*

confirmed by the observation of Fe⁺ and Ti⁺ (Hoeijmakers et al. 2018, 2019).

In comparison with standard thermal evolution calculations, the observationally constrained radius of many HJs appears inflated (Thorngren & Fortney 2018), since their radii are larger than thermal evolution models suggest. This inflation seems particularly present for intermediately tempered HJ with equilibrium temperatures around between 1570 K (Thorngren & Fortney 2018) and 1860 K (Sarkis et al. 2021) depending on the atmosphere model used. Various studies investigate possible inflation mechanisms (Sarkis et al. 2021) and conclude that Ohmic heating is a promising candidate (Batygin & Stevenson 2010). However, previous estimates of Ohmic heating were based on a steady and linear induction process that might not be readily applicable to hotter planets.

The importance of electromagnetic effects and the nature of the induction process can be characterized by estimating the ratio between the induction of magnetic fields and the dissipation. This is cast into the magnetic Reynolds number,

$$\text{Rm} = \mu_0 \sigma_e U d, \quad (1)$$

here μ_0 is the vacuum permeability, U is a typical flow velocity, σ_e the electrical conductivity, and d a typical length scale. As long as Rm remains below one, the magnetic field induced in the outer part of the atmosphere will be smaller than the internal magnetic field originating from a convective, deep interior dynamo process. This allows estimating the induced field and the related electric current in a linear approach for an assumed internal field strength.

The linear approach has been used to predict magnetic effects caused by the observed zonal winds in the outer atmosphere of Jupiter and Saturn by Liu, Goldreich & Stevenson (2008), Cao & Stevenson (2017), and Wicht et al. (2019b). In these planets, the electrical conductivity increases sharply with depth due to the growing ionization degree of hydrogen until its transition into a metallic phase at around 1 Mbar. The electrical conductivity scale height is then the relevant length scale d in equation (1). Adopting for example the conductivity model by French et al. (2012) for Jupiter yields d between $10^{-3}R_J$ and $10^{-2}R_J$, where R_J is Jupiter's radius. As a consequence, Rm remains below one for the outer few per cent in radius so that the linear approximation for estimating electric currents and, thus, Ohmic dissipation can be applied.

In contrast to Jupiter and caused by the irradiation-driven ionization of metals, for HJs electromagnetic effects become important at much lower pressures, namely in the lower atmosphere around 1 and 10^{-3} bar (Kumar et al. 2021). They are important when strong flows interact with a sizeable electrical conductivity. The permanent stellar irradiation will not reach deeper than about 1 bar, where the infrared opacity reaches unity (Iro, Bézard & Guillot 2005). Atmospheric flows driven by the irradiation gradients thus dominate above 1 bar.

In HJs with a moderate equilibrium temperature of 1500 K, such as HD 209458b with zero-albedo $T_{\text{eq}} = 1440$ K, the electrical conductivity reaches up to $\sigma_e \approx 10^{-3} \text{ S m}^{-1}$ (Kumar et al. 2021). Assuming typical wind velocities of about 2 km s^{-1} yields $\text{Rm} \leq 1$. The linear approach for estimating the electric current is therefore still applicable and has been adopted by several authors (Batygin & Stevenson 2010; Kumar et al. 2021).

For even hotter planets, such as the UHJ KELT-9b, faster winds (Fossati et al. 2021) and higher electrical conductivity (as we will show later) will likely boost Rm to value much larger than one ($\text{Rm} \gg 1$). The linear approach becomes questionable and significant alteration of a deep dynamo field can be expected. The everlasting induction of atmospheric magnetic fields must be balanced by other processes. Even an independent self-excited atmospheric dynamo

may become possible, which could survive without the presence of a deep dynamo field.

In this paper, we discuss the induction of atmospheric magnetic fields in HJs and UHJs, its linear and non-linear processes, and which amplitudes the induced fields and electrical currents can reach. This includes a general description of thermal ionization of metals and the subsequent calculation of electrical conductivity. In a second step, we apply this to a specific planet by calculating the ionization degree and the electrical conductivity in the atmosphere of the UHJ KELT-9b with our previously published ionization and transport model (Kumar et al. 2021). Both quantities are calculated for several atmospheric profiles, including distinguished profiles for the dayside and nightside. Lastly, we characterize the induction effects and give estimates for the induced magnetic field in the atmosphere.

Our paper is organized as follows. In Section 2, we discuss the general induction of atmospheric magnetic fields and show how to characterize the induction process. In Section 3.2.1, we apply the derived estimates and calculate explicitly the ionization degree and the electrical conductivity along P - T profiles of the atmosphere of UHJ KELT-9b. Conclusions are given in Section 4.

2 ELECTROMAGNETIC INDUCTION IN HOT JUPITERS

2.1 Induction of atmospheric magnetic fields

The electric current, $\mu_0 \mathbf{j} = \nabla \times \mathbf{B}$, in a moving conductor is given by Ohm's law:

$$\mathbf{j} = \sigma_e (\mathbf{U} \times \mathbf{B} + \mathbf{E}), \quad (2)$$

where \mathbf{U} is the flow, \mathbf{B} is the magnetic, and \mathbf{E} the electrical field. Using the Maxwell equations this can be rewritten as the induction equation, which describes the evolution of magnetic fields by the competition of induction and diffusion:

$$\partial_t \mathbf{B} = \nabla \times (\mathbf{U} \times \mathbf{B}) - \nabla \times (\eta \nabla \times \mathbf{B}), \quad (3)$$

where $\eta = 1/(\mu_0 \sigma_e)$ is the magnetic diffusivity. The importance of the dynamo term relative to the diffusion term is estimated by the magnetic Reynolds number:

$$\text{Rm} = \frac{|\nabla \times (\mathbf{U} \times \mathbf{B})|}{|\nabla \times (\eta \nabla \times \mathbf{B})|} \approx \frac{U}{\eta} \min(d_\eta, d_U, d_B), \quad (4)$$

where U is a typical flow velocity, d_η , d_U , d_B characteristic length scales for electrical conductivity, the flow, or the magnetic field, respectively. Estimating the relevant length scale of the induction or diffusion process is a key ingredient for Rm.

The induction becomes particularly simple if we assume that azimuthal zonal flows dominate the atmospheric dynamics while the radial flow component remains negligible. This seems a reasonable assumption for irradiation-driven flows in the stably stratified atmospheres of HJs and UHJs (Showman & Guillot 2002).

The induction process is then limited to creating azimuthal field (see Fig. 1a) via shear flows from a background field \mathbf{B}_{int} that is produced by the deep, internal dynamo process. If we furthermore assume that η is constant, and that the background field, the induced azimuthal field, and the flow are predominantly axisymmetric (indicated by the overbar), the induction equation reduces to

$$\partial_t \bar{\mathbf{B}}_\phi = -\bar{\mathbf{B}}_{\text{int}} \cdot \nabla \bar{\mathbf{U}} + \eta \Delta \bar{\mathbf{B}}_\phi. \quad (5)$$

The stellar irradiation drives fast horizontal winds in the outer atmosphere of HJs and UHJs. Since the winds likely remain confined

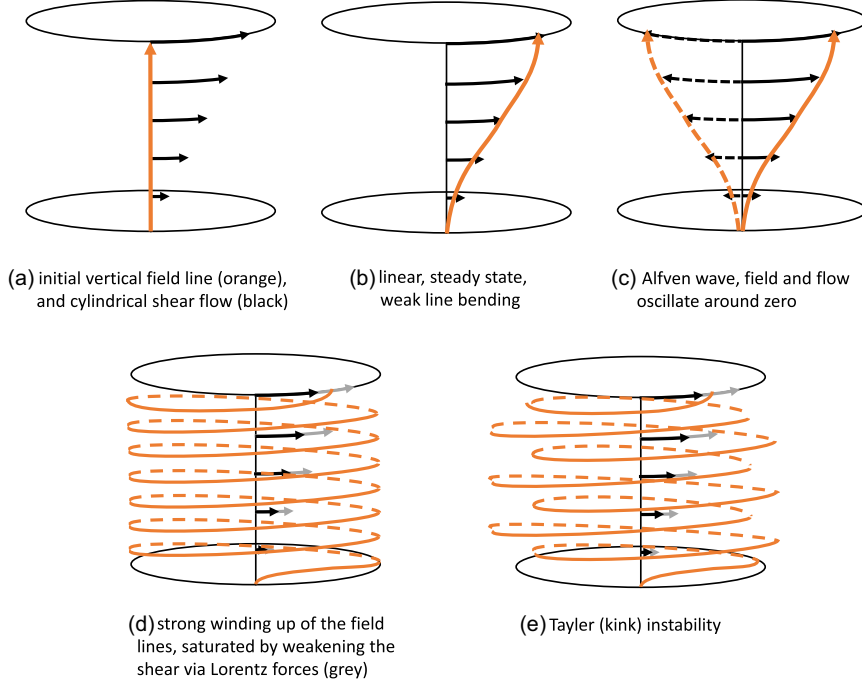


Figure 1. Induction of azimuthal field by bending of field lines (orange) via atmospheric shear flows (black arrows). If the induction is stopped by efficient magnetic diffusion due to low electrical conductivity (panel b), the induced field remains weak compared to the background field and no Lorentz forces act on the flow. If the induction is rapid, the induced azimuthal field could quickly overpower the internal one and cause strong Lorentz forces. This could lead to the occurrence of Alfvén waves flow and field oscillate (panel c). Or alternatively, that the Lorentz forces associated with the wound-up field ultimately weakens the shear flow (panel d). This tied-up magnetic field tends to develop instabilities, such as the Tayler instability with the kink mode (panel e).

to the low-opacity region we expect a steep radial gradient in the wind profile with a typical scale height d_U of

$$d_U = \left| \frac{\bar{U}_\phi}{\partial \bar{U}_\phi / \partial r} \right|. \quad (6)$$

Since numerical simulations indicate that the horizontal scales are typically large (Showman & Guillot 2002), we neglect the respective gradients in comparison to the radial one.

2.2 Internal dynamo process

Here we estimate the field strength of the internal dipole field, which is sheared by the atmospheric flows. As hydrogen becomes metallic at large pressures (>1 Mbar) the electrical conductivity in the deep interior of gas planets reaches about 10^6 S m^{-1} (French et al. 2012). We know that Jupiter and Saturn host interior dynamos, and therefore it is likely that HJs and UHJs also generate internal magnetic fields. The typical field strength in the dynamo regions can be estimated based on scaling laws. Here we use such laws that rely on the available convective power that itself can be expressed in terms of the heat flux density q_{int} out of the convective interior (Christensen, Holzwarth & Reiners 2009; Christensen 2010). The typical field strength for a self-sustained, convectively driven dynamo in gas giants scales like

$$B \propto f_{\text{ohm}} \rho_c^{1/6} (q_{\text{int}} H_\rho / H_T)^{1/3}, \quad (7)$$

where f_{ohm} is the ratio of Ohmic to total dissipation, ρ_c is the bulk density in the dynamo region, q_{int} the heat flux at the radiative-convective boundary, H_T the temperature scale height, and H_ρ the density scale height (Christensen et al. 2009).

We assume $f_{\text{ohm}} = 1$, normalize this scaling relation with the well-constrained values of Jupiter, and use the mean planetary density $\rho_c = 3M_p/4\pi R_p^3$, where R_p and M_p are the radius and the mass of the HJ under consideration:

$$B_{\text{int}} = B_{\text{int,J}} \left(\frac{R_J}{R_p} \right)^{1/2} \left(\frac{M_p}{M_J} \right)^{1/6} \left(\frac{q_{\text{int}}}{q_{\text{int,J}}} \right)^{1/3}. \quad (8)$$

This is based on the assumption that the temperature and density scale heights are similar. The surface field strength and interior heat flux of Jupiter is roughly 0.5 mT and $q_{\text{int,J}} = 5.4 \text{ W m}^{-2}$.

The internal heat flux density q_{int} of the planet is difficult to access, since a variety of sources, such as secular cooling, gravitational contraction, tidal effects, or Ohmic heating might contribute.

Classically, the amount of heat released from the radiative-convective boundary is primarily governed by the contraction and cooling during the thermal evolution of the planet. Thus larger and younger planets possess a larger luminosity. Thermal evolution models, e.g. Baraffe et al. (2003) and Burrows et al. (2001), were used to derive scaling relations for the total luminosity as a function of age, radius, and mass (Burrows et al. 2001; Zaghoo & Collins 2018):

$$q_{\text{int}} = q_{\text{int,J}} \left(\frac{\tau_p}{\tau_J} \right)^{-1/3} \left(\frac{M_p R_p}{M_J R_J} \right)^{2.64}, \quad (9)$$

where τ_p and $\tau_J = 4.5$ Gyr are the age of the planet and of Jupiter, respectively.

However, for HJs, the heat budget seems more complex as the majority of them appear larger than thermal evolution models for non-irradiated planets would predict. This suggests additional heat

3116 *W. Dietrich et al.*

sources that slow down secular cooling, and Ohmic dissipation is one of possible mechanisms (Batygin & Stevenson 2010; Sarkis et al. 2021). This would indicate that HJs that receive more intense stellar radiation and are thus hotter tend to be more inflated by Ohmic dissipation since the higher electrical conductivity allows for higher induced magnetic fields and currents, which transfer irradiation energy into the deeper interior through Ohmic dissipation. But if the atmospheric temperatures are too high, the Lorentz forces tend to suppress horizontal flows and thus Ohmic dissipation (Menou 2012).

If the atmosphere of HJ is in thermal equilibrium with the incident flux, the internal heat flux and the one associated with dissipating the irradiation must balance (Thorngren & Fortney 2018; Sarkis et al. 2021). Both studies found indeed statistical evidence for a relation between the internal heat flux due to extra heating and equilibrium temperature in the upper atmosphere with a pronounced maximum around $T_{\text{eq}} = 1850$ K (Thorngren, Gao & Fortney 2019, 2020):

$$T_{\text{int}} \approx 0.39 T_{\text{eq}} \exp\left(-\frac{(\log(\sigma_{\text{SB}}^* T_{\text{eq}}^4) - 6.14)^2}{1.095}\right), \quad (10)$$

where σ_{SB}^* is the Stefan–Boltzmann constant taken in units of 1 K^{-4} . The associated internal heat flux can be calculated via $q_{\text{int}} = \sigma_{\text{SB}} T_{\text{int}}^4$. Note that the exact mechanism of dissipating the irradiation is not undisputed (Sarkis et al. 2021).

Equations (10) and (9) together with equation (8) provide a strategy to estimate the field strength of a convectively driven dynamo for a dedicated planet.

2.3 Ionization of metals and the electrical conductivity

The main ingredient for assessing the electromagnetic induction effects, quantified by Rm , is the electrical conductivity σ_e . HJs reach atmospheric temperatures at which metals are partially or even fully ionized via thermal ionization. We only consider the first degree of ionization and therefore partial and full ionizations are to be understood with respect to the total abundance. Free electrons interact via collisions with ions, neutrals, and other electrons to generate a macroscopic electrical resistivity. In the temperature range up to a few thousand of K, the relevant constituents that ionize are the alkali metals, such as lithium, potassium, sodium, rubidium, caesium, and the common metals calcium and iron (Lodders 2003). Hydrogen dominates the overall composition and acts mainly as scatterer for the electrons. It gets ionized only when temperatures exceed 5000 K. Here we use the Solar system abundances for the atmospheric stoichiometry. For the calculation of the ionization degree and electrical conductivity, we follow our model for a partially ionized plasma previously employed in Kumar et al. (2021). There, mass-action laws are used to calculate the composition of the partially ionized plasma (PIP; Redmer et al. 1988; Redmer 1999; Kuhlbrodt & Redmer 2000; Kuhlbrodt, Holst & Redmer 2005; Schöttler, Redmer & French 2013), from which the mass density ρ is derived for a given P – T profile. Furthermore, the electrical conductivity is calculated from electron–ion and electron–neutral transport cross-sections (French & Redmer 2017). The effect of electron–electron scattering on the transport properties is accounted for by introducing correction factors to the electron–ion contributions. The abundance of constituents considered in this work is the same (solar abundance) as we have considered in our PIP model (Kumar et al. 2021).

For general illustration, we calculate σ_e as function of temperature, but keep the density fixed to three different values between $\rho = 10^{-3}$ and $10^{-5} \text{ kg m}^{-3}$ (Fig. 2, solid, dashed, and dotted black). The temperature axis can be interpreted as the radiative equilibrium tem-

perature T_{eq} or temperatures representing the dayside or nightside. It can be seen that σ_e increases with temperature as more and more electrons contribute to build up the electrical conductivity. However, the increase includes rather steep slopes and quite flat plateaus in between. These structures are caused by different species that are ionized subsequently as the temperature rises.

Given their high ionization energy and small mass fraction, lithium, rubidium, and caesium can safely be ignored in this consideration. Potassium on the other hand has the smallest ionization energy and, thus, is the predominant source of electrons at low temperatures. It is strongly ionized already at temperatures below and up to 2000 K. At $T = 2200$ K almost all of the free electrons stem from potassium. As an example, the HJ HD 209485b has an equilibrium temperature of roughly 1500 K and thus a $\sigma_e \approx 10^{-3} \text{ S m}^{-1}$ (Kumar et al. 2021). Because of the partial ionization of potassium, the temperature dependence around this value is relatively steep and small radial or azimuthal temperature variations might cause strong variations in σ_e .

Between $T = 2300$ and 3500 K, the ionization of calcium and sodium boost σ_e to values between 0.1 and 1 S m^{-1} , where a plateau at an elevated electrical conductivity of 1 S m^{-1} is visible. Thus for HJs that feature atmospheric temperatures in that range, σ_e is rather independent and thus constant across the entire irradiated atmosphere. The width of this conductivity plateau is given by difference in ionization energies between calcium/sodium and iron. Marking the high-temperature end of the plateau (at $T = 3500$ K) the next element providing more electrons is iron, which singly ionized at around $T = 5000$ K. The last σ_e boost is due to electrons from hydrogen that begin to ionize at $T = 5000$ K and dominate σ_e at higher temperatures.

To show the parameter dependence, we display σ_e along several isochores (dashed and dotted in Fig. 2) and calculate a temperature variability, $\sigma_e^{-1} d\sigma_e/dT$ (red profile). It can be seen that a larger density smooths out the structures and decreases the magnitude of σ_e due to a shift in the chemical ionization equilibria according to Le Chatelier’s principle.

The temperature dependence is most pronounced at the low-temperature end of the plot, where only a single species, potassium here, is partially ionized. This leads to quite a strong temperature sensitivity of roughly 0.01 K^{-1} . At higher temperatures and in particular around 3300 K this drops down to 10^{-4} K^{-1} indicating that σ_e is very insensitive to thermal variations.

Moreover, we add estimates of Rm in the figure (blue). Those are based on the actual value of σ_e , a (conservative) flow amplitude of $U = 2 \times 10^3 \text{ m s}^{-1}$ and a length scale representing the conductivity scale height of $d_\sigma = 3 \times 10^5 \text{ m}$ (dark blue) or the radial length scale of the shear flow $d_U = 0.02 R_p \approx 3 \times 10^6 \text{ m}$ (light blue). For the colder part, Rm_σ might be more realistic, as d_σ is smaller than d_U and hence is the dominant diffusion length scale. Both curves are larger than unity from $T < 1200$ – 1500 K suggesting that all HJ atmospheres exceeding these temperatures tend to host non-linear induction processes that are characterized by $\text{Rm} \gg 1$. This already indicates that a better understanding of the atmospheric induction processes in atmospheres with high conductivity is strongly needed.

2.4 Linear regime, $\text{Rm} \leq 1$

Previous approaches for estimating the magnetic induction in HJs assumed that the growth is limited by magnetic diffusion (e.g. Batygin & Stevenson 2010).

As already discussed in the Introduction and in Kumar et al. (2021), for HJs like HD 209485b, Rm may actually remain below

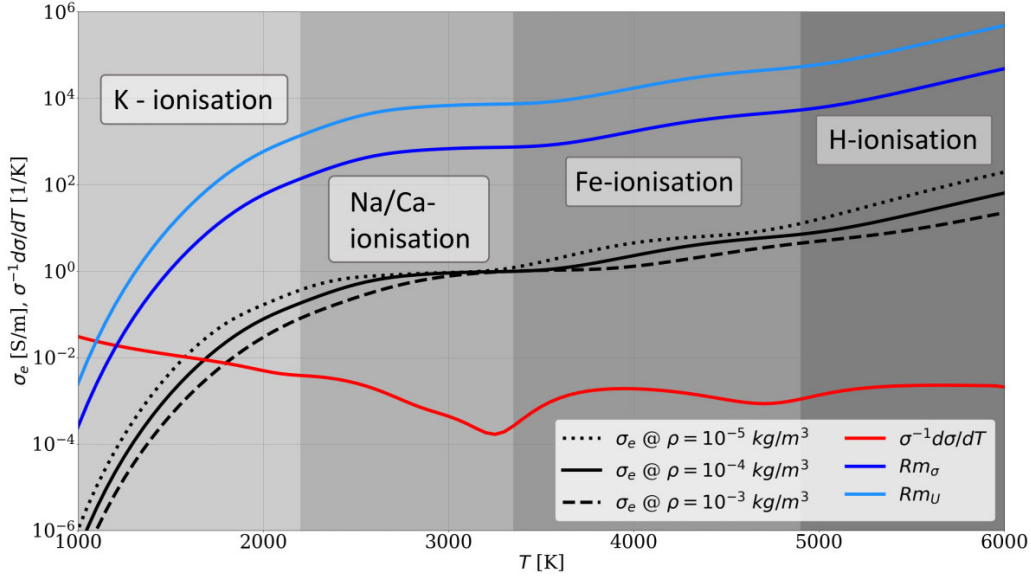


Figure 2. Electrical conductivity due to ionization of metals as a function of temperature along three isochores with $\rho = 10^{-3}$ to 10^{-5} kg m^{-3} (black solid, dashed, and dotted line). The grey shaded areas indicate the main donors of electrons. The red profile shows the temperature variability of the electrical conductivity: $1/\sigma_e d\sigma_e/dT$. The blue profiles show two magnetic Reynolds numbers based on the solid conductivity profile, a flow velocity of $U = 2 \times 10^3$ m s^{-1} (Snellen et al. 2010), and either $d_U = 3 \times 10^6$ m or $d_\eta = 3 \times 10^5$ m (Wicht, Gastine & Duarte 2019a) as length scale. Both curves cross unity around 1300 or 1500 K, suggesting that the linear estimate of induction is not valid at temperatures higher than that.

one, because both σ_e and the characteristic length scale $d = d_\eta$ are rather small. The latter is the correct choice for the relevant diffusive length scale to account for the strong variability of σ_e (Liu et al. 2008; Wicht et al. 2019a). This will likely apply to HJs on the potassium branch of Fig. 2 or be the case in HJ atmospheres where $T < 1500$ K. For $\text{Rm} \leq 1$, the dynamics establishes a quasi-stationary ($\partial_t B \approx 0$) state where the magnetic dissipation balances the induction term in equation (5). The locally induced field can then be estimated via

$$B_\phi = \text{Rm} B_{\text{int}}. \quad (11)$$

This implies that the maximum amplitude of the induced field where this approximation is still valid is the internal field strength. Thus the radial field lines will be only slightly bent in the direction of the shear as indicated in Fig. 1(b).

Another consequence of the quasi-stationarity is that the electric currents obey a simplified Ohm's law where the gradient of the electric potential can be neglected,

$$\mathbf{j} = \sigma_e (\mathbf{U} \times \mathbf{B}_{\text{int}}), \quad (12)$$

and can thus be calculated for a given flow and background field if we assume that $\mathbf{j} = \sigma_e \bar{U} \bar{B}_\phi$ (Wicht et al. 2019a). It is important to stress that the local currents and induced magnetic fields depend on the electrical conductivity, the internal field strength, and the zonal wind speed. In this scenario, the induced field cannot reach sufficient strength to modify or abate the flow via Lorentz forces (Fig. 1b).

2.5 Non-linear induction: winding up the field

If σ_e is larger or the atmospheric winds more energetic, the induction equation (equation 5) shows that the zonal flow shear will very efficiently induce azimuthal magnetic field from winding up the radial background field. If the rate of field induction cannot be balanced by the diffusion alone, a steady linear model as discussed

before cannot be applied anymore. As long as the radial field is provided from the deep, internal dynamo, the winding up of magnetic field lines around the planet continues until a non-linear effect stops this process. This by itself does not work as a self-sustained dynamo, for which the atmospheric dynamics would itself replenish the radial field and thus become independent of the internal field. We discuss the requirements of the self-excited dynamo in Section 2.7.

The rapid induction process is represented by magnetic Reynolds number that strongly exceeds unity. Thus the diffusive term can be ignored and the induction equation (equation 5) simplifies to

$$\frac{\partial \bar{B}_\phi}{\partial t} = \frac{\bar{U}}{d_U} \bar{B}_{\text{int}}. \quad (13)$$

The atmospheric shear flow efficiently produces an azimuthal field component by shearing the radial component of the background field. It effectively winds up the field lines in azimuthal direction as illustrated in Figs 1(b) and (d). The induced field \bar{B}_ϕ thus increases linearly with time until some critical strength is reached where the process is modified.

The related electrical current must then be calculated from the curl of the azimuthal field B_ϕ . If the induced field remain axisymmetric, this is given by

$$\mathbf{j} = \left| \frac{1}{\mu_0} \nabla \times \mathbf{B} \right| \approx \frac{\bar{B}_\phi}{\mu_0 d_U}, \quad (14)$$

where we assumed that the electrical current is dominated by the $\partial_r(r \bar{B}_\phi)$ term of the latitudinal component.

2.5.1 Alfvén waves

The interaction between the current of induced azimuthal field and internal field defines a Lorentz force, $\mathbf{j} \times \mathbf{B}$, that accelerates \bar{U}_ϕ in the opposite direction. Using the axisymmetric approximation of the

3118 *W. Dietrich et al.*

electrical current in equation (14) leads to

$$\rho \frac{\partial \bar{U}_\phi}{\partial t} = -\frac{\bar{B}_\phi \bar{B}_{\text{int}}}{\mu_0 d_U}. \quad (15)$$

The action of the Lorentz force thereby reduces the radial shear and thus the growth rate of \bar{B}_ϕ . Equations (13) and (15) define a wave equation for the azimuthal flow:

$$\frac{\partial^2 \bar{U}_\phi}{\partial t^2} = -\frac{1}{\mu_0 \rho} \frac{B_{\text{int}}^2}{d_U^2} \bar{U}_\phi. \quad (16)$$

This describes an Alfvén wave (see Fig. 1c) that travels along the field lines of the internal field and has a frequency

$$\omega_A = \frac{\bar{B}_{\text{int}}}{d_U (\mu_0 \rho)^{1/2}}. \quad (17)$$

There is ample time for the winding action to take place before the internal field changes. We expect Lorentz forces and Alfvén waves to play an important role for atmospheric dynamics. When assuming that \bar{U}_ϕ represents the maximum flow amplitude, the maximum field amplitude of the wave is

$$\bar{B}_\phi = (\mu_0 \rho)^{1/2} \bar{U}_\phi. \quad (18)$$

Since this estimate neglects diffusive effects and assumes that \bar{U}_ϕ represents a pure Alfvén wave, it can only serve as an upper bound. However, Alfvén waves are well-studied magnetohydrodynamics (MHD) phenomena that might play an important role in the dynamics of HJ atmospheres. In fact, the study of Rogers (2017) performing MHD simulations of the irradiated atmosphere of the HJ HAT-P-7b showed that temporal variability of the winds stems from magnetic effects. This is in line with the observed variability of the hotspot offset for that specific planet. In general, the hotspot offsets are typically prograde and not very time dependent (Parmentier et al. 2018).

2.5.2 Radial force balance

The derivation of the Alfvén wave above was based on neglecting the Coriolis force. A balance between Coriolis and Lorentz forces is typically expected in dynamo theory. We thus study the non-azimuthal component of this force balance:

$$\bar{\rho} \boldsymbol{\Omega} \times \mathbf{U} \approx \frac{1}{\mu_0} \mathbf{j} \times \mathbf{B}. \quad (19)$$

Choosing the axisymmetric radial component of this balance involves the zonal flow \bar{U} , the zonal magnetic field \bar{B}_ϕ , and equation (14) yields

$$\rho \Omega \bar{U}_\phi \approx \frac{\bar{B}_\phi^2}{\mu_0 d_U}. \quad (20)$$

We find for the azimuthal field a saturation value of

$$B_\phi \approx (\mu_0 \rho d_U \Omega \bar{U})^{1/2}. \quad (21)$$

Physically, this could be interpreted such that meridional circulation cells redistribute zonal angular momentum in such a way that the radial shear is suppressed (Fig. 1d). It is then the magnetic tension that saturates the initial shear flow (grey arrows) at a weaker final amplitude (black).

2.5.3 Tayler instability

There are different magnetic instabilities that can limit the growth of B_ϕ . For an introduction we refer to Spruit (1999). In a stably stratified

layer like the outer atmosphere of HJs, the so-called Tayler instability is likely to set in first. This instability refers to the unconstrained growth of non-axisymmetric magnetic field contributions when the axisymmetric part is sufficiently wound-up (see Fig. 1e). A condition is that the atmospheric environment is sufficiently stratified and that Alfvén waves are slower than the rotation frequency:

$$N \gg \Omega \gg \omega_A, \quad (22)$$

where N is the Brunt–Väisälä frequency that characterizes the degree of stratification. N can be calculated from observable quantities if the atmosphere is to first order isothermal:

$$N_T = \frac{g_P}{\sqrt{c_P T_{\text{eq}}}}, \quad (23)$$

here g_P is the gravity and T_{eq} the equilibrium temperature of the planet. N typically exceeds the rotation rate Ω_P by a factor of 30–300. The Alfvén frequency of the wound-up azimuthal field is given by

$$\omega_A = \frac{\bar{B}_\phi}{R_P (\mu_0 \rho)^{1/2}}. \quad (24)$$

The relation equation (22) should be fulfilled for most HJs, when the induced field is not exceedingly large.

The most unstable azimuthal wavenumber is $m = 1$ and thus the instability assumes the form of predominantly horizontal displacements on a small radial scale (see Fig. 1e). This mode is also called the kink instability. The details of the analytical description are discussed in Appendix A. The critical field strength for the onset of the Tayler instability is given by (Spruit 2002)

$$B_\phi = \Omega R (\mu_0 \rho)^{1/2} \left(\frac{N}{\Omega} \right)^{1/2} \left(\frac{\eta}{R^2 \Omega} \right)^{1/4}, \quad (25)$$

which saturates at a field strength of

$$B_\phi = (\mu_0 \rho)^{1/2} \frac{\Omega R \bar{U}}{N d_t}. \quad (26)$$

A characteristic of the instability mechanism is the displacement of the original wound-up field. We suggest that this displacement seeks to increase dissipation until this balances the growth without changing the field strength. The estimate, i.e. equation (25), then still holds, but the magnetic field structure changes in a way illustrated in Fig. 1(e). This heuristic view seems to be supported by a numerical simulation where axisymmetric zonal field and Tayler instability field assume a similar amplitude (Zahn, Brun & Mathis 2007).

2.6 Ohmic heating

For the linear case of limited, weak atmospheric induction characterized by $\text{Rm} \leq 1$, the induced electrical currents are given by $J_{\text{lin}} = \sigma_c \bar{U}_\phi \bar{B}_{\text{int}}$ and the Ohmic dissipation is

$$P_{\text{lin}} = \int_V \sigma_c \bar{U}_\phi^2 B_{\text{int}}^2 dV. \quad (27)$$

In this limit, the Ohmic power scales with electrical conductivity and the square of the internal field strength.

If $\text{Rm} > 1$, the non-linear nature of the induction process makes it necessary to find the currents via $\mathbf{j} = \mu_0^{-1} (\nabla \times \mathbf{B})$. However, if the induced field remains axisymmetric, the strongest gradient remains the radial derivative of the azimuthal field and thus $j = B_\phi / (\mu_0 d_U)$ (see equation 14). Assuming that the non-axisymmetric Tayler instability preferentially develops an $m = 1$ azimuthal structure, this

approximation still holds. This then yields an Ohmic power of

$$P_{\text{nl}} = \frac{1}{\mu_0^2} \int_V \frac{B_\phi^2}{\sigma_e d_V^2} dV. \quad (28)$$

Since the induced field B_ϕ is independent of σ_e , the Ohmic dissipation for the non-linear case shrinks rather than grows with higher σ_e .

Most of the dissipation happens in the atmospheric region, where the currents are induced initially. One can thus expect that just a small fraction of the currents connect down to the convective interior and could potentially interfere with the secular cooling (Batygin & Stevenson 2010).

Consequently, Ohmic heating was proposed as one of the mechanisms that could explain the radius anomaly of HJs (Batygin & Stevenson 2010; Thongren & Fortney 2018; Sarkis et al. 2021). Radial currents would flow to deeper regions below the radiative–convective boundary where the related Ohmic heating,

$$P = \int_{V_i} dV \frac{j^2}{\sigma_i}, \quad (29)$$

could explain the inflation. Here V_i denotes an integration over this deeper region with electrical conductivity σ_i . The currents are induced in the wind region and decay in the deeper region that has been denoted ‘leakage region’ by Kumar et al. (2021). Relevant for the amount of deeper heating are (i) the current strength in the induction layer above, (ii) the deeper electrical conductivity, but also (iii) the electric current pattern at the transition to the deeper region, which determines how deep the currents would penetrate. Here we assume that the pattern is dominated by the action of large-scale zonal winds on a large-scale internal field and therefore generally very similar.

2.7 Self-sustained atmospheric dynamo

In a self-excited dynamo, a small seed field will be amplified by the atmospheric flows until the associated Lorentz forces are strong enough to sufficiently modify these flows. Here we analyse whether the prerequisites for self-sustained dynamo action are met and evaluate the possibility of atmospheric dynamo action. Modelling this complex phenomenon requires dedicated MHD numerical simulations, which are beyond the scope of this study.

A dynamo can only be maintained when various conditions on the flow amplitude, direction, and complexity are met. A necessary condition is that Rm is sufficiently larger than one. This is certainly true for the azimuthal (toroidal) field generation discussed above. However, for an independent atmospheric dynamo that could operate even without a background field, the process also has to generate radial (poloidal) field from the azimuthal (toroidal) field. This generally requires radial flows fast enough so that the respective magnetic Reynolds number $Rm_r = \mu_0 \sigma_e u_r d_r$ to exceed one. For this condition to be fulfilled, it seems sufficient that $u_r \sigma_e > 1 \text{ S s}^{-1}$.

In the study by Showman & Guillot (2002), the non-zonal part of the irradiation-driven winds in numerical models for Pegasi 51 b amounts to 20 m s^{-1} . More recently, the analysis of the vertical mixing rates in a broad suite of general circulation models (GCM) suggested radial flows on the order of 2 and 20 m s^{-1} (Komacek, Showman & Parmentier 2019). This already suggests that independent atmospheric dynamos are possible where the dynamics of the irradiated atmosphere could generate magnetic fields even when there is no deep-seated dynamo. A more definitive answer to this question would require 3D simulations of the induction processes in the dynamic atmosphere.

Magnetic induction processes in hot Jupiters 3119

A relevant alternative process to induce radial field was suggested by Busse & Wicht (1992) and Rogers & McElwaine (2017) and is driven by the lateral variations in electrical conductivity. As along as these variations are relatively modest, this process is too inefficient.

Furthermore, Spruit (2002) envisioned self-sustained dynamo action for stars where the field generated by the Tayler instability would replace the interior field and replenish the reservoir of the poloidal field component. An alternative mechanism turning the atmospheric induction into a self-consistent dynamo is the strong horizontal variation of electrical conductivity. This was theoretically predicted by Busse & Wicht (1992) and numerically investigated by Rogers & McElwaine (2017).

Note that a self-sustained dynamo might generate a magnetic field and thus dissipate magnetic energy at much smaller length scales. This would in fact drastically increase the total Ohmic power.

3 APPLICATION TO HOT JUPITERS

Before we apply the ionization model to atmospheric P – T profiles of two dedicated HJs, we give a general, order of magnitude, assessment of Rm . According to equation (1) this requires a flow speed, a length scale, and the electrical conductivity. The zonal atmospheric winds driven by irradiation gradients reach amplitudes of several km s^{-1} , hence even exceeding the angular velocity at the planetary surface due to its solid body rotation. A conservative estimate for the zonal flow is thus $\bar{U}_\phi \geq \Omega R$. For the length scale, we use the depth of the winds $d \approx 0.02R$. Note that for colder HJ, σ_e might be very temperature dependent and hence the radial conductivity scale height could be the relevant (dissipative) length scale.

The most influential quantity is the electrical conductivity, σ_e , which can vary by orders of magnitude (see Fig. 2). For a quick characterization of HJ, we calculate σ_e for a fixed density and as a function of the respective atmospheric equilibrium temperature T_{eq} . This gives a planet-specific estimate of Rm by

$$Rm_p \approx 0.02 \mu_0 \sigma_e(T_{\text{eq}}) \Omega R^2. \quad (30)$$

Note that this Rm estimate is calculated only from (apart from σ_e) on observable quantities, such as the orbital rotation rate or the planetary radius. Fig. 3 shows the so derived Rm values for set of ca. 350 HJs (masses between 0.1 and $10 M_J$, semimajor axis smaller than 0.1 au, and radii between 0.5 and $2.1 R_J$) as a function of their T_{eq} . It can be seen that Rm exceeds unity at $T_{\text{eq}} \approx 1400 \text{ K}$. For all planets below that temperature the linear induction model for which $Rm < 1$, can readily be applied. For all planets with temperatures significantly exceeding this threshold the atmospheric induction of electromagnetic currents is a runaway process that can only be saturated by non-linear feedback.

Here we study two examples, HD 209458b and KELT-9b. Both are well-characterized HJs or UHJs, but with very different characteristics of electromagnetic induction in the irradiated atmosphere. Whereas HD 209458b is an example of $Rm \approx 1$, KELT-9b is the hottest HJ observed so far with $Rm \gg 1$.

As discussed in Section 2, the assessment of their general magnetic properties depends on Rm and yields estimates for the leading contribution to electric currents j , amplitude of induced magnetic fields B_ϕ , and the available Ohmic dissipation P_{ohm} . Table 1 shows these quantities that are discussed underneath for both planets in more detail. For both planets exist published, observation-based atmospheric temperature profiles. In the case of KELT-9b, even dayside and nightside profiles were calculated. This more detailed

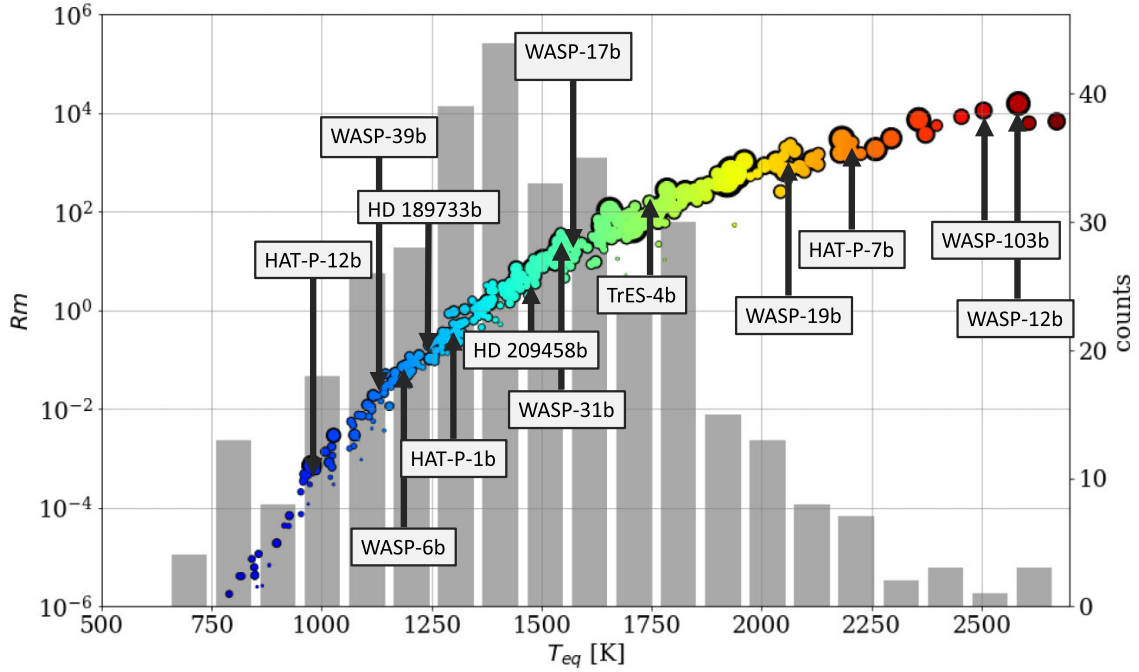
3120 *W. Dietrich et al.*

Figure 3. Estimate of R_m for hot Jupiters (HJs) as a function of T_{eq} for a density of $10^{-4} \text{ kg m}^{-3}$. The colour refers to the equilibrium temperature, the size of the dots to the radius. The histogram shows the population of the selected group of HJs. A few popular planets are marked. For $T_{\text{eq}} > 1300 \text{ K}$, R_m exceeds unity. Thus, roughly the colder half of HJs host strongly non-linear atmospheric induction processes.

Table 1. Properties of the atmospheric induction based on the scaling laws and relations given in the text.

		HD 209458b	KELT-9b
Internal heat flux	$q_{\text{int}} (\text{W m}^{-2})$	$5\text{--}6.5 \times 10^3$	29–553
Internal field	$B_{\text{int}} (\text{mT})$	0.39–4.3	0.72–1.93
Electr. cond.	$\sigma_e (\text{S m}^{-1})$	$10^{-4}\text{--}10^{-2}$	1–5
Length scale	$d (\text{m})$	3×10^5	2.7×10^6
Flow speed	$U (\text{m s}^{-1})$	2×10^3	1.3×10^4
R_m		≈ 1	4×10^4
Induced field	$B_\phi (\text{mT})$	0.3	40–400
Local current	$j (\text{A m}^{-2})$	0.8×10^{-3}	0.01–0.1
Ohmic heat	$P_{\text{ohm}} (\text{W})$	1.35×10^{20}	$8.15 \times 10^{19}\text{--}5.34 \times 10^{21}$

analysis yields a deeper inspection of the thermal ionization, electrical conductivity, and subsequent induction process across various atmospheric layers.

3.1 HD 209458b

For HD 209458b – a typical HJ – the electrical conductivity reaches values between 10^{-4} and 10^{-2} S m^{-1} as shown in Fig. 5, blue curves. The thermal ionization at this temperature causes only a partial ionization of the potassium atoms (compare also the ionization coefficient, α) and thus a strong temperature sensitivity. Using $d = 3 \times 10^5 \text{ m}$ in equation (1) this leads to $R_m \leq 1$, suggesting that the magnetic diffusion indeed limits the growth of the induced field such that steady solutions are possible at $B_\phi = R_m B_{\text{int}}$.

The available estimates for the internal field strength B_{int} are based on indirect magnetospheric observations and amount to 0.05 mT,

a field strength 10 times weaker than Jupiter’s (Kislyakova et al. 2014). On the other hand, the field strength estimate based on the thermal evolution (equation 9) and the energy balance (equation 10) suggests higher values of 0.4 and 4 mT, respectively. HD 209458b is an inflated planet thus matching the proposed peak efficiency of Ohmic heating (Thomgren & Fortney 2018). This favours the energy balance estimate.

Using $\sigma_e = 10^{-3} \text{ S m}^{-1}$, the local currents reach strength of roughly 10^{-3} A m^{-2} and according to equation (27) a total atmospheric Ohmic power of $1.35 \times 10^{20} \text{ W}$ for an internal field strength of 0.4 mT. Using the upper field estimate of 4 mT based on the energy balance would yield a two order of magnitude larger Ohmic dissipation matching the bolometric luminosity. The study of Batygin & Stevenson (2010) used a 1 mT internal field and $\sigma_e \approx 10^{-2} \text{ S m}^{-1}$ and showed that roughly 1 per cent of the available Ohmic power is sufficient to explain the radius inflation.

For the deeper Ohmic heating, Batygin & Stevenson (2010) considered the region between 100 and 3000 bar where the conductivity increases from $\sigma_e = 10^{-2} \text{ S m}^{-1}$ to $\sigma_i = 10 \text{ S m}^{-1}$. This value should be used in equation (29). Even though only a small fraction of the total Ohmic power is necessary to be deployed below the radiative–convective boundary, the larger uncertainty on the internal field strength and the strong temperature dependence of σ_e makes a proper quantification very challenging.

3.2 KELT-9b

As a high-temperature counter example, we investigate the atmospheric structure and the induction process of KELT-9b. Planetary parameters from observations are summarized in Table 2, the derived

Table 2. KELT-9b properties. The Brunt–Väisälä frequency is calculated assuming an isothermal atmosphere $N_T = g/\sqrt{T_{\text{eq}} c_p}$.

Name	Variable	Value	Reference
Planetary radius	R_p	1.354×10^8 m	Borsa et al. (2019)
Planetary mass	M_p	5.467×10^{27} kg	Borsa et al. (2019)
Eq. temperature	T_{eq}	3921 K	Borsa et al. (2019)
Surface gravity	g	20.8 m s^{-2}	Borsa et al. (2019)
Rotation frequency	Ω	$4.91 \times 10^{-5} \text{ s}^{-1}$	Gaudi et al. (2017)
Stratification	N_T/Ω	61.8	
Wind speed	U	$1.3 \times 10^4 \text{ m s}^{-1}$	Fossati et al. (2020)
Density at 0.1 bar	ρ	$7.16 \times 10^{-4} \text{ kg m}^{-3}$	Fig. 2
Specific heat	c_p	$1.2 \times 10^4 \text{ J kg}^{-1} \text{ K}$	
Radial scale height	d_U	2.7×10^6 m	2 per cent radius

quantities of the interior and atmospheric magnetic properties are given in Table 1 and compared to HD 209458b.

3.2.1 Ionization degree and the electrical conductivity

First, we calculate the ionization degree α and the electrical conductivity σ_e for P – T conditions as assumed to be present in the atmosphere of KELT-9b. The P – T profiles used for the calculation of the transport properties are fundamental input parameters to our induction model. The atmospheric conditions of KELT-9b have been extensively studied, e.g. to investigate the source of the high upper atmospheric temperatures indicated by observations of Balmer series and spectral lines of metal atoms (Hoeijmakers et al. 2018, 2019; Wyttenbach et al. 2020).

We first summarize two studies whose outcomes we find adequate to use in our work, particularly the P – T profiles presented in there. Mansfield et al. (2020) present *Spitzer* phase curve observations of KELT-9b, deducing dayside and nightside planetary temperatures of about 4600 and 2600 K, respectively. They employ a global circulation model (GCM) to investigate the effect of additional heat transport mechanisms such as H_2 dissociation and recombination, which are included in the energy balance. The synthetic phase curves based on the GCM profiles yield better agreement with the observations than those without heat transport involving chemical reactions, but cannot reproduce the planetary temperatures derived from the phase curve observations. The corresponding P – T profiles yield too small planetary temperatures with a temperature difference between the averaged dayside and nightside profiles of about 1000 K. Fossati et al. (2021) take a different approach to investigate the source of the upper atmospheric heating. They generate synthetic P – T profiles and compare the ensuing synthetic transmission spectra with the observed $\text{H}\alpha$ and $\text{H}\beta$ line profiles. The inclusion of non-local thermal effects (NLTE) above 10^{-4} bar in their models shows a strong influence on the atmospheric thermal balance, resulting in a very good agreement with the line profiles. Additionally, the model of Fossati et al. (2021) accounts for heat redistribution from dayside to nightside in such way that the dayside temperature of 4600 K is met (Mansfield et al. 2020).

To illustrate the effect of different atmospheric conditions on the transport properties, particularly of varying temperature conditions on the dayside and nightside, we here use both the averaged dayside and nightside profiles from the GCM by Mansfield et al. (2020) (despite the fact that they yield too low temperatures as described above) and the dayside profile by Fossati et al. (2021). We display the three P – T profiles for KELT-9b in Fig. 4. Note that the pressure ranges of the profiles are different due to different scopes of the

Magnetic induction processes in hot Jupiters 3121

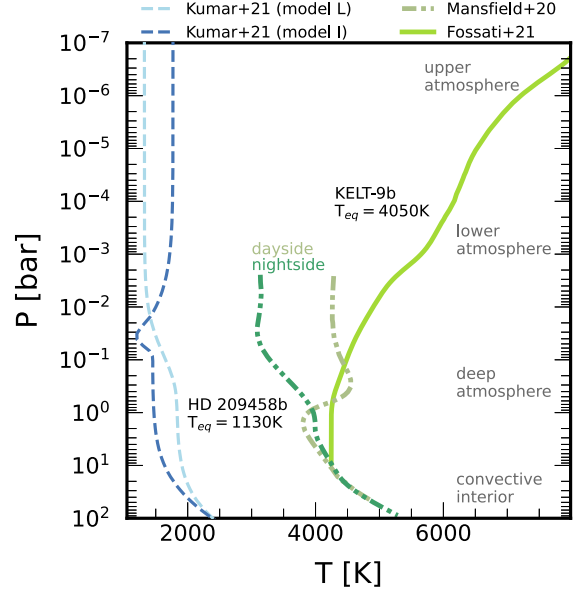


Figure 4. Pressure–temperature profiles of the atmosphere of the UHJ KELT-9b as used in our work to illustrate the dependence of the transport properties on the atmospheric conditions. The dayside profile of Fossati et al. (2021) is shown as a solid line. The dayside and nightside profiles by Mansfield et al. (2020) are displayed as dash–dotted lines. Additionally, the atmospheric profiles used in our previous work on the HJ HD 209458b (Kumar et al. 2021) are shown in blue.

atmospheric studies. Additionally, we show the profiles from our previous work in which we investigated the transport properties in the atmosphere of the HJ HD 209458b (Kumar et al. 2021) with an equilibrium temperature of 1130 K for various P – T profiles.

Our results for the ionization degree and conductivity along the P – T profiles are shown in Fig. 5. We also compare with results from our previous work for HD 209458b (Kumar et al. 2021). In general, ionization degree (Fig. 5b) and electrical conductivity (Fig. 5c) are closely related and follow a very similar behaviour as the pressure decreases.

The dayside P – T profile of KELT-9b shows a temperature inversion, i.e. the temperature increases with decreasing pressure in the outer atmosphere. The increasing temperature and decreasing density leads to a growing degree of thermal ionization. Since the ionization degree increases and the electrons scatter less frequently at lower density, the electrical conductivity σ_e increases toward the outer atmosphere. In the isothermal region (0.5–10 bar), the conductivity remains nearly constant.

The dayside-to-nightside variation in temperature can be significant in UHJs. Thus, the amount of thermally ionized constituents may also differ on each side. For that reason, we calculate the ionization degree and electrical conductivity for both dayside and nightside. For the profiles of Mansfield et al. (2020), the dayside temperature in the lower atmosphere is ≈ 1600 – 2000 K hotter than the nightside, followed by an inversion in the deep atmosphere. The ionization degree (Fig. 5b) is decreasing in the isothermal region (0.002–0.02 bar) due to an increase in the pressure that is followed by a sharp decrease at 0.3 bar. This sharp decrease is a consequence of the decrease of temperature in the inversion layer. The electrical conductivity is following the ionization degree profile.

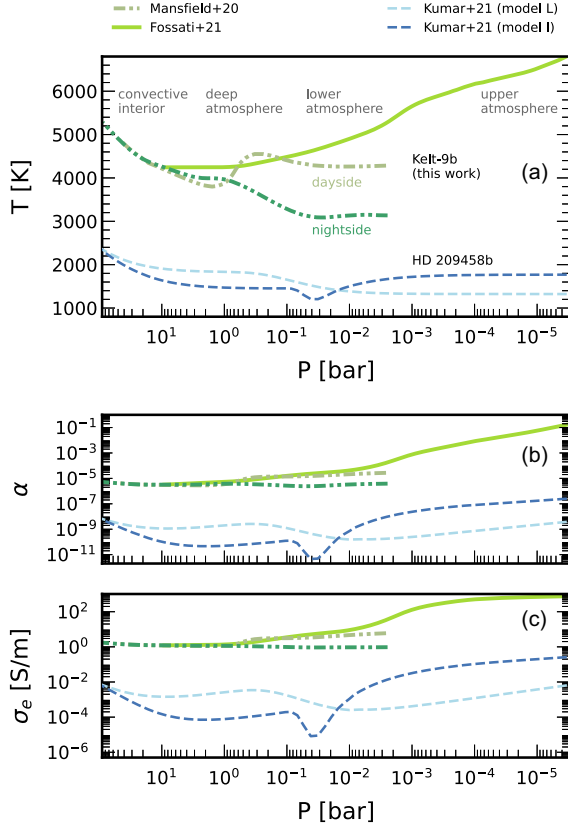
3122 *W. Dietrich et al.*

Figure 5. Atmospheric temperature T , ionization degree α , and electrical conductivity σ_e along pressure P for KELT-9b. For comparison, two atmospheric profiles (L and I) of HD 209458b (dashed line) are also added in blue (Kumar et al. 2021).

Similarly to the dayside, the ionization degree on the nightside is decreasing in the isothermal region (0.001–0.01 bar), which is followed by an increase due to the rising temperature in the outer atmosphere. The electrical conductivity is following a very similar behaviour as the ionization degree. The σ_e values in the lower atmosphere are 5–6 times lower than the dayside values, and in the deep atmosphere they are similar as on the dayside.

In comparison with the colder HJ HD 209458b, α and σ_e have higher values because of the higher temperatures for KELT-9b (Fig. 4, green profiles). However as the rather constant ionization degree suggests, the temperature typical KELT-9b, even on the nightside, is high enough to sustain a plasma in which the bulk of the alkali metals is singly ionized. In comparison to colder HJs, the electrical conductivity σ_e does not show the strong temperature dependence characteristic for ionization processes.

The absolute values of electrical conductivity in KELT-9b are between two and four orders of magnitude higher than in HD 209458b. For a detailed discussion of the HD 209458b profiles, see Kumar et al. (2021).

Note that we have restricted our calculation of ionization and electrical conductivity to as low as 10^{-6} bar pressure because at further lower pressure (outer atmosphere) non-equilibrium processes and magnetic field will impact these properties. This is a subject left for future work.

3.2.2 Internal heat flux and magnetic field strength

The strength of the internal, dynamo-generated magnetic field for KELT-9b is a function of the available buoyancy power. The associated internal heat flux can be based on the thermal evolution (equation 9). KELT-9b is young (300 Myr; Borsa et al. 2019), heavy, and large. Thus following this scaling relation, the intrinsic heat flux is $q_{\text{int}} = 550 \text{ W m}^{-2}$. On the other hand, the relation from Thorngren & Fortney (2018) or equation (10) yields a smaller heat flux of $q_{\text{int}} = 29 \text{ W m}^{-2}$. The internal, dynamo-generated magnetic field based on equation (8) reaches between 1 and 2 mT.

3.2.3 Atmospheric induction

Fig. 2 illustrates that the electrical conductivity σ_e in the atmosphere of KELT-9b (green profiles) is up to four order of magnitude higher than in HD 209458b. The profiles also show that the atmosphere of KELT-9b is to first-order isothermal in the dynamically relevant pressure range between 0.01 and 1 bar. Electrical conductivities are of the order 1 S m^{-1} on the nightside and can become one order of magnitude larger on the dayside. Given the quite strong dayside-to-nightside temperature contrast of 1500 K, the associated contrast in σ_e is rather small. This once more shows that the almost all alkali metals are ionized at such temperatures and the depth and lateral gradients remain rather small.

The length scale d entering the magnetic Reynolds number will thus be determined by the induction process itself. Whereas simulations suggest rather broad zonal flows (Showman & Guillot 2002), they might be more constrained in radius. As they are driven by irradiation gradients, the winds will not reach deeper than 1 bar, where the optical depth in infrared wavelength range reaches unity. We therefore estimate a radial wind scale height of one pressure scale height, i.e. $d_U = 0.02R \approx 2700 \text{ km}$. Assuming furthermore wind velocities of about 13 km s^{-1} (Fossati et al. 2021), then yields magnetic Reynolds numbers of about 4.5×10^4 for KELT-9b. Under these conditions, the time variability of the induced field remains a key contribution and the induction is strongly non-linear.

Thus the induction of atmospheric magnetic fields will be runaway process that cannot be stopped by diffusion. First, we consider Alfvén waves as a possible scenario (see Fig. 1c). The maximum azimuthal field during cycle of the Alfvén wave is given by equation (18):

$$\bar{B}_\phi = (\mu_0 \rho)^{1/2} \bar{U}_\phi \approx 400 \text{ mT}. \quad (31)$$

The oscillation period is the inverse Alfvén frequency, $t_A \approx 150 \text{ d}$. This field amplitude will not be reached, since the shear is suppressed with regard to the force balance (equation 21 and Fig. 1d) at an amplitude of

$$B_\phi \approx (\bar{\rho} \mu_0)^{1/2} (d_U \Omega U)^{1/2} \approx 40 \text{ mT}. \quad (32)$$

However, at a very similar field strength of 50 mT, and according to equation (25) the Tayler instability will set in with the form of a ($m = 1$)-kink instability (see Fig. 2e). The radial scale of the instability given by equation (A1), KELT-9b radial scale is somewhat smaller than $0.02R$, a value very similar to our assumed zonal flow scale d_U . This instability grows until the saturation field strength is reached. Using our KELT-9b values suggests a field strength (equation 26) of roughly 400 mT, about an order of magnitude larger than the critical strength.

For the larger field amplitude of 400 mT, the related local electrical current in this non-linear regime is given by equation (28):

$$j = 0.1 \text{ A m}^{-2}, \quad (33)$$

where we used $d_U = 2.7 \times 10^6$ m. This leads to a total Ohmic power of 5.34×10^{21} . Compared to the bolometric luminosity of

$$L = 4R_p^2 \sigma_{\text{SB}} T_{\text{eq}}^4 \approx 10^{24} \text{ W}, \quad (34)$$

this is a negligible fraction suggesting that other mechanisms, such as tidal heating, dissipate much more energy and are responsible for excessive luminosity.

Using the electrical conductivity for KELT-9b, the minimal radial flow speeds allowing for dynamo action in the atmosphere independent of the internal field is

$$u_r = \frac{1}{\mu_0 \sigma_e d_r} \approx 10 \text{ m s}^{-1}, \quad (35)$$

a value that is matched in numerical simulations and observations for KELT-9b (Komacek et al. 2019). An alternative is the Tayler–Spruit dynamo, where the emerging instability replenishes the poloidal field component and thus maintains the dynamo, seems a possibility. Dynamos based on the horizontal variation of the electrical conductivity seem unlikely given the small horizontal variation indicated by Fig. 5, bottom panel.

4 DISCUSSION

The small semimajor axis of HJs and the synchronous orbits cause high atmospheric temperatures, at which a sizeable electrical conductivity is generated from the thermal ionization of metals.

Here we show that as the temperature increases several metals ionize and contribute stepwise to an increase of electrical conductivity σ_e , which can amount 10^{-4} S m^{-1} at 1500 K (potassium) and 1 S m^{-1} at 3000 K (sodium and calcium). The absolute values depend on the abundance of the particular metal species. Iron and hydrogen start to play a role only at temperatures in excess of 4000 K. Together with the atmospheric winds, which are driven by irradiation gradients and have been measured to reach velocities of a few km s^{-1} (Snellen et al. 2010; Fossati et al. 2021), strong electromagnetic currents are to be expected.

Thus, electromagnetic effects, such as Ohmic dissipation (Batygin & Stevenson 2010), magnetic drag (Perna et al. 2010), or weakening of the azimuthal flows via Lorentz forces (Rogers & Showman 2014) that tend to equilibrate the strong azimuthal irradiation contrasts, have been suggested to explain the large radii, strong dayside-to-nightside brightness contrasts, or infrared phase shifts (Menou 2012; Showman et al. 2015; Rogers & McElwaine 2017). All of those require a reliable estimate of the electrical conductivity, atmospheric flows pattern, and of the induction of electrical currents, magnetic fields and their dissipation.

Our results suggest that HJs can be categorized in two distinct groups depending on their temperature. Colder planets, e.g. HD 209458b, host a linear induction process in the irradiated atmosphere, characterized by $\text{Rm} = \sigma_e \mu_0 dU < 1$, where the induced field is limited by magnetic diffusion (Batygin & Stevenson 2010; Kumar et al. 2021). Here the electrical conductivity is exclusively due to the (partial) ionization of potassium. This approximation is valid only for HJs with an equilibrium temperature of $T_{\text{eq}} < 1500$ K. The induced atmospheric currents are then simply $j = \sigma_e U_\phi B_{\text{int}}$, i.e. a function of flow speed, the internal field strength, and the electrical conductivity. The Ohmic power scales with σ and the square of flow speeds and internal field strength.

In hotter planets with larger electrical conductivity the induction of atmospheric magnetic fields is very rapid ($\text{Rm} \gg 1$) and can only be saturated by non-linear effects, e.g. back-reaction of the Lorentz

Magnetic induction processes in hot Jupiters 3123

forces on to the flow or the emergence of magnetic instabilities. This requires new estimates for the electromagnetic induction effects. As an example, we have calculated ionization degree and electrical conductivity in the atmospheric plasma of the UHJ KELT-9b being the hottest HJ observed so far. The dayside and nightside temperature in the relevant part of the atmosphere around 0.001 and 1 bar reach 4600 and 3000 K, respectively. At these temperatures, all sodium and calcium atoms are singly ionized, whereas the ionization of iron only starts to contribute on the dayside. The electrical conductivity, σ_e , reaches values of roughly 1 S m^{-1} . Consequently, σ_e is rather constant in the relevant T range. Even for such dayside-to-nightside temperature contrast the difference in σ_e is less than on order of magnitude. This is in strong contrast to colder HJs, where even small temperature variations will lead to large horizontal and radial variations in σ_e .

In addition, the atmospheric winds, driven by the irradiation gradients, are strong and thus lead to high magnetic Reynolds number. For KELT-9b, we estimate $\text{Rm} = 4 \times 10^4$ and thus the induced magnetic field will quickly outgrow the internal field. Radial field lines representing the internal field will be wound-up around the planet by the atmospheric shear. Thus the induced field \bar{B}_ϕ is predominantly axisymmetric and azimuthal. This process shares strong similarities with the solar tachocline, where the radial field is wound-up. We therefore relied on other fundamental theoretical considerations from planetary and stellar dynamo physics.

We have discussed different mechanisms that would limit this process and determine the saturated field strength of \bar{B}_ϕ . The respective estimates suggest atmospheric, horizontal field strengths between 40 and 400 mT. The larger values are based on the saturation field strength of the Tayler instability. This is still an active area of research and should be seen with caution.

The smaller estimate, derived from the leading order force balance between the Coriolis and the Lorentz force, is more conservative and has thus higher credibility. At 40 mT the azimuthal field would be two orders of magnitude larger than Jupiter’s observed field and also significantly larger than the interior field of KELT-9b. For all estimates of the induced field, the strength is independent of the internal field strength and the electrical conductivity, but scales for example with the rotation rate, the wind speed, or atmospheric stratification.

The axisymmetric, azimuthal field \bar{B}_ϕ stays inside the planet and cannot be observed, but it contributes to the internal dynamics via Lorentz forces and via Ohmic heating. Because of the efficient winding-up, the Lorentz forces will be so high that they play a substantial role in the atmospheric dynamics

The associated electrical currents are calculated via $j = B_\phi / \mu_0 d_U$ and reach local values between 0.01 and 0.1 A m^{-2} . For the entire layer involved in the atmospheric induction, the Ohmic power amounts to between 10^{20} and $5 \times 10^{21} \text{ W}$. This is a small fraction of the overall bolometric luminosity of roughly 10^{24} W . This indicates that other processes such as tidal heating are of greater importance in maintaining the high luminosity of KELT-9b.

The weakness of the available Ohmic power ($\propto j^2 / \sigma_e$) is a natural consequence of the non-linear induction process. That is the fact that the induced field is independent of the electrical conductivity, thus the Ohmic power decreases with increasing σ_e .

Many HJs are inflated. The degree of inflation seems to first increase with planetary equilibrium temperature T_{eq} but decreases again beyond a maximum at about 1500 K (Thorngren & Fortney 2018). Several authors tried to explain the behaviour with the fact that Lorentz forces slow down the atmospheric winds for higher T_{eq} values (Menou 2012; Rogers & Showman 2014). Our analysis

3124 *W. Dietrich et al.*

suggests a simpler explanation: the increased conductivity of the very hot planets makes deep Ohmic heating too inefficient.

We have only briefly touched on the possibility that additional overturning or radial motions in the stably stratified atmosphere could play in the induction process. These motions are bound to be slower than the zonal winds but could nevertheless play an important role. They will convert azimuthal field into smaller scale radial field, thereby limit the winding-up process but ultimately allow for an independent atmospheric dynamo. Our estimates for KELT-9b strongly suggests that radial flows of the order of a few tens of metres per second suffice to turn the induction process into a self-sustained dynamo.

This bears the question whether both dynamos could be considered separately, as we have done here, or would influence each other. It has been suggested that a negative feedback between an internal and an external dynamo could explain the weakness of Mercury's magnetic field (Vilim, Stanley & Hauck 2010; Heyner et al. 2011). In the model studied by Heyner et al. (2011), the addition of an external magnetospheric dynamo quenched the overall field strength by nearly three orders of magnitude. Such a coupled dynamo would prevent us from ever detecting the magnetic field of a UHJ. Numerical dynamo simulations are required to explore these different options and to verify our theoretical predictions in the future.

ACKNOWLEDGEMENTS

We thank D. Shulyak for providing P - T profile data of the atmosphere of KELT-9b. This work was supported by the Deutsche Forschungsgemeinschaft (DFG) within the Priority Program SPP 1992 'The Diversity of Exoplanets' and the Research Unit FOR 2440 'Matter under Planetary Interior Conditions'. This work was partially supported by the Center for Advanced Systems Understanding (CASUS) that is financed by Germany's Federal Ministry of Education and Research (BMBF) and by the Saxon State Government out of the state budget approved by the Saxon State Parliament.

DATA AVAILABILITY

The data underlying this paper will be shared on reasonable request to the corresponding author.

REFERENCES

- Baraffe I., Chabrier G., Barman T. S., Allard F., Hauschildt P. H., 2003, *A&A*, 402, 701
- Batygin K., Stevenson D. J., 2010, *ApJ*, 714, L238
- Borsa F. et al., 2019, *A&A*, 631, A34
- Burrows A., Hubbard W. B., Lunine J. I., Liebert J., 2001, *Rev. Mod. Phys.*, 73, 719
- Busse F. H., Wicht J., 1992, *Geophys. Astrophys. Fluid Dyn.*, 64, 135
- Cao H., Stevenson D. J., 2017, *Icarus*, 296, 59
- Christensen U. R., 2010, *Space Sci. Rev.*, 152, 565
- Christensen U. R., Holzwarth V., Reiners A., 2009, *Nature*, 457, 167
- Fossati L. et al., 2020, *A&A*, 643, A131
- Fossati L., Young M. E., Shulyak D., Koskinen T., Huang C., Cubillos P. E., France K., Sreejith A. G., 2021, *A&A*, 653, A52
- French M., Redmer R., 2017, *Phys. Plasmas*, 24, 092306
- French M., Becker A., Lorenzen W., Nettelmann N., Bethkenhagen M., Wicht J., Redmer R., 2012, *ApJS*, 202, 5
- Fuller J., Piro A. L., Jermyn A. S., 2019, *MNRAS*, 485, 3661
- Gaudi B. S. et al., 2017, *Nature*, 546, 514
- Guillot T., Burrows A., Hubbard W. B., Lunine J. I., Saumon D., 1996, *ApJ*, 459, L35

- Heyner D., Wicht J., Gómez-Pérez N., Schmitt D., Auster H.-U., Glassmeier K.-H., 2011, *Science*, 334, 1690
- Hoeijmakers H. J. et al., 2018, *Nature*, 560, 453
- Hoeijmakers H. J. et al., 2019, *A&A*, 627, A165
- Iro N., Bézard B., Guillot T., 2005, *A&A*, 436, 719
- Kislyakova K. G., Holmström M., Lammer H., Odert P., Khodachenko M. L., 2014, *Science*, 346, 981
- Komacek T. D., Showman A. P., Parmentier V., 2019, *ApJ*, 881, 152
- Kuhlbrodt S., Redmer R., 2000, *Phys. Rev. E*, 62, 7191
- Kuhlbrodt S., Holst B., Redmer R., 2005, *Contr. Plasma Phys.*, 45, 73
- Kumar S., Poser A. J., Schöttler M., Kleinschmidt U., Dietrich W., Wicht J., French M., Redmer R., 2021, *Phys. Rev. E*, 103, 063203
- Liu J., Goldreich P. M., Stevenson D. J., 2008, *Icarus*, 196, 653
- Lodders K., 2003, *ApJ*, 591, 1220
- Mansfield M. et al., 2020, *ApJ*, 888, L15
- Menou K., 2012, *ApJ*, 745, 138
- Parmentier V. et al., 2018, *A&A*, 617, A110
- Perna R., Menou K., Rauscher E., 2010, *ApJ*, 719, 1421
- Pitts E., Tayler R. J., 1985, *MNRAS*, 216, 139
- Redmer R., 1999, *Phys. Rev. E*, 59, 1073
- Redmer R., Rother T., Schmidt K., Kraeft W. D., Röpke G., 1988, *Contr. Plasma Phys.*, 28, 41
- Rogers T. M., 2017, *Nat. Astron.*, 1, 0131
- Rogers T. M., McElwaine J. N., 2017, *ApJ*, 841, L26
- Rogers T., Showman A., 2014, *ApJ*, 782, L4
- Sarkis P., Mordasini C., Henning T., Marleau G. D., Mollière P., 2021, *A&A*, 645, A79
- Schöttler M., Redmer R., French M., 2013, *Contr. Plasma Phys.*, 53, 336
- Showman A. P., Guillot T., 2002, *A&A*, 385, 166
- Showman A. P., Lewis N. K., Fortney J. J., 2015, *ApJ*, 801, 95
- Snellen I. A. G., de Kok R. J., de Mooij E. J. W., Albrecht S., 2010, *Nature*, 465, 1049
- Spruit H. C., 1999, *A&A*, 349, 189
- Spruit H. C., 2002, *A&A*, 381, 923
- Thorngren D. P., Fortney J. J., 2018, *AJ*, 155, 214
- Thorngren D., Gao P., Fortney J. J., 2019, *ApJ*, 884, L6
- Thorngren D., Gao P., Fortney J. J., 2020, *ApJ*, 889, L39
- Vilim R., Stanley S., Hauck S. A., 2010, *J. Geophys. Res.*, 115, E11003
- Wicht J., Gastine T., Duarte L. D. V., 2019a, *J. Geophys. Res.*, 124, 837
- Wicht J., Gastine T., Duarte L. D. V., Dietrich W., 2019b, *A&A*, 629, A125
- Wong I. et al., 2020, *AJ*, 160, 88
- Wytenbach A. et al., 2020, *A&A*, 638, A87
- Zaghoo M., Collins G. W., 2018, *ApJ*, 862, 19
- Zahn J. P., Brun A. S., Mathis S., 2007, *A&A*, 474, 145

APPENDIX: TAYLER INSTABILITY

The mathematical description of this instability is based on the works of Spruit (1999, 2002) and has been derived in the context of the solar dynamo, where a stably stratified zone of strong shear (tachocline) relentlessly creates azimuthal field from radial field lines. This winding up of the field was suggested to be stopped by the Tayler instability.

The kinetic energy for this instability is provided by the restoring magnetic force of the wound-up field B_ϕ . In analogy to the Alfvén waves discussed above we conclude that the (maximum) kinetic energy is $1/2\omega_A^2\xi^2$, where ξ is a displacement perpendicular to the loop of induced azimuthal field lines. The stable stratification provides an obstacle that requires the energy $1/2N^2\xi_r^2$, where $\xi_r^2 = \xi^2 - \xi_h^2$ is the squared displacement in the direction of stratification and ξ_h^2 its horizontal counterpart. The condition that the provided kinetic energy should exceed the one required to work against the stable stratification yields $d_U < (\omega_A/N)d_h$ where we have assumed that the displacement reflects the radial scale d_r and horizontal scale d_h so that $d_r^2/d_h^2 = \xi_r^2/\xi_h^2$. Using R_p as an upper bound for d_h then leads to the first condition for the instability that relates field strength and

radial scale:

$$\frac{d_r}{R} < \frac{\omega_A}{N}. \quad (\text{A1})$$

The second condition is that the growth rate of the instability must exceed the dissipation rate, i.e. η/d_r^2 . The growth rate in the presence of a strong Coriolis force is ω_A^2/Ω (Pitts & Tayler 1985). Using equation (A1), the second condition provides a constraint for the Alfvén velocity:

$$\frac{\omega_A}{\Omega} > \left(\frac{N}{\Omega}\right)^{1/2} \left(\frac{\eta}{R^2\Omega}\right)^{1/4}. \quad (\text{A2})$$

This translates into a critical field strength for the onset of the Tayler instability:

$$B_\phi = \Omega R (\mu_0 \rho)^{1/2} \left(\frac{N}{\Omega}\right)^{1/2} \left(\frac{\eta}{R^2\Omega}\right)^{1/4}. \quad (\text{A3})$$

The magnetic continuity condition $\nabla \cdot \mathbf{B} = 0$ relates instability components \mathbf{B}' and length scales:

$$\frac{B'_r}{B'_\phi} \approx \frac{d_r}{R}. \quad (\text{A4})$$

The primed field quantities denote the magnetic field components of the Tayler instability with the most unstable azimuthal wavenumber $m = 1$.

The growth of the instability will stop once dissipation balances the rate at which the field is amplified. The amplification rate is given by equation (13),

$$\frac{\overline{U}}{d_r} \frac{B'_r}{B'_\phi} \approx \frac{\overline{U}}{d_r} \frac{d_U}{R}, \quad (\text{A5})$$

Magnetic induction processes in hot Jupiters 3125

where we have used equation (A4). To quantify the effective dissipation rate in the presence of the instability, Spruit (2002) assumes that it remains close to the growth rate of the instability:

$$\frac{\eta}{d_r^2} \approx \frac{\omega_A^2}{\Omega}. \quad (\text{A6})$$

Combining equations (A5) and (A6) and using condition equation (A1) with the largest possible scale $d_r = \omega_A/(NR_\rho)$ to minimize dissipation yields

$$\frac{\omega_A}{\Omega} = \frac{\overline{U}}{d_r N}. \quad (\text{A7})$$

This translated into the field strength,

$$B_\phi = (\mu_0 \rho)^{1/2} \frac{\Omega R \overline{U}}{N d_r}. \quad (\text{A8})$$

While equation (A3) estimates the field strength at which the instability would set in, equation (A8) estimates the field strength where it would saturate.

The different assumptions made by Spruit (2002) have been criticized, in particular the way the saturation field strength equation (26) has been derived (see e.g. Zahn et al. 2007; Fuller, Piro & Jermyn 2019). So far, there seems to be no consensus. Note that estimate (26) can become smaller than equation (25) for large values of N/Ω . It seems likely that equation (26) actually describes the field strength of the non-axisymmetric instability but unfortunately Spruit (2002) is not clear about this.

This paper has been typeset from a $\text{\TeX}/\text{\LaTeX}$ file prepared by the author.

A. Appendix

A.1. Entropy of Hydrogen and Helium-EoS in the Temperature-Pressure Plane

The equations of state for hydrogen and helium are crucial for understanding the interior structure of gas giants. The SCvH95 and CD21 tables provide comprehensive coverage of the temperature-pressure conditions relevant to these planets. Fig. A.1 illustrates the EoS of SCvH95 [356] and CD21 [357] for hydrogen and helium in the temperature-pressure plane. The third axis shows the corresponding tabulated entropy. The specific entropy s is a crucial quantity, as the intrinsic heat flux is carried by convection, thus determining the thermal evolution of the giant planets, $Q = ds/dt$ where Q is the heat, and t the time.

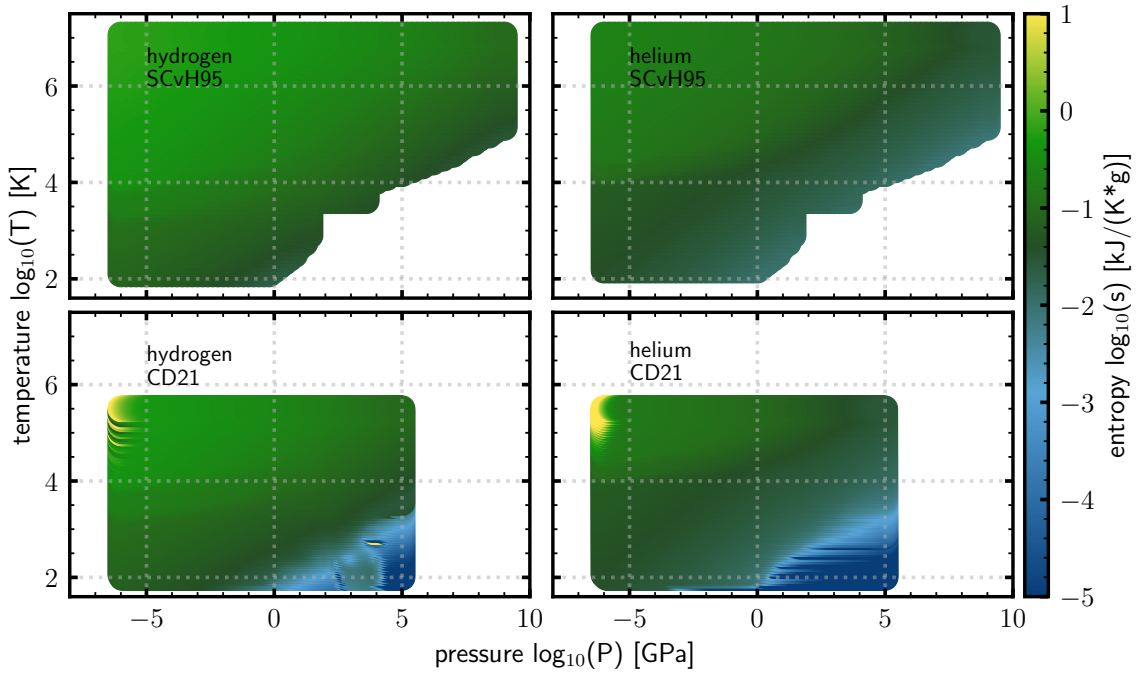


Figure A.1.: Entropy in the temperature-pressure plane of the pure EoS tables of CD21 [357] and SCvH95 [356] for the main components of giant planets, hydrogen and helium. The EoS by CD21 take interactions of the H/He-mixture in the warm dense matter regime into account.

A.2. Introduction to Mass Fractions, Solar Abundances, and Conversions

The definitions and nomenclature in this section follow Thorngren and Fortney [141], Fortney *et al.* [402] and Nettelmann [330].

A.2.1. Mass Fractions, Number of Particles and Molecular Masses

Consider a volume of gas with mass M with the mass fractions X (hydrogen H), Y (helium He) and Z (metals, all elements heavier than helium and hydrogen). The corresponding mass fractions are defined as

$$X = \frac{\mu_X N_H}{M}, \quad Y = \frac{\mu_{\text{He}} N_{\text{He}}}{M}, \quad Z = \frac{\mu_Z N_Z}{M}, \quad (\text{A.1})$$

with $N = N_H + N_{\text{He}} + N_Z$ as the number of particles and the molecular masses μ_H , μ_{He} , μ_Z . The molecular weights are defined in units of hydrogen atom masses: $\mu = \bar{m}/m_H$. It is for hydrogen $\mu_H = 1$ or $\mu_H = 2$ (atomic or molecular), for helium $\mu_{\text{He}} = 4$, and for metals representative in this work, $\mu_Z = \mu_{\text{H}_2\text{O}} = 18$ (g mole⁻¹).

Globally, it holds that

$$X + Y + Z = 1. \quad (\text{A.2})$$

For the total mass M follows:

$$\begin{aligned} M &= M_H + M_{\text{He}} + M_Z \\ &= \mu_X N_X + \mu_Y N_Y + \mu_Z N_Z. \end{aligned} \quad (\text{A.3})$$

With the definition of the total mass, it follows for X and Y :

$$X = \frac{\mu_H N_H}{\mu_H N_H + \mu_{\text{He}} N_{\text{He}} + \mu_Z N_Z} = \frac{M_H}{M_H + M_{\text{He}} + M_Z}, \quad (\text{A.4})$$

$$Y = \frac{\mu_{\text{He}} N_{\text{He}}}{\mu_H N_H + \mu_{\text{He}} N_{\text{He}} + \mu_Z N_Z} = \frac{M_{\text{He}}}{M_H + M_{\text{He}} + M_Z}. \quad (\text{A.5})$$

For a given composition of atomic heavy elements with atomic weights μ_i , the metal mass fraction can be generalised to:

$$Z = \frac{\sum_i \mu_i N_i}{\mu_H N_H + \mu_{\text{He}} N_{\text{He}} + \sum_i \mu_i N_i}. \quad (\text{A.6})$$

Further, Nettelmann [330] defines the mean helium abundance in mass with respect to the H/He subsystem

$$Y' := \frac{M_{\text{He}}}{M_H + M_{\text{He}}}. \quad (\text{A.7})$$

The mass fraction of helium is then $Y = (1 - Z)Y' = (X + Y)Y'$. This definition is used in MOGROP to calculate the corresponding mass fractions: (1) the atmospheric/envelope

mass fraction $Z_{\text{atm/env}}$ and the bulk abundance of helium Y' are set; (2) $Y = (1 - Z)$, Y' is calculated; and (3) the hydrogen mass fraction is found as $X = 1 - Y - Z$.

General Mass Ratios for the whole Planet (including core)

If a core of heavy elements exists, it significantly contributes to the total amount of heavy elements. The total mass of heavy elements is M_Z and the bulk metallicity Z_P can be calculated from:

$$\begin{aligned} M_Z &= Z_{\text{atm}} M_{\text{atm}} + Z_{\text{env}} M_{\text{env}} + M_{\text{core}} \\ Z_P &= M_Z / M_P \\ &= (M_{Z,\text{atm}} + M_{Z,\text{env}} + M_{\text{core}}) / M_P \\ &= Z_{\text{atm}} M_{\text{atm}} / M_P + Z_{\text{env}} M_{\text{env}} / M_P + M_{\text{core}} / M_P. \end{aligned}$$

For a fully mixed planet ($M_{\text{core}} = 0$ and $Z_{\text{atm}} = Z_{\text{env}}$) the equation above simplifies, so that the total bulk metallicity equals the fraction of metals in the planet.

A.2.2. Protosolar and Present-Day Photospheric Mass Fractions

The occurrence of a certain element is usually presented in terms of solar abundances, categorised as sub-solar, solar, or super-solar. However, it is important to carefully consider the reference values, as both protosolar and present-day photospheric elemental abundances and mass fractions are used in different contexts. An overview of the nomenclature can be found in Lodders [530].

Protosolar abundances refer to the elemental abundances of the proto-Sun at its formation time, 4.57 billion years ago. In the literature, protosolar abundances are often equated with Solar System abundances. The term Solar System abundance includes the elemental inventory of all solar system bodies such as planets, the Sun, moons, comets, meteorites, and interplanetary dust [530].

Photospheric abundances refer to the present-day elemental abundances of the Sun's photosphere. The present-day photosphere is not representative of the proto-Sun due to processes such as heavy-element fractionation (including helium diffusion and gravitational settlement from the convective zone to the interior, partially counteracted by radiation levitation). Consequently, the protosolar metal abundance is derived from present-day photospheric abundances by considering these settling effects, e.g. [495].

Table A.1 shows mass fractions of the present-day photosphere and the proto-Sun from common sources used in the literature.

Throughout this work, the protosolar mass fraction of metals $Z = 0.015$ from Lodders [495] was used as the reference value for $1 \times$ solar (bulk) metallicity. For the H/He mass fraction Y' (Eq. (A.7)), a value of $Y' = 0.275$ was mostly used, unless otherwise specified. This value is taken from Bahcall *et al.* [531], which derives a protosolar range of $0.270 - 0.278$.

	present-day photosphere				protosolar			
	X	Y	Z	X/Z	X ₀	Y ₀	Z ₀	X ₀ /Z ₀
Lodders 2003 ¹	0.7491	0.2377	0.0133		0.7110	0.2741	0.0149	0.0210
Lodders+2009 ²	0.7390	0.2469	0.0141	0.0191	0.7112	0.2735	0.0153	0.0215
Asplund+2009 ³	0.7381	0.2485	0.0134	0.0181	0.7154	0.2703	0.0142	0.0199

Table A.1.: Ref.: ¹[495], ²[412], ³[532]. In Lodders [530], a detailed overview on abundances is given.

A.2.3. From Metal Mass Fractions to Abundance Ratios

The amount of metals of a planet, both in bulk and atmosphere, is an essential input for exoplanet formation theories. The term metallicity is used frequently to describe the amount of metals, in both communities of atmospheric astronomers and astronomers modelling the interiors of planets. Often, different definitions of metallicity lay underneath. However, it is necessary to understand and to convert the definitions, so both communities can have a joint communication.

When modelling the bulk metallicity, astronomers speak of the heavy element mass fraction Z or of the metallicity $[M/H]$ - where M refers to all elements heavier than hydrogen and helium. For stars, one speaks of the ratio $[Fe/H]$ to distinguish between a metal-rich and a metal-poor star. On the other hand, atmospheric astronomers often speak of elemental abundances, e.g. of oxygen $[O/H]$. Writing styles might differ, e.g. $[Z/H]$, (Z/H) , $Z:H$, or $(Z:H)$.

This section introduces some of the frequently used terms found in the literature, with the hope that this will be useful for future readers.

(1) The terminus enrichment is defined as the number of an element compared to the number of that element in the Sun.

(2) The metal abundance ratio $Z:H$ is defined by number of particles in comparison to the number of hydrogen particles. The following equation can be derived with the equations in Sect. A.2.1, see also Thorngren and Fortney [141]:

$$\begin{aligned}
 Z : H &= \frac{N_Z}{N_H} = \frac{MZ/\mu_Z}{MX/\mu_H} \\
 &= \frac{Z}{(1-Z)} \frac{1}{X/(X+Y)} \frac{1}{\mu_Z/\mu_H} \\
 &= \frac{1}{Z^{-1}-1} (1+Y/X) \frac{1}{\mu_Z/\mu_H} \\
 &= \frac{1+Y/X}{Z^{-1}-1} \frac{1}{\mu_Z/\mu_H} .
 \end{aligned} \tag{A.8}$$

N_i is the number and μ_i the mean molecular mass of particle i , X/Y is the H/He mass ratio, and Z the metal mass fraction of a gas with mass M .

The solar metal abundance ratio $(Z:H)_{\text{Sun}}$ can be obtained by inserting the mass fraction Y and X from Table A.1 in Asplund *et al.* [532], and the molecular masses $\mu_Z = 18$ (H_2O),

$\mu_{\text{H}} = 2$ (H_2) or $\mu_{\text{H}} = 1$ (H) in Eq. (A.8):

$$\begin{aligned} (\text{Z} : \text{H})_{\text{Sun}, \text{H}_2} &= \frac{1 + 0.2485/0.7381}{0.0134^{-1} - 1} \cdot \frac{1}{18/2} = \frac{1 + 0.3367}{0.0134^{-1} - 1} \cdot \frac{1}{18/2} \\ &\approx 0.002017 \approx 2.02 \times 10^{-3} \\ (\text{Z} : \text{H})_{\text{Sun}, \text{H}} &= \frac{1 + 0.2485/0.7381}{0.0134^{-1} - 1} \cdot \frac{1}{18/1} = \frac{1 + 0.3367}{0.0134^{-1} - 1} \cdot \frac{1}{18/1} \\ &\approx 0.001008 \approx 1.01 \times 10^{-3} \quad . \end{aligned}$$

Thorngrén and Fortney [141] propose to use a solar photospheric metal abundance as reference of $(\text{Z}:\text{H})_{\text{Sun}, \text{H}, \text{TF19}} = 1.04 \times 10^{-3}$.

(3) The metallicity is defined using the decadic logarithm of the metal abundance ratio and the solar reference abundance:

$$[\text{M}/\text{H}] = \log_{10} \left(\frac{N_{\text{Z}}}{N_{\text{H}}} \right) - \log_{10} \left(\frac{N_{\text{Z}}}{N_{\text{H}}} \right)_{\text{Sun}} \quad . \quad (\text{A.9})$$

where $[\text{M}/\text{H}]$ can also be noted as $[\text{Z}/\text{H}]$, as Z and M both denote the heavy elements. The ratio $(N_{\text{Z}}/N_{\text{H}})$ is the metal abundance ratio $(\text{Z}:\text{H})$ from Eq. (A.8).

$[\text{M}/\text{H}]$	-2	-1.5	-1	-0.5	0	+0.5	+0.7	+1	+1.5	+2
$x \times \text{solar}$	0.01	0.03	0.10	0.32	1	3.16	5.01	10.0	31.62	100

Table A.2.: Conversion from $x \times \text{solar}$ to $[\text{M}/\text{H}]$. The column of $x \times \text{solar}$ is equivalent to $(\text{Z}:\text{H})/(\text{Z}:\text{H})_{\text{Sun}}$.

Z	$\text{Z}:\text{H}$	$x \times \text{solar}$	$[\text{M}/\text{H}]$
0.001	0.00015	0.07	-1.18
0.003	0.00046	0.20	-0.70
0.005	0.00076	0.33	-0.48
0.010	0.00154	0.66	-0.18
0.015	0.00232	1.00	0.00
0.050	0.00801	3.46	0.54
0.100	0.01691	7.30	0.86
0.150	0.02686	11.59	1.06
0.200	0.03805	16.42	1.22
0.300	0.06523	28.14	1.45
0.320	0.07163	30.90	1.49
0.440	0.11959	51.60	1.71
0.500	0.15221	65.67	1.82

Table A.3.: Conversion for selected metallicities Z to $[\text{M}/\text{H}]$, derived with the solar metal abundance reference $(\text{Z}:\text{H})_{\text{Sun}}=0.001159$ ($\mu_{\text{Z}} = 18$, $\mu_{\text{H}} = 2$, $Y/X = 0.3699$). $x \times \text{solar}$ is equivalent to $(\text{Z}:\text{H})/(\text{Z}:\text{H})_{\text{Sun}}$.

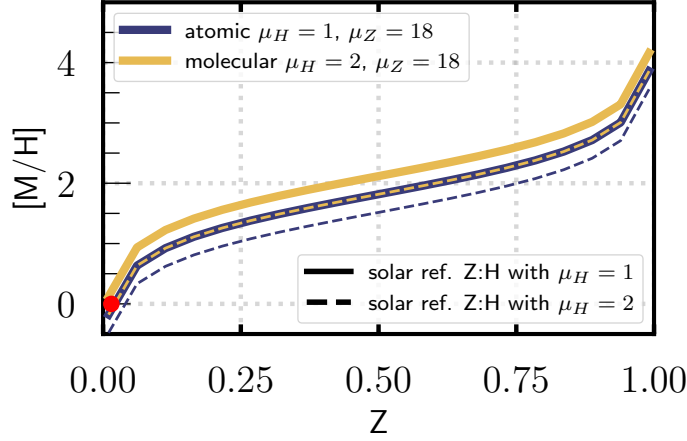


Figure A.2.: Displaying the conversion from Z to $[M/H]$. The orange dashed curve is equivalent to the values in Tab. A.3. The red dot displays the reference condition where $Z = 0.015$ yields $[M/H] = 0$.

To make sure the conversion from Z over $Z:H$ to $[M/H]$ yields for a solar Z $[M/H] = 0$, one may need to adjust the solar reference value [533]. For example, using the protosolar value of $Z_{\text{solar}} = 0.015$ for $1 \times$ solar metallicity [495], it is intended to match $[M/H] = 0$ for Z_{solar} . Applying Eq. (A.8) with $Y' = 0.27$ ($Y/X = 0.3699$), $\mu_H = 1$, and $\mu_{H_2O} = 18$, the solar metal abundance reference is calculated as $(Z:H)_{\text{Sun}} = \left(\frac{N_Z}{N_H}\right)_{\text{Sun}} = 1.159 \times 10^{-3}$. Tab. A.2 and Tab. A.3 show the conversions from $[M/H]$ to solar abundances and from Z to $[M/H]$, respectively. Fig. A.2 illustrates the relation from Tab. A.3. It is important to note, that the relation between $[M/H]$ and Z is not linear. Linder [533] presents a detailed calculation example of the conversion from Z as oxygen to the metallicity $[O/H]$, see Sect. (2.3) in [533].

(4) The abundance scale for a (single) element E in the epsilon-notation is:

$$\log_{10} \varepsilon_E = \log_{10} \frac{E}{H} = \log_{10} \frac{N_E}{N_H}. \quad (\text{A.10})$$

(5) The astronomical log abundance scale uses H as reference element, e.g. [530, 532]. Here, H is defined to be $\log \varepsilon_H = 12.00$, and

$$A(E) = \log \varepsilon_E = \log_{10} \left(\frac{N_E}{N_H} \right) + 12. \quad (\text{A.11})$$

(6) The term dex in astronomy refers to decadic logarithmic units, where 1 dex equals a factor of 10 ($= 10^1$) [530].

A.3. MOGROP

This section first highlights the code scheme. Second, it explains how the $T_{\text{int}}-Z_{\text{env}}-Z_{\text{P}}$ phase space from Paper II is derived from the output of the MOGROP code and serves as supplement to Sect. 2.4 in Paper II. Additionally, the calculation of the thermal evolution curves is explained.

A.3.1. Programme Overview

Input to MOGROP are:

1. Observables, such as planetary mass M_{P} and radius R_{P} , and stellar parameter
2. The outer boundary condition determining where the interior adiabat starts. This can happen through a given P_{ad} and/or T_{ad} , measured luminosities (only solar giants), fit formulae, or model atmospheres and the parameters needed within.
3. Composition and EoS
4. The core mass M_{core} and/or the heavy element content of the outer layers denoted by Z_{env} , see Sect. A.3.2.

The algorithm of MOGROP then works as follows:

1. (1: **EoS**) First, for a given mixture of H, He, and metals, the EoS tables are prepared.
2. (2: **Isoline**) Second, the pressure-temperature is pre-computed. In the case where a model atmosphere is used, the $P-T$ profile is computed or given, the outer boundary condition for the convective interior is determined, resulting in $(P_{\text{ad}}, T_{\text{ad}})$, where the $P-T$ of the interior adiabat continues. The density profile follows the pre-computed profile along the atmosphere and adiabat, yielding $P-T-\rho$.
3. (3: **Planet**) Third, the differential system is solved numerically in an iterative process, until the resulting model replicates the observational parameters within a given error range. **Outer boundary conditions** are $m(r = R_{\text{P}}) = M_{\text{P}}$ and a value for $P(R_{\text{P}})$ (depending on the outer boundary used for the convective interior). Throughout this work, it is $P(R_{\text{P}}) = 10^{-6}$ GPa using a model atmosphere.

Output is the planetary profile along the mass coordinate m : pressure $P(m)$, radius $r(m)$, temperature $T(m)$, density $\rho(m)$, if a model has been found. If not, the input has to be adapted.

A.3.2. Interior Phase Space and Evolution Curves

When modelling the interior structure of a planet, the desired outcome is the planetary profile: mass m - radius r - temperature T - pressure P - density ρ - entropy s . The profile matches the observed planetary mass M_{P} (at $m = M_{\text{P}}$) and radius R_{P} at $r(m = M_{\text{P}}) = R_{\text{P}}$.

Assuming a bulk (envelope) composition of H, He and metals, with a fixed H/He ratio and a

given envelope metal mass fraction Z_{env} , the algorithm yields at finding $M_{\text{core}} \geq 0$ to obtain the overall M_{P} . It is then for the planetary mass M_{P} and planetary metal mass fraction Z_{P}

$$M_{\text{P}} = M_{\text{atm}} + M_{\text{env}} + M_{\text{core}} \quad (\text{A.12})$$

$$\begin{aligned} Z_{\text{P}} &= M_{\text{Z}}/M_{\text{P}}, \\ &= (M_{\text{Z,atm}} + M_{\text{Z,env}} + M_{\text{core}})/M_{\text{P}} \\ &= Z_{\text{atm}} M_{\text{atm}}/M_{\text{P}} + Z_{\text{env}} M_{\text{env}}/M_{\text{P}} + M_{\text{core}}/M_{\text{P}} \\ &= Z_{\text{env}} (M_{\text{atm}} + M_{\text{env}})/M_{\text{P}} + M_{\text{core}}/M_{\text{P}}. \end{aligned} \quad (\text{A.13})$$

In the works presented in this thesis, it is $Z_{\text{atm}} = Z_{\text{env}}$. Input parameters to our model are the planetary mass, planetary radius, Z_{env} , as well as the parameter T_{int} which is a parameter of the atmosphere model, and the H/He ratio (among the EoS data for all matter). Output is the planetary profile, and M_{core} . Note, that the core and the metals of the envelope are composed of different matter (core: ice+rock mix, envelope: water).

An additional and necessary input assumption is how warm the planet is inside, roughly, a young planet possesses a hotter interior than an evolved planet. This is parameterized by the intrinsic temperature T_{int} . If a planet now has $T_{\text{int,high}} > T_{\text{int,low}}$, the density of the envelope is smaller than for $T_{\text{int,low}}$. That means that $M_{\text{Z,env}}(T_{\text{int,high}}) < M_{\text{Z,env}}(T_{\text{int,low}})$ for the same envelope metal mass fraction Z_{env} . Now, to account for the total planetary mass M_{P} , the algorithm has to increase the core mass M_{core} , so that resulting model fulfils the boundary conditions of observed planetary mass and radius.

This modelling procedure – without considering further thermal evolution calculations – is what is named static (meaning no explicit time-dependence taking into consideration).

$T_{\text{int}}-Z_{\text{env}}-Z_{\text{P}}$ phase space. From the consideration above, calculating models matching R_{P} , M_{P} for a constant envelope metal mass fraction Z_{env} but varying T_{int} leads to different core masses M_{core} and therefore to a different total metal mass fractions Z_{P} for each model. Generally, for higher T_{int} values, a higher Z_{P} , due to an increasing core mass, is obtained. This behaviour is shown in Fig. 6 in [Paper II](#). Each constant Z_{env} corresponds to one color in the colour scale on the right hand side, yielding one curve. The lighter the color is, the lower is the Z_{env} value. The darkest shade corresponds to $Z_{\text{env}} = 0.52$. Exception happens when the results using the planetary mass/radius combination for the lowest/highest density (grey shade) is shown.

With setting a higher Z_{env} as input, each curve starts at an increasing higher T_{int} value: For lower T_{int} values, no model is found. No Bayesian or MCMC method is used as the algorithm has not be designed to do so (yet).

Measurements of the atmospheric metallicity can help constrain the bulk metallicity as $Z_{\text{P}} < Z_{\text{atm/env}}$ as the atmosphere cannot be more metal rich than the interior.

Evolution models. With the age constraint of the planetary system, one can set a tighter constraint on the metal content of the planet apart from a single consideration of the $T_{\text{int}}-Z_{\text{env}}-Z_{\text{P}}$ phase space. As T_{int} is connected to the age of the planet via Eqs. (6,7) in [Paper II](#).

Applying the equations mentioned above involves two steps: First, for a fixed set of M_{P} , M_{core} , and Z_{env} , interior models are calculated for approximately 60–80 T_{int} values in the range of

100 – 1000 K. Here, the free parameter is the planetary radius R_P . As T_{int} increases, R_P becomes larger. Each model with a specific T_{int} has an associated interior adiabat. In the next step, the secular cooling equation is applied to calculate the time interval between two profiles. This yields the radius evolution of the planet, $R_P(t)$. This procedure is applied in Sects. 3.3 and 3.4 of [Paper II](#).

A.4. Interior Metallicity Relations

The total metal mass fraction of the planet, Z_P , is defined as the sum of the core mass M_{core} and the mass of the heavy elements in the envelope, $M_{Z,\text{env}}$ in relation to the total planetary mass, M_P :

$$Z_P = \frac{M_{\text{core}} + M_{Z,\text{env}}}{M_P}. \quad (\text{A.14})$$

The relations between all of the parameters above has been used to study the solution space when inferring the metal masses of planets. For example, Fortney and Nettelmann [44] study the influence of different H, He, and metal-EoS for Jupiter, as well as different metal mass fractions in the two-layer envelope model.

The interior space is such constructed, that, for a given planetary mass M_P , the planetary radius R_P is matched given the additional assumption of the envelope metallicity mass fraction Z_{env} or the core mass M_{core} ; compare Sect. 2.1.1. Setting one of them, lets the algorithm determine the other, such that M_P is matched. For instance, an input parameter is Z_{env} , the output of the algorithm is the core mass M_{core} .

Among Z_{env} or M_{core} , a crucial input parameter to the interior model is the intrinsic temperature T_{int} that determines the heat in the envelope and therefore the density of the envelope. That, in turn, influences the output of M_{core} , if the input is chosen to be Z_{env} , as the metal mass of the envelope is smaller for lower densities, matching a higher T_{int} .

A.4.1. $M_{\text{core}}-T_{\text{int}}$ relation

Plotting $M_{\text{core}}-T_{\text{int}}$ for else constant parameters is a common way to make first-order estimation of the metal content of a planet. For example, Fig. 8 in [Paper I](#) shows this relation for WASP-10b, for a constant Z_{env} but different model atmospheres. In Fig. A.3, the same relation is shown for WASP-39b for a varied Z_{env} is shown. Each equally-coloured line is calculated for a specific constant Z_{env} . For larger T_{int} values, the density is lower, the smaller is the envelope metal mass, the larger M_{core} must become to match M_P . It is for the $M_{\text{core}}-T_{\text{int}}$ -relations:

$$\frac{\partial M_{\text{core}}}{\partial Z_{\text{env}}} < 0. \quad (\text{A.15})$$

A.4.2. Z_P-T_{int} relation

In [Paper II](#), among the main results presented are the radius evolution curves and the interior space of specific model setups for TOI-1268b and WASP-10b. Additionally, an exploration of

the relationship between M_{core} , T_{int} , Z_{env} , and Z_{P} is provided.

In Fig. 6 of [Paper II](#), T_{int} is plotted on the x-axis, the envelope metallicity Z_{env} is shown as the third variable, and the total metal mass fraction Z_{P} is shown on the y-axis.

While calculating the $M_{\text{core}}-T_{\text{int}}-Z_{\text{env}}$ in [Paper II](#), some of the lines for constant Z_{env} are crossing each other, e.g. Fig. 6 for WASP-10b. From a naive view, that does not seem plausible, as linear relation is expected.

The total heavy element mass $M_{\text{Z,P}}$ is defined:

$$M_{\text{Z,P}} := M_{\text{core}} + M_{\text{Z,env}} = M_{\text{core}} + Z_{\text{env}} M_{\text{env}} = M_{\text{core}} + Z_{\text{env}} (M_{\text{P}} - M_{\text{core}}),$$

and subsequently aim at calculating the derivation which is

$$\frac{\partial M_{\text{Z,P}}}{\partial Z_{\text{env}}} = \frac{\partial M_{\text{core}}}{\partial Z_{\text{env}}} + \frac{\partial (Z_{\text{env}} (M_{\text{P}} - M_{\text{core}}))}{\partial Z_{\text{env}}}. \quad (\text{A.16})$$

The derivation of the second term is calculated using the product rule with

$$\frac{\partial (u(x)v(x))}{\partial x} = \frac{\partial u(x)}{\partial x} v(x) + u(x) \frac{\partial v(x)}{\partial x}, \text{ defined as}$$

$$\begin{aligned} u &= Z_{\text{env}}, & v &= (M_{\text{P}} - M_{\text{core}}), \\ u' &= \frac{\partial Z_{\text{env}}}{\partial Z_{\text{env}}} = 1, & v' &= \frac{\partial M_{\text{P}}}{\partial Z_{\text{env}}} - \frac{\partial M_{\text{core}}}{\partial Z_{\text{env}}} = \frac{\partial (M_{\text{P}} - M_{\text{core}})}{\partial Z_{\text{env}}}, \end{aligned} \quad (\text{A.17})$$

yielding

$$\frac{\partial \Omega}{\partial Z_{\text{env}}} = \frac{\partial M_{\text{core}}}{\partial Z_{\text{env}}} + 1 \cdot (M_{\text{P}} - M_{\text{core}}) + Z_{\text{env}} \frac{\partial (M_{\text{P}} - M_{\text{core}})}{\partial Z_{\text{env}}}. \quad (\text{A.18})$$

Evaluating the last term gives: $Z_{\text{env}}(M_{\text{P}} - M_{\text{core}}) = \underbrace{Z_{\text{env}} M_{\text{P}}}_{\text{const.}} - Z_{\text{env}} M_{\text{core}}$ and $M_{\text{core}} = M_{\text{core}}(Z_{\text{env}})$.

Finally, it follows with $Z_{\text{env}} \frac{\partial M_{\text{P}}}{\partial Z_{\text{env}}} = 0$, and Eq. (A.15):

$$\frac{\partial M_{\text{Z,P}}}{\partial Z_{\text{env}}} = \underbrace{\frac{\partial M_{\text{core}}}{\partial Z_{\text{env}}}}_{<0} + \underbrace{(M_{\text{P}} - M_{\text{core}})}_{>0} - Z_{\text{env}} \underbrace{\frac{\partial M_{\text{core}}}{\partial Z_{\text{env}}}}_{<0}. \quad (\text{A.19})$$

Investigating $\frac{\partial M_{\text{Z,P}}}{\partial Z_{\text{env}}} = 0$ and doing some algebra leads to

$$\begin{aligned} 0 &= \frac{\partial M_{\text{core}}}{\partial Z_{\text{env}}} (1 - Z_{\text{env}}) + (M_{\text{P}} - M_{\text{core}}) \\ \underbrace{\frac{\partial M_{\text{core}}}{\partial Z_{\text{env}}}}_{<0} (1 - Z_{\text{env}}) &= -(M_{\text{P}} - M_{\text{core}}) = -M_{\text{Z,env}}. \end{aligned} \quad (\text{A.20})$$

Due to the different EoS used for the core and in the envelope, it is possible for pairs of $M_{\text{Z,env}}$ and M_{core} to result in same Z_{P} values.

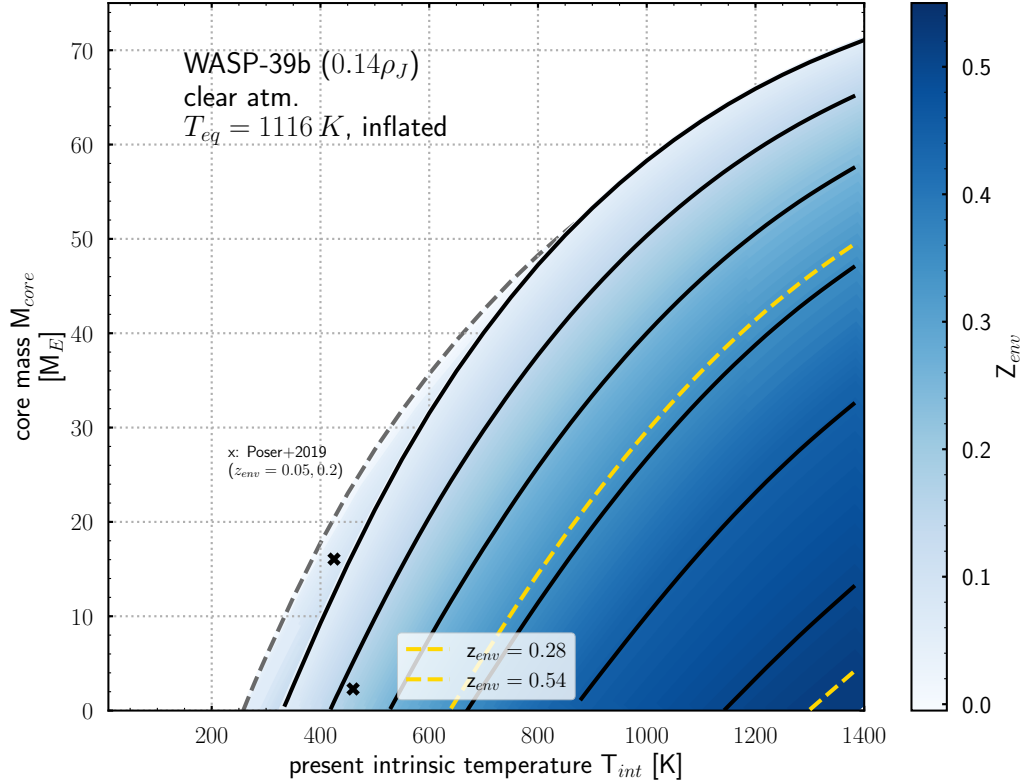


Figure A.3.: Relation between derived core mass M_{core} and intrinsic temperature T_{int} for WASP-39b. The black lines indicate the results for constant $Z_{\text{env}} = 0, 0.1, 0.2, 0.3, 0.4, 0.5$. The dashed yellow lines indicate the lower and upper range of the observed atmospheric metallicity by Wakeford *et al.* [129], translated into $Z_{\text{env}} = 0.28, 0.54$. Assuming $Z_{\text{atm}} = Z_{\text{env}}$, the solution for the interior M_{core} lies in between the yellow lines. The blue shades in the foreground are the results obtained with CD21, whereas the background shows the results for SCvH95, the outer boundary indicated by the grey dashed line. Black crosses indicate the solutions obtained in Paper I with SCvH95 and additional thermal evolution calculations.

A.4.3. Additional Calculations for WASP-39b

Here are presented calculations for WASP-39b that did not make it into Paper II. The decision was made based on the aspect that the inflated nature of WASP-39b imposed a free parameter which would not support the main message of the paper, the effect of clouds.

In Fig. A.3, the $M_{\text{core}}-T_{\text{int}}$ relation of the interior structure model is shown. For higher T_{int} , M_{core} is higher. The phase space $T_{\text{int}}-Z_{\text{P}}-Z_{\text{env}}$ with and without clouds is shown in Fig. A.4.

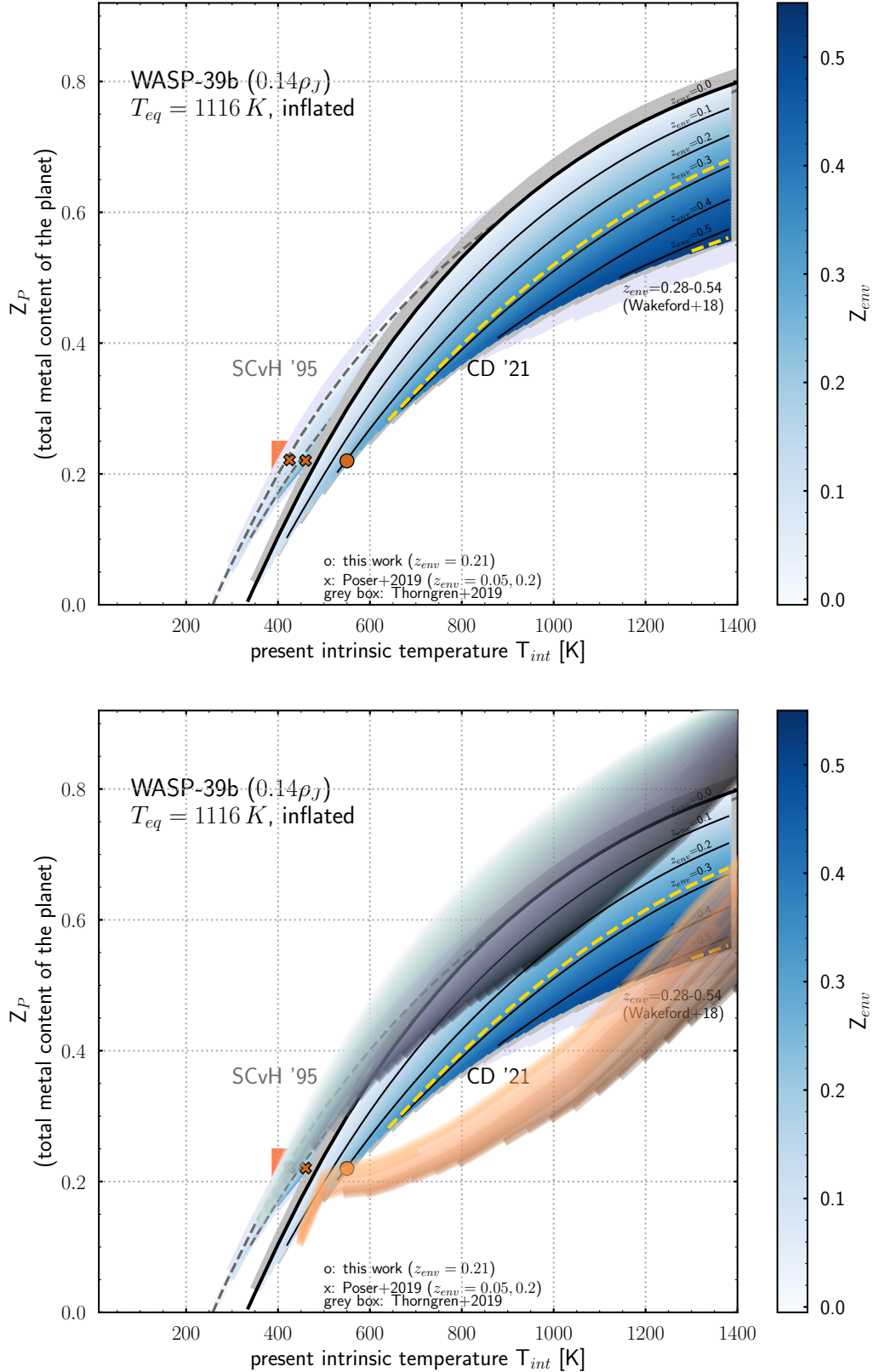


Figure A.4: Phase space ($T_{int} - Z_P - Z_{env}$) of the structure model setup for WASP-39b, highlighting the influence of uncertainties in mass and radius, EoS (upper panel) and atmosphere model (lower panel). The higher the present T_{int} , the more metals can (theoretically) be included in the envelope (with higher Z_{env} values possible), and subsequently a higher Z_P may arise. The same degree of colour shade is used in the panels (lighter shade: lower Z_{env} , darker shade: higher Z_{env}). Additionally, the grey area indicates the resulting model space when taking the observational uncertainties in M_P and R_P into account (shown for CD21 EoS and a clear atmosphere model in the left figure).

A.5. On Grey and Mean Opacities

Generally, opacities describe the absorption and scattering in a medium. Here, they depend on the atmospheric chemical composition; further, they are pressure-, temperature-, and wavelength-dependent.

Two grey opacities are needed in the thermal and visible wavelength range to calculate atmospheric P - T conditions using the *Guillot10* model [180] or the clear version of the *Heng12* model [321]. The grey opacities κ_{th} and κ_{vis} , in the main body text referred to a κ_{L} and κ_{S} , and their ratio $\gamma = \kappa_{\text{vis}}/\kappa_{\text{th}}$ determine the thermal structure.

Fig. A.5 shows the thermal structures arising from the clear, cloud-free model for a constant intrinsic temperature T_{int} value, but varied equilibrium temperature T_{eq} . In the upper panel, the γ -ratio is set constant while varying the opacity κ_{th} . The change of κ_{th} leads to a vertical shift of the P - T profile. In the lower panel, the opacity κ_{th} is constant, while γ and therefore κ_{vis} vary. Here, a higher γ is proportional to a higher κ_{vis} . For a higher grey opacity in the visible wavelength range, the upper atmosphere becomes hotter, whereas the lower atmosphere is cooled. On closer examination of the deep isothermal temperature T_{iso} , there is an overlapping for close T_{eq} values: For a higher T_{eq} value, a high γ could lead to the same deep isotherm as a lower T_{eq} value with a low γ . When aiming at using the clear model, and setting the free parameters, one should be aware of that aspect. Despite the sufficient thermal structure arising of the *Guillot10* model in this work, a better description of the atmosphere is left to future work. One idea to implement more realistic, non-grey opacities is the use of opacities, that are temperature and pressure-dependent, but weighted averages over the wavelength range of a given composition. During this research, the possibility of using Rosseland mean opacities for the clear *Guillot10* or *Heng12* models was explored, though the results were not published. The integration of these models with interior and evolution models is left for future work. In this section, the idea proposed by Nadine Nettelmann is presented, along with an introduction to mean opacities. This serves as documentation.

A.5.1. Obtaining Planck and Rosseland Mean Opacities

This section provides an overview of the derivation of Planck and Rosseland mean opacities, which are weighted averages of wavelength-dependent opacities, following the works of Freedman *et al.* [247] and Freedman *et al.* [248].

Two weighting functions are commonly used. The Rosseland mean opacity κ_{R} is defined as

$$\frac{1}{\kappa_{\text{R}}} = \frac{\int_0^{\infty} \frac{1}{\kappa_{\lambda}} \frac{dB_{\lambda}}{dT} d\lambda}{\int_0^{\infty} \frac{dB_{\lambda}}{dT} d\lambda}, \quad (\text{A.21})$$

with T as the temperature and λ as the wavelength. B_{λ} is the Planck function describing the intensity of black body radiation in thermal equilibrium at temperature T :

$$B_{\lambda} = \frac{2hc^2}{\lambda^5} \frac{1}{\exp\left\{\left(\frac{hc}{\lambda k_{\text{B}} T}\right)\right\} - 1}, \quad (\text{A.22})$$

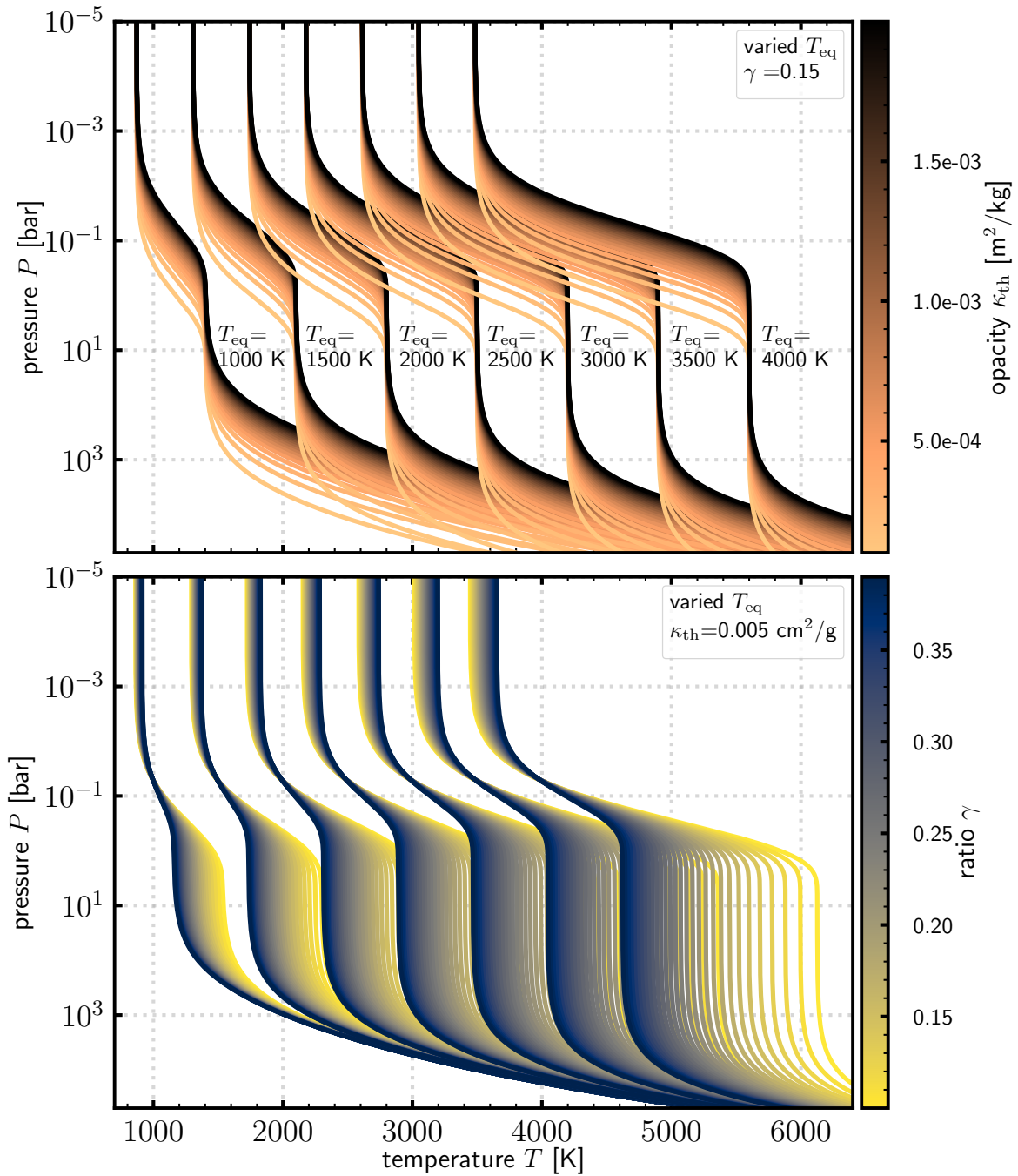


Figure A.5.: P - T for the cloud-free clear *Guillot10* model for several T_{eq} values. In the upper panel, the γ -ratio is set constant while varying the opacity κ_{th} . In the lower panel, the opacity κ_{th} is constant, while γ and therefore κ_{vis} is varied.

with h as Planck's constant, k_B as Boltzmann's constant, c is the speed of light. The unit is $[\text{J m}^{-2} \text{sr}^{-1} \text{s}^{-1} \text{Hz}^{-1}]$. Note, the description includes the radiation per frequency ν bin, so that $d\nu = -c/\lambda^2 d\lambda$. κ_λ as the wavelength-dependent opacity. For an overview on intensity and flux in an exoplanets atmosphere, see Seager [245].

The Planck mean opacity κ_P is defined as

$$\kappa_P = \frac{\int_0^\infty \kappa_\lambda B_\lambda d\lambda}{\int_0^\infty B_\lambda d\lambda}. \quad (\text{A.23})$$

For a specific composition, temperature, and pressure, the Rosseland mean opacity weights stronger the contribution of weak opacity lines. Contrary, the Planck mean weights stronger the strong opacities lines.

In Freedman *et al.* [248], Fig. 2, the Rosseland mean opacity is about two orders of magnitude lower than the Planck mean opacity at the same temperature (1000 K) and pressure (1 bar) conditions for the same wavelength range (0.1 – 200 μm). In that Fig. 2, they also show the integral of the running opacity, clearly showing that the contribution of the Planck mean is stronger at opacity maxima (and for the Rosseland mean at the opacity minima).

Missing data for absorption lines are crucial for calculating Rosseland mean gas opacity, as it is dominated by transparent spectral regions due to the harmonic averaging. Thus, each Rosseland mean is a lower limit. Conversely, missing data for weak lines in Planck mean opacity cause overestimation of strong lines, making the Planck mean an upper limit.¹

The Rosseland mean approximates best an optically thick plasma, while the Planck mean suits an optically thin plasma. Neither is accurate for the entire frequency range due to spectrum complexity.²

Thus, the Rosseland mean opacity is used when the atmospheric plasma is optically thick, and the Planck mean is used when it is optically thin. In an optically thick plasma, photon transport is approximately diffusional, involving less absorption and more scattering [534–536].

Recipe to derive the Rosseland and Planck mean opacities, following [247, 248]:

1. Molecular line lists are needed, such as EXOMOL [537] (for exoplanetary and other atmospheres), HITRAN [538] or others, see Tennyson [539] in [278] for an overview.
2. The abundances of the relevant atoms and molecules at a pressure and temperature are needed to obtain the wavelength-dependent opacity, often making use of thermodynamic equilibrium.
3. The wavelength-dependent opacities for a specific composition, temperature T , and pressure P are calculated. For example, in Freedman *et al.* [248], the opacities are tabulated at 1060 P – T points on a grid for 0.268 – 227 μm , 75 – 4000 K, 10^{-6} – 300 bar, e.g. Fig. 1 in Freedman *et al.* [248].
4. The Planck and Rosseland mean opacities are calculated for each P – T –composition (in terms of $[\text{M}/\text{H}]$), e.g. Fig. 2 in Freedman *et al.* [248]. Effects of the weighting tempera-

¹<https://www2.mpia-hd.mpg.de/~semenov/Opacities/op/node7.html>, accessed on October 20, 2023

²https://www.eeict.cz/eeict_download/archiv/sborniky/EEICT_2012_sbornik/03doktorskeprojekty/05teoreticka_elektrotechnikafyzikaamatematika/04-xbogato0.pdf, accessed on October 20, 2023

ture, e.g. the local temperature in the weighting function for κ_{th} or the effective stellar temperature in the weighting function for κ_{vis} are discussed in Freedman *et al.* [248], Sect. 4.

5. Fits to the tabulated Planck mean and Rosseland mean opacities can be made, e.g. Freedman *et al.* [248], Valencia *et al.* [256].

Weighted Mean Opacities by V13 and F14

Freedman *et al.* [247] (F08) and Freedman *et al.* [248] (F14) published Rosseland and Planck mean opacities over a wide temperature, pressure and metallicity space.

Valencia *et al.* [256] (V13) provide an analytical fit to the Rosseland mean opacity tables published by F08 with $\kappa_{\text{R}} = \kappa_{\text{R}}(P, T, [\text{M}/\text{H}])$. Following their previous work, F14 themselves provide fits to their updated opacity tables.

Fig. A.6 shows the fits to the opacity tables $\kappa_{\text{R}}(P, T)$ along isobars. In Fig. A.6, upper panel, the F14 fits are shown for different metallicities $[\text{M}/\text{H}] = -0.3, 0, +0.3$. The deviation to the V13 fits are shown in Fig. A.6, middle panel. Fig. A.6, lower panel, shows planetary profiles from this thesis in the $\kappa_{\text{R}}-T-P$ phase space.

A.5.2. Semi-grey Model Extension with Rosseland Mean Opacities

The calibration of γ and the grey opacities is important for the thermal structure. A starting point on how to set the opacities or γ is needed.

In Paper I, the planetary profiles of WASP-10b and WASP-39b were compared in the $(\kappa_{\text{R}}-T-P)$ -space using the fits from V13. That validated our choice of the constant, i.e. (T, P) -independent, mean κ_{th} .

Efforts on how to set the grey opacities have been made: Guillot10 proposes a value of $\kappa_{\text{th}} = 0.01 \text{ cm}^2/\text{g}$ and $\kappa_{\text{vis}} = 6 \times 0.001 \sqrt{T_{\text{irr}}/2000\text{K}} \text{ cm}^2/\text{g}$ as a result of adjusting the opacities to obtain a match with more detailed models. Jin *et al.* [257] suggest a $\gamma(T_{\text{eq}})$ -relation. In Paper II, a $\gamma(T_{\text{eq}})$ -relation is presented, following the approach of Guillot10 and Jin *et al.* [257], namely adjusting γ to match the deep isotherms of more detailed atmospheric models. Other works have been published, using the semi-grey Guillot10 model. MacKenzie *et al.* [534] use Guillot10 for their coupled interior-atmosphere calculations of sub-Neptunes. They obtain κ_{vis} and κ_{th} from the Rosseland mean opacities from F14. Using the provided values either of weighting with the Planck function B_{λ} using the local temperature or the stellar effective temperature for κ_{th} and κ_{vis} , respectively. However, the resulting opacities are constant throughout the atmosphere, and thus pressures and temperature independent.

In Sect. A.5.2, the extension of the grey atmosphere model with Rosseland mean opacities is discussed. Here, the Rosseland mean opacity $\kappa_{\text{R}}(P, T)$ is used for a constant $\gamma = \kappa_{\text{vis}}/\kappa_{\text{th}}(P, T)$.

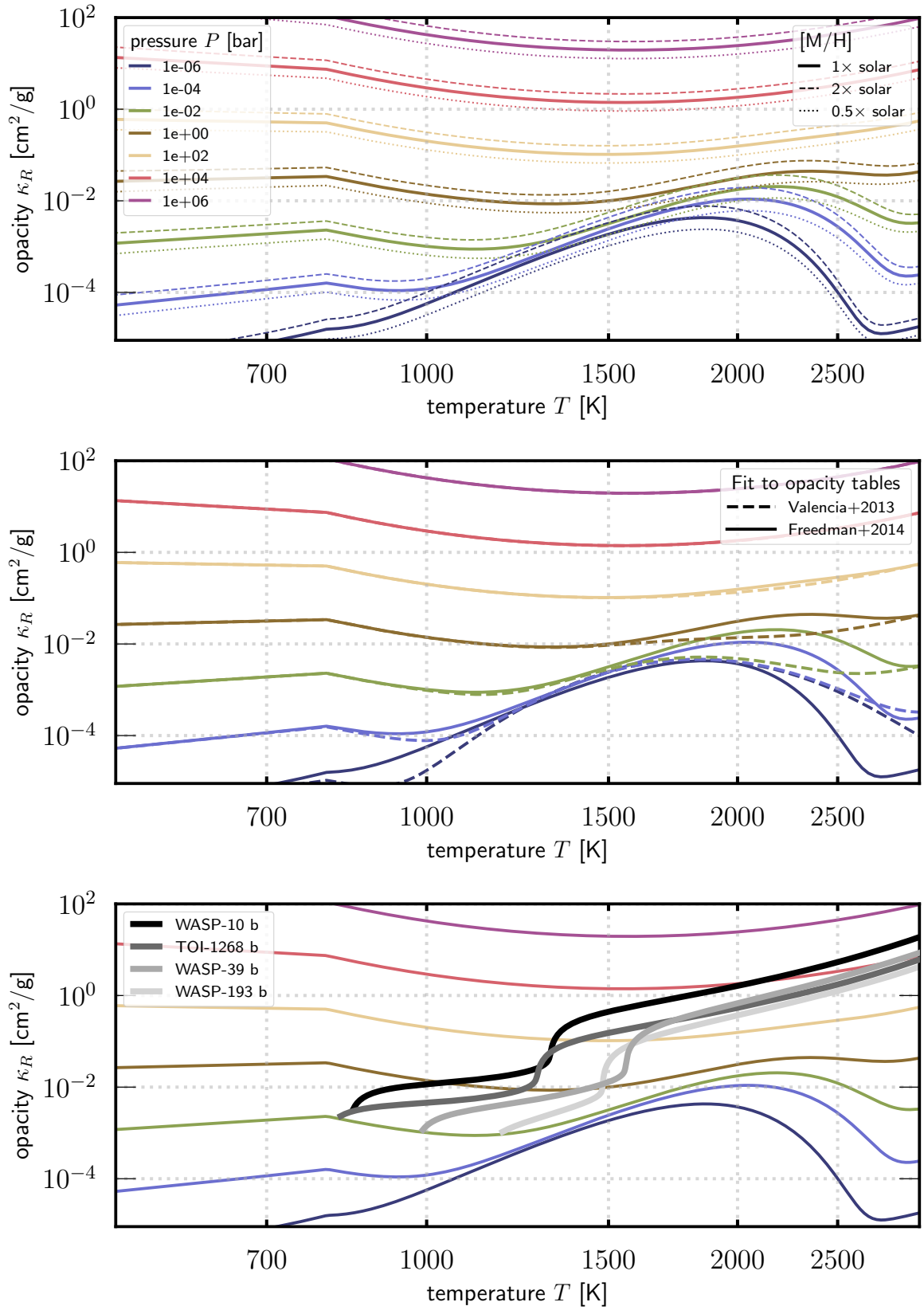


Figure A.6.: Upper panel: κ_R from the fit of F14 for metallicities $[M/H] = -0.3, 0, 0.3$ corresponding to $\sim 0.5, 1, 2 \times$ solar metallicity (dotted, solid, dashed). Middle panel: κ_R from the fit of F14 (solid) compared to the fit from V13 (dashed) along isobars. Lower panel: planetary profiles along the opacity phase space with κ_R from the fit of F14.

Implementation

First, one calculates the $T(\tau)$ -relation from Eq. (49) in *Guillot10*, e.g. $\tau = [10^{-8}, 10^{-4}]$:

$$T^4 = \frac{3T_{\text{int}}^4}{4} (2 + 3\tau) + \frac{3T_{\text{eq}}^4}{4} \left\{ \frac{2}{3} + \frac{2}{3\gamma} \left[1 + \left(\frac{\gamma\tau}{2} e^{-\gamma\tau} \right) \right] + \frac{2\gamma}{3} \left(1 - \frac{\tau^2}{2} \right) E_2(\gamma\tau) \right\}. \quad (\text{A.24})$$

Here, the input parameter are T_{int} , T_{eq} , γ . In a second step, the pressure $P(\tau, \kappa_{\text{R}}(P, T))$ is calculated

$$P = \frac{\tau g}{\kappa_{\text{R}}(P, T)}, \quad (\text{A.25})$$

assuming constant gravity g as an additional input parameter.

The numerical Newton-Raphson scheme is used to find P for which applies $f(P) = 0$ for $f(P) = P - \tau g / \kappa_{\text{R}}(P, T)$. To calculate κ_{R} , the fits to opacity tables by V13 or F14 were implemented, or the opacity tables can be used directly via interpolation.

Effect of Metallicity and Weighted Mean Opacities on the P - T Profiles

The thermal structures arising from the approach above, are now compared to the original thermal structures arising from the *Guillot10* model.

In Fig. A.7, both lines show P - T profiles of the atmosphere for two inflated hot Jupiters, WASP-193b and WASP-39b. The γ -value, that determines the characteristic deep isotherm T_{iso} , has been obtained by the approach described in Poser and Redmer [395]. In the left column, the resulting P - T profiles for constant κ_{th} (grey dashed) or (P, T) -dependent Rosseland mean opacity κ_{R} (green/blue solid) for constant γ are shown. For WASP-39b, κ_{R} by F14 is shown in blue solid, whereas the resulting profile with κ_{R} by V13 is shown in light blue dash-dotted. The difference between both fits is small. The right column illustrates the effect of using different metallicities $[M/H] = 0, -1, +1$ for κ_{R} , while keeping γ constant. With higher metallicity $[M/H] = +1$, the profile shifts to lower pressures, while the deep isothermal temperature remains constant.

Fig. A.6, upper panel, shows that κ_{R} moves to smaller values for higher metallicities for same P and T . However, with higher metallicity, one expects the grey opacity in the visible to change as well, so that γ would ultimately change to higher values for higher metallicities. Consequently, the deep isotherm would change to higher temperatures. This behaviour is expected and has been discussed in the literature, such as in Valencia *et al.* [256].

For different metallicities, different gamma values arise. In our approach, γ is kept constant, and the visible opacity is adjusted, so that: $\kappa_{\text{vis}} = \gamma \kappa_{\text{R}}(P, T)$, and the deep isotherm remains constant as a natural consequence.

Note that using κ_{R} in the clear option of the *Heng12* model is possible as it equals the *Guillot10* model. However, for the cloudy case, using the pressure- and temperature dependent Rosseland mean opacities is not possible because the additional thermal opacity due to clouds/hazes

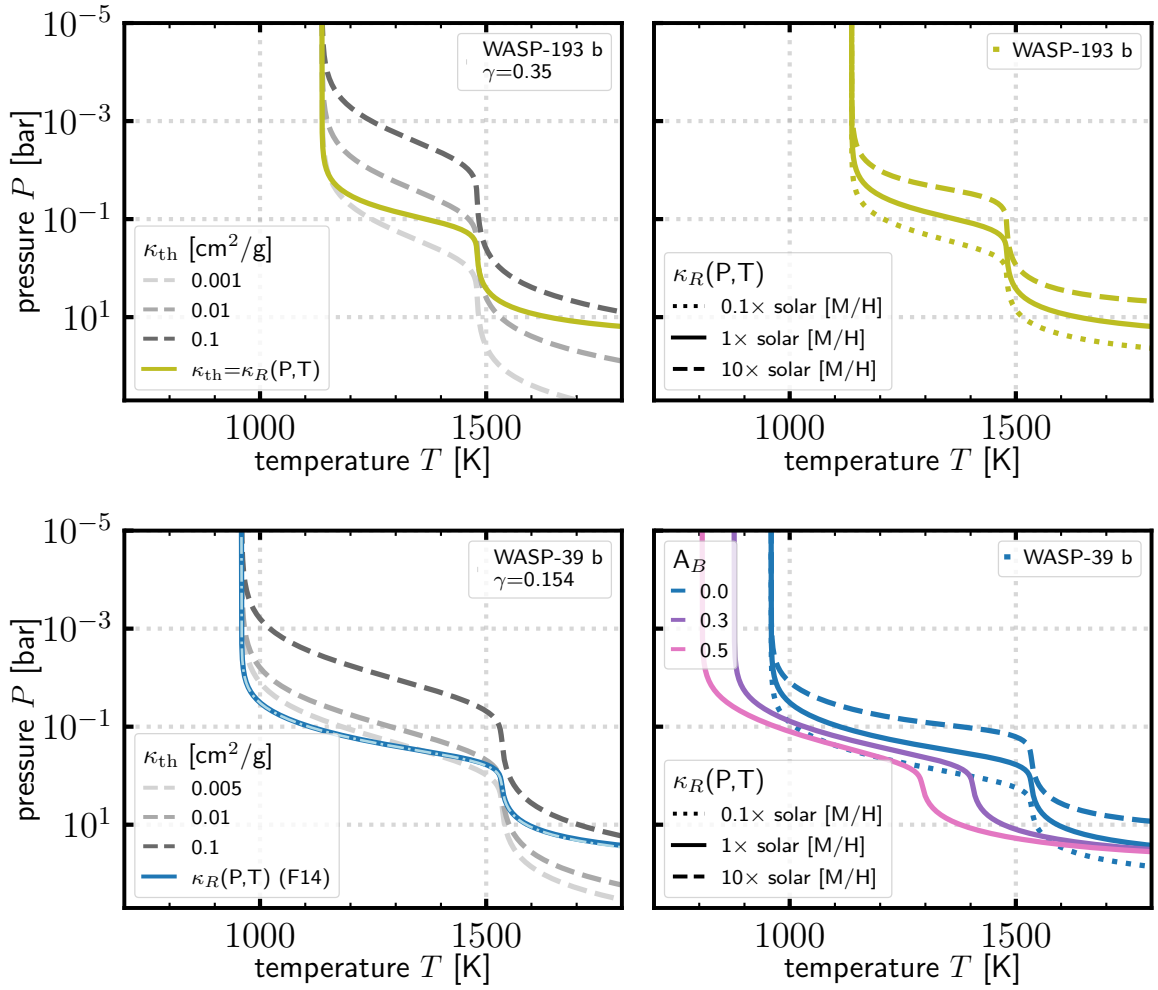


Figure A.7.: Obtained clear atmospheric P-T profiles for WASP-193 b (constant $\gamma = 0.35$) and WASP-39 b (constant $\gamma = 0.154$) with the Guillot2010 model. Left column: comparison of constant κ_{th} versus $\kappa_{\text{th}} = \kappa_{\text{R}}(P, T)$. Right column: comparison between different metallicities $[M/H] = -1, 0, 1$ for constant $\gamma = 0.35$. For the Rosseland mean opacity κ_{R} , the analytical fit of Freedman *et al.* [248] has been used.

does not depend on P or T . Therefore, in the publications with a focus on the effect of clouds, $\kappa_{\text{R}}(P, T)$ was not used.

A.6. Condensate Clouds

The study of condensate clouds requires knowledge of the thermal structure (P - T) and the abundance of condensable species [285]. Equilibrium cloud formation occurs from vapour pressure saturation facilitated by vertical mixing in an atmospheric column [136]. In 1969, Lewis [389] developed this framework for Jupiter. Thermal stability curves, also known as condensation curves, are used to understand clouds in atmospheres, predicting lower cloud bases and potential constituents. If the temperature in a cloud-free P - T profile is below the condensation temperature at a given pressure, the atmosphere is considered cloudy.

The cloud formation process in gaseous atmospheres is highly complex. An overview is provided in the following paragraph, based on Helling *et al.* [189].

Clouds in gaseous atmospheres require the formation of seed particles, which provide surfaces for condensation. In the solar giants, photochemistry might generate these seed particles. Generally, subsequent chemical reactions result in seed particles, starting from simple molecules like MgO and SiO to form more complex molecules like Mg₂SiO₄. It is important to note that large molecules like Mg₂SiO₄ do not exist in the gas phase. In microphysical cloud models, the nucleation rate determines the number of cloud particles, while their size is governed by surface growth and evaporation reactions, which depend on the composition of the gas phase. Typical cloud particle sizes range from 0.01 – 10 μm.

Once formed, cloud particles are influenced by gravity and gas friction. The balance between these forces dictates the particles' coupling to the gas and their falling through the atmosphere, a process known as gravitational settling. This settling defines a cloud's vertical extent. As the particles descend, they grow and their composition evolves due to changing, i.e. increasing, density and temperature. When nucleation and growth are inefficient, gravitational settling drives global cloud formation, with element loss counterbalanced by vertical mixing processes.

A.6.1. Thermal Stability Curves

The base pressure levels of clouds can be predicted using the Clausius-Clapeyron equation [540] or by minimising the Gibbs free energy. This results in thermal stability curves [541–543].

The Clausius-Clapeyron equation can be used to assess first-order phase transitions, as used in Sanchez-Lavega *et al.* [540] for calculating saturation pressure curves:

$$\frac{dP}{dT} = \frac{L}{T\Delta V}, \quad (\text{A.26})$$

where L is the latent heat released of the phase transition (vapour to liquid or vapour to ice phase), P , T and V the pressure, temperature and volume, respectively.

In irradiated Jupiter atmospheres, temperatures are so high that thermochemical equilibrium calculations predict exotic clouds such as KCl, Mg₂SiO₄, and Fe, see Fig. A.8.

Thermal stability curves, or condensation curves, are therefore used in several works to first consider cloud content, e.g. [136].

Among others, Morley *et al.* [543], Visscher *et al.* [541], and Visscher *et al.* [542] present condensation temperatures as a function of pressure and metallicity. They derive expressions for

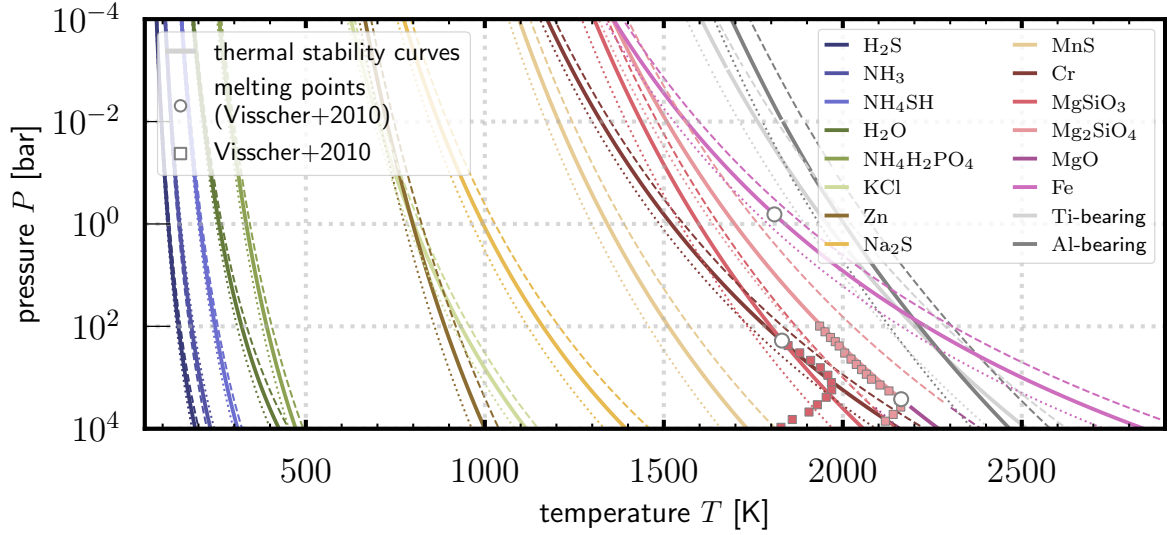


Figure A.8.: Thermal stability curves for the species and corresponding references listed in Table A.4 for solar, super-solar and sub-solar metallicities: $[M/H]=0, 0.3, -0.3$ (solid, dashed, dotted). The melting points for enstatite (MgSiO_3) and forsterite (Mg_2SiO_4) from Visscher *et al.* [542] are shown as dots. Derivations to Visscher *et al.* [542] from the formulas $P(T)$ given in the literature are marked as squares, such as for MgSiO_3 and Mg_2SiO_4 . Their condensation temperatures are depressed for high pressures which is not captured by the formulas.

saturation vapour pressures for possible cloud forming species, such as Cr, MnS, Na_2S , ZnS, KCl, producing higher temperatures for greater pressures and/or higher metallicities. Higher metallicity drives the condensation point, i.e. the intersection between the clear P - T structure and the condensation curve, deeper into the planetary atmosphere where the cloud density follows enlarged [136]. Wakeford *et al.* [136] add high temperature condensates to the list, such as Al-bearing condensates – grossite (CaAl_4O_7), hibonite ($\text{CaAl}_{12}\text{O}_{19}$), corundum (Al_2O_3) – and Ti-bearing condensates such as $\text{Ca}_3\text{Ti}_2\text{O}_7$, $\text{Ca}_4\text{Ti}_3\text{O}_{10}$, CaTiO_3 . Table A.4 shows the condensable species and where to find thermal stability curves in the literature. The species from Table A.4 are plotted in Fig. A.8 for different metallicities.

However, caution is needed when assuming cloud formation based solely on the condensation curves presented in Fig. A.8, as these do not fully represent the complexities of cloud-forming processes. Phase diagrams, which consider evaporation and melting, along with chemical abundance calculations, are also important to provide a more comprehensive understanding.

Further, the condensation sequence varies with changes in pressure [544]. For example, the initial Al-bearing condensate is CaAl_4O_7 at high pressures, $\text{CaAl}_{12}\text{O}_{19}$ at intermediate pressures, and Al_2O_3 at low pressures in a solar-composition gas Wakeford *et al.* [136]. Morley *et al.* [96] argue that Mg_2SiO_4 condenses at deeper pressures as MgSiO_3 , so that MgSiO_3 forms above the Mg_2SiO_4 cloud.

Condensable Cloud Species		
<i>Solar System Giant Atmospheres:</i>		
H ₂ S	hydrogen sulfide	Visscher <i>et al.</i> [541]
NH ₃	ammonia	Lodders and Fegley [544]
NH ₄ SH	ammonium hydrosulfide	Visscher <i>et al.</i> [541]
H ₂ O	water	Lodders and Fegley [544]
NH ₄ H ₂ PO ₄	ammonium dihydrogen phosphate	Visscher <i>et al.</i> [541]
<i>Warmer Atmospheres:</i>		
KCl	potassium chloride	Morley <i>et al.</i> [543]
Zn	zinc	Visscher <i>et al.</i> [541]
Na ₂ S	sodium sulfide	Visscher <i>et al.</i> [541]
MnS	manganese sulfide	Visscher <i>et al.</i> [541]
Cr	chromium	Morley <i>et al.</i> [543]
MgSiO ₃	enstatite	Visscher <i>et al.</i> [542]
Mg ₂ SiO ₄	forsterite	Visscher <i>et al.</i> [542]
MgO	magnesium peroxide	Visscher <i>et al.</i> [542]
Fe	iron	Visscher <i>et al.</i> [542]
SiO ₂	quartz	Grant <i>et al.</i> [78]
<i>Al-bearing species:</i>		
CaAl ₄ O ₇	grossite	Wakeford <i>et al.</i> [136]
CaAl ₁₂ O ₁₉	hibonite	Wakeford <i>et al.</i> [136]
Al ₂ O ₃	corundum	Wakeford <i>et al.</i> [136]
<i>Ti-bearing species:</i>		
Ca ₃ Ti ₂ O ₇	calcium titanate	Wakeford <i>et al.</i> [136]
Ca ₄ Ti ₃ O ₁₀	calcium titanate	Wakeford <i>et al.</i> [136]
CaTiO ₃	perovskite	Wakeford <i>et al.</i> [136]

Table A.4.: Selection of cloud condensates that are expected from thermochemical equilibrium calculations in exoplanetary atmospheres, depending on temperature and abundances, sorted from low to high temperatures. Fig. A.8 shows the corresponding thermal stability curves from the literature given in this table.

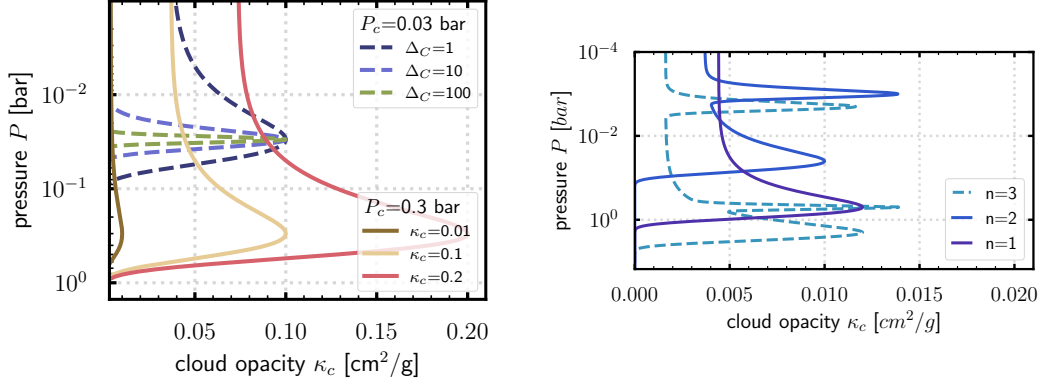


Figure A.9.: Left panel: κ_c for one cloud layer at cloud deck location $P_c = 0.03$ bar and varied cloud deck thickness $\Delta_c = 1, 10, 100$ (dashed), and for $P_c = 0.03, 0.3$ bar, and varied cloud deck opacity normalisations $\kappa_{c,0} = 0.01, 0.1, 0.2$ cm^2/g (solid). Right panel: κ_c for several cloud layers $n = 1, 2, 3$.

A.6.2. Selected Other Works on Cloud Opacities

In Dobbs-Dixon and Agol [392] (Sect. 2.2.3), a parameterised purely absorbing cloud opacity is introduced, Eq. (4.16), ignoring scattering by cloud particles:

$$\kappa_c(\lambda) = \kappa_{\text{grey}} + \kappa_{\text{RS}} \left(\frac{\lambda}{0.9 \mu\text{m}} \right)^{-1}. \quad (\text{A.27})$$

The grey opacity is set to $\kappa_{\text{grey}} = 0.035$ cm^2/g , and the second component with $\kappa_{\text{RS}} = 0.6$ cm^2/g that scales with λ^{-4} as expected from Rayleigh scattering. Fig. 4.13 in Lee [214] shows the cloud, gas and total opacities calculated from Showman *et al.* [267], as well as the parameterised cloud opacity from Dobbs-Dixon and Agol [392]. For higher pressures $P > 1$ bar, the parameterised cloud opacity is smaller than the non-parameterised opacity, reaching values $\kappa_c = 10^{-1} - 10^1$ cm^2/g . Values in this range are used in Paper II.

A popular cloud model is that of Ackerman and Marley (2001) [315]. The model balances upward mixing and sedimentation of cloud particles via the key parameter f_{sed} as the sedimentation efficiency. Morley *et al.* [96] uses the Ackerman and Marley model. In Fig. 3 of [96], cloud models are always warmer than cloud-free models with the same effective temperatures, which Paper II reproduces.

A.6.3. Several Cloud Layers

The gas and ice giants of the Solar System, Jupiter, Saturn, Uranus, and Neptune, inhibit several cloud decks [77]. The *Heng12* model could be extended to account for the cloud layers:

$$\kappa_c(P) = \sum_{n=0}^N \kappa_{c0,n} \cdot \exp \left[-\Delta_{c,n} \left(1 - \frac{P}{P_{c,n}} \right)^2 \right]. \quad (\text{A.28})$$

The cloud decks can then be added via the additional contribution to the longwave opacity κ_L : $\kappa_L(P) = \kappa_{L,0}(P) + \kappa_c(P)$, see Fig. A.9, right panel.

A.7. Electromagnetic Processes in Atmospheres

Due to strong irradiation, the hot Jupiter's atmosphere is thermally ionised, coupling the magnetic field with this irradiation. The induced current density \mathbf{j}_{ind} is derived from Ohm's law:

$$\mathbf{j}_{\text{ind}} = \sigma_e(\mathbf{U} \times \mathbf{B}_{\text{int}} + \mathbf{E}), \quad (\text{A.29})$$

where \mathbf{B}_{int} is the internal planetary magnetic field, often approximated by a dipole field, \mathbf{U} is the velocity field of the wind, \mathbf{E} the electrical field. The electric current is given as $\mu_0 \mathbf{j} = \nabla \times \mathbf{B}$ with μ_0 as the magnetic diffusivity.

The Ohmic heating power \mathcal{P} is given by

$$\mathcal{P} = \int_V \frac{\mathbf{j}_{\text{ind}}^2}{\sigma_e} dV, \quad (\text{A.30})$$

with dV as the volume element.

The evolution of the magnetic field in the wind zone is a complex task and often approximated. It is governed by the induction equation

$$\partial_t \mathbf{B} = \nabla \times (\mathbf{U} \times \mathbf{B}) - \nabla \times (\eta \nabla \times \mathbf{B}), \quad (\text{A.31})$$

with $\eta = 1/(\mu_0 \sigma_e)$ as the magnetic diffusivity where μ_0 is the vacuum permeability, see Eq. (3) in [Paper IV](#). The induction equation can be derived from Maxwell's equations and Ohm's law:

$$\nabla \times \mathbf{E} = -\frac{\partial \mathbf{B}}{\partial t}, \quad \nabla \times \mathbf{B} = \mu_0 \mathbf{J}, \quad (\text{A.32})$$

$$\sigma_e(\mathbf{E} + \mathbf{v} \times \mathbf{B}) = \mathbf{J}. \quad (\text{A.33})$$

In Eq. (A.31), the evolution of \mathbf{B} is determined by the competition of induction (1st term) and diffusion (2nd term). The latter dissipates magnetic field energy as heat. Magnetic diffusion describes the movement of magnetic fields in conducting fluids like plasma, governed by the magnetic induction equation, Eq. (A.31), primarily due to induction and diffusion through the material.

Eq. (A.31) becomes with further assumptions

$$\partial_t B_\Phi = -\mathbf{B}_{\text{int}} \cdot (\nabla \mathbf{U}) + \eta \nabla^2 B_\Phi, \quad (\text{A.34})$$

where B_Φ is the locally induced field, see Eq. (5) in [Paper IV](#). The magnetic Reynolds number Rm estimates the importance of the induction contribution relative to diffusion contribution of the magnetic field:

$$\text{Rm} = \frac{\nabla \times (\mathbf{U} \times \mathbf{B})}{\nabla \times (\eta \nabla \times \mathbf{B})} \approx \mu_0 \sigma_e U \min(d_\eta, d_U, d_B), \quad (\text{A.35})$$

with $\eta = 1/(\mu_0 \sigma_e)$ where μ_0 is the vacuum permeability, d is the characteristic length scale for the electrical conductivity scale length, the flow, or the magnetic field, and U a typical flow velocity (Eq. (4) in [Paper IV](#)).

The induction process depends on Rm . Without further derivation (see [Paper IV](#) for the details), it can be divided into two regimes, resulting in a different treatment of the induced currents and Ohmic power:

- Linear Regime, $Rm \leq 1$:
 - Magnetic diffusion limits the growth of the induced field due to the low electrical conductivity. Consequently, the induced field remains weak compared to the background field. Furthermore, no Lorentz forces act on the flow, see Fig. 1 a,b in [Paper IV](#).
 - A quasi-stationary state is established: $\partial_t B \approx 0$, so that Eq. (A.34) balances magnetic dissipation the induction. The magnetic field induced in the outer part of the atmosphere is smaller than the internal magnetic field ($B_\phi = Rm B_{\text{int}}$, see Eq. (11) in [Paper IV](#)).
 - The induced electrical currents are $\mathbf{j}_{\text{ind}} = \sigma_e (\mathbf{U} \times \mathbf{B}_{\text{int}})$ (Eq. (12) in [Paper IV](#)), resulting in $j_{\text{lin}} = \sigma_e U_\Phi B_{\text{int}}$ (Eq. (27) in [Paper IV](#)).
 - The Ohmic power is: $\mathcal{P}_{\text{lin}} = \int_V \sigma_e U_\Phi^2 B_{\text{int}}^2 dV$ (Eq. (27) in [Paper IV](#)), scaling with σ_e and B_{int}^2 .
- Non-linear regime, $Rm > 1$:
 - If Induction is rapid, the induced magnetic field overpowers quickly the internal magnetic field, causing strong Lorentz forces (Fig. 1 c-e in [Paper IV](#)).
 - Neglecting diffusion, Eq. (A.34) becomes $\partial_t B_\Phi = (U/d_U) B_{\text{int}}$.
 - The induced electrical currents are $\mathbf{j}_{\text{non-lin}} = \mu_0^{-1} (\nabla \times \mathbf{B})$, and with further assumptions it is $j_{\text{non-lin}} = B_\phi / (\mu_0 d_U)$ with d_U as the radial wind scale height. The induced field is independent of σ_e .
 - The Ohmic power is: $\mathcal{P}_{\text{non-lin}} = 1/\mu_0^2 \int_V B_\phi^2 / (\sigma_e d_U^2) dV$ (Eq. (28) in [Paper IV](#)). The induced field is independent of σ_e . With higher σ_e , the Ohmic dissipation efficiency decreases.

A.8. Software

MOGROP [330] written in C/C++ [545], Bash [546], SLURM [456], CYTHON [454, 455], PYTHON [547] with libraries Matplotlib [548], NumPy [549], AstroPy [550] and SciPy [551].

Schematics with INKSCAPE [552]. Colour schemes from colors and colorbrewer [553, 554].

Retrieving data from plots manually: Webplotdigitizer [555].

A.9. Fundamental Constants and Planetary Data

Description	Symbol	Definition
Earth mass	M_E	$5.9722 \cdot 10^{24}$ kg
Jupiter mass	M_J	$1,898.13 \cdot 10^{24}$ kg
Earth radius (equatorial)	R_E	6356.752 km
Jupiter radius (equatorial)	R_J	71,492 km
Jupiter density	ρ_J	$1,326$ kg m ⁻³
astronomical unit	au	149,597,870.7 km
Stefan-Boltzmann constant	σ_B	$5.67037 \cdot 10^{-8}$ W m ⁻² K ⁻⁴
Newtonian gravitational constant	G	$6.67430 \cdot 10^{-11}$ m ³ kg ⁻¹ s ⁻²
Planck constant	h	$6.62607015 \cdot 10^{-34}$ J s ⁻¹

Table A.5.: Fundamental constants and planetary data from NIST^a and NASA Planetary Fact Sheet^b, accessed on February 2, 2024.

^a<https://physics.nist.gov/cuu/Constants/>

^b<https://nssdc.gsfc.nasa.gov/planetary/factsheet/index.html>

Bibliography

- [1] W. J. Borucki, D. Koch, G. Basri, N. Batalha, T. Brown, D. Caldwell, J. Caldwell, J. Christensen-Dalsgaard, W. D. Cochran, E. Devore, E. W. Dunham, A. K. Dupree, T. N. Gautier, J. C. Geary, R. Gilliland, A. Gould, S. B. Howell, J. M. Jenkins, Y. Kondo, D. W. Latham, G. W. Marcy, S. Meibom, H. Kjeldsen, J. J. Lissauer, D. G. Monet, D. Morrison, D. Sasselov, J. Tarter, A. Boss, D. Brownlee, T. Owen, D. Buzasi, D. Charbonneau, L. Doyle, J. Fortney, E. B. Ford, M. J. Holman, S. Seager, J. H. Steffen, W. F. Welsh, J. Rowe, H. Anderson, L. Buchhave, D. Ciardi, L. Walkowicz, W. Sherry, E. Horch, H. Isaacson, M. E. Everett, D. Fischer, G. Torres, J. A. Johnson, M. Endl, P. MacQueen, S. T. Bryson, J. Dotson, M. Haas, J. Kolodziejczak, J. Van Cleve, H. Chandrasekaran, J. D. Twicken, E. V. Quintana, B. D. Clarke, C. Allen, J. Li, H. Wu, P. Tenenbaum, E. Verner, F. Bruhweiler, J. Barnes, and A. Prsa, *Science* **327**, 977 (2010).
- [2] W. J. Borucki, *Reports Prog. Phys.* **79**, 036901 (2016).
- [3] M. Auvergne, P. Bodin, L. Boissard, J. Buey, S. Chaintreuil, G. Epstein, and M. Joutet, *Astron. Astrophys.* **506**, 411 (2009).
- [4] J. P. Gardner, J. C. Mather, M. Clampin, R. Doyon, M. A. Greenhouse, H. B. Hammel, J. B. Hutchings, P. Jakobsen, S. J. Lilly, K. S. Long, J. I. Lunine, M. J. McCaughrean, M. Mountain, J. Nella, G. H. Rieke, M. J. Rieke, H. W. Rix, E. P. Smith, G. Sonneborn, M. Stiavelli, H. S. Stockman, R. A. Windhorst, and G. S. Wright, *Space Sci. Rev.* **123**, 485 (2006).
- [5] H. Rauer, C. Catala, C. Aerts, T. Appourchaux, W. Benz, A. Brandeker, J. Christensen-Dalsgaard, M. Deleuil, L. Gizon, M. J. Goupil, M. Güdel, E. Janot-Pacheco, M. Mas-Hesse, I. Pagano, G. Piotto, D. Pollacco, Santos, A. Smith, J. C. Suárez, R. Szabó, S. Udry, V. Adibekyan, Y. Alibert, J. M. Almenara, P. Amaro-Seoane, M. A. Eiff, M. Asplund, E. Antonello, S. Barnes, F. Baudin, K. Belkacem, M. Bergemann, G. Bihain, A. C. Birch, X. Bonfils, I. Boisse, A. S. Bonomo, F. Borsa, I. M. Brandão, E. Brocato, S. Brun, M. Burleigh, R. Burston, J. Cabrera, S. Cassisi, W. Chaplin, S. Charpinet, C. Chiappini, R. P. Church, S. Csizmadia, M. Cunha, M. Damasso, M. B. Davies, H. J. Deeg, R. F. Díaz, S. Dreizler, C. Dreyer, P. Eggenberger, D. Ehrenreich, P. Eigmüller, A. Erikson, R. Farmer, S. Feltzing, F. de Oliveira Fialho, P. Figueira, T. Forveille, M. Fridlund, R. A. García, P. Giommi, G. Giuffrida, M. Godolt, J. G. da Silva, T. Granzer, J. L. Grenfell, A. Grottsch-Noels, E. Günther, C. A. Haswell, A. P. Hatzes, G. Hébrard, S. Hekker, R. Helled, K. Heng, J. M. Jenkins, A. Johansen, M. L. Khodachenko, K. G. Kislyakova, W. Kley, U. Kolb, N. Krivova, F. Kupka, H. Lammer, A. F. Lanza, Y. Lebreton, D. Magrin, P. Marcos-Arenal, P. M. Marrese, J. P. Marques, J. Martins, S. Mathis, S. Mathur, S. Messina, A. Miglio, J. Montalbán, M. Montalto, M. J. P. F. G. Monteiro, H. Moradi, E. Moravveji, C. Mordasini, T. Morel, A. Mortier, V. Nascimbeni, R. P. Nelson, M. B. Nielsen, L. Noack, A. J. Norton, A. Ofir, M. Oshagh, R. M. Ouaz-

- zani, P. Pápics, V. C. Parro, P. Petit, B. Plez, E. Poretti, A. Quirrenbach, R. Ragazzoni, G. Raimondo, M. Rainer, D. R. Reese, R. Redmer, S. Reffert, B. Rojas-Ayala, I. W. Roxburgh, S. Salmon, A. Santerne, J. Schneider, J. Schou, S. Schuh, H. Schunker, A. Silva-Valio, R. Silvotti, I. Skillen, I. Snellen, F. Sohl, S. G. Sousa, A. Sozzetti, D. Stello, K. G. Strassmeier, M. Švanda, G. M. Szabó, A. Tkachenko, D. Valencia, V. Van Grootel, S. D. Vauclair, P. Ventura, F. W. Wagner, N. A. Walton, J. Weingrill, S. C. Werner, P. J. Wheatley, and K. Zwintz, *Exp. Astron.* **38**, 249 (2014).
- [6] H. Rauer, C. Aerts, and J. Cabrera, *Astron. Nachrichten* **337**, 961 (2016).
- [7] G. Tinetti, P. Drossart, P. Eccleston, P. Hartogh, A. Heske, J. Leconte, G. Micela, M. Ollivier, G. Pilbratt, L. Puig, D. Turrini, B. Vandebussche, P. Wolkenberg, E. Pascale, J.-P. Beaulieu, M. Güdel, M. Min, M. Rataj, T. Ray, I. Ribas, J. Barstow, N. Bowles, A. Coustenis, V. Coudé du Foresto, L. Decin, T. Encrenaz, F. Forget, M. Friswell, M. Griffin, P. O. Lagage, P. Malaguti, A. Moneti, J. C. Morales, E. Pace, M. Rocchetto, S. Sarkar, F. Selsis, W. Taylor, J. Tennyson, O. Venot, I. P. Waldmann, G. Wright, T. Zingales, and M. R. Zapatero-Osorio, in *Sp. Telesc. Instrum. Opt. Infrared, Millim. Wave*, Vol. 9904 (2016) p. 99041X.
- [8] G. Tinetti, P. Drossart, P. Eccleston, P. Hartogh, A. Heske, J. Leconte, G. Micela, M. Ollivier, G. Pilbratt, L. Puig, D. Turrini, B. Vandebussche, P. Wolkenberg, J. P. Beaulieu, L. A. Buchave, M. Ferus, M. Griffin, M. Guedel, K. Justtanont, P. O. Lagage, P. Machado, G. Malaguti, M. Min, H. U. Nørgaard-Nielsen, M. Rataj, T. Ray, I. Ribas, M. Swain, R. Szabo, S. Werner, J. Barstow, M. Burleigh, J. Cho, V. C. du Foresto, A. Coustenis, L. Decin, T. Encrenaz, M. Galand, M. Gillon, R. Helled, J. C. Morales, A. G. Muñoz, A. Moneti, I. Pagano, E. Pascale, G. Piccioni, D. Pinfield, S. Sarkar, F. Selsis, J. Tennyson, A. Triaud, O. Venot, I. Waldmann, D. Waltham, G. Wright, J. Amiaux, J. L. Auguères, M. Berthé, N. Bezawada, G. Bishop, N. Bowles, D. Coffey, J. Colomé, M. Crook, P. E. Crouzet, V. Da Peppo, I. E. Sanz, M. Focardi, M. Frericks, T. Hunt, R. Kohley, K. Middleton, G. Morgante, R. Ottensamer, E. Pace, C. Pearson, R. Stamper, K. Symonds, M. Rengel, E. Renotte, P. Ade, L. Affer, C. Alard, N. Allard, F. Altieri, Y. André, C. Arena, I. Argyriou, A. Aylward, C. Baccani, G. Bakos, M. Banaszkiwicz, M. Barlow, V. Batista, G. Bellucci, S. Benatti, P. Bernardi, B. Bézard, M. Blecka, E. Bolmont, B. Bonfond, R. Bonito, A. S. Bonomo, J. R. Brucato, A. S. Brun, I. Bryson, W. Bujwan, S. Casewell, B. Charnay, C. C. Pestellini, G. Chen, A. Ciaravella, R. Claudi, R. Clédassou, M. Damasso, M. Damiano, C. Danielski, P. Deroo, A. M. Di Giorgio, C. Dominik, V. Doublier, S. Doyle, R. Doyon, B. Drummond, B. Duong, S. Eales, B. Edwards, M. Farina, E. Flaccomio, L. Fletcher, F. Forget, S. Fossey, M. Fränz, Y. Fujii, Á. García-Piquer, W. Gear, H. Geoffray, J. C. Gérard, L. Gesa, H. Gomez, R. Graczyk, C. Griffith, D. Grodent, M. G. Guarcello, J. Gustin, K. Hamano, P. Hargrave, Y. Hello, K. Heng, E. Herrero, A. Hornstrup, B. Hubert, S. Ida, M. Ikoma, N. Iro, P. Irwin, C. Jarchow, J. Jaubert, H. Jones, Q. Julien, S. Kameda, F. Kerschbaum, P. Kervella, T. Koskinen, M. Krijger, N. Krupp, M. Lafarga, F. Landini, E. Lellouch, G. Leto, A. Luntzer, T. Rank-Lüftinger, A. Maggio, J. Maldonado, J. P. Maillard, U. Mall, J. B.

- Marquette, S. Mathis, P. Maxted, T. Matsuo, A. Medvedev, Y. Miguel, V. Minier, G. Morello, A. Mura, N. Narita, V. Nascimbeni, N. Nguyen Tong, V. Noce, F. Oliva, E. Palle, P. Palmer, M. Pancrazzi, A. Papageorgiou, V. Parmentier, M. Perger, A. Petralia, S. Pezzuto, R. Pierrehumbert, I. Pillitteri, G. Piotto, G. Pisano, L. Prisinzano, A. Radioti, J. M. Réess, L. Rezac, M. Rocchetto, A. Rosich, N. Sanna, A. Santerne, G. Savini, G. Scandariato, B. Sicardy, C. Sierra, G. Sindoni, K. Skup, I. Snellen, M. Sobiecki, L. Soret, A. Sozzetti, A. Stiepen, A. Strugarek, J. Taylor, W. Taylor, L. Terenzi, M. Tessenyi, A. Tsiaras, C. Tucker, D. Valencia, G. Vasisht, A. Vazan, F. Vilardell, S. Vinatier, S. Viti, R. Waters, P. Wawer, A. Wawrzaszek, A. Whitworth, Y. L. Yung, S. N. Yurchenko, M. R. Z. Osorio, R. Zellem, T. Zingales, and F. Zwart, *Exp. Astron.* **46**, 135 (2018).
- [9] Z. Rustamkulov, D. K. Sing, S. Mukherjee, E. M. May, J. Kirk, E. Schlawin, M. R. Line, C. Piaulet, A. L. Carter, N. E. Batalha, J. M. Goyal, M. López-Morales, J. D. Lothringer, R. J. MacDonald, S. E. Moran, K. B. Stevenson, H. R. Wakeford, N. Espinoza, J. L. Bean, N. M. Batalha, B. Benneke, Z. K. Berta-Thompson, I. J. Crossfield, P. Gao, L. Kreidberg, D. K. Powell, P. E. Cubillos, N. P. Gibson, J. Leconte, K. Molaverdikhani, N. K. Nikolov, V. Parmentier, P. Roy, J. Taylor, J. D. Turner, P. J. Wheatley, K. Aggarwal, E. Ahrer, M. K. Alam, L. Alderson, N. H. Allen, A. Banerjee, S. Barat, D. Barrado, J. K. Barstow, T. J. Bell, J. Blecic, J. Brande, S. Casewell, Q. Changeat, K. L. Chubb, N. Crouzet, T. Daylan, L. Decin, J. Désert, T. Mikal-Evans, A. D. Feinstein, L. Flagg, J. J. Fortney, J. Harrington, K. Heng, Y. Hong, R. Hu, N. Iro, T. Kataria, E. M. Kempton, J. Krick, M. Lendl, J. Lillo-Box, A. Louca, J. Lustig-Yaeger, L. Mancini, M. Mansfield, N. J. Mayne, Y. Miguel, G. Morello, K. Ohno, E. Palle, D. J. Petit dit de la Roche, B. V. Rackham, M. Radica, L. Ramos-Rosado, S. Redfield, L. K. Rogers, E. L. Shkolnik, J. Southworth, J. Teske, P. Tremblin, G. S. Tucker, O. Venot, W. C. Waalkes, L. Welbanks, X. Zhang, and S. Zieba, *Nature* **614**, 659 (2023).
- [10] E. M. Ahrer, K. B. Stevenson, M. Mansfield, S. E. Moran, J. Brande, G. Morello, C. A. Murray, N. K. Nikolov, D. J. Petit dit de la Roche, E. Schlawin, P. J. Wheatley, S. Zieba, N. E. Batalha, M. Damiano, J. M. Goyal, M. Lendl, J. D. Lothringer, S. Mukherjee, K. Ohno, N. M. Batalha, M. P. Battley, J. L. Bean, T. G. Beatty, B. Benneke, Z. K. Berta-Thompson, A. L. Carter, P. E. Cubillos, T. Daylan, N. Espinoza, P. Gao, N. P. Gibson, S. Gill, J. Harrington, R. Hu, L. Kreidberg, N. K. Lewis, M. R. Line, M. López-Morales, V. Parmentier, D. K. Powell, D. K. Sing, S. M. Tsai, H. R. Wakeford, L. Welbanks, M. K. Alam, L. Alderson, N. H. Allen, D. R. Anderson, J. K. Barstow, D. Bayliss, T. J. Bell, J. Blecic, E. M. Bryant, M. R. Burleigh, L. Carone, S. L. Casewell, Q. Changeat, K. L. Chubb, I. J. Crossfield, N. Crouzet, L. Decin, J. M. Désert, A. D. Feinstein, L. Flagg, J. J. Fortney, J. E. Gizis, K. Heng, N. Iro, E. M. Kempton, S. Kendrew, J. Kirk, H. A. Knutson, T. D. Komacek, P. O. Lagage, J. Leconte, J. Lustig-Yaeger, R. J. MacDonald, L. Mancini, E. M. May, N. J. Mayne, Y. Miguel, T. Mikal-Evans, K. Molaverdikhani, E. Palle, C. Piaulet, B. V. Rackham, S. Redfield, L. K. Rogers, P. A. Roy, Z. Rustamkulov, E. L. Shkolnik, K. S. Sotzen, J. Taylor, P. Tremblin, G. S. Tucker, J. D. Turner, M. de Val-Borro, O. Venot, and X. Zhang, *Nature* **614**, 653 (2023).

- [11] A. D. Feinstein, M. Radica, L. Welbanks, C. A. Murray, K. Ohno, L. P. Coulombe, N. Espinoza, J. L. Bean, J. K. Teske, B. Benneke, M. R. Line, Z. Rustamkulov, A. Saba, A. Tsiaras, J. K. Barstow, J. J. Fortney, P. Gao, H. A. Knutson, R. J. MacDonald, T. Mikal-Evans, B. V. Rackham, J. Taylor, V. Parmentier, N. M. Batalha, Z. K. Berta-Thompson, A. L. Carter, Q. Changeat, L. A. dos Santos, N. P. Gibson, J. M. Goyal, L. Kreidberg, M. López-Morales, J. D. Lothringer, Y. Miguel, K. Molaverdikhani, S. E. Moran, G. Morello, S. Mukherjee, D. K. Sing, K. B. Stevenson, H. R. Wakeford, E. M. Ahrer, M. K. Alam, L. Alderson, N. H. Allen, N. E. Batalha, T. J. Bell, J. Blečić, J. Brande, C. Caceres, S. L. Casewell, K. L. Chubb, I. J. Crossfield, N. Crouzet, P. E. Cubillos, L. Decin, J. M. Désert, J. Harrington, K. Heng, T. Henning, N. Iro, E. M. Kempton, S. Kendrew, J. Kirk, J. Krick, P. O. Lagage, M. Lendl, L. Mancini, M. Mansfield, E. M. May, N. J. Mayne, N. K. Nikolov, E. Palle, D. J. Petit dit de la Roche, C. Piaulet, D. Powell, S. Redfield, L. K. Rogers, M. T. Roman, P. A. Roy, M. C. Nixon, E. Schlawin, X. Tan, P. Tremblin, J. D. Turner, O. Venot, W. C. Waalkes, P. J. Wheatley, and X. Zhang, *Nature* **614**, 670 (2023).
- [12] L. Alderson, H. R. Wakeford, M. K. Alam, N. E. Batalha, J. D. Lothringer, J. Adams Redai, S. Barat, J. Brande, M. Damiano, T. Daylan, N. Espinoza, L. Flagg, J. M. Goyal, D. Grant, R. Hu, J. Inglis, E. K. Lee, T. Mikal-Evans, L. Ramos-Rosado, P. A. Roy, N. L. Wallack, N. M. Batalha, J. L. Bean, B. Benneke, Z. K. Berta-Thompson, A. L. Carter, Q. Changeat, K. D. Colón, I. J. Crossfield, J. M. Désert, D. Foreman-Mackey, N. P. Gibson, L. Kreidberg, M. R. Line, M. López-Morales, K. Molaverdikhani, S. E. Moran, G. Morello, J. I. Moses, S. Mukherjee, E. Schlawin, D. K. Sing, K. B. Stevenson, J. Taylor, K. Aggarwal, E. M. Ahrer, N. H. Allen, J. K. Barstow, T. J. Bell, J. Blečić, S. L. Casewell, K. L. Chubb, N. Crouzet, P. E. Cubillos, L. Decin, A. D. Feinstein, J. J. Fortney, J. Harrington, K. Heng, N. Iro, E. M. Kempton, J. Kirk, H. A. Knutson, J. Krick, J. Lecante, M. Lendl, R. J. MacDonald, L. Mancini, M. Mansfield, E. M. May, N. J. Mayne, Y. Miguel, N. K. Nikolov, K. Ohno, E. Palle, V. Parmentier, D. J. Petit dit de la Roche, C. Piaulet, D. Powell, B. V. Rackham, S. Redfield, L. K. Rogers, Z. Rustamkulov, X. Tan, P. Tremblin, S. M. Tsai, J. D. Turner, M. de Val-Borro, O. Venot, L. Welbanks, P. J. Wheatley, and X. Zhang, *Nature* **614**, 664 (2023).
- [13] JWST Transiting Exoplanet Community Early Release Science Team, *Nature* **614**, 649 (2023).
- [14] J. Seidel, L. D. Nielsen, and S. Sarkar, *Nature* **614**, 632 (2023).
- [15] D. R. Anderson, A. Collier Cameron, L. Delrez, A. P. Doyle, M. Gillon, C. Hellier, E. Jehin, M. Lendl, P. F. Maxted, N. Madhusudhan, F. Pepe, D. Pollacco, D. Queloz, D. Ségransan, B. Smalley, A. M. Smith, A. H. Triaud, O. D. Turner, S. Udry, and R. G. West, *Astron. Astrophys.* **604**, A110 (2017).
- [16] C. Piaulet, B. Benneke, R. A. Rubenzahl, A. W. Howard, E. J. Lee, D. Thorngren, R. Angus, M. Peterson, J. E. Schlieder, M. Werner, L. Kreidberg, T. Jaouni, I. J. M. Crossfield, D. R. Ciardi, E. A. Petigura, J. Livingston, C. D. Dressing, B. J. Fulton,

- C. Beichman, J. L. Christiansen, V. Gorjian, K. K. Hardegree-Ullman, J. Krick, and E. Sinukoff, *Astron. J.* **161**, 70 (2021).
- [17] A. Dyrek, M. Min, L. Decin, J. Bouwman, N. Crouzet, P. Mollière, P. O. Lagage, T. Konings, P. Tremblin, M. Güdel, J. Pye, R. Waters, T. Henning, B. Vandenbussche, F. Ardevol Martinez, I. Argyriou, E. Ducrot, L. Heinke, G. van Looveren, O. Absil, D. Barrado, P. Baudoz, A. Boccaletti, C. Cossou, A. Coulais, B. Edwards, R. Gastaud, A. Glasse, A. Glauser, T. P. Greene, S. Kendrew, O. Krause, F. Lahuis, M. Mueller, G. Olofsson, P. Patapis, D. Rouan, P. Royer, S. Scheithauer, I. Waldmann, N. Whiteford, L. Colina, E. F. van Dishoeck, G. Östlin, T. P. Ray, and G. Wright, *Nature* **625**, 51 (2024).
- [18] L. Welbanks, T. J. Bell, T. G. Beatty, M. R. Line, K. Ohno, J. J. Fortney, E. Schlawin, T. P. Greene, E. Rauscher, P. McGill, M. Murphy, V. Parmentier, Y. Tang, I. Edelman, S. Mukherjee, L. S. Wisner, P.-O. Lagage, A. Dyrek, and K. E. Arnold, *Nature* **630**, 836 (2024).
- [19] J. J. Fortney, C. Visscher, M. S. Marley, C. E. Hood, M. R. Line, D. P. Thorngren, R. S. Freedman, and R. Lupu, *Astron. J.* **160**, 288 (2020).
- [20] D. Sing, Z. Rustankulov, D. P. Thorngren, J. K. Barstow, P. Tremblin, C. Alves de Oliveira, T. L. Beck, S. M. Birkmann, R. C. Challener, N. Crouzet, N. Espinoza, P. Ferruit, G. Giardino, A. Gressier, E. K. Lee, N. K. Lewis, and R. Maiolino, *Nature* **630**, 831 (2024).
- [21] K. I. Öberg and E. A. Bergin, *Phys. Rep.* **893**, 1 (2021).
- [22] S. N. Raymond and A. Morbidelli, in *Demographics of Exoplanetary Systems* (Springer International Publishing, Cham (Switzerland), 2022) pp. 3–82.
- [23] C. Baruteau, X. Bai, C. Mordasini, and P. Mollière, *Space Sci. Rev.* **205**, 77 (2016).
- [24] H. Lammer and M. Blanc, *Space Sci. Rev.* **214**, A60 (2018).
- [25] Y. Miguel and A. Vazan, *Remote Sens.* **1**, 0 (2023).
- [26] T. S. Kruijjer, C. Burkhardt, G. Budde, and T. Kleine, *Proc. Natl. Acad. Sci. U. S. A.* **114**, 6712 (2017).
- [27] A. P. Hatzes and H. Rauer, *Astrophys. J. Lett.* **810**, L25 (2015).
- [28] R. Helled, P. Bodenheimer, M. Podolak, A. C. Boley, F. Meru, S. Nayakshin, J. J. Fortney, L. Mayer, Y. Alibert, and A. P. Boss, in *Protostars Planets VI*, edited by H. Beuther, R. S. Klessen, C. P. Dullemond, and T. Henning (University of Arizona Press, Tucson (Arizona), 2014).
- [29] J. J. Lissauer, *Annu. Rev. Ast* **31**, 129 (1993).
- [30] J. B. Pollack, O. Hubickyj, P. Bodenheimer, J. J. Lissauer, M. Podolak, and Y. Greenzweig, *Icarus* **124**, 62 (1996).

- [31] J. J. Lissauer and D. J. Stevenson, in *Protostars Planets IV* (University of Arizona Press, 2007).
- [32] A. Johansen and M. Lambrechts, *Annu. Rev. Earth Planet. Sci.* **45**, 359 (2017).
- [33] A. G. W. Cameron, *Earth, Moon, and Planets* **18**, 5 (1978).
- [34] A. P. Boss, *Science* **276**, 1836 (1997).
- [35] R. Helled, S. Werner, C. Dorn, T. Guillot, M. Ikoma, Y. Ito, M. Kama, T. Lichtenberg, Y. Miguel, O. Shorttle, P. J. Tackley, D. Valencia, and A. Vazan, *Exp. Astron.* **53**, 323 (2022).
- [36] D. P. Thorngren, J. J. Fortney, R. A. Murray-Clay, and E. D. Lopez, *Astrophys. J.* **831**, 64 (2016).
- [37] R. E. Pudritz, A. J. Cridland, and M. Alessi, in *Handbook of Exoplanets*, edited by J. e. Deeg, H., Belmonte (Springer, Cham (Switzerland), 2018) pp. 2475–2521.
- [38] A. Morbidelli, K. Tsiganis, A. Crida, H. F. Levison, and R. Gomes, *Astron. J.* **134**, 1790 (2007).
- [39] A. C. Childs, E. Quintana, T. Barclay, and J. H. Steffen, *Mon. Not. R. Astron. Soc.* **485**, 541 (2019).
- [40] D. J. Stevenson, *Ann. Rev. Earth Planet. Sci.*, Tech. Rep. (1982).
- [41] W. B. Hubbard, *Planetary interiors* (Van Nostrand Reinhold Co., New York, 1984).
- [42] R. Helled and T. Guillot, in *Handbook of Exoplanets*, edited by H. J. Deeg and J. A. Belmonte (Springer, Cham (Switzerland), 2018) pp. 167–185.
- [43] R. Helled, G. Mazzola, and R. Redmer, *Nat. Rev. Phys.* **2**, 562 (2020).
- [44] J. J. Fortney and N. Nettelmann, *Space Sci. Rev.* **152**, 423 (2010).
- [45] I. Baraffe, G. Chabrier, J. Fortney, and C. Sotin, in *Protostars Planets VI*, edited by H. Beuther, Ralf S. Klessen, C. P. Dullemond, and T. Henning (University of Arizona Press, Tucson (Arizona), 2014).
- [46] B. Militzer, F. Soubiran, S. M. Wahl, and W. Hubbard, *J. Geophys. Res. Planets* **121**, 1552 (2016).
- [47] R. Helled, in *Oxford Res. Encycl. Planet. Sci.* (Oxford University Press, 2019).
- [48] R. Helled, N. Movshovitz, and N. Nettelmann, in *Planetary Systems Now*, edited by L. M. Lara and D. Jewitt (2023) Chap. 7, pp. 181–210.
- [49] R. Helled and D. J. Stevenson, *AGU Adv.* **5**, e2024AV001171 (2024).
- [50] California Institute of Technology, NASA Exoplanet Archive.

- [51] S. R. Kane, G. N. Arney, P. K. Byrne, P. A. Dalba, S. J. Desch, J. Horner, N. R. Izenberg, K. E. Mandt, V. S. Meadows, and L. C. Quick, *J. Geophys. Res. Planets* **126**, e2020JE006643 (2021).
- [52] D. C. Hsu, E. B. Ford, D. Ragozzine, and K. Ashby, *Astron. J.* **158**, 109 (2019).
- [53] B. J. Fulton, E. A. Petigura, A. W. Howard, H. Isaacson, G. W. Marcy, P. A. Cargile, L. Hebb, L. M. Weiss, J. A. Johnson, T. D. Morton, E. Sinukoff, I. J. M. Crossfield, and L. A. Hirsch, *Astron. J.* **154**, 109 (2017).
- [54] R. Burn, C. Mordasini, L. Mishra, J. Haldemann, J. Venturini, A. Emsenhuber, and T. Henning, *Nat. Astron.* **8**, 463 (2024).
- [55] M. Mayor and D. Queloz, *Nature* **378**, 355 (1995).
- [56] NobelPrize.org, *The Nobel Prize in Physics 2019* (2019).
- [57] D. E. Trilling, W. Benz, T. Guillot, J. I. Lunine, W. B. Hubbard, and A. Burrows, *Astrophys. J.* **500**, 428 (1998).
- [58] R. D. Alexander and P. J. Armitage, *Astrophys. J.* **704**, 989 (2009).
- [59] A. Brucalassi, J. Koppenhoefer, R. Saglia, L. Pasquini, M. T. Ruiz, P. Bonifacio, L. R. Bedin, M. Libralato, K. Biazzo, C. Melo, C. Lovis, and S. Randich, *Astron. Astrophys.* **592**, L1 (2016).
- [60] A. Triaud, *Nature* **537**, 496 (2016).
- [61] K. Barkaoui, F. J. Pozuelos, C. Hellier, B. Smalley, L. D. Nielsen, C. Dorn, P. Niraula, M. Gillon, J. de Wit, R. Helled, S. Müller, E. Jehin, B.-O. Demory, V. Van Grootel, A. Soubkiou, M. Ghachoui, D. R. Anderson, Z. Benkhaldoun, F. Bouchy, A. Burdanov, L. Delrez, E. Ducrot, L. Garcia, A. Jabiri, M. Lendl, P. F. L. Maxted, C. A. Murray, P. Pihlmann Pedersen, D. Queloz, D. Sebastian, O. Turner, S. Udry, M. Timmermans, A. H. M. J. Triaud, and R. G. West, *Nat. Astron.* **8**, 909 (2024).
- [62] A. Burrows, T. Guillot, W. B. Hubbard, M. S. Marley, D. Saumon, J. I. Lunine, and D. Sudarsky, *Astrophys. J.* **534**, L97 (2000).
- [63] A. Burrows, I. Hubeny, J. Budaj, and W. B. Hubbard, *Astrophys. J.* **661**, 502 (2007).
- [64] D. P. Thorngren and J. J. Fortney, *Astron. J.* **155**, 214 (2018).
- [65] P. Sarkis, C. Mordasini, T. Henning, G. D. Marleau, and P. Mollière, *Astron. Astrophys.* **645**, A79 (2021).
- [66] K. Batygin and D. J. Stevenson, *Astrophys. J. Lett.* **714**, L238 (2010).
- [67] J. J. Fortney, R. I. Dawson, and T. D. Komacek, *J. Geophys. Res. Planets* **126**, e2020JE006629 (2021).
- [68] R. I. Dawson and J. A. Johnson, *Annu. Rev. Astron. Astrophys.* **56**, 175 (2018).

- [69] S. Müller and R. Helled, *Front. Astron. Sp. Sci.* **10**, 123 (2023).
- [70] A. Cumming, R. P. Butler, G. W. Marcy, S. S. Vogt, J. T. Wright, and D. A. Fischer, *Publ. Astron. Soc. Pacific* **120**, 531 (2008).
- [71] A. W. Howard, G. W. Marcy, J. A. Johnson, D. A. Fischer, J. T. Wright, H. Isaacson, J. A. Valenti, J. Anderson, D. N. Lin, and S. Ida, *Science* **330**, 653 (2010).
- [72] A. Cumming, *Exoplanets*, edited by S. Seager (University of Arizona Press, 2011) pp. 191–214.
- [73] M. Zechmeister, M. Kürster, M. Endl, G. Lo Curto, H. Hartman, H. Nilsson, T. Henning, A. P. Hatzes, and W. D. Cochran, *Astron. Astrophys.* **552**, A78 (2013).
- [74] J. N. Winn and D. C. Fabrycky, *Annu. Rev. Astron. Astrophys.* **53**, 409 (2015).
- [75] L. Zeng, S. B. Jacobsen, D. D. Sasselov, M. I. Petaev, A. Vanderburg, M. Lopez-Morales, J. Perez-Mercader, T. R. Mattsson, G. Li, M. Z. Heising, A. S. Bonomo, M. Damasso, T. A. Berger, H. Cao, A. Levi, and R. D. Wordsworth, *Proc. Natl. Acad. Sci. U. S. A.* **116**, 9723 (2019).
- [76] J. F. Otegi, F. Bouchy, and R. Helled, *Astron. Astrophys.* **634**, A43 (2020).
- [77] A. Sánchez-Lavega, P. Irwin, and A. García Muñoz, *Astron. Astrophys. Rev.* **31**, 5 (2023).
- [78] D. Grant, N. K. Lewis, H. R. Wakeford, N. E. Batalha, A. Glidden, J. Goyal, E. Mullens, R. J. MacDonald, E. M. May, S. Seager, K. B. Stevenson, J. A. Valenti, C. Visscher, L. Alderson, N. H. Allen, C. I. Cañas, K. Colón, M. Clampin, N. Espinoza, A. Gressier, J. Huang, Z. Lin, D. Long, D. R. Louie, M. Peña-Guerrero, S. Ranjan, K. S. Sotzen, D. Valentine, J. Anderson, W. O. Balmer, A. Bellini, K. K. W. Hoch, J. Kammerer, M. Libralato, C. M. Mountain, M. D. Perrin, L. Pueyo, E. Rickman, I. Rebollido, S. T. Sohn, R. P. van der Marel, and L. L. Watkins, *Astrophys. J. Lett.* **956**, L32 (2023).
- [79] F. Yan, N. Casasayas-Barris, K. Molaverdikhani, F. J. Alonso-Floriano, A. Reiners, E. Pallé, T. Henning, P. Mollière, G. Chen, L. Nortmann, I. A. Snellen, I. Ribas, A. Quirrenbach, J. A. Caballero, P. J. Amado, M. Azzaro, F. F. Bauer, M. Cortés Contreras, S. Czesla, S. Khalafinejad, L. M. Lara, M. López-Puertas, D. Montes, E. Nagel, M. Os-hagh, A. Sánchez-López, M. Stangret, and M. Zechmeister, *Astron. Astrophys.* **632**, A69 (2019).
- [80] J. V. Seidel, D. Ehrenreich, R. Allart, H. J. Hoeijmakers, C. Lovis, V. Bourrier, L. Pino, A. Wyttenbach, V. Adibekyan, Y. Alibert, F. Borsa, N. Casasayas-Barris, S. Cristiani, O. D. Demangeon, P. Di Marcantonio, P. Figueira, J. I. González Hernández, J. Lillo-Box, C. J. Martins, A. Mehner, P. Molaro, N. J. Nunes, E. Palle, F. Pepe, N. C. Santos, S. G. Sousa, A. Sozzetti, H. M. Taberner, and M. R. Zapatero Osorio, *Astron. Astrophys.* **653**, A73 (2021).
- [81] H. Vogt, *Astron. Nachrichten* **222**, 97 (1924).

- [82] A. S. Grossman, *Astrophys. J.* **161**, 619 (1970).
- [83] A. S. Eddington, *Intern. Const. Stars* (Cambridge University Press, 1988).
- [84] R. Kippenhahn, A. Weigert, and A. Weiss, *Stellar Structure and Evolution*, 2nd ed., Astronomy and Astrophysics Library (Springer, Berlin, Heidelberg, 2012) p. 604.
- [85] I. N. Reid, in *Planets, Stars and Stellar Systems Volume 4: Stellar Structure and Evolution* (Springer Netherlands, 2013) pp. 337–395.
- [86] M. S. Marley, P. Gomez, and M. Podolak, *J. Geophys. Res. Planets* **100**, 23349 (1995).
- [87] M. Podolak, J. I. Podolak, and M. S. Marley, *Planet. Space Sci.* **48**, 143 (2000).
- [88] R. Helled, G. Schubert, and J. D. Anderson, *Icarus* **199**, 368 (2009).
- [89] J. I. Podolak, U. Malamud, and M. Podolak, *Icarus* **382**, 115017 (2022).
- [90] B. A. Neuenschwander, R. Helled, N. Movshovitz, and J. J. Fortney, *Astrophys. J.* **910**, 38 (2021).
- [91] B. A. Neuenschwander and R. Helled, *Mon. Not. R. Astron. Soc.* **512**, 3124 (2022).
- [92] B. A. Neuenschwander, S. Müller, and R. Helled, *Astron. Astrophys.* **684**, A191 (2024).
- [93] M. W. Phillips, P. Tremblin, I. Baraffe, G. Chabrier, N. F. Allard, F. Spiegelman, J. M. Goyal, B. Drummond, and E. Hébrard, *Astron. Astrophys.* **637**, A38 (2020).
- [94] M. S. Marley, D. Saumon, C. Visscher, R. Lupu, R. Freedman, C. Morley, J. J. Fortney, C. Seay, A. J. R. W. Smith, D. J. Teal, and R. Wang, *Astrophys. J.* **920**, 85 (2021).
- [95] T. Karalidi, M. Marley, J. J. Fortney, C. Morley, D. Saumon, R. Lupu, C. Visscher, and R. Freedman, *Astrophys. J.* **923**, 269 (2021).
- [96] C. V. Morley, S. Mukherjee, M. S. Marley, J. J. Fortney, C. Visscher, R. Lupu, E. Gharib-Nezhad, D. Thorngren, R. Freedman, and N. Batalha, *Astrophys. J.* **975**, 59 (2024).
- [97] W. B. Hubbard, *Astrophys. J.* **152**, 745 (1968).
- [98] F. J. Low, *Astron. J.* **71**, 391 (1966).
- [99] N. Nettelmann, K. Wang, J. J. Fortney, S. Hamel, S. Yellamilli, M. Bethkenhagen, and R. Redmer, *Icarus* **275**, 107 (2016).
- [100] L. Scheibe, N. Nettelmann, and R. Redmer, *Astron. Astrophys.* **632**, A70 (2019).
- [101] L. Scheibe, N. Nettelmann, and R. Redmer, *Astron. Astrophys.* **650**, A200 (2021).
- [102] J. Leconte and G. Chabrier, *Astron. Astrophys.* **540**, A20 (2012).
- [103] J. Leconte and G. Chabrier, *Nat. Geosci.* **6**, 347 (2013).
- [104] D. J. Stevenson and E. E. Salpeter, *Astrophys. J. Suppl. Ser.* **35**, 239 (1977).

- [105] N. Nettelmann, J. J. Fortney, K. Moore, and C. Mankovich, *Mon. Not. R. Astron. Soc.* **447**, 3422 (2015).
- [106] C. Mankovich, J. J. Fortney, and K. L. Moore, *Astrophys. J.* **832**, 113 (2016).
- [107] M. Schöttler and R. Redmer, *Phys. Rev. Lett.* **120**, 115703 (2018).
- [108] J. Fuller, *Icarus* **242**, 283 (2014).
- [109] C. R. Mankovich and J. Fuller, *Nat. Astron.* **5**, 1103 (2021).
- [110] B. Militzer, W. B. Hubbard, S. Wahl, J. I. Lunine, E. Galanti, Y. Kaspi, Y. Miguel, T. Guillot, K. M. Moore, M. Parisi, J. E. Connerney, R. Helled, H. Cao, C. Mankovich, D. J. Stevenson, R. S. Park, M. Wong, S. K. Atreya, J. Anderson, and S. J. Bolton, *Planet. Sci. J.* **3**, 185 (2022).
- [111] S. Howard, T. Guillot, M. Bazot, Y. Miguel, D. J. Stevenson, E. Galanti, Y. Kaspi, W. B. Hubbard, B. Militzer, R. Helled, N. Nettelmann, B. Idini, and S. Bolton, *Astron. Astrophys.* **672**, A33 (2023).
- [112] Y. Miguel, M. Bazot, T. Guillot, S. Howard, E. Galanti, Y. Kaspi, W. B. Hubbard, B. Militzer, R. Helled, S. K. Atreya, J. E. Connerney, D. Durante, L. Kulowski, J. I. Lunine, D. Stevenson, and S. Bolton, *Astron. Astrophys.* **662**, A18 (2022).
- [113] R. Helled, D. J. Stevenson, J. I. Lunine, S. J. Bolton, N. Nettelmann, S. Atreya, T. Guillot, B. Militzer, Y. Miguel, and W. B. Hubbard, *Icarus* **378**, 114937 (2022).
- [114] Y. Kaspi, E. Galanti, W. B. Hubbard, D. J. Stevenson, S. J. Bolton, L. Iess, T. Guillot, J. Bloxham, J. E. Connerney, H. Cao, D. Durante, W. M. Folkner, R. Helled, A. P. Ingersoll, S. M. Levin, J. I. Lunine, Y. Miguel, B. Militzer, M. Parisi, and S. M. Wahl, *Nature* **555**, 223 (2018).
- [115] C. A. Jones, *Nat. Astron.* **7**, 1417 (2023).
- [116] D. J. Stevenson, *Annu. Rev. Earth Planet. Sci.* **48**, 465 (2020).
- [117] B. Militzer and W. B. Hubbard, *Icarus* **411**, 115955 (2024).
- [118] T. Cavalié, J. Lunine, and O. Mousis, *Nat. Astron.* **7**, 678 (2023).
- [119] T. Guillot, D. Gautier, G. Chabrier, and B. Mosser, *Icarus* **112**, 337 (1994).
- [120] T. Guillot, G. Chabrier, P. Morel, and D. Gautier, *Icarus* **112**, 354 (1994).
- [121] S. Müller and R. Helled, *Astrophys. J.* **967**, 7 (2024).
- [122] S. M. Wahl, W. B. Hubbard, and B. Militzer, *Icarus* **282**, 183 (2017).
- [123] N. Nettelmann, *Astrophys. J.* **874**, 156 (2019).
- [124] B. Idini and D. J. Stevenson, *Planet. Sci. J.* **3**, 89 (2022).

- [125] K. Heng, *Exoplanetary Atmospheres: Theoretical Concepts and Foundations* (Princeton University Press, 2017) p. 296.
- [126] S. Sengupta and S. Sengupta, *New Astron.* **100**, 101987 (2023).
- [127] L. Kreidberg, J. L. Bean, J. M. Désert, M. R. Line, J. J. Fortney, N. Madhusudhan, K. B. Stevenson, A. P. Showman, D. Charbonneau, P. R. McCullough, S. Seager, A. Burrows, G. W. Henry, M. Williamson, T. Kataria, and D. Homeier, *Astrophys. J. Lett.* **793**, L27 (2014).
- [128] D. K. Sing, J. J. Fortney, N. Nikolov, H. R. Wakeford, T. Kataria, T. M. Evans, S. Aigrain, G. E. Ballester, A. S. Burrows, D. Deming, J. M. Désert, N. P. Gibson, G. W. Henry, C. M. Huitson, H. A. Knutson, A. L. D. Etangs, F. Pont, A. P. Showman, A. Vidal-Madjar, M. H. Williamson, and P. A. Wilson, *Nature* **529**, 59 (2016).
- [129] H. R. Wakeford, D. K. Sing, D. Deming, N. K. Lewis, J. Goyal, T. J. Wilson, J. Barstow, T. Kataria, B. Drummond, T. M. Evans, A. L. Carter, N. Nikolov, H. A. Knutson, G. E. Ballester, and A. M. Mandell, *Astron. J.* **155**, 29 (2018).
- [130] N. Nikolov, D. K. Sing, J. J. Fortney, J. M. Goyal, B. Drummond, T. M. Evans, N. P. Gibson, E. J. De Mooij, Z. Rustamkulov, H. R. Wakeford, B. Smalley, A. J. Burgasser, C. Hellier, C. Helling, N. J. Mayne, N. Madhusudhan, T. Kataria, J. Baines, A. L. Carter, G. E. Ballester, J. K. Barstow, J. McCleery, and J. J. Spake, *Nature* **557**, 526 (2018).
- [131] C. Von Essen, M. Mallonn, S. Hermansen, M. C. Nixon, N. Madhusudhan, H. Kjeldsen, and G. Tautvaišienė, *Astron. Astrophys.* **637**, A76 (2020).
- [132] J. Llama, A. A. Vidotto, M. Jardine, K. Wood, R. Fares, and T. I. Gombosi, *Mon. Not. R. Astron. Soc.* **436**, 2179 (2013).
- [133] P. W. Cauley, S. Redfield, A. G. Jensen, T. Barman, M. Endl, and W. D. Cochran, *Astrophys. J.* **810**, 13 (2015).
- [134] L. Ben-Jaffel, G. E. Ballester, A. G. Muñoz, P. Lavvas, D. K. Sing, J. Sanz-Forcada, O. Cohen, T. Kataria, G. W. Henry, L. Buchhave, T. Mikal-Evans, H. R. Wakeford, and M. López-Morales, *Nat. Astron.* **6**, 141 (2022).
- [135] L. Kreidberg, J. L. Bean, J. M. Désert, B. Benneke, D. Deming, K. B. Stevenson, S. Seager, Z. Berta-Thompson, A. Seifahrt, and D. Homeier, *Nature* **505**, 69 (2014).
- [136] H. R. Wakeford, C. Visscher, N. K. Lewis, T. Kataria, M. S. Marley, J. J. Fortney, and A. M. Mandell, *Mon. Not. R. Astron. Soc.* **464**, 4247 (2017).
- [137] M. Mallonn, J. Köhler, X. Alexoudi, C. Von Essen, T. Granzer, K. Poppenhaeger, and K. G. Strassmeier, *Astron. Astrophys.* **624**, A62 (2019).
- [138] E. M. Kempton, M. Zhang, J. L. Bean, M. E. Steinrueck, A. A. Piette, V. Parmentier, I. Malsky, M. T. Roman, E. Rauscher, P. Gao, T. J. Bell, Q. Xue, J. Taylor, A. B. Savel, K. E. Arnold, M. C. Nixon, K. B. Stevenson, M. Mansfield, S. Kendrew, S. Zieba,

- E. Ducrot, A. Dyrek, P. O. Lagage, K. G. Stassun, G. W. Henry, T. Barman, R. Lupu, M. Malik, T. Kataria, J. Ih, G. Fu, L. Welbanks, and P. McGill, *Nature* **620**, 67 (2023).
- [139] I. A. Snellen, R. J. De Kok, E. J. De Mooij, and S. Albrecht, *Nature* **465**, 1049 (2010).
- [140] N. Casasayas-Barris, E. Pallé, F. Yan, G. Chen, S. Albrecht, L. Nortmann, V. Van Eylen, I. Snellen, G. J. Talens, J. I. González Hernández, R. Rebolo, and G. P. Otten, *Astron. Astrophys.* **616**, A151 (2018).
- [141] D. Thorngren and J. J. Fortney, *Astrophys. J. Lett.* **874**, L31 (2019).
- [142] H. F. Wilson and B. Militzer, *Astrophys. J.* **745**, 54 (2012).
- [143] W. C. Demarcus, *Astron. J.* **63**, 2 (1958).
- [144] P. J. E. Peebles, *Astrophys. J.* **140**, 328 (1964).
- [145] F. Soubiran and B. Militzer, *Astrophys. J.* **829**, 14 (2016).
- [146] M. Bethkenhagen, E. R. Meyer, S. Hamel, N. Nettelmann, M. French, L. Scheibe, C. Tیکنور, L. A. Collins, J. D. Kress, J. J. Fortney, and R. Redmer, *Astrophys. J.* **848**, 67 (2017).
- [147] F. Graziani, M. P. Desjarlais, R. Redmer, and S. B. Trickey, eds., *Lecture Notes in Computational Science and Engineering* (Springer, Cham (Switzerland), 2014) p. 282.
- [148] D. Riley, *Warm Dense Matter: Laboratory Generation and Diagnosis*, 2053-2563 (IOP Publishing, 2021) p. 145.
- [149] T. G. White, J. Dai, and D. Riley, *Philos. Trans. R. Soc. A* **381**, 20220223 (2023).
- [150] M. Ross, *Nature* **292**, 435 (1981).
- [151] D. Kraus, J. Vorberger, A. Pak, N. J. Hartley, L. B. Fletcher, S. Frydrych, E. Galtier, E. J. Gamboa, D. O. Gericke, S. H. Glenzer, E. Granados, M. J. MacDonald, A. J. MacKinnon, E. E. McBride, I. Nam, P. Neumayer, M. Roth, A. M. Saunders, A. K. Schuster, P. Sun, T. Van Driel, T. Döppner, and R. W. Falcone, *Nat. Astron.* **1**, 606 (2017).
- [152] Z. He, M. Rödel, J. Lütgert, A. Bergermann, M. Bethkenhagen, D. Chekrygina, T. E. Cowan, A. Descamps, M. French, E. Galtier, A. E. Gleason, G. D. Glenn, S. H. Glenzer, Y. Inubushi, N. J. Hartley, J. A. Hernandez, B. Heuser, O. S. Humphries, N. Kamimura, K. Katagiri, D. Khaghani, H. J. Lee, E. E. McBride, K. Miyanishi, B. Nagler, B. Ofori-Okai, N. Ozaki, S. Pandolfi, C. Qu, D. Ranjan, R. Redmer, C. Schoenwaelder, A. K. Schuster, M. G. Stevenson, K. Sueda, T. Togashi, T. Vinci, K. Voigt, J. Vorberger, M. Yabashi, T. Yabuuchi, L. M. Zinta, A. Ravasio, and D. Kraus, *Sci. Adv.* **8**, eabo0617 (2022).
- [153] B. Cheng, S. Hamel, and M. Bethkenhagen, *Nat. Commun.* **14**, 1104 (2023).

- [154] M. Frost, R. S. McWilliams, E. Bykova, M. Bykov, R. J. Husband, L. M. Andriambariar-ijaona, S. Khandarkhaeva, B. Massani, K. Appel, C. Baetz, O. B. Ball, V. Cerantola, S. Chariton, J. Choi, H. Cynn, M. J. Duff, A. Dwivedi, E. Edmund, G. Fiquet, H. Graaf-sma, H. Hwang, N. Jaisle, J. Kim, Z. Konôpková, T. Laurus, Y. Lee, H.-P. Liermann, J. D. McHardy, M. I. McMahon, G. Morard, M. Nakatsutsumi, L. A. Nguyen, S. Ninet, V. B. Prakapenka, C. Prescher, R. Redmer, S. Stern, C. Strohm, J. Sztuk-Dambietz, M. Turcato, Z. Wu, S. H. Glenzer, and A. F. Goncharov, *Nat. Astron.* **8**, 174 (2024).
- [155] P. Hohenberg and W. Kohn, *Phys. Rev.* **136**, B864 (1964).
- [156] W. Kohn and L. J. Sham, *Phys. Rev.* **140**, A1133 (1965).
- [157] R. Car and M. Parrinello, *Phys. Rev. Lett.* **55**, 2471 (1985).
- [158] M. Preising and R. Redmer, *Phys. Rev. B* **102**, 224107 (2020).
- [159] M. Preising and R. Redmer, *Contrib. to Plasma Phys.* **61**, e202100105 (2021).
- [160] M. Schöttler and R. Redmer, *J. Plasma Phys.* **84**, 755840401 (2018).
- [161] Y. Cytter, E. Rabani, D. Neuhauser, M. Preising, R. Redmer, and R. Baer, *Phys. Rev. B* **100**, 195101 (2019).
- [162] A. Bergermann, M. French, M. Schöttler, and R. Redmer, *Phys. Rev. E* **103**, 013307 (2021).
- [163] A. Bergermann, M. French, and R. Redmer, *Phys. Chem. Chem. Phys.* **23**, 12637 (2021).
- [164] A. Vazan, R. Sari, and R. Kessel, *Mon. Not. R. Astron. Soc.* **926**, 150 (2022).
- [165] T. Kovačević, F. González-Cataldo, S. T. Stewart, and B. Militzer, *Sci. Rep.* **12**, 13055 (2022).
- [166] H. F. Wilson and B. Militzer, *Phys. Rev. Lett.* **108**, 111101 (2012).
- [167] S. M. Wahl, H. F. Wilson, and B. Militzer, *Astrophys. J.* **773**, 95 (2013).
- [168] R. Chau, S. Hamel, and W. J. Nellis, *Nat. Commun.* **2**, A203 (2011).
- [169] M. Bethkenhagen, D. Cebulla, R. Redmer, and S. Hamel, *J. Phys. Chem. A* **119**, 10582 (2015).
- [170] E. R. Meyer, C. Ticknor, M. Bethkenhagen, S. Hamel, R. Redmer, J. D. Kress, and L. A. Collins, *J. Chem. Phys.* **143**, 164513 (2015).
- [171] V. Naden Robinson and A. Hermann, *J. Phys. Condens. Matter* **32**, 184004 (2020).
- [172] K. de Villa, F. González-Cataldo, and B. Militzer, *Nat. Commun.* **14**, 7580 (2023).
- [173] S. Mazevet, A. Licari, G. Chabrier, and A. Y. Potekhin, *Astron. Astrophys.* **621**, A128 (2019).

- [174] M. Millot, F. Coppari, J. R. Rygg, A. Correa Barrios, S. Hamel, D. C. Swift, and J. H. Eggert, *Nature* **569**, 251 (2019).
- [175] M. French, A. Becker, W. Lorenzen, N. Nettelmann, M. Bethkenhagen, J. Wicht, and R. Redmer, *Astrophys. J. Suppl. Ser.* **202**, 5 (2012).
- [176] A. Becker, M. Bethkenhagen, C. Kellermann, J. Wicht, and R. Redmer, *Astron. J.* **156**, 149 (2018).
- [177] M. Preising, M. French, C. Mankovich, F. Soubiran, and R. Redmer, *Astrophys. J. Suppl. Ser.* **269**, 47 (2023).
- [178] T. Guillot, *Science* **286**, 72 (1999).
- [179] J. J. Fortney, M. S. Marley, and J. W. Barnes, *Astrophys. J.* **659**, 1661 (2007).
- [180] T. Guillot, *Astron. Astrophys.* **520**, A27 (2010).
- [181] R. T. Pierrehumbert and M. Hammond, *Annu. Rev. Fluid Mech.* **51**, 275 (2019).
- [182] T. Guillot, A. Burrows, W. B. Hubbard, J. I. Lunine, and D. Saumon, *Astrophys. J.* **459**, L35 (1996).
- [183] S. Seager and D. D. Sasselov, *Astrophys. J.* **502**, L157 (1998).
- [184] T. Guillot and A. P. Showman, *Astron. Astrophys.* **385**, 156 (2002).
- [185] S. M. Wahl, D. Thorngren, T. Lu, and B. Militzer, *Astrophys. J.* **921**, 105 (2021).
- [186] X. Lyu, D. D. B. Koll, N. B. Cowan, R. Hu, L. Kreidberg, and B. E. J. Rose, *Astrophys. J.* **964**, 152 (2023).
- [187] N. J. Mayne, I. Baraffe, D. M. Acreman, C. Smith, M. K. Browning, D. S. Amundsen, N. Wood, J. Thuburn, and D. R. Jackson, *Astron. Astrophys.* **561**, A1 (2014).
- [188] A. P. Showman and T. Guillot, *Astron. Astrophys.* **385**, 166 (2002).
- [189] C. Helling, G. Lee, I. Dobbs-Dixon, N. Mayne, D. S. Amundsen, J. Khaimova, A. A. Unger, J. Manners, D. Acreman, and C. Smith, *Mon. Not. R. Astron. Soc.* **460**, 855 (2016).
- [190] P. Gao and D. Powell, *Astrophys. J. Lett.* **918**, L7 (2021).
- [191] T. Foken, ed., *Springer Handbook of Atmospheric Measurements* (Springer Nature Switzerland AG, Cham (Switzerland), 2021).
- [192] P. G. J. Irwin, *Giant Planets of Our Solar System*, 2nd ed. (Springer Berlin, Heidelberg, 2009).
- [193] S. J. Bolton, J. Lunine, D. Stevenson, J. E. Connerney, S. Levin, T. C. Owen, F. Bagenal, D. Gautier, A. P. Ingersoll, G. S. Orton, T. Guillot, W. Hubbard, J. Bloxham, A. Coradini, S. K. Stephens, P. Mokashi, R. Thorne, and R. Thorpe, *Space Sci. Rev.* **213**, 5

- (2017).
- [194] D. Grassi, A. Adriani, A. Mura, B. M. Dinelli, G. Sindoni, D. Turrini, G. Filacchione, A. Migliorini, M. L. Moriconi, F. Tosi, R. Noschese, A. Cicchetti, F. Altieri, F. Fabiano, G. Piccioni, S. Stefani, S. Atreya, J. Lunine, G. Orton, A. Ingersoll, S. Bolton, S. Levin, J. Connerney, A. Olivieri, and M. Amoroso, *Geophys. Res. Lett.* **44**, 4615 (2017).
- [195] Z. Zhang, V. Adumitroaie, M. Allison, J. Arballo, S. Atreya, G. Bjoraker, S. Bolton, S. Brown, L. N. Fletcher, T. Guillot, S. Gulkis, A. Hodges, A. Ingersoll, M. Janssen, S. Levin, C. Li, L. Li, J. Lunine, S. Misra, G. Orton, F. Oyafuso, P. Steffes, and M. H. Wong, *Earth Sp. Sci.* **7**, e2020EA001229 (2020).
- [196] H. B. Niemann, S. K. Atreya, G. R. Carignan, T. M. Donahue, J. A. Haberman, D. N. Harpold, R. E. Hartle, D. M. Hunten, W. T. Kasprzak, P. R. Mahaffy, T. C. Owen, and S. H. Way, *J. Geophys. Res. Planets* **103**, 22831 (1998).
- [197] R. V. Yelle, J. Serigano, T. T. Koskinen, S. M. Hörst, M. E. Perry, R. S. Perryman, and J. H. Waite, *Geophys. Res. Lett.* **45**, 10951 (2018).
- [198] N. Madhusudhan, *Annu. Rev. Astron. Astrophys.* **57**, 617 (2019).
- [199] L. Kreidberg, in *Handbook of Exoplanets* (San Francisco, W. H. Freeman and Co., Cham (Switzerland), 2018).
- [200] J. M. Lee, L. N. Fletcher, and P. G. Irwin, *Mon. Not. R. Astron. Soc.* **420**, 170 (2012).
- [201] M. R. Line, H. Knutson, A. S. Wolf, and Y. L. Yung, *Astrophys. J.* **783**, 70 (2014).
- [202] J. K. Barstow and K. Heng, *Space Sci. Rev.* **216**, A82 (2020).
- [203] J. J. Fortney, R. Helled, N. Nettelmann, D. J. Stevenson, M. S. Marley, W. B. Hubbard, and L. Iess, in *Saturn 21st Century*, edited by K. H. Baines, F. M. Flasar, N. Krupp, and T. Stallard (Cambridge University Press, Cambridge (UK), 2018).
- [204] J. B. Pollack and Y. L. Yung, *Annu. Rev. Earth Planet. Sci.* **8**, 425 (1980).
- [205] A. Sánchez-Lavega, *An Introduction to Planetary Atmospheres* (CRC Press, Boca Raton, 2010) pp. 1–629.
- [206] H. Lammer, *Origin and Evolution of Planetary Atmospheres*, 1st ed. (Springer Berlin, Heidelberg, 2013).
- [207] E. S. Kite and M. N. Barnett, *Proc. Natl. Acad. Sci. U. S. A.* **117**, 18264 (2020).
- [208] R. Mbarek and E. M.-R. Kempton, *Astrophys. J.* **827**, 121 (2016).
- [209] P. Gao, H. R. Wakeford, S. E. Moran, and V. Parmentier, *J. Geophys. Res. Planets* **126**, e2020JE006655 (2021).
- [210] M. S. Marley, C. Gelino, D. Stephens, J. I. Lunine, and R. Freedman, *Astrophys. J.* **513**, 879 (1999).

- [211] D. Sudarsky, A. Burrows, and P. Pinto, *Astrophys. J.* **538**, 885 (2000).
- [212] P. Gao, D. P. Thorngren, G. K. Lee, J. J. Fortney, C. V. Morley, H. R. Wakeford, D. K. Powell, K. B. Stevenson, and X. Zhang, *Nat. Astron.* **4**, 951 (2020).
- [213] P. Woitke, C. Helling, and O. Gunn, *Astron. Astrophys.* **634**, A23 (2020).
- [214] E. K. H. Lee, *Glass rain: modelling the formation, dynamics and radiative-transport of cloud particles in hot Jupiter exoplanet atmospheres*, Thesis (ph.d.), University of St Andrews (2017).
- [215] C. Helling, *Annu. Rev. Earth Planet. Sci.* **47**, 583 (2019).
- [216] C. Helling, D. Lewis, D. Samra, L. Carone, V. Graham, O. Herbort, K. L. Chubb, M. Min, R. Waters, V. Parmentier, and N. Mayne, *Astron. Astrophys.* **649**, A44 (2021).
- [217] C. Helling, in *ExoFrontiers*, edited by N. Madhusudhan (IOP Publishing, Bristol, UK, 2021) Chap. 20.
- [218] C. Helling, in *Planetary Systems Now*, edited by L. M. Lara and D. Jewitt (World Scientific Publishing Co., 2023) pp. 235–258.
- [219] E. K. H. Lee, *Mon. Not. R. Astron. Soc.* **524**, 2918 (2023).
- [220] H. A. Knutson, B. Benneke, D. Deming, and D. Homeier, *Nature* **505**, 66 (2014).
- [221] H. A. Knutson, D. Dragomir, L. Kreidberg, E. M. Kempton, P. R. McCullough, J. J. Fortney, J. L. Bean, M. Gillon, D. Homeier, and A. W. Howard, *Astrophys. J.* **794**, 155 (2014).
- [222] A. Pinhas and N. Madhusudhan, *Mon. Not. R. Astron. Soc.* **471**, 4355 (2017).
- [223] A. Pinhas, N. Madhusudhan, S. Gandhi, and R. MacDonald, *Mon. Not. R. Astron. Soc.* **482**, 1485 (2019).
- [224] Kreidberg, *Am. Astron. Soc.* (2016).
- [225] J. M. Vos, B. Burningham, J. K. Faherty, S. Alejandro, E. Gonzales, E. Calamari, D. B. Gagliuffi, C. Visscher, X. Tan, C. V. Morley, M. Marley, M. E. Gemma, N. Whiteford, J. Gaarn, and G. Park, *Astrophys. J.* **944**, 138 (2023).
- [226] A. Burrows, I. Hubeny, J. Budaj, H. A. Knutson, and D. Charbonneau, *Astrophys. J.* **668**, L171 (2007).
- [227] H. A. Knutson, D. Charbonneau, L. E. Allen, A. Burrows, and S. T. Megeath, *Astrophys. J.* **673**, 526 (2008).
- [228] H. Diamond-Lowe, K. B. Stevenson, J. L. Bean, M. R. Line, and J. J. Fortney, *Astrophys. J.* **796**, 66 (2014).
- [229] H. Schwarz, M. Brogi, R. De Kok, J. Birkby, and I. Snellen, *Astron. Astrophys.* **576**, A111 (2015).

- [230] M. R. Line, K. B. Stevenson, J. Bean, J.-M. Desert, J. J. Fortney, L. Kreidberg, N. Madhusudhan, A. P. Showman, and H. Diamond-lowe, *Astron. J.* **152**, 203 (2016).
- [231] R. Alonso, in *Handbook of Exoplanets*, edited by H. J. Deeg and J. A. Belmonte (Springer, Cham (Switzerland), 2018).
- [232] J. J. Fortney, K. Lodders, M. S. Marley, and R. S. Freedman, *Astrophys. J.* **678**, 1419 (2008).
- [233] D. S. Spiegel, K. Silverio, and A. Burrows, *Astrophys. J.* **699**, 1487 (2009).
- [234] J. D. Lothringer, T. Barman, and T. Koskinen, *Astrophys. J.* **866**, 27 (2018).
- [235] J. K. Barstow, *Mon. Not. R. Astron. Soc.* **497**, 4183 (2020).
- [236] O. Venot and M. Agúndez, *Exp. Astron.* **40**, 469 (2015).
- [237] T. T. Koskinen, A. D. Aylward, and S. Miller, *Nature* **450**, 845 (2007).
- [238] J. J. Spake, D. K. Sing, T. M. Evans, A. Oklopčić, V. Bourrier, L. Kreidberg, B. V. Rackham, J. Irwin, D. Ehrenreich, A. Wyttenbach, H. R. Wakeford, Y. Zhou, K. L. Chubb, N. Nikolov, J. M. Goyal, G. W. Henry, M. H. Williamson, S. Blumenthal, D. R. Anderson, C. Hellier, D. Charbonneau, S. Udry, and N. Madhusudhan, *Nature* **557**, 68 (2018).
- [239] J. E. Owen, *Annu. Rev. Earth Planet. Sci.* **47**, 67 (2019).
- [240] J. Chadney, *Modelling the Upper Atmosphere of Gas-Giant Exoplanets Irradiated by Low-Mass Stars*, Springer Theses (Springer International Publishing, Cham, 2017).
- [241] B. Fleury, M. S. Gudipati, B. L. Henderson, and M. Swain, *Astrophys. J.* **871**, 158 (2019).
- [242] F. P. Mills, J. I. Moses, P. Gao, and S. M. Tsai, *Space Sci. Rev.* **217**, 43 (2021).
- [243] S. M. Tsai, E. K. Lee, D. Powell, P. Gao, X. Zhang, J. Moses, E. Hébrard, O. Venot, V. Parmentier, S. Jordan, R. Hu, M. K. Alam, L. Alderson, N. M. Batalha, J. L. Bean, B. Benneke, C. J. Bierson, R. P. Brady, L. Carone, A. L. Carter, K. L. Chubb, J. Inglis, J. Lecointe, M. Line, M. López-Morales, Y. Miguel, K. Molaverdikhani, Z. Rustamkulov, D. K. Sing, K. B. Stevenson, H. R. Wakeford, J. Yang, K. Aggarwal, R. Baeyens, S. Barat, M. de Val-Borro, T. Daylan, J. J. Fortney, K. France, J. M. Goyal, D. Grant, J. Kirk, L. Kreidberg, A. Louca, S. E. Moran, S. Mukherjee, E. Nasedkin, K. Ohno, B. V. Rackham, S. Redfield, J. Taylor, P. Tremblin, C. Visscher, N. L. Wallack, L. Welbanks, A. Youngblood, E. M. Ahrer, N. E. Batalha, P. Behr, Z. K. Berta-Thompson, J. Blečić, S. L. Casewell, I. J. Crossfield, N. Crouzet, P. E. Cubillos, L. Decin, J. M. Désert, A. D. Feinstein, N. P. Gibson, J. Harrington, K. Heng, T. Henning, E. M. Kempton, J. Krick, P. O. Lagage, M. Lendl, J. D. Lothringer, M. Mansfield, N. J. Mayne, T. Mikal-Evans, E. Palte, E. Schlawin, O. Shorttle, P. J. Wheatley, and S. N. Yurchenko, *Nature* **617**, 483 (2023).
- [244] T. J. Bell and N. B. Cowan, *Astrophys. J. Lett.* **857**, L20 (2018).

- [245] S. Seager, *Exoplanet Atmospheres: Physical Processes*, edited by D. N. Spergel (Princeton University Press, 2010).
- [246] C. M. Sharp and A. Burrows, *Astrophys. J. Suppl. Ser.* **168**, 140 (2007).
- [247] R. Freedman, M. Marley, and K. Lodders, *Astrophys. J. Suppl.* **174**, 504 (2008).
- [248] R. S. Freedman, J. Lustig-Yaeger, J. J. Fortney, R. E. Lupu, M. S. Marley, and K. Lodders, *Astrophys. J. Suppl. Ser.* **214**, 25 (2014).
- [249] K. Lodders, *Astrophys. J.* **519**, 793 (1999).
- [250] J. Blečić, J. Harrington, and M. O. Bowman, *Astrophys. J. Suppl. Ser.* **225**, 4 (2016).
- [251] J. J. Fortney, in *Astrophys. Exopl. Atmos.* (Springer International Publishing, 2018) pp. 51–88.
- [252] B. M. S. Hansen, *Astrophys. J. Suppl. Ser.* **179**, 484 (2008).
- [253] K. Heng, J. M. Mendonça, and J. M. Lee, *Astrophys. J. Suppl. Ser.* **215**, 4 (2014).
- [254] T. D. Robinson and D. C. Catling, *Astrophys. J.* **757**, 104 (2012).
- [255] V. Parmentier and T. Guillot, *Astron. Astrophys.* **562**, A133 (2014).
- [256] D. Valencia, T. Guillot, V. Parmentier, and R. S. Freedman, *Astrophys. J.* **775**, 10 (2013).
- [257] S. Jin, C. Mordasini, V. Parmentier, R. Van Boekel, T. Henning, and J. Ji, *Astrophys. J.* **795**, 65 (2014).
- [258] C. Dorn, N. R. Hinkel, and J. Venturini, *Astron. Astrophys.* **597**, 38 (2017).
- [259] C. P. McKay, J. B. Pollack, and R. Courtin, *Icarus* **80**, 23 (1989).
- [260] J. J. Fortney, M. S. Marley, K. Lodders, D. Saumon, and R. Freedman, *Astrophys. J.* **627**, L69 (2005).
- [261] J.-L. Baudino, B. Bézard, A. Boccaletti, M. Bonnefoy, A. M. Lagrange, and R. Galicher, *Astron. Astrophys.* **582**, A83 (2015).
- [262] J.-L. Baudino, P. Mollière, O. Venot, P. Tremblin, B. Bézard, and P.-O. Lagage, *Astrophys. J.* **850**, 150 (2017).
- [263] P. Mollière, R. Van Boekel, C. Dullemond, T. Henning, and C. Mordasini, *Astrophys. J.* **813**, 47 (2015).
- [264] B. Drummond, P. Tremblin, I. Baraffe, D. S. Amundsen, N. J. Mayne, O. Venot, and J. Goyal, *Astron. Astrophys.* **594**, A69 (2016).
- [265] M. Malik, L. Grosheintz, J. M. Mendonça, S. L. Grimm, B. Lavie, D. Kitzmann, S.-M. Tsai, A. Burrows, L. Kreidberg, M. Bedell, J. L. Bean, K. B. Stevenson, and K. Heng, *Astron. J.* **153**, 56 (2017).

- [266] I. Hubeny, *Mon. Not. R. Astron. Soc.* **469**, 841 (2017).
- [267] A. P. Showman, J. J. Fortney, Y. Lian, M. S. Marley, R. S. Freedman, H. A. Knutson, and D. Charbonneau, *Astrophys. J.* **699**, 564 (2009).
- [268] B. Drummond, N. J. Mayne, I. Baraffe, P. Tremblin, J. Manners, D. S. Amundsen, J. Goyal, and D. Acreman, *Astron. Astrophys.* **612**, A105 (2018).
- [269] K. Heng and A. P. Showman, *Annu. Rev. Earth Planet. Sci.* **43**, 509 (2015).
- [270] A. P. Showman, X. Tan, and V. Parmentier, *Space Sci. Rev.* **216**, A139 (2020).
- [271] S. M. Tsai, E. K. Lee, and R. Pierrehumbert, *Astron. Astrophys.* **664**, 1 (2022).
- [272] A. D. Schneider, L. Carone, L. Decin, U. G. Jørgensen, P. Mollière, R. Baeyens, S. Kiefer, and C. Helling, *Astron. Astrophys.* **664**, A56 (2022).
- [273] A. D. Schneider, L. Carone, L. Decin, U. G. Jørgensen, and C. Helling, *Astron. Astrophys.* **666**, L11 (2022).
- [274] T. D. Komacek, P. Gao, D. P. Thorngren, E. M. May, and X. Tan, *Astrophys. J. Lett.* **941**, L40 (2022).
- [275] R. T. Pierrehumbert, *Principles of Planetary Climate* (Cambridge University Press, Cambridge, 2010) p. 674.
- [276] S. Seager and D. Deming, *Annu. Rev. Astron. Astrophys.* **48**, 631 (2010).
- [277] M. S. Marley and T. D. Robinson, *Annu. Rev. Astron. Astrophys.* **53**, 279 (2015).
- [278] V. Bozza, L. Mancini, and A. Sozzetti, eds., *Astrophysics of Exoplanetary Atmospheres*, Astrophysics and Space Science Library, Vol. 450 (Springer International Publishing, Cham, 2018).
- [279] B. A. Wielicki, R. D. Cess, M. D. King, D. A. Randall, and E. F. Harrison, *Bull. - Am. Meteorol. Soc.* **76**, 2125 (1995).
- [280] C. Goldblatt, V. L. McDonald, and K. E. McCusker, *Nat. Geosci.* **14**, 143 (2021).
- [281] T. Schneider, J. Teixeira, C. S. Bretherton, F. Brient, K. G. Pressel, C. Schär, and A. P. Siebesma, *Nat. Clim. Chang.* **7**, 3 (2017).
- [282] J. Mülmenstädt, M. Salzmann, J. E. Kay, M. D. Zelinka, P. L. Ma, C. Nam, J. Kretzschmar, S. Hörnig, and J. Quaas, *Nat. Clim. Chang.* **11**, 508 (2021).
- [283] G. L. Stephens, *Nat. Clim. Chang.* **11**, 468 (2021).
- [284] F. Montmessin and A. Määttänen, in *Handbook of Exoplanets* (Springer, Cham (Switzerland), 2018) pp. 235–263.
- [285] R. A. West, in *Handbook of Exoplanets* (Springer, Cham, 2017) pp. 265—283.
- [286] C. Palotai, S. Brueshaber, R. Sankar, and K. Sayanagi, *Remote Sens.* **15**, 41 (2023).

- [287] R. M. Ramirez and J. F. Kasting, *Icarus* **281**, 248 (2017).
- [288] X. Zhang, D. F. Strobel, and H. Imanaka, *Nature* **551**, 352 (2017).
- [289] R. A. West, *Nature* **551**, 302 (2017).
- [290] K. Ohno, X. Zhang, R. Tazaki, and S. Okuzumi, *Astrophys. J.* **912**, 37 (2021).
- [291] K. Rages and J. B. Pollack, *Icarus* **55**, 50 (1983).
- [292] S. M. Hörst, *J. Geophys. Res. Planets* **122**, 432 (2017).
- [293] A. Guzmán-Mesa, D. Kitzmann, C. Fisher, A. J. Burgasser, H. J. Hoeijmakers, P. Márquez-Neila, S. L. Grimm, A. M. Mandell, R. Sznitman, and K. Heng, *Astron. J.* **160**, 15 (2020).
- [294] S. Hörst, *Planet. Soc.* (2016).
- [295] C. Marois, B. Macintosh, T. Barman, B. Zuckerman, I. Song, J. Patience, D. Lafrenière, and R. Doyon, *Science* **322**, 1348 (2008).
- [296] B. O. Demory, J. De Wit, N. Lewis, J. Fortney, A. Zsom, S. Seager, H. Knutson, K. Heng, N. Madhusudhan, M. Gillon, T. Barclay, J. M. Desert, V. Parmentier, and N. B. Cowan, *Astrophys. J. Lett.* **776**, L25 (2013).
- [297] M. Oreshenko, K. Heng, and B. O. Demory, *Mon. Not. R. Astron. Soc.* **457**, 3420 (2016).
- [298] N. Nikolov, G. Maciejewski, S. Constantinou, N. Madhusudhan, J. J. Fortney, B. Smalley, A. L. Carter, E. J. W. de Mooij, B. Drummond, N. P. Gibson, C. Helling, N. Mayne, T. Mikal-Evans, D. K. Sing, and J. Wilson, *Astron. J.* **162**, 88 (2021).
- [299] Y. Chachan, H. A. Knutson, P. Gao, T. Kataria, I. Wong, G. W. Henry, B. Benneke, M. Zhang, J. Barstow, J. L. Bean, T. Mikal-Evans, N. K. Lewis, M. Mansfield, M. López-Morales, N. Nikolov, D. K. Sing, and H. Wakeford, *Astron. J.* **158**, 244 (2019).
- [300] D. Charbonneau, T. M. Brown, R. W. Noyes, and R. L. Gilliland, *Astrophys. J.* **568**, 377 (2002).
- [301] E. M.-R. Kempton, J. L. Bean, and V. Parmentier, *Astrophys. J.* **845**, L20 (2017).
- [302] C. He, S. M. Hörst, N. K. Lewis, X. Yu, J. I. Moses, E. M.-R. Kempton, M. S. Marley, P. McQuiggan, C. V. Morley, J. A. Valenti, and V. Vuitton, *Astron. J.* **156**, 38 (2018).
- [303] C. He, S. M. Hörst, N. K. Lewis, X. Yu, J. I. Moses, E. M.-R. Kempton, P. McQuiggan, C. V. Morley, J. A. Valenti, and V. Vuitton, *Astrophys. J. Lett.* **856**, L3 (2018).
- [304] C. He, S. M. Hörst, N. K. Lewis, J. I. Moses, E. M. Kempton, M. S. Marley, C. V. Morley, J. A. Valenti, and V. Vuitton, *ACS Earth Sp. Chem.* **3**, 39 (2019).
- [305] C. He, M. Radke, S. E. Moran, S. M. Hörst, N. K. Lewis, J. I. Moses, M. S. Marley, N. E. Batalha, E. M. Kempton, C. V. Morley, J. A. Valenti, and V. Vuitton, *Nat. Astron.* **8**, 182 (2024).

- [306] S. M. Hörst, C. He, N. K. Lewis, E. M.-R. Kempton, M. S. Marley, C. V. Morley, J. I. Moses, J. A. Valenti, and V. Vuitton, *Nat. Astron.* **2**, 303 (2018).
- [307] S. E. Moran, S. M. Hörst, V. Vuitton, C. He, N. K. Lewis, L. Flandinet, J. I. Moses, N. North, F. R. Orthous-Daunay, J. Sebree, C. Wolters, E. M. Kempton, M. S. Marley, C. V. Morley, and J. A. Valenti, *Planet. Sci. J.* **1**, 17 (2020).
- [308] S. E. Moran, S. M. Hörst, C. He, M. J. Radke, J. A. Sebree, N. R. Izenberg, V. Vuitton, L. Flandinet, F. R. Orthous-Daunay, and C. Wolters, *J. Geophys. Res. Planets* **127**, e2021JE006984 (2022).
- [309] B. Charnay, B. Bézard, J.-L. Baudino, M. Bonnefoy, A. Boccaletti, and R. Galicher, *Astrophys. J.* **854**, 172 (2018).
- [310] C. Helling, A. Ackerman, F. Allard, M. Dehn, P. Hauschildt, D. Homeier, K. Lodders, M. Marley, F. Rietmeijer, T. Tsuji, and P. Woitke, *Mon. Not. R. Astron. Soc.* **391**, 1854 (2008).
- [311] F. Allard, D. Homeier, B. Freytag, and C. M. Sharp, *EAS Publ. Ser.* **57**, 3 (2012).
- [312] F. Allard, D. Homeier, and B. Freytag, *Philos. Trans. R. Soc. A Math. Phys. Eng. Sci.* **370**, 2765 (2012).
- [313] F. Allard, in *Proc. Int. Astron. Union*, Vol. 8 (2013) pp. 271–272.
- [314] P. Gao, M. S. Marley, and A. S. Ackerman, *Astrophys. J.* **855**, 86 (2018).
- [315] A. Ackerman and M. Marley, *Astrophys. J.* **556**, 872 (2001).
- [316] T. Tsuji, *Astrophys. J.* **575**, 264 (2002).
- [317] M. S. Marley, A. S. Ackerman, J. N. Cuzzi, and D. Kitzmann, in *Sp. Sci. Ser.* (The University of Arizona Press, 2013).
- [318] D. Kitzmann, A. B. Patzer, P. Von Paris, M. Godolt, and H. Rauer, *Astron. Astrophys.* **534**, A63 (2011).
- [319] M. W. Webber, N. K. Lewis, M. Marley, C. Morley, J. J. Fortney, and K. Cahoy, *Astrophys. J.* **804**, 1 (2015).
- [320] F. Wang, Y. Fujii, and J. He, *Astrophys. J.* **931**, 48 (2022).
- [321] K. Heng, W. Hayek, F. Pont, and D. Sing, *Mon. Not. R. Astron. Soc.* **420**, 20 (2012).
- [322] L. Fossati, C. A. Haswell, C. S. Froning, L. Hebb, S. Holmes, U. Kolb, C. Helling, A. Carter, P. Wheatley, A. C. Cameron, B. Loeillet, D. Pollacco, R. Street, H. C. Stempels, E. Simpson, S. Udry, Y. C. Joshi, R. G. West, I. Skillen, and D. Wilson, *Astrophys. J. Lett.* **714**, L222 (2010).
- [323] N. Casasayas-Barris, E. Pallé, F. Yan, G. Chen, S. Kohl, M. Stangret, H. Parviainen, C. Helling, N. Watanabe, S. Czesla, A. Fukui, P. Montañés-Rodríguez, E. Nagel,

- N. Narita, L. Nortmann, G. Nowak, J. H. M. M. Schmitt, and M. R. Zapatero Osorio, *Astron. Astrophys.* **628**, A9 (2019).
- [324] C. Helling, M. Worters, D. Samra, K. Molaverdikhani, and N. Iro, *Astron. Astrophys.* **648**, A80 (2021).
- [325] C. Helling, in *J. Phys. Conf. Ser.*, Vol. 1322 (2019) p. 012028.
- [326] C. Helling and P. B. Rimmer, *Philos. Trans. R. Soc. A Math. Phys. Eng. Sci.* **377**, 20180398 (2019).
- [327] C. Helling, M. Jardine, D. Diver, and S. Witte, *Planet. Space Sci.* **77**, 152 (2013).
- [328] R. Perna, K. Menou, and E. Rauscher, *Astrophys. J.* **724**, 313 (2010).
- [329] S. J. Benavides, K. J. Burns, B. Gallet, and G. R. Flierl, *Astrophys. J.* **938**, 92 (2022).
- [330] N. Nettelmann, *Matter under extreme conditions: modelling giant planets*, Ph.D. thesis, University of Rostock (2009).
- [331] N. Nettelmann, B. Holst, A. Kietzmann, M. French, R. Redmer, and D. Blaschke, *Astrophys. J.* **683**, 1217 (2008).
- [332] N. Nettelmann, R. Redmer, and D. Blaschke, *Phys. Part. Nucl.* **39**, 1122 (2008).
- [333] N. Nettelmann, *Astrophys. Space Sci.* **336**, 47 (2011).
- [334] N. Nettelmann, A. Becker, B. Holst, and R. Redmer, *Astrophys. J.* **750**, 52 (2012).
- [335] N. Nettelmann, R. Püstow, and R. Redmer, *Icarus* **225**, 548 (2013).
- [336] N. Nettelmann, R. Helled, J. J. Fortney, and R. Redmer, *Planet. Space Sci.* **77**, 143 (2013).
- [337] A. Becker, W. Lorenzen, J. J. Fortney, N. Nettelmann, R. Redmer, and M. Schöttler, *Astrophys. J. Suppl. Ser.* **215**, 21 (2014).
- [338] N. Nettelmann, *Contrib. to Plasma Phys.* **55**, 116 (2015).
- [339] R. Püstow, N. Nettelmann, W. Lorenzen, and R. Redmer, *Icarus* **267**, 323 (2016).
- [340] N. Nettelmann, *Astron. Astrophys.* **606**, A139 (2017).
- [341] N. Nettelmann, N. Movshovitz, D. Ni, J. J. Fortney, E. Galanti, Y. Kaspi, R. Helled, C. R. Mankovich, and S. Bolton, *Planet. Sci. J.* **2**, 241 (2021).
- [342] N. Nettelmann, U. Kramm, R. Redmer, and R. Neuhäuser, *Astron. Astrophys.* **523**, A26 (2010).
- [343] N. Nettelmann, J. J. Fortney, U. Kramm, and R. Redmer, *Astrophys. J.* **733**, 2 (2011).
- [344] W. B. Hubbard, *Astrophys. J.* **155**, 333 (1969).
- [345] C. Guervilly, *J. Geophys. Res. Planets* **127**, e2022JE007350 (2022).

- [346] M. Salaris and S. Cassisi, *R. Soc. Open Sci.* **4**, 170192 (2017).
- [347] E. H. Anders, A. S. Jermyn, D. Lecoanet, A. E. Fraser, I. G. Cresswell, M. Joyce, and J. R. Fuentes, *Astrophys. J. Lett.* **928**, L10 (2022).
- [348] L. Scheibe, *Thermal Evolution Models for Uranus and Neptune*, Ph.D. thesis, University of Rostock, Germany (2021).
- [349] A. Vazan, R. Helled, A. Kovetz, and M. Podolak, *Astrophys. J.* **803**, 32 (2015).
- [350] G. Chabrier and I. Baraffe, *Astrophys. J.* **661**, L81 (2007).
- [351] N. Miller and J. J. Fortney, *Astrophys. J. Lett.* **736**, L29 (2011).
- [352] S. Müller, M. Ben-Yami, and R. Helled, *Astrophys. J.* **903**, 147 (2020).
- [353] D. Sudarsky, A. Burrows, and I. Hubeny, *Astrophys. J.* **588**, 1121 (2003).
- [354] D. Thorngren, P. Gao, and J. J. Fortney, *Astrophys. J. Lett.* **884**, L6 (2019).
- [355] J. M. McMahon, M. A. Morales, C. Pierleoni, and D. M. Ceperley, *Rev. Mod. Phys.* **84**, 1607 (2012).
- [356] D. Saumon, G. Chabrier, and H. M. van Horn, *Astrophys. J. Suppl. Ser.* **99**, 713 (1995).
- [357] G. Chabrier and F. Debras, *Astrophys. J.* **917**, 4 (2021).
- [358] G. Chabrier, S. Mazevet, and F. Soubiran, *Astrophys. J.* **872**, 51 (2019).
- [359] B. Militzer and W. B. Hubbard, *Astrophys. J.* **774**, 148 (2013).
- [360] G. Chabrier and A. Y. Potekhin, *Phys. Rev. E* **58**, 4941 (1998).
- [361] M. D. Knudson and M. P. Desjarlais, *Phys. Rev. Lett.* **118**, 035501 (2017).
- [362] G. Chabrier, I. Baraffe, M. Phillips, and F. Debras, *Astron. Astrophys.* **671**, A119 (2023).
- [363] B. Holst, N. Nettelmann, and R. Redmer, in *Contrib. to Plasma Phys.* (2007).
- [364] Y. Miguel, T. Guillot, and L. Fayon, *Astron. Astrophys.* **596**, A114 (2016).
- [365] S. Mazevet, A. Licari, and F. Soubiran, *Astron. Astrophys.* **664**, 9 (2022).
- [366] W. B. Hubbard and M. S. Marley, *Icarus* **78**, 102 (1989).
- [367] W. B. Hubbard, *Icarus* **30**, 305 (1977).
- [368] I. Baraffe, G. Chabrier, T. S. Barman, F. Allard, and P. H. Hauschildt, *Astron. Astrophys.* **402**, 701 (2003).
- [369] T. Guillot, *The interiors of giant planets: Models and outstanding questions* (2005).
- [370] I. Baraffe, G. Chabrier, and T. Barman, *Astron. Astrophys.* **482**, 315 (2008).
- [371] K. J. Zahnle and D. C. Catling, *Astrophys. J.* **843**, 122 (2017).

- [372] K. Kurosaki, M. Ikoma, and Y. Hori, *Astron. Astrophys.* **562**, A80 (2014).
- [373] J. M. Chadney, M. Galand, Y. C. Unruh, T. T. Koskinen, and J. Sanz-Forcada, *Icarus* **250**, 357 (2014).
- [374] T. D. Komacek, D. P. Thorngren, E. D. Lopez, and S. Ginzburg, *Astrophys. J.* **893**, 36 (2020).
- [375] M. Mol Lous and Y. Miguel, *Mon. Not. R. Astron. Soc.* **495**, 2994 (2020).
- [376] S. Müller and R. Helled, *Mon. Not. R. Astron. Soc.* **507**, 2094 (2021).
- [377] A. Vazan, C. W. Ormel, L. Noack, and C. Dominik, *Astrophys. J.* **869**, 163 (2018).
- [378] A. Vazan, C. W. Ormel, and C. Dominik, *Astron. Astrophys.* **610**, L1 (2018).
- [379] G. I. Ogilvie, *Annu. Rev. Astron. Astrophys.* **52**, 171 (2014).
- [380] J. Fuller, T. Guillot, S. Mathis, and C. Murray, *Space Sci. Rev.* **220**, A22 (2024).
- [381] T. D. Komacek and A. N. Youdin, *Astrophys. J.* **844**, 94 (2017).
- [382] W. E. Meador and W. R. Weaver, *J. Atmos. Sci.* **37**, 630 (1980).
- [383] C. P. Dullemond, *Lecture Notes: Radiative Transfer in Astrophysics*, Tech. Rep. (Zentrum für Astronomie, Heidelberg, 2013).
- [384] M. Abramowitz and I. Stegun, *Handbook of Mathematical Functions* (Dover Publications, 1964).
- [385] G. B. Arfken and H. J. Weber, *Mathematical Methods for Physicists*, 4th ed. (Academic Press, San Diego, 1995).
- [386] A. J. Poser, Der Einfluss von Wolken in der Berechnung der Struktureigenschaften großer Exoplaneten (MSc thesis) (2018).
- [387] V. Parmentier, T. Guillot, J. J. Fortney, and M. S. Marley, *Astron. Astrophys.* **574**, A35 (2015).
- [388] E. A. Milne, *Mon. Not. R. Astron. Soc.* **81**, 510 (1921).
- [389] J. S. Lewis, *Icarus* **10**, 365 (1969).
- [390] S. Lines, N. J. Mayne, I. A. Boutle, J. Manners, G. K. Lee, C. Helling, B. Drummond, D. S. Amundsen, J. Goyal, D. M. Acreman, P. Tremblin, and M. Kerslake, *Astron. Astrophys.* **615**, A97 (2018).
- [391] M. S. Marley, in *From Giant Planets to Cool Stars*, Vol. 212, edited by C. A. Griffith and M. S. Marley (ASP Conference Series, San Francisco, 2000) p. 152.
- [392] I. Dobbs-Dixon and E. Agol, *Mon. Not. R. Astron. Soc.* **435**, 3159 (2013).

- [393] G. K. Lee, K. Wood, I. Dobbs-Dixon, A. Rice, and C. Helling, *Astron. Astrophys.* **601**, A22 (2017).
- [394] A. J. Poser, N. Nettelmann, and R. Redmer, *Atmosphere* **10**, 664 (2019).
- [395] A. J. Poser and R. Redmer, *Mon. Not. R. Astron. Soc.* **529**, 2242 (2024).
- [396] S. Kumar, A. J. Poser, M. Schöttler, U. Kleinschmidt, W. Dietrich, J. Wicht, M. French, and R. Redmer, *Phys. Rev. E* **103**, 063203 (2021).
- [397] W. Dietrich, S. Kumar, A. J. Poser, M. French, N. Nettelmann, R. Redmer, and J. Wicht, *Mon. Not. R. Astron. Soc.* **517**, 3113 (2022).
- [398] J. J. Fortney, D. Saumon, M. S. Marley, K. Lodders, and R. S. Freedman, *Astrophys. J.* **642**, 495 (2006).
- [399] M. Ikoma, T. Guillot, H. Genda, T. Tanigawa, and S. Ida, *Astrophys. J.* **650**, 1150 (2006).
- [400] S. Shibata, R. Helled, and M. Ikoma, *Astron. Astrophys.* **633**, A33 (2020).
- [401] E. Nasedkin, P. Mollière, S. Lacour, M. Nowak, L. Kreidberg, T. Stolker, J. J. Wang, W. O. Balmer, J. Kammerer, J. Shangguan, R. Abuter, A. Amorim, R. Asensio-Torres, M. Benisty, J. P. Berger, H. Beust, S. Blunt, A. Boccaletti, M. Bonnefoy, H. Bonnet, M. S. Bordini, G. Bourdarot, W. Brandner, F. Cantalloube, P. Caselli, B. Charnay, G. Chauvin, A. Chavez, E. Choquet, V. Christiaens, Y. Clénet, V. C. du Foresto, A. Cridland, R. Davies, R. Dembet, J. Dexter, A. Drescher, G. Duvert, A. Eckart, F. Eisenhauer, N. M. F. Schreiber, P. Garcia, R. G. Lopez, E. Gendron, R. Genzel, S. Gillessen, J. H. Girard, S. Grant, X. Haubois, G. Heißel, T. Henning, S. Hinkley, S. Hippler, M. Houllé, Z. Hubert, L. Jocou, M. Keppler, P. Kervella, N. T. Kurtovic, A. M. Lagrange, V. Lapeyrère, J. B. L. Bouquin, D. Lutz, A. L. Maire, F. Mang, G. D. Marleau, A. Mérand, J. D. Monnier, C. Mordasini, T. Ott, G. P. P. L. Otten, C. Paladini, T. Paumard, K. Perraut, G. Perrin, O. Pfuhl, N. Pourré, L. Pueyo, D. C. Ribeiro, E. Rickman, J. B. Ruffio, Z. Rustankulov, T. Shimizu, D. Sing, J. Stadler, O. Straub, C. Straubmeier, E. Sturm, L. J. Tacconi, E. F. van Dishoeck, A. Vigan, F. Vincent, S. D. von Fellenberg, F. Widmann, T. O. Winterhalder, J. Woillez, S. Yazici, and t. G. Collaboration, *AA* **687**, A298 (2024).
- [402] J. J. Fortney, C. Mordasini, N. Nettelmann, E. M. Kempton, T. P. Greene, and K. Zahnle, *Astrophys. J.* **775**, 80 (2013).
- [403] J. Venturini, Y. Alibert, and W. Benz, *Astron. Astrophys.* **596**, A90 (2016).
- [404] K. I. Öberg, R. Murray-Clay, and E. A. Bergin, *Astrophys. J. Lett.* **743**, L16 (2011).
- [405] P. Mollière, T. Molyarova, B. Bitsch, T. Henning, A. Schneider, L. Kreidberg, C. Eistrup, R. Burn, E. Nasedkin, D. Semenov, C. Mordasini, M. Schlecker, K. R. Schwarz, S. Lacour, M. Nowak, and M. Schulik, *Astrophys. J.* **934**, 74 (2022).

- [406] T. O. Hands and R. Helled, *Mon. Not. R. Astron. Soc.* **509**, 894 (2022).
- [407] L. Welbanks, N. Madhusudhan, N. F. Allard, I. Hubeny, F. Spiegelman, and T. Leininger, *Astrophys. J. Lett.* **887**, L20 (2019).
- [408] T. Guillot, N. C. Santos, F. Pont, N. Iro, C. Melo, and I. Ribas, *Astron. Astrophys.* **453**, L21 (2006).
- [409] N. Nettelmann, *Nat. Astron.* **5**, 744 (2021).
- [410] D. A. Fischer and J. Valenti, *Astrophys. J.* **622**, 1102 (2005).
- [411] P. Bodenheimer and J. B. Pollack, *Icarus* **67**, 391 (1986).
- [412] K. Lodders, H. Palme, and H.-P. Gail, in *Landolt-Börnstein, New Ser. Astron. Astrophys.*, Vol. VI/4, edited by J.E. Trümper (ed.) (Springer-Verlag, Berlin, Heidelberg, New York, 2009) Chap. 4.4, pp. 560–630.
- [413] M. Lambrechts, A. Johansen, and A. Morbidelli, *Astron. Astrophys.* **572**, A35 (2014).
- [414] B. Bitsch, A. Izidoro, A. Johansen, S. N. Raymond, A. Morbidelli, M. Lambrechts, and S. A. Jacobson, *Astron. Astrophys.* **623**, A88 (2019).
- [415] S. Shibata and M. Ikoma, *Mon. Not. R. Astron. Soc.* **487**, 4510 (2019).
- [416] T. Guillot, *Nature* **572**, 315 (2019).
- [417] S. Ginzburg and E. Chiang, *Mon. Not. R. Astron. Soc.* **498**, 680 (2020).
- [418] J. Inglis, N. L. Wallack, J. W. Xuan, H. A. Knutson, Y. Chachan, M. L. Bryan, B. P. Bowler, A. Iyer, T. Kataria, and B. Benneke, *Astron. J.* **167**, 218 (2024).
- [419] J. L. Bean, Q. Xue, P. C. August, J. Lunine, M. Zhang, D. Thorngren, S. M. Tsai, K. G. Stassun, E. Schlawin, E. M. Ahrer, J. Ih, and M. Mansfield, *Nature* **618**, 43 (2023).
- [420] L. Finnerty, J. W. Xuan, Y. Xin, J. Liberman, T. Schofield, M. P. Fitzgerald, S. Agrawal, A. Baker, R. Bartos, G. A. Blake, B. Calvin, S. Cetre, J.-R. Delorme, G. Doppmann, D. Echeverri, C.-C. Hsu, N. Jovanovic, R. A. López, E. C. Martin, D. Mawet, E. Morris, J. Pezzato, J.-B. Ruffio, B. Sappéy, A. Skemer, T. Venenciano, J. K. Wallace, N. L. Wallack, J. J. Wang, and J. Wang, *Astron. J.* **167**, 43 (2024).
- [421] Q. Sun, S. X. Wang, L. Welbanks, J. Teske, and J. Buchner, *Astron. J.* **167**, 167 (2024).
- [422] L. A. Sromovsky, K. H. Baines, and P. M. Fry, *Icarus* **362**, 114409 (2021).
- [423] L. N. Fletcher, K. H. Baines, T. W. Momary, A. P. Showman, P. G. Irwin, G. S. Orton, M. Roos-Serote, and C. Merlet, *Icarus* **214**, 510 (2011).
- [424] M. H. Wong, P. R. Mahaffy, S. K. Atreya, H. B. Niemann, and T. C. Owen, *Icarus* **171**, 153 (2004).
- [425] E. Karkoschka and M. G. Tomasko, *Icarus* **211**, 780 (2011).

- [426] H. R. Wakeford and P. A. Dalba, *Philos. Trans. R. Soc. A Math. Phys. Eng. Sci.* **378**, 20200054 (2020).
- [427] K. Heng, *Res. Notes AAS* **2**, 128 (2018).
- [428] T. Guillot, L. N. Fletcher, R. Helled, M. Ikoma, M. R. Line, and V. Parmentier, in *Protostars Planets VII* (Astronomical Society of the Pacific, 2023).
- [429] P. Ledoux, *Astrophys. J.* **105**, 305 (1947).
- [430] A. Vazan, R. Helled, M. Podolak, and A. Kovetz, *Astrophys. J.* **829**, 118 (2016).
- [431] S. Müller, R. Helled, and A. Cumming, *Astron. Astrophys.* **638**, A121 (2020).
- [432] H. F. Wilson and B. Militzer, *Phys. Rev. Lett.* **104**, 121101 (2010).
- [433] H. B. Niemann, S. K. Atreya, G. R. Carignan, T. M. Donahue, J. A. Haberman, D. N. Harpold, R. E. Hartle, D. M. Hunten, W. T. Kasprzak, P. R. Mahaffy, T. C. Owen, N. W. Spencer, S. H. Way, H. B. Niemann, J. A. Haberman, D. N. Harpold, R. E. Hartle, W. T. Kasprzak, P. R. Mahaffy, S. H. Way, S. K. Atreya, G. R. Cangnan, T. M. Donahue, D. M. Hunten, and T. C. Owen, *Science* **272**, 846 (1996).
- [434] V. Bourrier and A. Lecavelier des Etangs, in *Handbook of Exoplanets*, edited by J. Deeg, H., Belmonte (Springer, Cham (Switzerland), 2018) pp. 1509—1526.
- [435] D. Turrini, R. P. Nelson, and M. Barbieri, *Exp. Astron.* **40**, 501 (2015).
- [436] F. Faedi, S. C. Barros, D. R. Anderson, D. J. Brown, A. Collier Cameron, D. Pollacco, I. Boisse, G. Hébrard, M. Lendl, T. A. Lister, B. Smalley, R. A. Street, A. H. Triaud, J. Bento, F. Bouchy, O. W. Butters, B. Enoch, C. A. Haswell, C. Hellier, F. P. Keenan, G. R. Miller, V. Moulds, C. Moutou, A. J. Norton, D. Queloz, A. Santerne, E. K. Simpson, I. Skillen, A. M. Smith, S. Udry, C. A. Watson, R. G. West, and P. J. Wheatley, *Astron. Astrophys.* **531**, A40 (2011).
- [437] J. A. Kammer, H. A. Knutson, M. R. Line, J. J. Fortney, D. Deming, A. Burrows, N. B. Cowan, A. H. Triaud, E. Agol, J. M. Desert, B. J. Fulton, A. W. Howard, G. P. Laughlin, N. K. Lewis, C. V. Morley, J. I. Moses, A. P. Showman, and K. O. Todorov, *Astrophys. J.* **810**, 118 (2015).
- [438] P. D. Fischer, H. A. Knutson, D. K. Sing, G. W. Henry, M. W. Williamson, J. J. Fortney, A. S. Burrows, T. Kataria, N. Nikolov, A. P. Showman, G. E. Ballester, J.-M. Désert, S. Aigrain, D. Deming, A. L. des Etangs, and A. Vidal-Madjar, *Astrophys. J.* **827**, 19 (2016).
- [439] N. Nikolov, D. K. Sing, N. P. Gibson, J. J. Fortney, T. M. Evans, J. K. Barstow, T. Kataria, and P. A. Wilson, *Astrophys. J.* **832**, 191 (2016).
- [440] J. Kirk, M. López-Morales, P. J. Wheatley, I. C. Weaver, I. Skillen, T. Louden, J. McCormac, and N. Espinoza, *Astron. J.* **158**, 144 (2019).

- [441] D. Powell, A. D. Feinstein, E. K. H. Lee, M. Zhang, S.-M. Tsai, J. Taylor, J. Kirk, T. Bell, J. K. Barstow, P. Gao, J. L. Bean, J. Blecic, K. L. Chubb, I. J. M. Crossfield, S. Jordan, D. Kitzmann, S. E. Moran, G. Morello, J. I. Moses, L. Welbanks, J. Yang, X. Zhang, E.-M. Ahrer, A. Bello-Arufe, J. Brande, S. L. Casewell, N. Crouzet, P. E. Cubillos, B.-O. Demory, A. Dyrek, L. Flagg, R. Hu, J. Inglis, K. D. Jones, L. Kreidberg, M. López-Morales, P.-O. Lagage, E. A. Meier Valdés, Y. Miguel, V. Parmentier, A. A. A. Piette, B. V. Rackham, M. Radica, S. Redfield, K. B. Stevenson, H. R. Wakeford, K. Aggarwal, M. K. Alam, N. M. Batalha, N. E. Batalha, B. Benneke, Z. K. Berta-Thompson, R. P. Brady, C. Caceres, A. L. Carter, J.-M. Désert, J. Harrington, N. Iro, M. R. Line, J. D. Lothringer, R. J. MacDonald, L. Mancini, K. Molaverdikhani, S. Mukherjee, M. C. Nixon, A. V. Oza, E. Palle, Z. Rustamkulov, D. K. Sing, M. E. Steinrueck, O. Venot, P. J. Wheatley, and S. N. Yurchenko, *Nature* **626**, 979 (2024).
- [442] L. Carone, D. A. Lewis, D. Samra, A. D. Schneider, and C. Helling, *preprint* (2023), [arXiv:2301.08492](https://arxiv.org/abs/2301.08492) .
- [443] J. A. Johnson, J. N. Winn, N. E. Cabrera, and J. A. Carter, *Astrophys. J.* **692**, L100 (2009).
- [444] D. J. Christian, N. P. Gibson, E. K. Simpson, R. A. Street, I. Skillen, D. Pollacco, A. C. Cameron, Y. C. Joshi, F. P. Keenan, H. C. Stempels, C. A. Haswell, K. Horne, D. R. Anderson, S. Bentley, F. Bouchy, W. I. Clarkson, B. Enoch, L. Hebb, G. Hébrard, C. Hellier, J. Irwin, S. R. Kane, T. A. Lister, B. Loeillet, P. Maxted, M. Mayor, I. McDonald, C. Moutou, A. J. Norton, N. Parley, F. Pont, D. Queloz, R. Ryans, B. Smalley, A. M. S. Smith, I. Todd, S. Udry, R. G. West, P. J. Wheatley, and D. M. Wilson, *Mon. Not. R. Astron. Soc* **392**, 1585 (2009).
- [445] G. Maciejewski, D. Dimitrov, R. Neuhäuser, N. Tetzlaff, A. Niedzielski, St. Raetz, W. P. Chen, F. Walter, C. Marka, S. Baar, T. Krejcová, J. Budaj, V. Krushevska, K. Tachihara, H. Takahashi, and M. Mugrauer, *Mon. Not. R. Astron. Soc.* **411**, 1204 (2011).
- [446] P. Mollière, R. Van Boekel, J. Bouwman, T. Henning, P. O. Lagage, and M. Min, *Astron. Astrophys.* **600**, A10 (2017).
- [447] K. Kurosaki and M. Ikoma, *Astron. J.* **153**, 260 (2017).
- [448] A. Vazan, A. Kovetz, M. Podolak, and R. Helled, *Mon. Not. R. Astron. Soc.* **434**, 3283 (2013).
- [449] C. Mordasini, H. Klahr, Y. Alibert, N. Miller, and T. Henning, *Astron. Astrophys.* **566**, A141 (2014).
- [450] E. F. Linder, C. Mordasini, P. Mollière, G. D. Marleau, M. Malik, S. P. Quanz, and M. R. Meyer, *Astron. Astrophys.* **623**, A85 (2019).
- [451] J. Šubjak, M. Endl, P. Chaturvedi, R. Karjalainen, W. D. Cochran, M. Esposito, D. Gandolfi, K. W. Lam, K. Stassun, J. Žák, N. Lodieu, H. M. Boffin, P. J. Macqueen, A. Hatzes, E. W. Guenther, I. Georgieva, S. Grziwa, H. Schmerling, M. Skarka, M. Blažek, M. Kar-

- jalainen, M. Špoková, H. Isaacson, A. W. Howard, C. J. Burke, V. Van Eylen, B. Falk, M. Fridlund, E. Goffo, J. M. Jenkins, J. Korth, J. J. Lissauer, J. H. Livingston, R. Luque, A. Muresan, H. P. Osborn, E. Pallé, C. M. Persson, S. Redfield, G. R. Ricker, S. Seager, L. M. Serrano, A. M. Smith, and P. Kabáth, *Astron. Astrophys.* **662**, A107 (2022).
- [452] T. Guillot, *Science* **269**, 1697 (1995).
- [453] J. Leconte, F. Selsis, F. Hersant, and T. Guillot, *Astron. Astrophys.* **598**, A98 (2017).
- [454] S. Behnel, R. Bradshaw, C. Citro, L. Dalcin, D. Seljebotn, and K. Smith, *Comput. Sci. Eng.* **13**, 31 (2011).
- [455] R. Bradshaw, S. Behnel, D. S. Seljebotn, G. Ewing, and E. Al., *The Cython compiler* (2024).
- [456] M. A. Jette and T. Wickberg, *Job Sched. Strateg. Parallel Process. JSSPP 2023. Lect. Notes Comput. Sci.*, edited by D. Klusáček, J. Corbalán, and G. Rodrigo, Vol. 14283 (Springer, Cham (Switzerland), 2023) pp. 3–23.
- [457] S. Müller and R. Helled, *Astron. Astrophys.* **669**, A24 (2023).
- [458] C. A. Beichman and T. P. Greene, in *Handbook of Exoplanets*, edited by H. J. Deeg and J. A. Belmonte (Springer International Publishing, Cham (Switzerland), 2018) pp. 1283–1308.
- [459] G. R. Ricker, J. N. Winn, R. Vanderspek, D. W. Latham, G. Á. Bakos, J. L. Bean, Z. K. Berta-Thompson, T. M. Brown, L. Buchhave, N. R. Butler, R. P. Butler, W. J. Chaplin, D. Charbonneau, J. Christensen-Dalsgaard, M. Clampin, D. Deming, J. Doty, N. De Lee, C. Dressing, E. W. Dunham, M. Endl, F. Fressin, J. Ge, T. Henning, M. J. Holman, A. W. Howard, S. Ida, J. M. Jenkins, G. Jernigan, J. A. Johnson, L. Kaltenegger, N. Kawai, H. Kjeldsen, G. Laughlin, A. M. Levine, D. Lin, J. J. Lissauer, P. MacQueen, G. Marcy, P. R. McCullough, T. D. Morton, N. Narita, M. Paegert, E. Palle, F. Pepe, J. Pepper, A. Quirrenbach, S. A. Rinehart, D. Sasselov, B. Sato, S. Seager, A. Sozzetti, K. G. Stassun, P. Sullivan, A. Szentgyorgyi, G. Torres, S. Udry, and J. Villaseñor, *J. Astron. Telesc. Instrum. Syst.* **1**, 014003 (2014).
- [460] D. Charbonneau, T. M. Brown, D. W. Latham, and M. Mayor, *Astrophys. J.* **529**, L45 (2000).
- [461] G. W. Henry, G. W. Marcy, R. Paul Butler, and S. S. Vogt, *Astrophys. J.* **529**, 41 (2000).
- [462] T. M. Brown, D. Charbonneau, R. L. Gilliland, R. W. Noyes, and A. Burrows, *Astrophys. J.* **552**, 699 (2001).
- [463] P. Bodenheimer, D. N. C. Lin, and R. A. Mardling, *Astrophys. J.* **548**, 466 (2001).
- [464] G. Chabrier, T. Barman, I. Baraffe, F. Allard, and P. H. Hauschildt, *Astrophys. J.* **603**, L53 (2004).

- [465] L. M. Weiss, G. W. Marcy, J. F. Rowe, A. W. Howard, H. Isaacson, J. J. Fortney, N. Miller, B. O. Demory, D. A. Fischer, E. R. Adams, A. K. Dupree, S. B. Howell, R. Kolbl, J. A. Johnson, E. P. Horch, M. E. Everett, D. C. Fabrycky, and S. Seager, *Astrophys. J.* **768**, 14 (2013).
- [466] G. Laughlin, M. Crismani, and F. C. Adams, *Astrophys. J. Lett.* **729**, L7 (2011).
- [467] B. Enoch, A. Collier Cameron, and K. Horne, *Astron. Astrophys.* **540**, A99 (2012).
- [468] B.-O. Demory, S. Seager, N. Madhusudhan, H. Kjeldsen, J. Christensen-Dalsgaard, M. Gillon, J. F. Rowe, W. F. Welsh, E. R. Adams, A. Dupree, D. McCarthy, C. Kulesa, W. J. Borucki, and D. G. Koch, *Astrophys. J.* **735**, L12 (2011).
- [469] M. Sestovic, B. O. Demory, and D. Queloz, *Astron. Astrophys.* **616**, 13 (2018).
- [470] N. Nettelmann and D. Valencia, in *ExoFrontiers*, edited by N. Madhusudhan (IOP Publishing, Bristol, UK, 2021) Chap. 16.
- [471] S. Ginzburg and R. Sari, *Astrophys. J.* **803**, 111 (2015).
- [472] H. Kurokawa and S. I. Inutsuka, *Astrophys. J.* **815**, 78 (2015).
- [473] A. Vazan, R. Helled, and T. Guillot, *Astron. Astrophys.* **610**, L14 (2018).
- [474] J. Leconte, G. Chabrier, and I. Baraffe, in *Proc. Int. Astron. Union*, Vol. 6 (2010) p. S276.
- [475] P. Arras and A. Socrates, *Astrophys. J.* **714**, 1 (2010).
- [476] P. Tremblin, G. Chabrier, N. J. Mayne, D. S. Amundsen, I. Baraffe, F. Debras, B. Drummond, J. Manners, and S. Fromang, *Astrophys. J.* **841**, 30 (2017).
- [477] F. Sainsbury-Martinez, P. Wang, S. Fromang, P. Tremblin, T. Dubos, Y. Meurdesoif, A. Spiga, J. Leconte, I. Baraffe, G. Chabrier, N. Mayne, B. Drummond, and F. Debras, *Astron. Astrophys.* **632**, A114 (2019).
- [478] A. N. Youdin and J. L. Mitchell, *Astrophys. J.* **721**, 1113 (2010).
- [479] E. D. Lopez and J. J. Fortney, *Astrophys. J.* **818**, 4 (2016).
- [480] J. D. Hartman, G. Á. Bakos, W. Bhatti, K. Penev, A. Bieryła, D. W. Latham, G. Kovács, G. Torres, Z. Csubry, M. de Val-Borro, L. Buchhave, T. Kovács, S. Quinn, A. W. Howard, H. Isaacson, B. J. Fulton, M. E. Everett, G. Esquerdo, B. Béky, T. Szklenar, E. Falco, A. Santerne, I. Boisse, G. Hébrard, A. Burrows, J. Lázár, I. Papp, P. Sári, M. de Val-Borro, L. Buchhave, T. Kovács, S. Quinn, A. W. Howard, H. Isaacson, B. J. Fulton, M. E. Everett, G. Esquerdo, B. Béky, T. Szklenar, E. Falco, A. Santerne, I. Boisse, G. Hébrard, A. Burrows, J. Lázár, I. Papp, and P. Sári, *Astron. J.* **152**, 182 (2016).
- [481] M. Rozner, H. Glanz, H. B. Perets, and E. Grishin, *Astrophys. J.* **931**, 10 (2022).
- [482] K. Batygin, S. Stanley, and D. J. Stevenson, *Astrophys. J.* **776**, 53 (2013).

- [483] R. Perna, K. Menou, and E. Rauscher, *Astrophys. J.* **719**, 1421 (2010).
- [484] R. Perna, K. Heng, and F. Pont, *Astrophys. J.* **751**, 59 (2012).
- [485] S. Ginzburg and R. Sari, *Astrophys. J.* **819**, 116 (2016).
- [486] K. Batygin, D. J. Stevenson, and P. H. Bodenheimer, *Astrophys. J.* **738**, 1 (2011).
- [487] D. S. Spiegel and A. Burrows, *Astrophys. J.* **772**, 76 (2013).
- [488] E. Rauscher and K. Menou, *Astrophys. J.* **764**, 103 (2013).
- [489] T. M. Rogers and T. D. Komacek, *Astrophys. J.* **794**, 132 (2014).
- [490] B. Pu and D. Valencia, *Astrophys. J.* **846**, 47 (2017).
- [491] H. Knierim, K. Batygin, and B. Bitsch, *Astron. Astrophys.* **658**, L7 (2022).
- [492] C. Soriano-Guerrero, D. Viganò, R. Perna, T. Akgün, and C. Palenzuela, *Mon. Not. R. Astron. Soc.* **525**, 626 (2023).
- [493] T. Akgün, C. Soriano-Guerrero, A. Elias-López, D. Viganò, R. Perna, and F. Del Sordo, *submitt. to AA* (2024), arXiv:2403.11501 .
- [494] K. Menou, *Astrophys. J.* **745**, 138 (2012).
- [495] K. Lodders, *Astrophys. J.* **591**, 1220 (2003).
- [496] Y. T. Lee and R. M. More, *Phys. Fluids* **27**, 1273 (1984).
- [497] M. French and R. Redmer, *Phys. Plasmas* **24**, 092306 (2017).
- [498] H. Beltz, E. Rauscher, M. T. Roman, and A. Guilliat, *Astron. J.* **163**, 35 (2022).
- [499] T. M. Rogers and J. N. McElwaine, *Astrophys. J. Lett.* **841**, L26 (2017).
- [500] F. Borsa, M. Rainer, A. S. Bonomo, D. Barbato, L. Fossati, L. Malavolta, V. Nascimbeni, A. F. Lanza, M. Esposito, L. Affer, G. Andreuzzi, S. Benatti, K. Biazzo, A. Bignamini, M. Brogi, I. Carleo, R. Claudi, R. Cosentino, E. Covino, M. Damasso, S. Desidera, A. Garrido Rubio, P. Giacobbe, E. González-Álvarez, A. Harutyunyan, C. Knapic, G. Leto, R. Ligi, A. Maggio, J. Maldonado, L. Mancini, A. F. Fiorenzano, S. Masiero, G. Micela, E. Molinari, I. Pagano, M. Pedani, G. Piotto, L. Pino, E. Poretti, G. Scandariato, R. Smareglia, and A. Sozzetti, *Astron. Astrophys.* **631**, A34 (2019).
- [501] M. Mansfield, J. L. Bean, K. B. Stevenson, T. D. Komacek, T. J. Bell, X. Tan, M. Malik, T. G. Beatty, I. Wong, N. B. Cowan, L. Dang, J.-M. Désert, J. J. Fortney, B. S. Gaudi, D. Keating, E. M.-R. Kempton, L. Kreidberg, M. R. Line, V. Parmentier, K. G. Stassun, M. R. Swain, and R. T. Zellem, *Astrophys. J.* **888**, L15 (2020).
- [502] I. Wong, A. Shporer, D. Kitzmann, B. M. Morris, K. Heng, H. J. Hoeijmakers, B.-O. Demory, J. P. Ahlers, M. Mansfield, J. L. Bean, T. Daylan, T. Fetherolf, J. E. Rodriguez, B. Benneke, G. R. Ricker, D. W. Latham, R. Vanderspek, S. Seager, J. N. Winn, J. M.

- Jenkins, C. J. Burke, J. L. Christiansen, Z. Essack, M. E. Rose, J. C. Smith, P. Tenenbaum, and D. Yahalomi, *Astron. J.* **160**, 88 (2020).
- [503] S. Csizmadia, H. Hellard, and A. M. Smith, *Astron. Astrophys.* **623**, A45 (2019).
- [504] S. C. Barros, B. Akınanmi, G. Boué, A. M. Smith, J. Laskar, S. Ulmer-Moll, J. Lillo-Box, D. Queloz, A. C. Cameron, S. G. Sousa, D. Ehrenreich, M. J. Hooton, G. Bruno, B. O. Demory, A. C. Correia, O. D. Demangeon, T. G. Wilson, A. Bonfanti, S. Hoyer, Y. Alibert, R. Alonso, G. A. Escudé, D. Barbato, T. Bárczy, D. Barrado, W. Baumjohann, M. Beck, T. Beck, W. Benz, M. Bergomi, N. Billot, X. Bonfils, F. Bouchy, A. Brandeker, C. Broeg, J. Cabrera, V. Cessa, S. Charnoz, C. C. Damme, M. B. Davies, M. Deleuil, A. Deline, L. Delrez, A. Erikson, A. Fortier, L. Fossati, M. Fridlund, D. Gandolfi, A. G. Muñoz, M. Gillon, M. Güdel, K. G. Isaak, K. Heng, L. Kiss, A. L. Des Etangs, M. Lendl, C. Lovis, D. Magrin, V. Nascimbeni, P. F. Maxted, G. Olofsson, R. Ottensamer, I. Pagano, E. Pallé, H. Parviainen, G. Peter, G. Piotto, D. Pollacco, R. Ragazzoni, N. Rando, H. Rauer, I. Ribas, N. C. Santos, G. Scandariato, D. Ségransan, A. E. Simon, M. Steller, G. M. Szabó, N. Thomas, S. Udry, B. Ulmer, V. Van Grootel, and N. A. Walton, *Astron. Astrophys.* **657**, A52 (2022).
- [505] H. Hellard, S. Csizmadia, S. Padovan, H. Rauer, J. Cabrera, F. Sohl, T. Spohn, and D. Breuer, *Astrophys. J.* **878**, 119 (2019).
- [506] H. Hellard, S. Csizmadia, S. Padovan, F. Sohl, and H. Rauer, *Astrophys. J.* **889**, 66 (2020).
- [507] B. Akınanmi, S. C. Barros, N. C. Santos, A. C. Correia, P. F. Maxted, G. Boué, and J. Laskar, *Astron. Astrophys.* **621**, A117 (2019).
- [508] U. Kramm, N. Nettelmann, R. Redmer, and D. J. Stevenson, *Astron. Astrophys.* **528**, A18 (2011).
- [509] U. Kramm, N. Nettelmann, J. J. Fortney, R. Neuhäuser, and R. Redmer, *Astron. Astrophys.* **538**, A146 (2012).
- [510] C. Kellermann, A. Becker, and R. Redmer, *Astron. Astrophys.* **615**, A39 (2018).
- [511] S. Padovan, T. Spohn, P. Baumeister, N. Tosi, D. Breuer, S. Csizmadia, H. Hellard, and F. Sohl, *Astron. Astrophys.* **620**, A178 (2018).
- [512] C. R. Lynch, T. Murphy, E. Lenc, and D. L. Kaplan, *Mon. Not. R. Astron. Soc.* **478**, 1763 (2018).
- [513] Y. Cendes, P. K. G. Williams, and E. Berger, *Astron. J.* **163**, 15 (2022).
- [514] D. A. Brain, M. M. Kao, and J. G. O'Rourke, *Rev. Mineral. Geochemistry* **90**, preprint (2024), [arXiv:arXiv.2404.15429](https://arxiv.org/abs/2404.15429) [10.48550] .
- [515] A. Oklopčić and C. M. Hirata, *Astrophys. J.* **855**, L11 (2018).

- [516] A. Oklopčić, M. Silva, P. Montero-Camacho, and C. M. Hirata, *Astrophys. J.* **890**, 88 (2020).
- [517] F. Soubiran, B. Militzer, K. P. Driver, and S. Zhang, *Phys. Plasmas* **24**, 041401 (2017).
- [518] M. A. Morales, E. Schwegler, D. Ceperley, C. Pierleoni, S. Hamel, and K. Caspersen, *Proc. Natl. Acad. Sci. U. S. A.* **106**, 1324 (2009).
- [519] M. A. Morales, S. Hamel, K. Caspersen, and E. Schwegler, *Phys. Rev. B* **87**, 174105 (2013).
- [520] J. J. Fortney and W. B. Hubbard, *Icarus* **164**, 228 (2003).
- [521] M. French and N. Nettelmann, *Astrophys. J.* **881**, 81 (2019).
- [522] M. Mayor, F. Pepe, D. Queloz, F. Bouchy, G. Rupprecht, G. Lo Curto, G. Avila, W. Benz, J.-L. Bertaux, and E. Al., *ESO Messenger* **114**, 20 (2003).
- [523] F. Bouchy, É. Artigau, O. Hernandez, C. Lovis, and P. Figueira, *Messenger* **169** **1**, 21 (2017).
- [524] F. Pepe, S. Cristiani, R. Rebolo, N. C. Santos, H. Dekker, A. Cabral, P. Di Marcantonio, P. Figueira, G. Lo Curto, C. Lovis, M. Mayor, D. Mégevand, P. Molaro, M. Riva, M. R. Zapatero Osorio, M. Amate, A. Manescau, L. Pasquini, F. M. Zerbi, V. Adibekyan, M. Abreu, M. Affolter, Y. Alibert, M. Aliverti, R. Allart, C. Allende Prieto, D. Álvarez, D. Alves, G. Avila, V. Baldini, T. Bandy, S. C. Barros, W. Benz, A. Bianco, F. Borsa, V. Bourrier, F. Bouchy, C. Broeg, G. Calderone, R. Cirami, J. Coelho, P. Conconi, I. Coretti, C. Cumani, G. Cupani, V. D’Odorico, M. Damasso, S. Deiries, B. Delabre, O. D. Demangeon, X. Dumusque, D. Ehrenreich, J. P. Faria, A. Fragoso, L. Genolet, M. Genoni, R. Génova Santos, J. I. González Hernández, I. Hughes, O. Iwert, F. Kerber, J. Knudstrup, M. Landoni, B. Lavie, J. Lillo-Box, J. L. Lizon, C. Maire, C. J. Martins, A. Mehner, G. Micela, A. Modigliani, M. A. Monteiro, M. J. Monteiro, M. Moschetti, M. T. Murphy, N. Nunes, L. Oggioni, A. Oliveira, M. Oshagh, E. Pallé, G. Pariani, E. Poretti, J. L. Rasilla, J. Rebordão, E. M. Redaelli, S. Santana Tschudi, P. Santin, P. Santos, D. Ségransan, T. M. Schmidt, A. Segovia, D. Sosnowska, A. Sozzetti, S. G. Sousa, P. Spanò, A. Suárez Mascareño, H. Taberner, F. Tenegi, S. Udry, and A. Zanutta, *Astron. Astrophys.* **645**, A96 (2021).
- [525] T. D. Gebhard, D. Angerhausen, B. S. Konrad, E. Alei, S. P. Quanz, and B. Schölkopf, *Astron. Astrophys.* **681**, A3 (2024).
- [526] P. Baumeister, S. Padovan, N. Tosi, G. Montavon, N. Nettelmann, J. MacKenzie, and M. Godolt, *Astrophys. J.* **889**, 42 (2020).
- [527] P. Baumeister and N. Tosi, *Astron. Astrophys.* **676**, A106 (2023).
- [528] A. W. Mann, M. C. Johnson, A. Vanderburg, A. L. Kraus, A. C. Rizzuto, M. L. Wood, J. L. Bush, K. Rockcliffe, E. R. Newton, D. W. Latham, E. E. Mamajek, G. Zhou, S. N. Quinn, P. C. Thao, S. Benatti, R. Cosentino, S. Desidera, A. Harutyunyan, C. Lovis,

- A. Mortier, F. A. Pepe, E. Poretti, T. G. Wilson, M. H. Kristiansen, R. Gagliano, T. Jacobs, D. M. LaCourse, M. Omohundro, H. M. Schwengeler, I. A. Terentev, S. R. Kane, M. L. Hill, M. Rabus, G. A. Esquerdo, P. Berlind, K. A. Collins, G. Murawski, N. H. Sallam, M. M. Aitken, B. Massey, G. R. Ricker, R. Vanderspek, S. Seager, J. N. Winn, J. M. Jenkins, T. Barclay, D. A. Caldwell, D. Dragomir, J. P. Doty, A. Glidden, P. Tenenbaum, G. Torres, J. D. Twicken, and S. Villanueva Jr, *Astron. J.* **160**, 179 (2020).
- [529] B. K. Capistrant, M. Soares-Furtado, A. Vanderburg, A. Jankowski, A. W. Mann, G. Ross, G. Srdoc, N. R. Hinkel, J. Becker, C. Magliano, M. A. Limbach, A. P. Stephan, A. C. Nine, B. M. Tofflemire, A. L. Kraus, S. Giacalone, J. N. Winn, A. Bieryla, L. G. Bouma, D. R. Ciardi, K. A. Collins, G. Covone, Z. L. de Beurs, C. X. Huang, J. M. Jenkins, L. Kreidberg, D. W. Latham, S. N. Quinn, S. Seager, A. Shporer, J. D. Twicken, B. Wohler, R. K. Vanderspek, R. Yarza, and C. Ziegler, *Astron. J.* **167**, 54 (2024).
- [530] K. Lodders, *Solar Elemental Abundances* (2020).
- [531] J. N. Bahcall, M. H. Pinsonneault, and G. J. Wasserburg, *Rev. Mod. Phys.* **67**, 781 (1995).
- [532] M. Asplund, N. Grevesse, A. J. Sauval, and P. Scott, *Annu. Rev. Astron. Astrophys.* **47**, 481 (2009).
- [533] E. Linder, *Linking planetary evolution and observations*, Ph.D. thesis, University of Bern (2019).
- [534] J. MacKenzie, J. L. Grenfell, P. Baumeister, N. Tosi, J. Cabrera, and H. Rauer, *Astron. Astrophys.* **671**, A65 (2023).
- [535] N. Bogatyreva, *PLANCK AND ROSSELAND MEANS OF ABSORPTION COEFFICIENTS IN SF₆* (2023).
- [536] D. Semenov, T. Henning, C. Helling, M. Ilgner, and E. Sedlmayr, *Astron. Astrophys.* **410**, 611 (2003).
- [537] J. Tennyson and S. N. Yurchenko, *Mon. Not. R. Astron. Soc.* **425**, 21 (2012).
- [538] I. E. Gordon, L. S. Rothman, R. J. Hargreaves, R. Hashemi, E. V. Karlovets, F. M. Skinner, E. K. Conway, C. Hill, R. V. Kochanov, Y. Tan, P. Weislo, A. A. Finenko, K. Nelson, P. F. Bernath, M. Birk, V. Boudon, A. Campargue, K. V. Chance, A. Coustenis, B. J. Drouin, J. M. Flaud, R. R. Gamache, J. T. Hodges, D. Jacquemart, E. J. Mlawer, A. V. Nikitin, V. I. Perevalov, M. Rotger, J. Tennyson, G. C. Toon, H. Tran, V. G. Tyuterev, E. M. Adkins, A. Baker, A. Barbe, E. Canè, A. G. Császár, A. Dudaryonok, O. Egorov, A. J. Fleisher, H. Fleurbaey, A. Foltynowicz, T. Furtenbacher, J. J. Harrison, J. M. Hartmann, V. M. Horneman, X. Huang, T. Karman, J. Karns, S. Kassi, I. Kleiner, V. Kofman, F. Kwabia-Tchana, N. N. Lavrentieva, T. J. Lee, D. A. Long, A. A. Lukevskaya, O. M. Lyulin, V. Y. Makhnev, W. Matt, S. T. Massie, M. Melosso, S. N. Mikhailenko, D. Mondelain, H. S. Müller, O. V. Naumenko, A. Perrin, O. L. Polyansky,

- E. Raddaoui, P. L. Raston, Z. D. Reed, M. Rey, C. Richard, R. Tóbiás, I. Sadiek, D. W. Schwenke, E. Starikova, K. Sung, F. Tamassia, S. A. Tashkun, J. Vander Auwera, I. A. Vasilenko, A. A. Vigin, G. L. Villanueva, B. Vispoel, G. Wagner, A. Yachmenev, and S. N. Yurchenko, *J. Quant. Spectrosc. Radiat. Transf.* **277**, 107949 (2022).
- [539] J. Tennyson, in *Astrophys. Exopl. Atmos.* (Springer, Cham, 2018) pp. 91–132.
- [540] A. Sanchez-Lavega, S. Perez-Hoyos, and R. Hueso, *Am. J. Phys.* **72**, 767 (2004).
- [541] C. Visscher, K. Lodders, and B. Fegley, Jr., *Astrophys. J.* **648**, 1181 (2006).
- [542] C. Visscher, K. Lodders, and B. Fegley, Jr., *Astrophys. J.* **716**, 1060 (2010).
- [543] C. V. Morley, J. J. Fortney, M. S. Marley, C. Visscher, D. Saumon, and S. K. Leggett, *Astrophys. J.* **756**, 172 (2012).
- [544] K. Lodders and B. Fegley, *Icarus* **155**, 393 (2002).
- [545] ISO International Standard ISO/IEC 14882:2020(E) – Programming Language C++.
- [546] P. Gnu, *Free Software Foundation Bash (3.2.48)[Unix shell program]*, Tech. Rep. (2007).
- [547] G. van Rossum, *Python tutorial, Technical Report CS-R9526*, Tech. Rep. (Centrum voor Wiskunde en Informatica (CWI), Amsterdam (Netherlands), 1995).
- [548] J. D. Hunter, *Comput. Sci. Eng.* **9**, 90 (2007).
- [549] S. Van Der Walt, S. C. Colbert, and G. Varoquaux, *Comput. Sci. Eng.* **13**, 22 (2011).
- [550] T. P. Robitaille, E. J. Tollerud, P. Greenfield, M. Droettboom, E. Bray, T. Aldcroft, M. Davis, A. Ginsburg, A. M. Price-Whelan, W. E. Kerzendorf, A. Conley, N. Crighton, K. Barbary, D. Muna, H. Ferguson, F. Grollier, M. M. Parikh, P. H. Nair, H. M. Günther, C. Deil, J. Woillez, S. Conseil, R. Kramer, J. E. Turner, L. Singer, R. Fox, B. A. Weaver, V. Zabalza, Z. I. Edwards, K. Azalee Bostroem, D. J. Burke, A. R. Casey, S. M. Crawford, N. Dencheva, J. Ely, T. Jenness, K. Labrie, P. L. Lim, F. Pierfederici, A. Pontzen, A. Ptak, B. Refsdal, M. Servillat, and O. Streicher, *Astron. Astrophys.* **558**, A33 (2013).
- [551] E. Jones, T. Oliphant, and P. Peterson, *SciPy: Open source scientific tools for Python* (2001).
- [552] B. Harrington and E. al., *Inkscape Project* (2004).
- [553] F. Bianchi, *Coolers - Color Palette Generator*.
- [554] C. Brewer, *Colorbrewer* (2013).
- [555] A. Rohatgi, *Webplotdigitizer* (2011).

Curriculum Vitae

Born on 17.02.1992 in Hagen, Germany

Education

- 06/2018 - 10/2024 Ph.D. student, Statistical Physics Group, University of Rostock, Germany
Supervisor: Prof. Dr. Ronald Redmer
- 04/2016 - 05/2018 Master of Science in Physics, University of Rostock, Germany
Thesis: *Der Einfluss von Wolken in der Berechnung der Struktureigenschaften großer Exoplaneten*
Supervisors: Prof. Dr. Ronald Redmer, Dr. Nadine Nettelmann
- 08/2015 - 02/2016 Semester abroad, Universidad Nacional de La Plata, Argentina
Courses: stellar evolution, planetary formation and evolution, computational methods in astrophysics
- 09/2011 - 08/2014 Bachelor of Science in Physics, University of Rostock, Germany
Thesis: *Masse-Radius-Relationen von Exoplaneten*
Supervisors: Prof. Dr. Ronald Redmer, Dr. Andreas Becker
- 2003 - 2011 Städtisches Gymnasium Gevelsberg, general qualification of university entrance (German: Abitur)

Research and Work Experience

- 06/2018 - 10/2023 Research assistant, Statistical Physics Group, U Rostock
- 12/2016 - 12/2018 Student assistant, PhySch (Teaching and Outreach Facility at Institute of Physics, U Rostock)
- 12/2016 - 12/2017 Student assistant, Rostock International House (International Office, U Rostock)
- 2016 Student assistant, Statistical Physics Group, U Rostock
- 10/2014 - 06/2015 Internship at SEAT, S.A. (Spain) in the automotive industry, departments: aerodynamics, acoustics, consumption, emissions, and CO₂
- 2013 - 2014 Student assistant, E-Learning Forum MNF (introductions to first-year students), PhySch (Teaching and Outreach Facility at Institute of Physics, U Rostock)

Commitment, Outreach, and Teaching

- 2023 Member of project team of the renovation of the *Planetenweg Warnemünde* in the context of the university competition of *Wissenschaft im Dialog*
- 2022 - 2023 Supervising a project for *Jugend forscht e. V.*
Implikationen eines Exoplaneten auf die Spin Evolution eines isolierten Pulsars by Emilia Lucia Artigas Träger, Bent Gröschner, and Weda Zeug
 (1st prize Landeswettbewerb Mecklenburg-Vorpommern 2023, Fachgebiet Geo- und Raumwissenschaften)
- 2019 - 2020 Supervising a project for *Jugend forscht e. V.*
Eigenheiten im äußeren Sonnensystem - Erforschung zweier Erklärungsansätze by Lukas Schicht
 (1st prize Landeswettbewerb Mecklenburg-Vorpommern 2020, Fachgebiet Geo- und Raumwissenschaften)
- 08/2020 - 02/2022 Speaker of the Mental Health Initiative (MHI) of the Institute of Physics
- 03/2020 - 10/2021 Speaker of the Graduate Research Training Group of the Institute of Physics
- 10/2019 - 03/2020 Co-speaker of the Graduate Research Training Group of the Institute of Physics
- WS 2019/20 Lab course *Physik für Humanmediziner*
- SS 2019 Lab course *Grundpraktikum I*
- WS 2018/19 Lab course *Physik für Humanmediziner*
- 2018 - 2020 Supervising several pupils in the context of school internships

List of Publications

1. A. J. Poser, N. Nettelmann, and R. Redmer
The Effect of Clouds as an Additional Opacity Source on the Inferred Metallicity of Giant Exoplanets
Atmosphere 10(11), **664** (2019)
18 pages
2. A. J. Poser and R. Redmer
The effect of cloudy atmospheres on the thermal evolution of warm giant planets from an interior modelling perspective
Monthly Notices of the Royal Astronomical Society **529** (3), 2242-2257 (2024)
16 pages
3. S. Kumar, A. J. Poser, M. Schöttler, U. Kleinschmidt, W. Dietrich, J. Wicht, M. French, and R. Redmer
Ionization and transport in partially ionized multicomponent plasmas: Application to atmospheres of hot Jupiters
Physical Review E **103** (6), 063203 (2021)
12 pages
4. W. Dietrich, S. Kumar, A. J. Poser, M. French, N. Nettelmann, R. Redmer, and J. Wicht
Magnetic induction processes in hot Jupiters, application to KELT-9b
Monthly Notices of the Royal Astronomical Society **517** (3), 3113-3125 (2022)
13 pages

List of Talks

- *The effect of clouds on the interior structure and thermal evolution of giant planets*
Symposium on matter in extreme conditions
Jerusalem, Israel (2023)
- *Towards a better understanding of hot Jupiter observations*
9th meeting of the graduate network - department life, light and matter, Rostock
Online meeting (2022)
- *Towards a better understanding of hot Jupiter observations - combining atmosphere, interior, and dynamo models*
Atoms, molecules, cluster and plasma (AMCP) seminar, Rostock
Online seminar (2022)
- *Towards a better understanding of hot Jupiter observations - combining atmosphere, interior, and dynamo models*
Webinar of the DFG-SPP 1992 "Exploring the Diversity of Extrasolar Planets"
Online seminar (2021)
- *Observing and modeling young transiting planets*
All-decks-on-hand Meeting of the DFG-SPP 1992 "Exploring the diversity of extrasolar planets"
Hamburg, Germany (2019)
- *Clouds and their implication for the inferred metallicity of giant planets*
8th Joint Workshop on High Pressure, Planetary and Plasma Physics (HP4)
Dresden, Germany (2019)
- *Clouds and the Inferred Metallicity of Giant Extrasolar Planets*
Seminar of the Graduate Research Training Group of the Institute of Physics
Rostock, Germany (2019)
- *Clouds (in irradiated atmospheres) and their implication for interior models*
European Planetary Science Congress (EPSC)
Geneva, Switzerland (2019)
- *About clouds & their implication for interior models*
Northern Astrophysical Colloquium (NAC)
Rostock, Germany (2019)
- *Clouds and the inferred metallicity of giant exoplanets*
Workshop on atmospheres and interiors of exoplanets at the Institute of Planetary Physics
of the German National Space Agency (DLR)
Berlin, Germany (2019)
- *Influence of clouds on atmosphere and interior models of young exoplanets*
Workshop of the Young Exoplanet Initiative (YETI)
Jena, Germany (2018)

- *Modeling young hot Jupiters as a window to formation processes - Do clouds influence the interior models of giant planets?*
7th Joint Workshop on High Pressure, Planetary and Plasma Physics (HP4)
Berlin, Germany (2018)
- *Modeling transiting exoplanets*
Workshop on low mass planets
Rostock, Germany (2018)
- *Influence of clouds on atmosphere and interior models of giant exoplanets*
Northern Astrophysical Colloquium (NAC)
Hamburg, Germany (2018)
- *Observing and modeling young transiting exoplanets - atmosphere models for young irradiated planets*
Kick-off meeting of the DFG-SPP 1992 "Exploring the Diversity of Extrasolar Planets"
Berlin, Germany (2018)

List of Poster Presentations

- *Modeling irradiated gaseous giant planets*
Defense of Helmholtz Institute for High Energy Density
Rostock, Germany (2023)
- *The impact of clouds on the radius evolution of gas giants*
Wilhelm and Else Heraeus Seminar: From the Heliosphere to Astrospheres - Lessons for Exoplanets and their Habitability
Bad Honnef, Germany (2023)
- *Clouds and the radius evolution of hot Jupiters*
10th Joint Workshop on High Pressure, Planetary and Plasma Physics (HP4)
Brussels, Belgium (2022)
- *The role of clouds in the radius evolution of hot Jupiters*
Planet Formation and Evolution (PFE) and DFG-SPP 1992 Joint Meeting
Berlin, Germany (2022)
- *Clouds and the inferred metallicity of giant planets*
All-decks-on-hand meeting of the DFG-SPP 1992 "Exploring the Diversity of Extrasolar Planets"
Hamburg, Germany (2019)
- *The effect of clouds on the inferred metallicity of giant exoplanets*
ExoClimes V
Oxford, United Kingdom (2019)

- *Irradiated atmospheres and the core mass of hot Jupiters*
Planet Formation and Evolution (PFE)
Rostock, Germany (2019)
- *Modelling young hot Jupiters as a window to formation processes*
6th Joint Workshop on High Pressure, Planetary and Plasma Physics (HP4)
Göttingen, Germany (2017)
- *Modelling young transiting planets - impact of different atmosphere models*
2nd Advanced School on Exoplanetary Science: Exoplanetary Atmospheres
Vietri sul Mare, Italy (2017)
- *Masse-Radius-Relationen extrasolarer Planeten*
Conference for women in physics by the German Physical Society (DPG)
Hamburg, Germany (2016)

List of Attended Conferences without Abstract Submission

- 11th Joint Workshop on High Pressure, Planetary and Plasma Physics (HP4), Rostock, Germany (2023)
- I, scientist. Berlin, Germany (2019) and online meeting (2020)
- European Planetary Science Congress (EPSC), Berlin, Germany (2018)
- 10. Forum Wissenschaftskommunikation, Braunschweig, Germany (2017)

List of Attended Schools

- *Planets, exoplanets and their systems in a broad and multidisciplinary context* by Severo Ochoa Project of the Instituto de Astrofísica de Andalucía, online school (2021)
- *2nd Advanced School on Exoplanetary Science: Exoplanetary Atmospheres*, in Vietri sul Mare, Italy (2017)
- *Joint Space Weather Summer School* by the German National Space Agency, the South African National Space Agency, and the University of Alabama (USA), in Hermanus, South Africa, and Neustrelitz, Germany (2016)

Acknowledgements

Many people have contributed to the completion of this journey, and I would like to express my sincere gratitude to all of them.

First of all, I wish to thank Ronald Redmer for the possibility of working on my dream topic of planets & atmospheres, for the introduction to the community, the support, supervision, and advice during the years.

Thank you, Nadine Nettelmann, for introducing me to the worlds of planets & stars, and for the first years of your supervision.

Thanks to Sandeep Kumar, Wieland Dietrich, Johannes Wicht, Uwe Kleinschmidt, and Martin French for the joint work on magnetic fields and hot atmospheres.

A heartfelt thank you to our secretaries, Peggy Preuß and Waltraud Dulinski, and to the administrators of our group, Armin and Martin.

Further thanks to all the people I met along the way – those I worked with, spent time with, and, most importantly, learned from:

To Barcelona, and especially to Vicent, where the spark for astrophysics was reignited in me, and to Argentina, and especially to Gabriela Parisi, whose passion inspired me to continue with astrophysics.

To the physics & planet enthusiasts from all over the world: Engin Keles, Esther Linder, Jubin Lirawi, Liam Reynard, Philipp Baumeister, Richard Bischoff, Yael Cytter. Thanks to Ayla, Benjamin, Chongbing, Ludwig, Max, Mohammad, Samuel, and the wonderful people of AGs Kraus and Redmer – for the tea, coffee, and double espresso breaks with amarettini, baby-plant potting, and baklava. To people who are committed to community involvement and education: Jenni, Eframir, Olya, Bent, Emilia, Weda, Dascha. To Amelie, Anna, Anna Lena, Charlotte, Elisabeth, Eric, Hendrikje, Julia, Lea, Ronja, Tobi, Tom, Wietje, and Wilm, and thanks to Annegret, Josi, and Manuela.

Thanks to Mandy Bethkenhagen, Wiebke Loseries, Ravit Helled, and Pascale Ehrenfreund for being role models and inspiration.

To my family and to my partner for their unending support, in every way and always.

Selbstständigkeitserklärung

Die Gelegenheit zum vorliegenden Promotionsvorhaben ist mir nicht kommerziell vermittelt worden. Insbesondere habe ich keine Organisation eingeschaltet, die gegen Entgelt Betreuer*innen für die Anfertigung von Dissertationen sucht oder die mir obliegenden Pflichten hinsichtlich der Prüfungsleistungen für mich ganz oder teilweise erledigt.

Ich versichere hiermit an Eides statt, dass ich die vorliegende Arbeit selbstständig angefertigt und ohne fremde Hilfe verfasst habe. Dazu habe ich keine außer den von mir angegebenen Hilfsmitteln und Quellen verwendet und die den benutzten Werken inhaltlich und wörtlich entnommenen Stellen habe ich als solche kenntlich gemacht.

Rostock, den 12. Juni 2024

Anna Julia Poser